Imperial College London
Department of Physics

Magnetic reconnection exhausts in the solar wind

Rishi Mistry

October 2016

Submitted in part fulfilment of the requirements for the degree of
Doctor of Philosophy in Physics of Imperial College London
and the Diploma of Imperial College London

Abstract

The restructuring of magnetic fields in plasmas through the process of magnetic reconnection is important in laboratory experiments, magnetospheres and many astrophysical systems. In-situ observations of reconnection processes in the near-Earth environment provide an excellent opportunity to probe the physics of magnetic reconnection. In the solar wind, reconnection between interplanetary magnetic fields accelerates and heats solar wind plasma, generating large exhaust structures which may be intercepted by spacecraft.

In this thesis solar wind reconnection exhausts are probed using in-situ measurements from multiple spacecraft. A statistical survey of 188 exhausts is used to determine their average properties and show that the plasma density and temperature of the reconnection exhaust depends on the plasma beta and reconnection guide field. Whilst the ion temperature is found to depend on the plasma Alfvén speed (as has been previously demonstrated), we show that this scaling is more tenuous in the presence of strong guide fields. Comparisons of measurements between multiple spacecraft for three different events shows that the structure of the reconnection current sheet changes with increasing distance downstream of the reconnection site. Additionally, measurements of solar wind exhausts often differ considerably between different events. We show that much of this variability may be attributed to different inflow region conditions, the magnetic shear angle and the distance downstream of the X-line at which the exhaust is observed.

In addition to their average properties, less frequently observed properties of reconnection exhausts are presented. Hall physics is observed for the first time in solar wind exhausts, which is confirmed through quantitative comparisons with an appropriately scaled fully kinetic particle-in-cell simulation. These measurements indicate that narrow regions of kinetic physics can persist thousands of ion inertial lengths downstream of the reconnection site. Additionally, multi-spacecraft measurements are used for a case study event to reveal the small-scale three dimensional structure of a reconnection exhaust, indicating that whilst exhausts may be planar on large scales, they may also exhibit small scale structure.

Dedicated to my grandparents, for the lift off.

I declare that the work presented in this thesis is my own, except where explicitly indicated otherwise.

The copyright of this thesis rests with the author and is made available under a Creative Commons Attribution Non-Commercial No Derivatives licence. Researchers are free to copy, distribute or transmit the thesis on the condition that they attribute it, that they do not use it for commercial purposes and that they do not alter, transform or build upon it. For any reuse or redistribution, researchers must make clear to others the licence terms of this work.

−Rishi Mistry, October 2016.

Studies carried out for this thesis have lead to the following three peer-reviewed publications:

Mistry, R., Eastwood, J. P., & Hietala, H. 2015. Detection of small-scale folds at a solar wind reconnection exhaust. *Journal of Geophysical Research: Space Physics*, **120**(1), 30-42.

Mistry, R., Eastwood, J. P., Phan, T. D., & Hietala, H. 2015. Development of bifurcated current sheets in solar wind reconnection exhausts. *Geophysical Research Letters*, **42**(24), 10513-10520.

Mistry, R., Eastwood, J. P., Haggerty, C. C., Shay, M. A., Phan, T. D., Hietala, H., & Cassak, P. A. 2016. Observations of Hall reconnection physics far downstream of the X line. *Physical Review Letters*, **117**, 185102.

Acknowledgements

I would firstly like to thank my PhD supervisor, Jonathan Eastwood, for his guidance and support over the last few years. It has been a pleasure to work with Jonathan, and I am truly lucky to have been given this opportunity.

I am extremely grateful to Tai Phan for hosting me on several occasions at University of California, Berkeley, where he so frequently made time to share his immense wisdom and experience with me. I also sincerely thank Michael Shay for sharing his knowledge with me on many occasions over long phone calls and conference meeting tables. It has been an inspiration to work alongside many great scientists who I have learnt a great deal from, and I thank Heli Hietala, Colby Haggerty and Paul Cassak for the invaluable contributions that they have made to this work.

It has been amazing to spend my time at Imperial within the Space and Atmospheric Physics group. I'd like to thank many people here for the numerous pub trips, holiday trips and tea & cake breaks, allowing me to distract them from work when I needed a distraction, weekly climbing (Josh, Luc, Mehdi, Benoit, Amy & Ruth) and putting up with me as an office mate for over three years (Mehdi). I'd also like to many of the staff, students and postdocs for helpful conversations over the years. Thank you also to my friends and family outside of Imperial, I would have been quite lost without you.

Finally I'd like to thank my brother, Amar, for having more confidence in me than I did myself, and my parents for their love and support since day one.

Contents

Abstract **2**

Acknowledgements **5**

List of Tables **9**

List of Figures **12**

Nomenclature **13**

1 Introduction **15**

1.1 Magnetic reconnection models 16

1.1.1 Sweet-Parker reconnection 18

1.1.2 Petschek reconnection 21

1.1.3 Collisionless reconnection 23

1.2 Important factors in magnetic reconnection 25

1.2.1 Guide field 27

1.2.2 Plasma β 27

1.2.3 Asymmetric reconnection 28

1.2.4 The third dimension 28

1.3 Simulations of reconnection 29

1.3.1 Magnetohydrodynamics 29

1.3.2 Particle-in-cell 30

1.3.3 Hybrid 31

1.4 The Sun and the solar wind 31

1.4.1 The Sun 32

1.4.2 The solar wind 33

1.5 Reconnection exhausts in the solar wind 37

1.5.1 Single spacecraft observations 37

1.5.2 Particle heating 40

1.5.3 Multi-spacecraft observations 40

1.5.4 High resolution measurements 42

1.5.5 Distance downstream of the X-line 42

1.5.6 Reconnection onset . . . 42
1.6 Near-Earth reconnection environments . . . 43
1.7 Outstanding questions . . . 47
1.8 Thesis overview . . . 48

2 Instrumentation, methods & data survey 50
2.1 Introduction . . . 50
2.2 Spacecraft . . . 50
2.2.1 Cluster . . . 50
2.2.2 Wind . . . 51
2.2.3 ACE . . . 51
2.3 Instruments . . . 52
2.3.1 Fluxgate magnetometer . . . 52
2.3.2 Electrostatic analyser . . . 54
2.3.3 Probing of electron density using high frequency waves . . . 58
2.4 Current sheet normal determination techniques . . . 58
2.4.1 Minimum variance analysis . . . 59
2.4.2 Hybrid-minimum variance analysis . . . 60
2.4.3 3-spacecraft determination of solar wind current sheet normals . . . 61
2.4.4 Multi-spacecraft discontinuity timing analysis . . . 63
2.5 Walén relation . . . 64
2.6 Survey for solar wind reconnection exhausts using Cluster . . . 65
2.6.1 Introduction . . . 65
2.6.2 Survey methodology . . . 66
2.6.3 Event detection rate . . . 71
2.6.4 Current sheet and reconnection exhaust properties . . . 73
2.6.5 Conclusions . . . 76

3 Statistical properties of reconnection exhausts in the solar wind 79
3.1 Introduction . . . 79
3.2 Data set . . . 81
3.3 Statistical overview of data set . . . 82
3.3.1 Current sheet and exhaust properties . . . 82
3.3.2 Current sheet normal coordinates . . . 85
3.3.3 Exhaust outflow speeds . . . 86
3.4 Average properties of reconnection exhausts far downstream of the X-line: Superposed epoch analysis . . . 88
3.4.1 Method . . . 91
3.4.2 Results . . . 92
3.4.3 Discussion . . . 97

3.5 Thermal and magnetic pressure within reconnection exhausts: the effects of guide fields and plasma beta . . . 100
3.6 Ion heating as a function of inflow region Alfvén speed . . . 108
3.7 Conclusions . . . 113

4 Current sheet bifurcations: dependence on distance downstream of the X-line 115
4.1 Introduction . . . 115
4.2 Observations . . . 117
4.2.1 Event 1 . . . 117
4.2.2 Event 2 . . . 120
4.2.3 Event 3 . . . 120
4.3 Distance downstream from the X-line: macroscopic reconnection geometry . 122
4.4 Estimates of the exhaust opening angle from local measurements . . . 124
4.4.1 Normal component of the magnetic field . . . 127
4.4.2 Normal component of inflow velocity . . . 127
4.4.3 Cluster multi-spacecraft timing analysis . . . 128
4.5 Discussion . . . 129
4.6 Conclusions . . . 133

5 Hall physics far downstream of the X-line 135
5.1 Introduction . . . 135
5.2 Identification of Hall magnetic fields . . . 139
5.3 Comparison of observed data and a PIC simulation . . . 142
5.4 Hall magnetic fields at 8 reconnection exhausts . . . 149
5.5 Observations of Hall fields on both sides of the X-line: dual spacecraft observations . . . 150
5.6 Conclusions . . . 154

6 Small-scale structure of a reconnection exhaust 156
6.1 Introduction . . . 156
6.2 Overview of Cluster observations . . . 158
6.3 Large scale current sheet structure . . . 162
6.4 Detailed analysis of exhaust structure at Cluster . . . 166
6.5 Discussion . . . 171
6.6 Conclusions . . . 172

7 Conclusions 174

Bibliography 178

List of Tables

1.1 Plasma properties in the solar wind, magnetosheath and magnetotail 36

2.1 Properties of events identified in a survey of Cluster data 74

3.1 Properties of 188 exhausts observed using Wind 82

4.1 Multi-spacecraft measurements of three reconnection exhausts 118

5.1 Properties of 8 exhausts with Hall fields 149

List of Figures

1.1 Sweet-Parker reconnection 19
1.2 Exhaust opening angle and reconnection rate 21
1.3 Petschek reconnection 22
1.4 Collisionless reconnection 26
1.5 Solutions to the Parker solar wind equation 34
1.6 Magnetic field lines from the Sun near solar minimum 35
1.7 ISEE-3 measurements of a reconnection exhaust 38
1.8 Interpretation of reconnection signatures 39
1.9 Reduced proton distributions at a solar wind reconnection exhaust 41
1.10 The solar wind-magnetosphere interaction 44

2.1 Fluxgate magnetometer design 54
2.2 Electrostatic analyser design 55
2.3 3-spacecraft determination of solar wind current sheet normals 62
2.4 Cluster inter-spacecraft distances 67
2.5 2 hour CSA plot of C-1 measurements in the solar wind 68
2.6 Example event in LMN coordinates 70
2.7 Monthly sunspot number 72
2.8 Solar wind velocity during surveyed periods 73
2.9 Exhaust duration, width and inflow region parameters 75
2.10 Inflow region asymmetry, exhaust speeds and guide field 77

3.1 Exhaust duration and width 83
3.2 Exhaust inflow region parameters 84
3.3 Asymmetry between inflow regions 85
3.4 Guide fields and magentic shear angles 85
3.5 Differences between LMN vectors determined from MVA and hybrid-MVA 86
3.6 Solar wind speed, exhaust outflow speed, velocity shear 88
3.7 Estimated X-line drift speed due to velocity shear 89
3.8 Comparison of Alfvén speeds 89
3.9 Exhaust outflow speed and inflow region Alfvén speed 90
3.10 Coordinate systems for events with different reconnection geometries 93

3.11 Superposed epoch analysis 94
3.12 1D reconnection exhaust simulation with a hybrid code 99
3.13 Superposed epoch analysis by guide field 101
3.14 Exhaust region parameters as a function of guide field 102
3.15 Inflow region and exhaust region pressures 103
3.16 Ratio of exhaust region to inflow region thermal pressure, as a function of plasma beta and guide field 105
3.17 Comparison between observed thermal pressure increase and best fit to the data 106
3.18 Exhaust region to inflow region thermal pressure: empirical fit 107
3.19 Ion temperature within reconnection exhausts 109
3.20 Ion temperature within reconnection exhausts by guide field 110

4.1 C-1 and Wind measurements of Event 1 119
4.2 C-1, Wind and ACE measurements of Event 2 121
4.3 C-1 and Wind measurements of Event 3 123
4.4 Estimated distance of spacecraft from the X-line 125
4.5 Spacecraft locations in the LM plane 126
4.6 Normal component of the inflow velocity measured by a spacecraft 128
4.7 Event 1: Cluster 4-spacecraft measurements of B_L 130
4.8 Event 1: Normal vectors generated from multi-spacecraft timing analysis . . 130
4.9 Event 3: Cluster 4-spacecraft measurements of B_L 131
4.10 Event 3: Normal vectors generated from multi-spacecraft timing analysis . . 131

5.1 Hall magnetic fields in the ion diffusion region and exhaust 137
5.2 Event with a unipolar increase in B_M 140
5.3 Event with multiple changes in B_M 141
5.4 Comparison of observed data and PIC simulation 144
5.5 PIC simulation results 145
5.6 $B_L - B_M$ hodograms from observations and PIC simulation 147
5.7 Ion and electron velocities in PIC simulation 148
5.8 B_M for 8 events with Hall fields 151
5.9 Wind and ACE measurements of Hall fields on both sides of the X-line . . . 152
5.10 Wind and ACE $B_L - B_M$ hodograms 153

6.1 Cluster, Wind and ACE positions - 17 January 2002 158
6.2 C-3 measurements 160
6.3 C-1 and C-3 measurements 161
6.4 ACE and Wind measurements 163
6.5 ACE and Wind positions relative to Cluster in the LM plane 165

6.6 Cluster 4-spacecraft measurements 167
6.7 Exhaust structure in the MN plane 169
6.8 Three dimensional visualisation of exhaust structure 170

Nomenclature

3DP	3D Plasma Analyzer (onboard Wind spacecraft)
ACE	Advanced Composition Explorer
AU	Astronomical unit, 1.50×10^8 km
β	Plasma beta - ratio of thermal to magnetic pressure
B	Magnetic field
B_G	Guide field - ratio of inflow region out-of-plane magnetic field to reconnecting magnetic field - B_M/B_L
C_{AS}	Inflow region Alfvén speed as defined by Cassak & Shay (2007)
C-1, C-2, C-3, C-4	Cluster spacecraft
CIS-HIA	Cluster Ion Spectrometry - Hot Ion Analyser (onboard Cluster spacecraft)
CSA	Cluster Science Archive
d_i	Ion inertial length using the density of the inflow region, unless otherwise specified
E	Electric field
GSE	Geocentric Solar Ecliptic coordinates
hybrid-MVA	Hybrid-Minimum Variance Analysis
ICME	Interplanetary coronal mass ejection
IMF	Interplanetary magnetic field
ISEE-3	International Sun-Earth Explorer 3
J	Current density
LMN	Current sheet aligned coordinates
m_e	Electron mass, 9.11×10^{-31} kg
MHD	Magnetohydrodynamics
m_i	Ion mass
MVA	Minimum Variance Analysis
n	Number density

ρ	mass density
PIC	Particle-in-cell
R_E	Earth radius, 6,371 km
SWEPAM	Solar Wind Electron Proton Alpha Monitor (onboard ACE spacecraft)
T	Temperature
UT	Universal time
$\mathbf{V}$	Velocity
$V_{A,L}$	Alfvén speed using the L-component of the magnetic field
$\mathbf{V_{SW}}$	Solar wind velocity
WHISPER	Waves of HIgh frequency and Sounder for Probing of Electron density by Relaxation (onboard Cluster spacecraft)

1 Introduction

Magnetic fields and plasmas are present across many scales in the universe. They are generated in small-scale laboratory experiments, extend from the Sun to throughout the solar system, and connect astrophysical objects across galactic scales. Plasmas and the magnetic fields within them are intimately connected and form highly complex systems governed by the microphysics of particle dynamics in the presence of magnetic and electric fields. These magnetic fields can store vast amounts of energy. The release of this energy most frequently occurs through a topological restructuring of magnetic fields. This process, termed *magnetic reconnection*, transfers stored magnetic energy to heating of the plasma, creating high speed plasma flows (Yamada *et al.*, 2010). Magnetic reconnection is a process of much interest as it has been recognised that magnetic reconnection is necessary for the efficient release of stored magnetic energy in planetary, stellar and astrophysical systems (Zweibel & Yamada, 2009).

Plasma that is accelerated by magnetic reconnection forms exhausts of fast plasma flow. These reconnection exhausts are a direct consequence of magnetic reconnection and their detection not only provides clear evidence that reconnection has occurred, but also provides insight into how reconnection accelerates and heats plasma. Reconnection exhausts have been directly observed using in-situ spacecraft measurements in the Earth's magnetotail and magnetopause, at the magnetospheres of other planets, and in the solar wind (e.g., Paschmann *et al.*, 2013). In the solar wind, reconnection between interplanetary magnetic fields results in the formation of large exhaust structures (e.g., Phan *et al.*, 2009). The exhaust outflows extend into the solar wind relatively unimpeded, which is in contrast to many other environments where the background plasma is not uniform and reconnection outflows often meet other plasma structures. Measurements made by spacecraft which pass through solar wind reconnection exhausts therefore provide an ideal opportunity to study the exhausts that reconnection forms, in the absence of other plasma interactions and processes.

In this chapter we introduce key concepts and theoretical models of magnetic reconnection, and how numerical simulations can be used to better understand the reconnection process. Magnetic reconnection processes in the solar wind are introduced and we summarise what has been learnt about solar wind reconnection exhausts using in-situ observa-

tions. Solar wind reconnection is also compared to reconnection at the magnetopause and magnetotail, where the solar wind couples to Earth's magnetosphere via reconnection.

1.1 Magnetic reconnection models

The idea of magnetic reconnection was built upon observations by Giovanelli (1946) that solar flares (enormous bursts of radiation from the Sun) occur near regions of intense magnetic fields near the solar surface, and suggestions that these flares occur at locations of magnetic nulls i.e., where the magnetic field is locally zero. The first model for reconnection was the Sweet-Parker model (Parker, 1957; Sweet, 1958) which described reconnection between oppositely directed magnetic fields using the magnetohydrodynamic (MHD) theory of plasmas. It was immediately realised, however, that the rates at which fields reconnect in this model were too slow compared to observed rates, which led to Petschek (1964) developing a model for *fast* reconnection. Whilst the Petschek model received much attention, it was later realised that the Petschek configuration with a small current sheet and open exhaust outflows was only achievable if an artificially large and localised plasma resistivity is imposed at the reconnection site (Biskamp, 1986). Considerable progress was made when non-MHD effects were included, which showed Hall effects to be critical in achieving fast reconnection (e.g., Mandt *et al.*, 1994; Birn *et al.*, 2001). Reconnection in these collisionless models also produces open outflow exhausts. The reconnection exhausts that result from such steady state reconnection are the subject of this thesis.

We also note that reconnection can occur in unsteady states (e.g., Furth *et al.*, 1963; Drake *et al.*, 2006; Lapenta, 2008; Tenerani *et al.*, 2015) as well as in turbulent media (Lazarian & Vishniac, 1999; Kowal *et al.*, 2009), however large scale reconnection exhausts are not formed from these processes. In this section the Sweet-Parker, Petschek and collisionless reconnection models are introduced.

Magnetic reconnection occurs in plasmas, which are quasi-neutral gases of charged particles. In ideal-MHD, plasmas are assumed to be perfect conductors. Under this assumption, the electric field $\mathbf{E}$ in a reference frame moving with the plasma is zero, in which case

$$\mathbf{E} = -\mathbf{V} \times \mathbf{B}, \tag{1.1}$$

where $\mathbf{V}$ is the plasma velocity and $\mathbf{B}$ is the magnetic field. If there is a finite resistivity the form of the electric field is modified to account for resistive effects. This is described by Ohm's law,

$$\mathbf{E} = -\mathbf{V} \times \mathbf{B} + \eta \mathbf{J}, \tag{1.2}$$

where η is the plasma resistivity and $\mathbf{J}$ is the current density. Faraday's law states that

$$\frac{\partial \mathbf{B}}{\partial t} = -\nabla \times \mathbf{E} \tag{1.3}$$

in which we can substitute Equation 1.2 to obtain

$$\frac{\partial \mathbf{B}}{\partial t} = \nabla \times (\mathbf{V} \times \mathbf{B}) - \nabla \times (\eta \mathbf{J}). \tag{1.4}$$

Using Ampère's law,

$$\frac{\partial \mathbf{B}}{\partial t} = \nabla \times (\mathbf{V} \times \mathbf{B}) - \nabla \times (\eta/\mu_0 \nabla \times \mathbf{B}), \tag{1.5}$$

where μ_0 is the permeability of free space. This simplifies to the magnetic induction equation

$$\frac{\partial \mathbf{B}}{\partial t} = \nabla \times (\mathbf{V} \times \mathbf{B}) + \zeta \nabla^2 \mathbf{B}, \tag{1.6}$$

where the magnetic diffusivity is $\zeta = \eta/\mu_0$. This equation describes the evolution of the magnetic field in a plasma. In a perfectly conducting plasma (ideal-MHD), $\eta \to 0$ and the magnetic field convects with the plasma as if the field lines were tied to a fluid element. This is the frozen-in field theorem of ideal-MHD. This also implies that the plasma is tied to the magnetic field, and as such plasma elements on different field lines can never mix.

The relative amplitude of the terms in the magnetic induction equation can be used to understand the behaviour of the magnetic field and plasma when η is not equal to zero. We consider variations in the plasma over length scales L and that have a characteristic speed V. The magnitude of the first and second terms of Equation 1.6 are then given as VB/L and $\zeta B/L^2$, respectively. The ratio of these terms is the magnetic Reynolds number R_M, and is given by

$$R_M = \frac{VL}{\zeta}. \tag{1.7}$$

For large R_M the convection term of Equation 1.6 dominates the magnetic field evolution, and a frozen-in plasma therefore has an extremely large magnetic Reynolds number.

In the case of large resistivity the magnetic Reynolds number is small. In the limit $R_M \to 0$, the magnetic field evolution is dominated by the second term of Equation 1.6, and neglecting the first term provides a diffusion equation for the magnetic field. This diffusion process, however, is typically very slow. In the corona, coronal loops of magnetic field have length scales of $L \sim 10^7$ m and $\zeta \sim 1$ m^2 s^{-1}. The time scale for the magnetic field to diffuse away is $\tau = L^2/\zeta = 10^{14}$ s i.e., over 3 million years, whereas solar flares are observed over time spans of 2 to 20 minutes (Biskamp, 2005).

Diffusion of magnetic fields is therefore a slow process for the release of large quantities

of magnetic energy. The Sweet-Parker reconnection model, however, provided a faster mechanism through the reconnection of magnetic fields across a current sheet.

1.1.1 Sweet-Parker reconnection

If frozen-in plasmas containing oppositely directed magnetic fields are brought together, a thin current sheet forms between them due to the curl of the magnetic field (Ampère's law). Cowling (1953) and Dungey (1953) recognised that thin current sheets can provide large amounts of dissipation. This led Sweet (1958) and Parker (1957) to provide an MHD model for steady state reconnection of magnetic fields at thin current sheets.

In the Sweet-Parker model, a macroscopic dissipation region of width $2L_L$ and height $2L_N$ is located at the thin current sheet (Figure 1.1). We use LMN current sheet normal coordinates, where L is the direction of exhaust outflow, N is normal to the current sheet, and M is orthogonal to both L and N. Plasma from the inflow regions enters the dissipation region from above and below the current sheet. At such thin current sheets the plasma is no longer frozen-in, and magnetic diffusion causes the magnetic field to dissipate. The annihilation of magnetic fields within this region allows fields from the two inflow regions to cross-connect at the 'X-line'. Newly connected field lines emerge from the dissipation region to form a magnetic connection between the plasma above and below the current sheet (i.e., the two inflow regions). These highly kinked field lines relax and the release of magnetic tension accelerates the field and the now frozen-in plasma away from the dissipation region. Magnetic field lines in the inflow regions and reconnected field lines in the outflow regions are separated by separatrices which distinguish between regions with different field line connectivity.

A key question is how fast does this process occur, and can it, therefore, account for the rates of energy release that are observed at known locations of magnetic reconnection? In the Sweet-Parker model, conservation of mass between the inflowing plasma and outflowing plasma implies that

$$L_L V_i = L_N V_o, \tag{1.8}$$

where V_i is the inflow velocity of the plasma into the dissipation region, and V_o is the velocity of the plasma as it is pushed out of the dissipation region. The following derivation follows the method of Priest & Forbes (2000).

The electric field is uniform in steady state reconnection. In the inflow regions (where the frozen-in theorem is valid) the inflow of the plasma at speed V_i in the presence of the

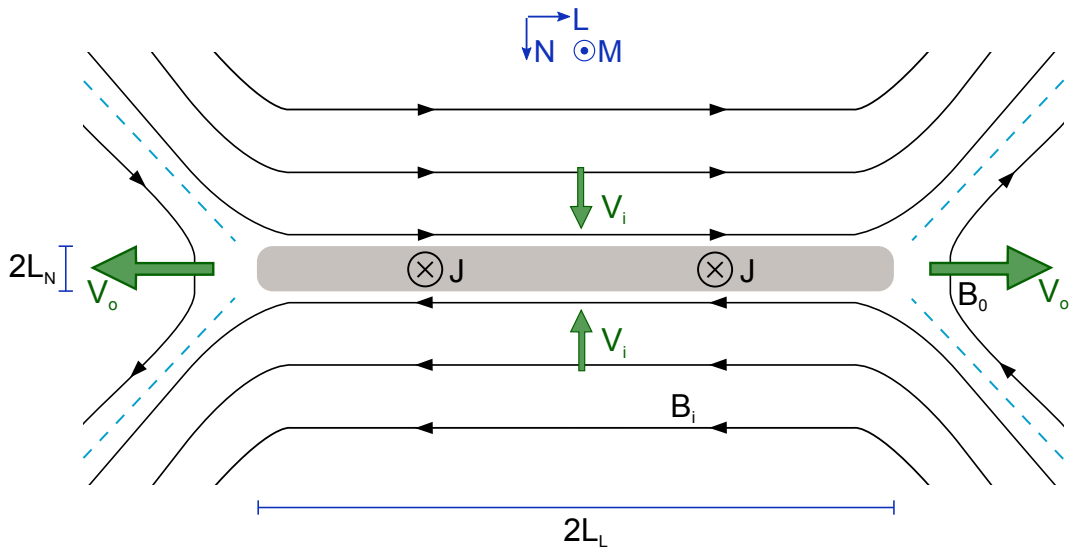


Figure 1.1: Sweet-Parker reconnection model. Plasma flows into the dissipation region (coloured grey) of dimensions $2L_L \times 2L_N$ from the inflow regions above and below the current sheet at a speed V_i, and flows out of the dissipation region in the outflow regions at a speed V_o. Separatrices are shown with light blue dashed lines. An LMN coordinate system is shown.

magnetic field B_i implies a convection electric field of

$$E = V_i B_i. \tag{1.9}$$

In the dissipation region the magnetic field is very weak and the large current means that the frozen-in theorem is not valid. The electric field is instead given by

$$E = \eta J. \tag{1.10}$$

At the dissipation region the magnetic field B_i varies over a length scale L_N. J is therefore given by Ampère's law as

$$J = \frac{B_i}{\mu_0 L_N}. \tag{1.11}$$

By equating Equations 1.9 and 1.10 and using Equation 1.11, we find that

$$L_N = \zeta / V_i. \tag{1.12}$$

This can be used in Equation 1.8 to show that

$$V_i^2 = \frac{\zeta V_o}{L_L}. \tag{1.13}$$

The magnetic Reynolds number based on the inflow region Alfvén speed $V_{A,i}$ is $R_M =$

$L_L V_{A,i}/\zeta$, which allows us to re-write the previous expression as

$$\frac{V_i}{V_{A,i}} = \frac{\sqrt{V_o/V_{A,i}}}{\sqrt{R_M}}. \tag{1.14}$$

In MHD the steady state equation of motion of the plasma is given by

$$\rho(\mathbf{V}\cdot\nabla)\mathbf{V} = -\nabla P + \mathbf{J}\times\mathbf{B}, \tag{1.15}$$

where ρ is the mass density and P is the plasma pressure. Considering the L direction, the Lorentz force is $(\mathbf{J}\times\mathbf{B})_L = JB_o = B_iB_o/\mu_o L_N$ (using Equation 1.11). This accelerates the plasma over a distance L_L, which allows the equation of motion (ignoring the plasma pressure gradient) to be written as

$$\rho\frac{V_o^2}{L_L} = \frac{B_iB_o}{\mu_o L_N}. \tag{1.16}$$

Since $\nabla\cdot\mathbf{B} = 0$, $B_o = B_iL_N/L_L$. Equation 1.16 can therefore be written in terms of the outflow speed as

$$V_o = \frac{B_i}{\sqrt{\mu_0\rho}} = V_{A,i}. \tag{1.17}$$

This states the the exhaust outflow speed in Sweet-Parker reconnection is the Alfvén speed of the inflow region. Equation 1.14 can therefore be expressed as

$$r = \frac{V_i}{V_o} = \frac{1}{\sqrt{R_M}}. \tag{1.18}$$

This quantity, the speed of the plasma flowing into the dissipation region as a fraction of that flowing out (termed 'the dimensionless reconnection rate'), provides a measure of the rate at which plasma passes through the dissipation region. In space plasmas ζ is typically very small and R_M is large. In the solar corona, if $R_M \sim 10^8$, $L_L \sim 10^7$ m and $V_{A,i} \sim 100$ km s^{-1}, this implies that $r \sim 10^{-4}$ which gives a timescale for reconnection of $T = L_L/V_i \sim 10^6$ s i.e., more than 11 days. Although this rate is significantly faster than the rate provide by magnetic diffusion alone, it was soon realised that magnetic reconnection in the Sweet-Parker model was too slow to account for observed dimensionless reconnection rates of $r \sim 0.1$.

The rate at which reconnection occurs is defined as the magnetic flux which is converted by reconnection per unit time and distance. Faraday's law states that this quantity is equal to the reconnection electric field in the inflow region, and is given by

$$E_{rec} = E_M = V_iB_L. \tag{1.19}$$

This is equal to the convection electric field of the plasma, which flows into the diffusion

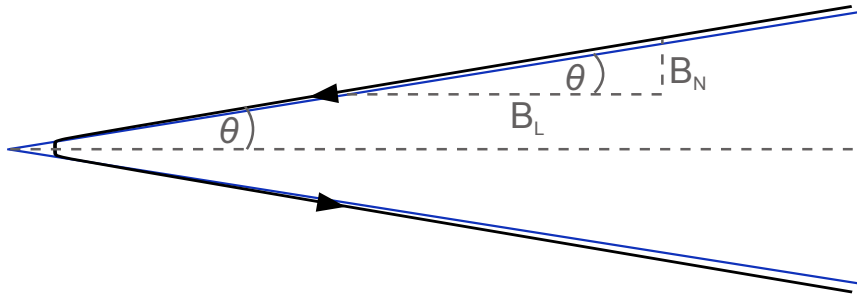


Figure 1.2: The exhaust opening angle θ is equal to the angle formed between magnetic field in the LN plane and the L direction.

region at a speed V_i. The reconnection electric field is often normalised and expressed as the quantity $r = E_{rec}/(V_o B_L) = V_i/V_o$, as per Equation 1.18. Since the outflow speed is of the order of the Alfvén speed, it can also be shown that (Sonnerup *et al.*, 1981)

$$r = \frac{B_N}{B_L}, \tag{1.20}$$

where B_N and B_L are the magnetic field components in the inflow regions.

This implies that the angle between the exhaust boundary and the mid-plane (the 'exhaust opening angle', θ) is related by

$$r = \frac{B_N}{B_L} = \tan(\theta), \tag{1.21}$$

as illustrated in Figure 1.2. Measurements of this opening angle may therefore be used to estimate the dimensionless reconnection rate. From hereon we refer to the dimensionless reconnection rate as the 'reconnection rate' for convenience.

1.1.2 Petschek reconnection

The Sweet-Parker reconnection model produces slow rates of reconnection because the aspect ratio of the diffusion region is large i.e., $L_N << L_L$ (as indicated by Equation 1.8 and $r << 1$). Furthermore, all of the plasma that is expelled from the reconnection site passes through the dissipation region where the change in magnetic topology occurs. Petschek (1964) proposed a new model for reconnection which reconsidered both of these limitations. In the Petschek model the reconnection rate is given by (Priest & Forbes, 2000)

$$r \approx \frac{\pi}{8 \log(R_M)}. \tag{1.22}$$

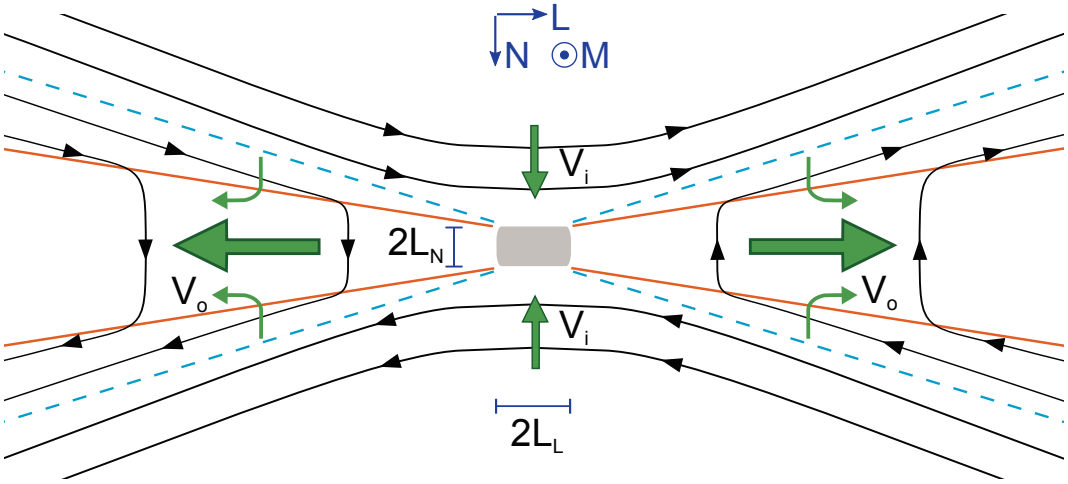


Figure 1.3: Petschek reconnection model. Plasma flows into the dissipation region (coloured grey) of dimensions $2L_L \times 2L_N$ from the inflow regions above and below the current sheet at a speed V_i, and flows out of the dissipation region in the outflow regions at a speed V_o. Slow shocks are shown in orange and separatrices with light blue dashed lines. Entry of plasma into the exhaust region across slow shock is shown in light green. An LMN coordinate system is shown.

For a given R_M, the reconnection rate in the Petschek model is much faster than that in the Sweet-Parker model, and provides reconnection rates which are in agreement with observed rates. This was the first model of *fast* reconnection.

In Petschek's model the dissipation region width ($2L_L$) is smaller with respect to its height ($2L_N$) than in the Sweet-Parker model (Figure 1.3). Since the outflow speed from the dissipation region is $\sim V_{A,i}$, this aspect ratio allows for a faster inflow speed and therefore a faster reconnection rate. Additionally, although the topological change in the field occurs in the dissipation region, Petschek suggested that not all of the plasma involved with reconnection need pass through it. Instead, the exhaust outflows are bound on either side by slow mode shocks which propagate from the dissipation region. The majority of exhaust plasma actually enters the exhaust across the shocks (which accelerate and heat the inflow region plasma), rather than through the dissipation region, and these are the primary sites of conversion of magnetic energy. The slow shocks affect the magnetic field structure within the exhaust. They reduce the component of the field parallel to the current sheet (B_L) from its inflow region value to zero within the exhaust. Since the field change occurs at the shocks, this is also where the current is located. In contrast to Sweet-Parker reconnection the current is not concentrated at the current sheet mid-plane, but rather splits or 'bifurcates' into two current layers.

Petschek's model is not a self-consistent theory of fast reconnection, however, as it relies on an efficient (but unspecified) dissipation mechanism at the dissipation region. A simple

way to overcome this obstacle is to assume a locally enhanced resistivity at the reconnection X-line. Artificially enhanced resistivities at the reconnection X-line produce a Petschek-like reconnection configuration in MHD simulations (Sato, 1979; Scholer, 1989). In the presence of a uniform plasma resistivity, however, a macroscopic Sweet-Parker current sheet tends to form, producing a slow reconnection rate (Biskamp, 1986). It was later shown that collisionless reconnection can provide a method for achieving fast reconnection without having to impose locally enhanced resistivities.

1.1.3 Collisionless reconnection

The Sweet-Parker and Petschek reconnection models are resistive-MHD models, which is to say that the plasma resistivity is provided by collisions between the charged particles of the plasma. Plasma in the magnetosphere and solar wind, which regularly undergoes reconnection, is so dilute that collisions between particles are extremely infrequent. Classical resistivity in the plasma is therefore negligible. How is it possible for reconnection to occur in such plasmas, and what is the dissipation mechanism at the reconnection X-line?

This problem has been addressed by going beyond the approximations of MHD and considering the finer details of particle motion in plasmas. Even for a completely collisionless plasma the frozen-in field theorem breaks down at thin current sheets, which allows for dissipative effects. Ions and electrons both gyrate around magnetic field lines in plasmas. In a uniform magnetic field the particles will undergo steady gyro-orbits. The radius of this orbit (the gyroradius) can be determined by equating the centripetal force acting on the particle with the Lorentz force which accelerates it, which gives the gyroradius as

$$r_g = \frac{mv_\perp}{qB}, \tag{1.23}$$

where m and q are the particle mass and charge, respectively, and $v_\perp$ is the particle velocity perpendicular to the magnetic field. When the magnetic field begins to vary on small scales and the field changes within a particle's gyroradius, that particle sees a varying magnetic field and can no longer steadily gyrate around a single field line. The particle becomes dissociated from the magnetic field line and 'demagnetised' or 'decoupled' from the field, and the frozen-in theorem breaks down.

Ions are heavier than electrons and therefore gyrate with a larger radius. In a varying magnetic field, the ions demagnetise from the field first, while the electrons only demagnetise when the field gradient is large enough that the field changes over the scale of their smaller gyroradius. Electron and ion motion at thin current sheets where magnetic field gradients are large can therefore differ substantially (Sonnerup, 1979; Terasawa, 1983). To

properly describe this behaviour one must consider the electron and ion equations of motion separately. This leads to the equation

$$\mathbf{E} + \mathbf{V} \times \mathbf{B} = \eta \mathbf{J} - \frac{1}{ne}\mathbf{J} \times \mathbf{B} - \frac{1}{ne}\nabla \cdot \mathbf{P_e} + \frac{m_e}{ne^2}\frac{d\mathbf{J}}{dt} \tag{1.24}$$

which is known as the 'generalised Ohm's law' (Rossi & Olbert, 1970). n is the particle number density and e is the elementary charge. The first term on the right hand side is the resistive term that was introduced earlier. The second term is the Hall term, which arises because of differences in electron and ion motion. The third term is the electron pressure gradient term (where $\mathbf{P_e}$ is the electron pressure tensor) and the last term is the electron inertia term. The inclusion of the electron equation of motion adds the Hall, electron pressure gradient and electron inertia terms to the MHD Ohm's law (Equation 1.2). Any of the terms on the right hand side of generalised Ohm's law can break the frozen-in condition of the plasma and allow for non-ideal effects (Vasyliunas, 1975).

The importance of each term in introducing non-ideal effects can be assessed by comparing an appropriate characteristic scale length for each term with the length scale of gradients in the system. The length scale associated with the Hall term is the ion inertial length d_i (Vasyliunas, 1975). This is given by the speed of light divided by the ion plasma frequency,

$$d_i = c/\omega_i. \tag{1.25}$$

The length scale associated with electron pressure gradient and electron inertia terms is the electron inertial length d_e (Vasyliunas, 1975) which is given by

$$d_e = c/\omega_e. \tag{1.26}$$

The electron plasma frequency ω_e is the frequency at which electrons oscillate around ions (assumed to be stationary), if displaced relative to the ions. This oscillation is caused as a result of the electric field that is produced when the electrons are displaced. The electron plasma frequency is given by (Baumjohann & Treumann, 1997)

$$\omega_e = \sqrt{\frac{ne^2}{m_e \epsilon_0}}, \tag{1.27}$$

where ϵ_0 is the permittivity of free space. ω_i is given by the same expression using m_i instead of m_e. This implies that

$$\frac{d_i}{d_e} = \sqrt{\frac{m_i}{m_e}}, \tag{1.28}$$

which gives $d_i/d_e \sim 43$, for a proton-electron plasma. This implies that the electron pressure gradient and inertia terms are important on much smaller scales than the Hall term.

Collisionless reconnection therefore takes on a considerably different form compared to resistive-MHD reconnection. At the current sheet electrons and ions decouple from the field, however this occurs on different spatial scales. The ions decouple from the field in the ion diffusion region. This is where the Hall term becomes important and it has a size of $\sim d_i$. The electrons only decouple where the field gradient is even stronger (i.e., closer to the location of field reversal), in a smaller region known as the electron diffusion region. This has a size of $\sim d_e$ and is where the electron pressure gradient and electron inertia terms are thought to be important in breaking the frozen-in condition and allowing for the topological change of the field (Burch *et al.*, 2016a; Goldman *et al.*, 2016).

The electron diffusion region and ion diffusion region of collisionless reconnection are shown in Figure 1.4. In the ion diffusion region the decoupled ions move relatively slowly, whereas the magnetised electrons flow away from the electron diffusion region. This electron flow produces the Hall current (Sonnerup, 1979; Terasawa, 1983). The Hall current has associated with it an out-of-plane Hall magnetic field (i.e., in the M direction). This has a quadrupolar structure which is shown in Figure 1.4 (Mandt *et al.*, 1994; Hesse *et al.*, 2001).

Comparisons of simulations where the frozen-in theorem was violated by including different terms in the generalised Ohm's law showed the Hall effect to be essential to achieving fast rates of reconnection (Birn *et al.*, 2001). Only simulations which included this effect were able to achieve fast rates of reconnection. Simulations which did not include the Hall term (i.e., resisitive-MHD simulations) produced slow rates of reconnection.

The collisionless nature of these plasmas also affects how the plasma enters the reconnection exhaust. Field lines which reconnect in the diffusion region are expelled into the exhausts, where they now form a magnetic connection between the two inflow regions. Ions from the two inflow regions are able to stream along the magnetic field lines within the exhaust. The plasma is too diffuse for particle collisions which prevents the two populations from mixing. Instead, two counterstreaming populations exist within the exhaust region (Hoshino *et al.*, 1998; Arzner & Scholer, 2001). Ions which stream into the exhaust in this manner can be accelerated and heated, and (as with Petschek reconnection) a large amount of energy conversion occurs at the exhaust boundaries rather than at the diffusion region (Drake *et al.*, 2009a; Hietala *et al.*, 2015).

1.2 Important factors in magnetic reconnection

The reconnection models introduced in the previous section are applicable in simple reconnection configurations, specifically reconnection between anti-parallel fields where the plasma on either side of the current sheet is symmetric. Reconnection occurs in many

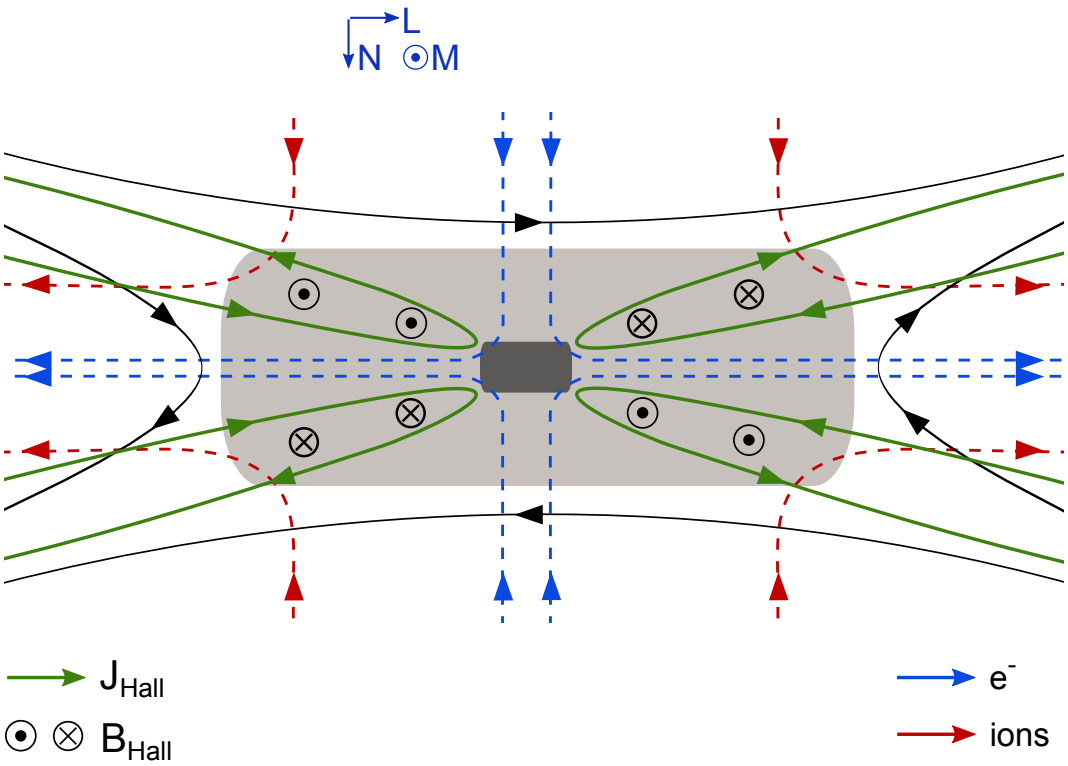


Figure 1.4: Collisionless reconnection. Electrons (blue) and ions (red) flow in from the inflow regions above and below the current sheet. The electron diffusion region is shown in dark grey and the ion diffusion region is shown in light grey. Differential motion of the ions and electrons in the ion diffusion region produces a Hall current (green), and associated Hall magnetic fields. An LMN coordinate system is shown.

different environments where plasma properties differ substantially, which can affect the reconnection process. In this section we introduce concepts which affect the reconnection process, which will be discussed further throughout this thesis.

1.2.1 Guide field

The magnetic fields which reconnect are oppositely directed (anti-parallel) in Figures 1.1, 1.3, 1.4. In general, these fields need not be anti-parallel. In this case, reconnection can be thought of as occurring in the plane shown in Figure 1.4, but with a component of the magnetic field directed out of the plane (i.e., the M direction) which is constant everywhere. The dimensionless guide field B_G is used throughout this thesis, which is the ratio of the out-of-plane component of the field to reconnecting component of the field in the inflow region, i.e., $B_G = B_M/B_L$. The angular difference between the two field vectors on either side of the current sheet is referred to as the magnetic shear angle θ, which is related to the guide field by $B_G = \tan((180 - \theta)/2)$.

Reconnection with a guide field is known to differ from the special case of anti-parallel reconnection. A non-zero guide field alters the boundary structure of reconnection exhausts, causing a different set of discontinuities to form from the anti-parallel case (e.g., Lin & Lee, 1993). Furthermore, a guide field distorts the quadrupolar Hall magnetic field that is present in anti-parallel reconnection, resulting in an asymmetry of the Hall field across the reconnection exhaust (e.g., Horiuchi & Sato, 1997; Huba, 2005). The effects of guide fields on reconnection exhausts are discussed further in Chapters 3 and 5.

1.2.2 Plasma β

In addition to the thermal pressure provided by the ions and electrons in a plasma, there is a pressure associated with the magnetic field, which is given by $P_B = B^2/(2\mu_0)$. The total plasma pressure is therefore given by the sum of the pressures of the ions and electrons (i.e., the thermal pressure) and the magnetic field pressure. The ratio of the thermal pressure to the magnetic pressure is given by the dimensionless quantity

$$\beta = \frac{nk_B(T_i + T_e)}{B^2/(2\mu_0)}, \tag{1.29}$$

for the general case where the ion and electron temperatures may differ. T is the temperature and k_B is Boltzmann's constant. If $\beta << 1$ the plasma is said to be cold and the magnetic pressure dominates over the thermal pressure. If $\beta >> 1$ the plasma is said to be warm and thermal properties of the plasma such as pressure anisotropies become important

in affecting its dynamics (Schoeffler *et al.*, 2011). In Chapter 3 we study how the plasma β affects plasma within the exhaust region, as well as the combined effects of the plasma β and guide field.

1.2.3 Asymmetric reconnection

Reconnection where the plasma on either side of the current sheet has the same properties is referred to as symmetric reconnection. In some situations the magnetic pressure and thermal pressure between the two inflow regions may differ. Such asymmetric reconnection has been the subject of much interest in recent years since reconnection at the magnetopause occurs between the magnetosheath (high density and low magnetic field) and magnetosphere (low density and high magnetic field). Differences between reconnecting plasmas cause inflowing plasma from the two inflow regions to meet at a slightly different location (the 'stagnation point') to the reconnection X-line, with the stagnation point displaced to the low density side (Cassak & Shay, 2007). Additionally, the difference in density on either side affects the current systems. These current systems differ to the case of symmetric anti-parallel reconnection and result in bipolar rather than quadrupolar Hall magnetic fields (Karimabadi *et al.*, 1999).

1.2.4 The third dimension

So far we have discussed reconnection in the two dimensional reconnection plane (i.e., the LN plane in Figures 1.1,1.3,1.4). Reconnection of course occurs in three-dimensional space, and we have assumed the process to be invariant in the out-of-plane M direction. Observations of reconnection in the magnetosphere and solar wind generally show this to be the case, and reconnection simulations regularly simulate systems with two spatial dimensions. In many cases, however, reconnection may not be invariant in the third dimension, particularly in the solar corona where field lines have complex three dimensional topologies. Even in three dimensional systems which are initially invariant in the out-of-plane direction, non-uniform structures in the out-of-plane direction can form (Yin *et al.*, 2008; Fujimoto, 2009; Daughton *et al.*, 2011). Although reconnection exhausts in the solar wind appear to have a two dimensional structure, in Chapter 6 a reconnection exhaust with complex three dimensional structure is presented.

1.3 Simulations of reconnection

The exceptional growth in the performance of computers has allowed many problems in physics to be approached through computational methods, where large amounts of calculations are used to determine the evolution of a physical system. This has been used extensively for the purposes of magnetic reconnection in space plasmas, and such simulations have contributed greatly to our understanding of reconnection processes. Whereas in-situ observations allow for detailed measurements of a very localised region of a reconnection system, simulations allow a larger region of the reconnection system to be analysed.

Simulations, although often run on high performance supercomputers, are often limited by computational constraints, and large simulations take long times to run on even the most powerful machines available today. For this reason the size of the simulated region is often restricted, invariance may be assumed in the out-of-plane dimension and artificially heavy electrons may be used (Büchner *et al.*, 2003). Many different numerical approaches have been used to simulate space plasmas. Here we introduce the most frequently used approaches for reconnection. Naturally, this is not a complete list, and various methods are often combined. For example, simulations may couple regions which are treated with PIC methods to larger regions which are treated with MHD methods in order to resolve both the small scale kinetic physics of the diffusion region and its effects on a larger scale system (e.g., Usami *et al.*, 2013).

1.3.1 Magnetohydrodynamics

This method treats the plasma as a continuous MHD fluid and as such the microscopic particle dynamics are not modelled. The equations of MHD are discretised and solved on a grid system. MHD simulations are generally appropriate for modelling the large scale bulk properties of plasmas including mass, momentum and and flux transport. The assumption of MHD means that the particle distribution functions are assumed to be Maxwellian. As a result, resolving the kinetic physics of reconnection is beyond the scope of MHD simulations. Furthermore, MHD simulations are only applicable when the length scales and time scales of interest are larger than scales over which the plasma microphysics is averaged i.e., the plasma gyroradius and inverse gyrofrequency. Length scales and timescales shorter than this cannot be accurately resolved using MHD.

Because of the various approximations that are made in an MHD treatment of a plasma, MHD simulations for a given system are computationally inexpensive relative to other simulation techniques. They are unable to accurately model the microphysics of reconnection, however MHD simulations are frequently used to model large systems such as the entire

terrestrial magnetosphere in three spatial dimensions, and to study the effects of reconnection on the global system (e.g., Lyon *et al.*, 2004; Raeder *et al.*, 2008). Simulations may use multiple MHD fluids to simultaneously model multiple plasma species. Localised reconnection has been modelled both with single-fluid resistive MHD and with multiple fluids to investigate the effects of Hall physics (e.g., Birn & Hesse, 2001; Otto, 2001; Shay *et al.*, 2001).

1.3.2 Particle-in-cell

Whilst MHD describes plasmas as fluids, one can also use the kinetic description which retains the kinetic microphysics of particle dynamics. This does not make approximations about the basic interactions of particles, and as such is able to retain the full kinetic nature of collisionless plasmas. It is therefore not necessary, for example, to approximate particle distributions as Maxwellian distribution functions. The plasma could be modelled by treating particles as discrete points and computing the forces on each particle as a result of Coulomb interactions with all other particles, however this is extremely computationally intensive.

A standard method is to instead discretise space into a grid or a series of 'cells'. Particle charges and current densities are accumulated across the cells nearest to them to calculate the charge and current density across the discretised space. Fields are then calculated across the discretised space using Maxwell's equations. Particles are then moved according to their equations of motion (by interpolating fields across the discretised space). Current and charge densities are again computed, fields calculated, and particles moved at the next time step. This method ensures that the fields are self-consistent. Moments of the particle distributions are often used to understand the reconnection process, however the full distribution functions are retained.

The fully kinetic PIC approach treats both electrons and ions kinetically. In order to successfully resolve particle motion there must be a sufficient number of particles in each cell for the method of computing charge and current densities to be valid. Many particles are collectively modelled using macroparticles in PIC simulations to reduce computational demands of the simulation. The grid spacing must be less than the kinetic spatial scales (gyroradius and inertial length) and the time step must be less than the kinetic temporal scales (inverse gyroperiod). Since these scales involve the particle mass, they are very different for protons and electrons. For example, the proton inertial length is 43 times that of an electron. The dynamics of low mass particles can therefore only be resolved if very high temporal and spatial resolutions are used. Electrons are consequently treated as artificially heavy to reduce the required temporal and spatial resolution of the simulation

and reduce computational time. This artificially large electron mass has been shown to have little effect on the large scale physics in reconnection simulations (Shay & Drake, 1998; Hesse *et al.*, 1999), however it can affect dynamics nearer to the reconnection X-line (Le *et al.*, 2013). The use of artificially large electron masses is a standard method employed to reduce the computational expense of running large-scale PIC simulations.

PIC simulations are regularly used to study localised reconnection systems (e.g., Pritchett, 2001; Zeiler *et al.*, 2002; Drake *et al.*, 2009a) and are often compared to in-situ space observations to aid their interpretation (e.g., Hoshino *et al.*, 1998; Eastwood *et al.*, 2010a). These simulations are often run in two spatial dimensions and assume the out-of-plane direction to be invariant, allowing the simulation size to extend to $\sim$100 d_i downstream of the X-line (e.g., Liu *et al.*, 2012), however three dimensional systems have been simulated using smaller domains (e.g., Daughton *et al.*, 2011).

1.3.3 Hybrid

In hybrid simulations one or more of the plasma species is treated as a fluid and the remaining species are treated kinetically, often using the PIC approach. This method is often used for reconnection and is less computationally intensive than fully kinetic PIC as only the ions are treated kinetically. Hybrid simulations are appropriate when the scales of interest and smaller than the ion spatial and temporal scales but larger than those of the electrons, and when the kinetic dynamics of electrons are not of interest. Localised reconnection has been modelled using hybrid simulations (e.g., Kuznetsova *et al.*, 2001; Shay *et al.*, 2001) and computational advances have allowed hybrid simulations to be used for global magnetosphere modelling (e.g., Karimabadi *et al.*, 2014).

1.4 The Sun and the solar wind

Magnetic reconnection occurs throughout the solar system and is key to the transfer of particles, magnetic flux and energy in many planetary systems. Our ability to access these environments with spacecraft and directly measure the fields and plasma in these systems has provided insight into the physics of reconnection and how it affects the systems in which it occurs, with the near-Earth environment being the most accessible and actively studied region of space. Geospace plasmas ($n < 10^2$ cm^{-3}) are significantly more tenuous than laboratory plasmas ($n \sim 10^{13}$ cm^{-3}), to the extent that collisions between particles are extremely rare. The absence of collisions significantly affects the reconnection process, and these in-situ measurements are therefore crucial to understanding reconnection processes in geospace. In this section and the following section we introduce the solar wind and

how it has been used as a laboratory to study collisionless reconnection, before discussing reconnection in other regions of near-Earth space in Section 1.6.

1.4.1 The Sun

The Sun is the source of the plasma and magnetic fields that fill the solar system. The Sun is held together and compressed by its gravitational attraction, with a mass of 2×10^{30} kg and radius of 7×10^5 km. At its core the temperature and pressure are so immense that hydrogen nuclei undergo nuclear fusion to produce helium, releasing vast amounts of energy. This energy radiates outwards through the radiative zone to approximately 75% of the Sun's radius, and is then transported to the solar surface via convective transport through the convective zone (Priest, 1995).

Magnetic field lines emerge from the solar surface, creating a complex pattern of magnetic field loops which can be seen through ultraviolet and X-ray imaging. When these come together they can reconnect and accelerate plasma away from the surface (Priest & Forbes, 2000). These reconnection events are responsible for solar flares and coronal mass ejections which expel large amounts of mass and energy away from the Sun. Solar reconnection is thought to be unsteady and not described by the steady state models discussed in Section 1.1.

The existence of sunspots on the solar surface has been recorded since as early as the fourth century B.C. (Priest, 1995). These are dark spots on the Sun's surface that are cooler than their surroundings, have an enhanced magnetic field, and can be as large as 2×10^4 km in diameter. Sunspots had been studied for some time, however it was not until 1851 that Heinrich Schwabe discovered that they occur over a regular 11 year cycle. The number of sunspots is now used as a proxy for the solar cycle (Priest, 1995). At solar minimum, the Sun's magnetic field near to the Sun is dipole-like. At high latitudes the magnetic fields lines are effectively 'open', extending to far from the Sun. At lower latitudes the field lines are closed which confines plasma. The Sun's magnetic field becomes less organised towards solar maximum, and open and closed field lines are not clearly confined to certain latitudes. The maximum amount of sunspots are observed near this stage of the cycle. As the Sun moves back to solar minimum it completes the solar cycle and the magnetic field dipole configuration is restored, however the dipole axis is opposite to that of the previous solar minimum. The magnetic dipole therefore reverses over a 22 year cycle.

1.4.2 The solar wind

The solar atmosphere reaches temperatures of up to $1-2$ million Kelvin (the processes which lead to such strong heating are still under debate (Owens & Forsyth, 2013)) and has a much larger pressure than the negligible pressure of the interstellar medium. This pressure imbalance accelerates the plasma away from the Sun, forming the solar wind. A theoretical basis for the solar wind was provided by Parker (1958), however the existence of a continuous supersonic plasma outflow from the Sun was the subject of debate until direct measurements of the solar wind were made using the Mariner-II spacecraft (Neugebauer & Snyder, 1962). Parker considered a purely radial outflow from the Sun with a constant temperature, and ignored the effects of the solar magnetic field. Under these assumptions he showed that plasma expands radially away from the Sun at supersonic speeds, forming the solar wind.

Parker's solution can be obtained by considering the conservation of momentum equation,

$$\rho\frac{\partial \mathbf{V}}{\partial t} + \rho(\mathbf{V}\cdot\nabla)\mathbf{V} = -\nabla P + \mathbf{J}\times\mathbf{B} + \mathbf{F_g}, \tag{1.30}$$

where $\mathbf{F_g}$ is the gravitational force. For a steady state, spherically symmetric system with zero magnetic field, which only depends on radial distance r, this may be written as

$$\rho V_r\frac{dV_r}{dr} = -\frac{dP}{dr} - \rho\frac{GM_S}{r^2}, \tag{1.31}$$

where V_r is the plasma velocity in the radial direction, G is the gravitational constant and M_S is the solar mass. If the solar wind is considered to be an ideal gas with equal electron and ion temperatures, this may be re-written as

$$m_i n V_r\frac{dV_r}{dr} = -2k_BT\frac{dn}{dr} - m_i n\frac{GM_S}{r^2}. \tag{1.32}$$

By applying the steady state mass continuity equation, $r^{-2}d(r^2\rho V_r)/dr = 0$, it may be shown that (Hundhausen, 1995)

$$\frac{1}{V_r}\frac{dV_r}{dr}\left(V_r^2 - \frac{2kT}{m_i}\right) = \frac{4k_BT}{m_i r} - \frac{GM_S}{r^2}, \tag{1.33}$$

which is known as the Parker solar wind equation. Solutions to this equation are shown in Figure 1.5. Of these, classes 3 and 4 can be ruled out as solutions to the solar wind as they predict supersonic speeds at the solar surface, which are not observed. Classes 1 and 2 show similar behaviour up to a critical radius $r_c = GM_Sm_i/(4k_BT)$ ($\sim$5.8 solar radii). For class 1, $V_r \to 0$ as $r \to \infty$. This would cause a much larger pressure at the boundary between the solar wind and the interstellar medium than what is observed, and is not a valid solution

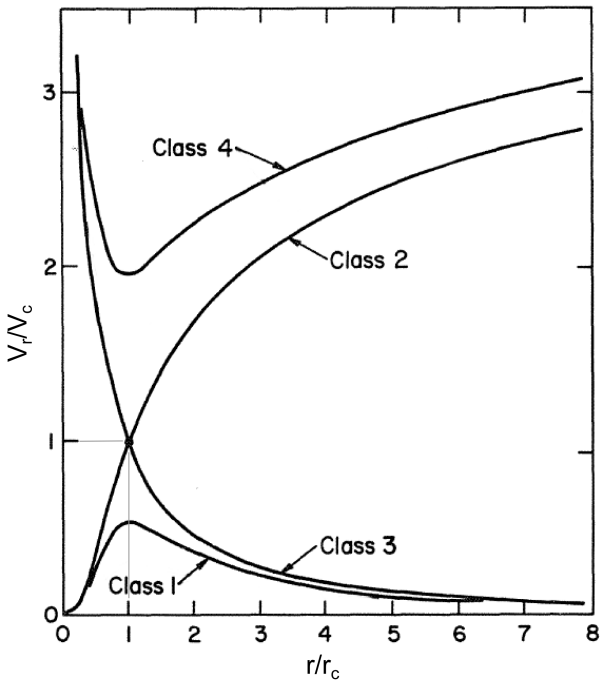


Figure 1.5: Solutions to the Parker solar wind equation. Adapted from Hundhausen (1972).

for the solar wind. At r_c, class 2 has a speed of $V_c = \sqrt{2k_BT/m}$ (the sound speed), and this solution most closely resembles the observed solar wind. Despite the simplicity of the Parker solar wind model, the class 2 solution provides a reasonably accurate form of the solar wind radial velocity as a function of radial distance from the Sun.

The solar wind fills a large region of space known as the heliosphere, and at its boundary (the heliopause) the solar wind is met by the interstellar medium. The solar wind is a collisionless frozen-in plasma (the mean free path of collisions is approximately 1 AU), and therefore carries with it the magnetic field generated by the Sun. This magnetic field is referred to as the interplanetary magnetic field (IMF). The solar wind and IMF flow radially away from the Sun, however the Sun rotates with a period of ∼26 days at its equator (the Sun undergoes differential rotation). The foot points of the IMF field lines remain rooted in the solar surface which rotates with respect to the radial solar wind. The relative motion between the free solar wind and the foot points of the magnetic field lines on the rotating solar surface causes the magnetic field in the solar wind to produce an Archimedian spiral in the equatorial plane, which is known as the Parker spiral (Parker, 1958). At increasing radial distances from the Sun the magnetic field forms a larger angle with respect to the radial direction. At Earth this is approximately 45° (Hundhausen, 1995).

During solar minimum the Sun's magnetic field is dipole-like, and closed field lines near the equator suppress the solar wind outflow. The solar wind flows more freely away from

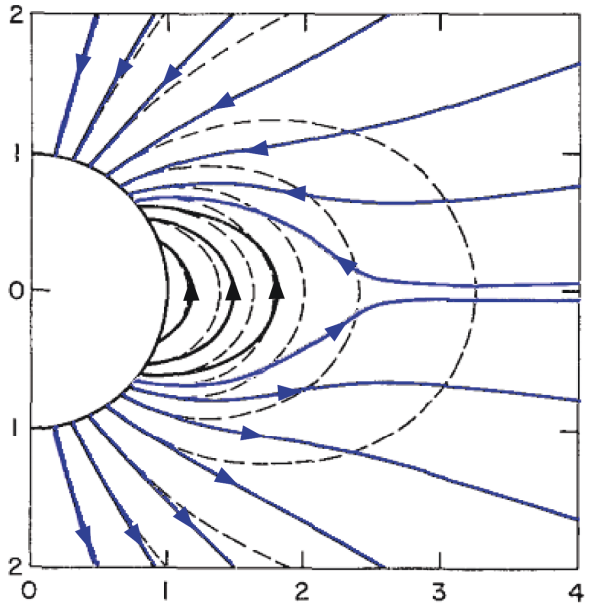


Figure 1.6: Magnetic field lines from the Sun near solar minimum. Open (closed) magnetic field lines are shown in blue (black). Dashed lines show a pure dipole field. The heliospheric current sheet is located between the magnetic field lines of opposite polarity at the magnetic equator. Adapted from Pneuman & Kopp (1971).

the Sun at regions of open field lines (coronal holes) closer to the magnetic poles (see Figure 1.6). The boundary separating field lines from the northern and southern poles is carried out by the solar wind and forms a current sheet referred to as the heliospheric current sheet. Two types of solar wind are typically observed. Fast solar wind (speeds of around 750 km s^{-1} at 1 AU) is thought to be sourced from coronal holes whereas the slow solar wind (speeds of around $300 - 450$ km s^{-1} at 1 AU) is observed at low latitudes near the magnetic equator (Hundhausen, 1995). At solar maximum the Sun's magnetic field is less ordered and coronal holes can be found at lower latitudes, therefore both fast and slow solar wind are frequently observed at equatorial latitudes.

Typical properties of the solar wind at 1 AU are shown in Table 1.1. The typical ion composition of the solar wind is 96% H^+ and 4% He^{2+}, with trace amounts of heavier ions. The solar wind may therefore be approximated as a proton-electron plasma for many purposes.

The solar wind, as described so far, appears to be a relatively uniform medium. It is a turbulent medium, however, and is filled with fluctuations of the magnetic field and plasma (Bruno & Carbone, 2013). These fluctuations include large changes in the magnetic field direction, which are less common than small changes in the magnetic field (e.g., Borovsky, 2008). Large changes in the magnetic field are frequently classified as discontinuities (e.g., Horbury *et al.*, 2001). Their origin, however, remains under debate. For example, it has

Table 1.1: Plasma properties in the solar wind (Hundhausen, 1995), magnetosheath and magnetotail (Hughes, 1995). Alfvén speeds and β are based on values shown in the table.

	Solar wind at 1AU	Magnetosheath	Magnetotail lobes
Proton density (cm^{-3})	6.6	8	0.01
Proton temperature (eV)	10	150	300
Electron temperature (eV)	12	25	50
$\|B\|$ (nT)	7	15	20
Alfvén speed (km s^{-1})	60	116	4,400
β	1.2	1.6	2×10^{-3}

been suggested that they are produced by the turbulence of the solar wind (Zhdankin *et al.*, 2012), whereas Borovsky (2008) suggested that they are the boundaries between adjacent flux tubes which originate from structures closer to the solar surface. The IMF on either side of these discontinuities can reconnect, forming large-scale reconnection exhausts (e.g., Gosling, 2012). Reconnection exhausts in the solar wind have arbitrary orientations because of the fluctuations of the solar wind magnetic field. Plasma properties of the inflow regions tend to be quite symmetric in the solar wind, and the magnetic shear angle can vary significantly. The plasma β is of the order $\beta \sim 1$ (Hundhausen, 1995). Spacecraft in the solar wind have a velocity of a few km s^{-1}, whereas the solar wind speed is several hundred km s^{-1}. Spacecraft therefore move in a straight line relative to solar wind reconnection exhausts and measurements along this path are readily determined from time series measurements.

In addition to these relatively small scale structures, the heliosphere contains much larger structures. The Sun's rotation axis and magnetic field axis are not aligned. As the Sun rotates, an observer at a fixed latitude will consequently observe alternating regions of slow and fast solar wind (sourced from low and high magnetic latitudes, respectively). As a fast stream of solar wind catches up with a slower solar wind ahead of it, the fast stream will compress the slow stream, increasing its magnetic field and density. Additionally, a rarefaction will form between the fast solar wind and the slower solar wind behind it. These structures, known as co-rotating interaction regions (Gosling & Pizzo, 1999) co-rotate with the Sun, and the interaction region between the fast and slow solar wind may drive shock waves in the heliosphere.

Reconnection of magnetic fields at the solar surface can result in coronal mass ejections which expel large amounts of coronal plasma (as much as 10^{13} kg) into the solar wind (Webb & Howard, 2012). Coronal mass ejections are transient large-scale coherent bodies of plasma which often contain a helical magnetic field structure at their core. They are rapidly accelerated away from the Sun at speeds of up to 2500 km s^{-1} (Gopalswamy, 2009) and can propagate into interplanetary space where they are then known as Interplanetary Coronal Mass Ejections (ICMEs). ICMEs typically have a low density and plasma β (Neugebauer &

Goldstein, 1997), and if their speed relative to the background solar wind exceeds the local fast magnetosonic speed, ICMEs may drive shock waves into the solar wind. Despite the structured magnetic field at their core, ICMEs contain current sheets where their magnetic field changes. Reconnection exhausts have been observed at current sheets within ICMEs (e.g., Gosling *et al.*, 2005, 2006a) in addition to being observed in the steady state solar wind.

1.5 Reconnection exhausts in the solar wind

Although there have been a number of suggestions that reconnection may occur in the solar wind (e.g., Burlaga, 1968; McComas *et al.*, 1994), direct observations of reconnection in the solar wind were only made as late as 2005 (Gosling *et al.*, 2005). Reconnection in the solar wind is still relatively unexplored, and in this section we provide a comprehensive review of the literature of solar wind reconnection.

1.5.1 Single spacecraft observations

Reconnection exhausts may be identified in what is now considered to be relatively low resolution (2 minute) ISEE-3 data from the 1970s (Gosling, 2012). The data shown in Figure 1.7 was observed just ahead of an ICME. A reconnection exhaust is identified in the data by approximately Alfvénic flows confined to the region where the magnetic field changes. This is most evident in the Y_{GSE} component of the field and results in magnetic field and velocity changes being correlated on one side of the reconnection exhaust and anti-correlated on the other side. The proton density and temperature increases are also confined to the reconnection exhaust region. The exhaust is observed over an interval of 28 minutes, indicating that reconnection persists for at least this duration. Note that this exhaust is clear in GSE coordinates because the exhaust outflow direction is approximately aligned with Y_{GSE}, however in general it is necessary to determine a current sheet normal coordinate system specific to the event under consideration in order to readily determine whether the changes in magnetic field and velocity correspond to a reconnection exhaust. This is discussed further in Section 2.4.

Figure 1.8 illustrates how observations of exhausts in the solar wind are interpreted. Newly reconnected field lines at the reconnection site are highly kinked. As a field line moves away from the reconnection site the kinks separate so that the field is sharply kinked at the boundaries of the exhaust (A1 and A2). Plasma from the inflow region enters the exhaust here and is accelerated as it becomes part of the exhaust outflow. The exhaust is at rest in the solar wind frame of reference and the effective spacecraft motion relative

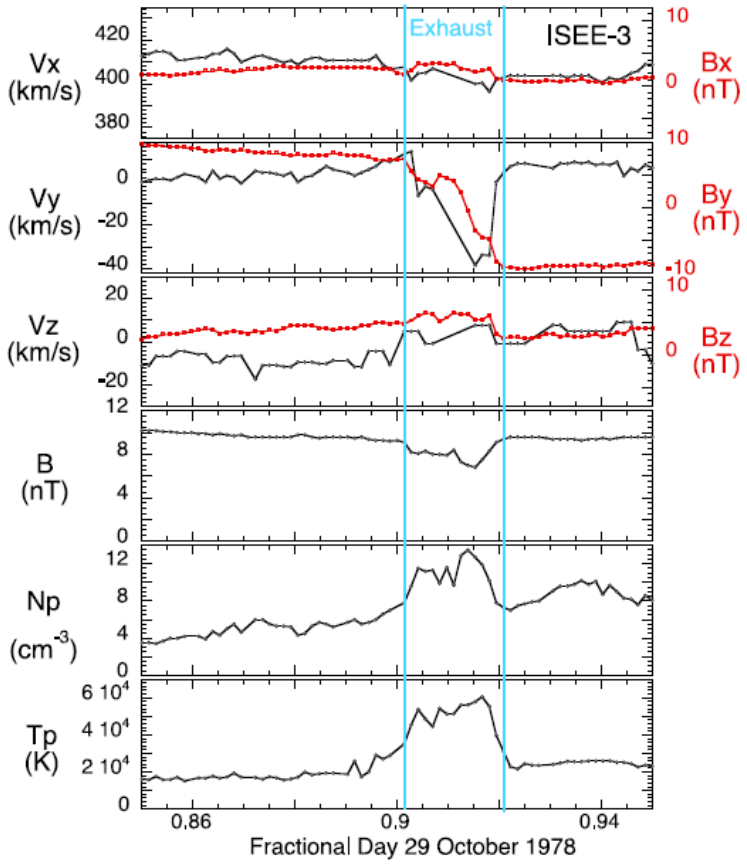


Figure 1.7: ISEE-3 data from 29 October 1978 showing a reconnection exhaust measured ahead of an ICME with 2 minute resolution. GSE components of the velocity and magnetic field are shown in the top three panels. The field magnitude, proton density and proton temperature are also shown. The exhaust interval is indicated with vertical lines. Taken from Gosling (2012).

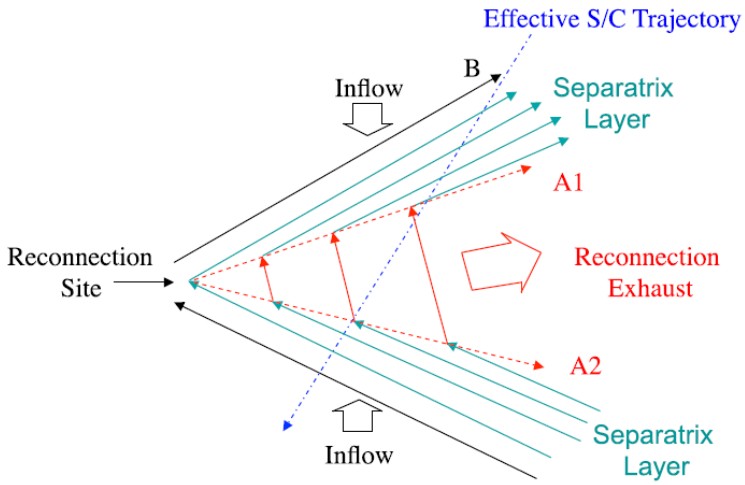


Figure 1.8: Reconnection exhaust in the solar wind. Exhaust boundaries are indicated by A1 and A2. For simplicity the oppositely directed exhaust is not shown. Taken from Gosling (2012).

to the exhaust is shown in blue. The spacecraft crosses from the inflow region on one side of the exhaust (inflow region 1) to the exhaust region, and then to the other side of the exhaust (inflow region 2). Changes in the magnetic field and velocity are anti-correlated and correlated at A1 and A2, respectively. Reconnected field lines that magnetically connect the two inflow regions form the separatrix layer.

This illustration implies that the reconnection current sheet is bifurcated (i.e., the magnetic field in the exhaust has two current layers at the exhaust boundaries) which is consistent with the Petschek reconnection model. Many observed reconnection exhausts in the solar wind exhibit bifurcations (e.g., Gosling *et al.*, 2005, 2006b; Phan *et al.*, 2006), however there are examples of solar wind reconnection current sheets which are not bifurcated (e.g., Gosling, 2007; Gosling *et al.*, 2007c, Figure 1.7 and Chapter 6 of this thesis). Figure 1.8 may suggest that these bifurcations are clearer further downstream of the reconnection site where the exhaust boundaries are well separated. This is investigated for the first time in Chapter 4.

Many of the first direct measurements of reconnection exhausts in the solar wind were associated with ICMEs (e.g., Gosling *et al.*, 2005, 2006a, 2007c). The relative lack of exhaust observations outside of ICMEs formed the picture that solar wind reconnection occurs in plasma environments which are found at ICMEs, i.e. in plasma with low β and relatively high Alfvén speeds.

The Helios and Ulysses spacecraft have been used to directly observe exhausts over distances of 0.3 AU (Gosling *et al.*, 2006a) to 5.4 AU (Gosling *et al.*, 2006b). These data do

not show any relationship between the size or occurrence rates of exhausts with heliocentric distance.

1.5.2 Particle heating

Many of these measurements also showed the density and temperature to increase within reconnection exhausts (e.g., Gosling *et al.*, 2005; Phan *et al.*, 2006; Davis *et al.*, 2006). Measurements of proton velocity distributions using ACE showed this to be related to the presence of counterstreaming beams of protons from the inflow regions, rather than from dissipation within the reconnection exhaust (Gosling *et al.*, 2005). A set of distribution functions measured using ACE are shown in Figure 1.9. Both of the single populations measured in the inflow regions can be seen in the exhaust region, where the distribution is composed of two populations with different parallel velocities. Distribution functions are rarely measured within solar wind exhausts as velocity distributions are typically acquired at a low cadence relative to the duration over which exhausts are observed, and relatively wide reconnection exhausts are required for such measurements.

Counterstreaming beams have also been measured at exhausts at the magnetopause (Gosling *et al.*, 1990), magnetotail (Hoshino *et al.*, 1998) and magnetosheath (Phan *et al.*, 2007a). The ion temperature increase associated with these ion beams is expected to be proportional to the inflow region Alfvén speed (Drake *et al.*, 2009a), which has been shown for exhausts in the solar wind (Drake *et al.*, 2009a) and at the magnetopause (Phan *et al.*, 2014). This is also expected for electrons (Phan *et al.*, 2013b), however in the solar wind the Alfvén speeds are typically too low to measure increases in electron temperatures (Pulupa *et al.*, 2014).

Furthermore, energetic electrons have been measured near the diffusion region in the magnetotail (Øieroset *et al.*, 2002), however no energetic electrons have been observed at solar wind exhausts (possibly because significant electron energisation is thought to occur near the diffusion region, however solar wind observations are typically made much further downstream).

1.5.3 Multi-spacecraft observations

The use of combined measurements of the same exhaust which was observed by multiple spacecraft has contributed considerably to our understanding solar wind exhausts. For example, in a study by Phan *et al.* (2006), ACE, Wind and Cluster observed the same exhaust despite being separated by hundreds of R_E in the out-of-plane direction. These measurements were used to infer that the X-line extended over a distance of at least 390

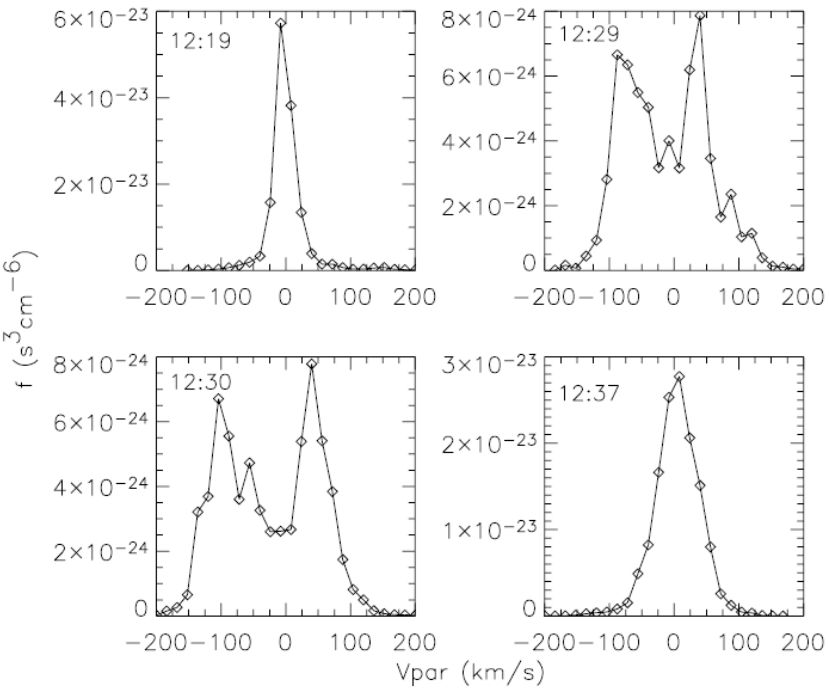


Figure 1.9: Reduced proton distributions obtained within (top right and bottom left panels) and immediately outside of (top left and bottom right panels) a solar wind reconnection exhaust. Taken from Gosling *et al.* (2005).

R_E (4×10^4 d_i). The time delay between observations at each spacecraft was found to agree with the expected delay for a planar boundary that propagates with the solar wind velocity, indicating that the exhaust was planar on the length scales that separate the spacecraft (hundreds of R_E). Similar magnetic field and ion velocity profiles at each spacecraft also indicated that the local orientation of the exhaust was similar at each spacecraft. These measurements therefore indicated that reconnection produced a two dimensional and planar exhaust structure. Furthermore, these observations were made over 2.5 hours, suggesting that reconnection was ongoing over this period in a quasi-steady manner.

Other observations of reconnection exhausts at multiple spacecraft have similarly indicated that the exhausts are large-scale and have extended X-lines, they are quasi-steady and planar (e.g. Gosling *et al.* (2007a,b); Phan *et al.* (2009)). Direct confirmation that reconnection produces oppositely directed exhausts came from observations using both ACE and Wind (Davis *et al.*, 2006). These observations also showed the exhaust outflows to extend ∼100 R_E (thousands of d_i) downstream of the X-line. In one case a magnetic island was observed which appeared to be located between two reconnection X-lines (Eriksson *et al.*, 2014), however this appears to be rare. In general, solar wind exhausts appear to produce large structures which originate from a single X-line.

1.5.4 High resolution measurements

The ability to resolve reconnection exhausts in the solar wind relies upon sufficiently high resolution magnetic field and plasma measurements. With 64 s cadence measurements from ACE, one can typically identify 10-20 exhausts per year at 1 AU, whereas with 3 s cadence measurements from Wind one can identify 40-80 exhausts per month at 1 AU (Gosling, 2012). In addition to observing more exhausts, these higher resolution measurements show that thin reconnection exhausts are observed at higher rates than wide ones (89% of events are observed over less than 100 s), and that the magnetic shear angles for most exhausts are less than 90° (Gosling *et al.*, 2007d). Exhausts with shear angles lower than 11° have been observed (Gosling & Szabo, 2008; Phan *et al.*, 2010; Gosling & Phan, 2013), and exhausts at low shear angles tend to be relatively thin.

1.5.5 Distance downstream of the X-line

We note that in the solar wind there is in general no way of determining whether reconnection is ongoing at the reconnection site or whether the observed flows are from an X-line at which reconnection is no longer active. Furthermore, it is generally very difficult to reliably estimate a spacecraft's distance downstream of the X-line. In many cases this is crudely estimated using the observed exhaust width and by assuming a canonical reconnection rate of 0.1, (where the distance downstream is (reconnection rate) × (exhaust width/2)), however Davis *et al.* (2006) were able to more accurately estimate the distance downstream using measurements of the reconnection rate. Exhaust outflows continue to flow freely away from the reconnection site in the solar wind, forming extremely extended structures. In many cases the exhaust width is significantly wider than exhausts at the magnetopause and magnetotail, and it is now clear that exhausts in the solar wind are typically measured much further downstream of the reconnection X-line than exhausts observed in the magnetosphere. The large extent of the exhausts relative to the size of the diffusion region makes encounters with the diffusion region statistically unlikely, which is probably why they have been observed at the magnetopause and magnetotail but not in the solar wind.

1.5.6 Reconnection onset

A study of 197 solar wind exhausts showed that for low $\Delta\beta$ (the difference in β between the two sides of the exhaust) reconnection can occur at low and high magnetic shears (Phan *et al.*, 2010). At large $\Delta\beta$, however, reconnection only occurs at high shears. This is in agreement with a theoretical prediction that reconnection is suppressed at low shears when there is a difference in plasma β between the inflow regions (Swisdak *et al.*, 2010),

because of a diamagnetic drift of the reconnection X-line. Specifically, reconnection can only occur where $\Delta\beta$ and the magnetic shear angle across the current sheet satisfy the following condition, as derived by Swisdak *et al.* (2010),

$$\Delta\beta < 2(\lambda/d_i)\tan(\theta/2), \tag{1.34}$$

where θ is the magnetic shear angle and λ is the width of the density gradient layer across the current sheet (assumed to be $\sim d_i$). This condition is a result of the diamagnetic drift that particles undergo in the presence of a guide field and asymmetry between the reconnecting plasmas (Swisdak *et al.*, 2003). The drift of the particles causes the X-line to drift, and reconnection is suppressed when this drift exceeds the reconnection outflow speed. This occurs for sufficiently large plasma pressure gradients and guide fields, therefore reconnection can occur only when the above condition is fulfilled. As a result, at low β, the difference in β on either side of the exhaust is also necessarily low, and reconnection is not suppressed by this mechanism. This may be why early observations of reconnection in the solar wind indicated that reconnection occurs in low β environments, however it is now clear that reconnection will also occur in high β environments when the shear angle is sufficiently high. Observations of reconnecting and non-reconnecting current sheets at the magnetopause have also been found to be in agreement with this reconnection onset criterion (Phan *et al.*, 2013a).

1.6 Near-Earth reconnection environments

In addition to the solar wind, reconnection occurs at other locations in near-Earth space, namely the magnetosheath, the magnetopause and the magnetotail. In this section we discuss reconnection in these locations and differences compared to solar wind reconnection.

At a distance of 150 million km from the Sun (1 AU) the solar wind approaches Earth. Earth has its own planetary magnetic field which presents an obstacle to the solar wind called the magnetosphere. Since the solar wind and magnetospheric plasmas are frozen-in they are unable to mix; the solar wind remains tied to the IMF and magnetospheric plasma remains frozen to the planetary magnetic field. As the solar wind approaches Earth's magnetosphere it is travelling at hundreds of km s^{-1} and must slow down to be able to deflect around the magnetosphere. Since the solar wind speed relative the Earth is greater than the local fast magnetosonic speed, a standing shock wave forms in front of Earth (Figure 1.10). This bow shock converts a substantial fraction of the particles' energy to thermal energy and slows down the solar wind (Walker & Russell, 1995). The shocked solar wind downstream of the shock is the magnetosheath, which has a higher density, temperature and magnetic field strength than the solar wind (see Table 1.1). The

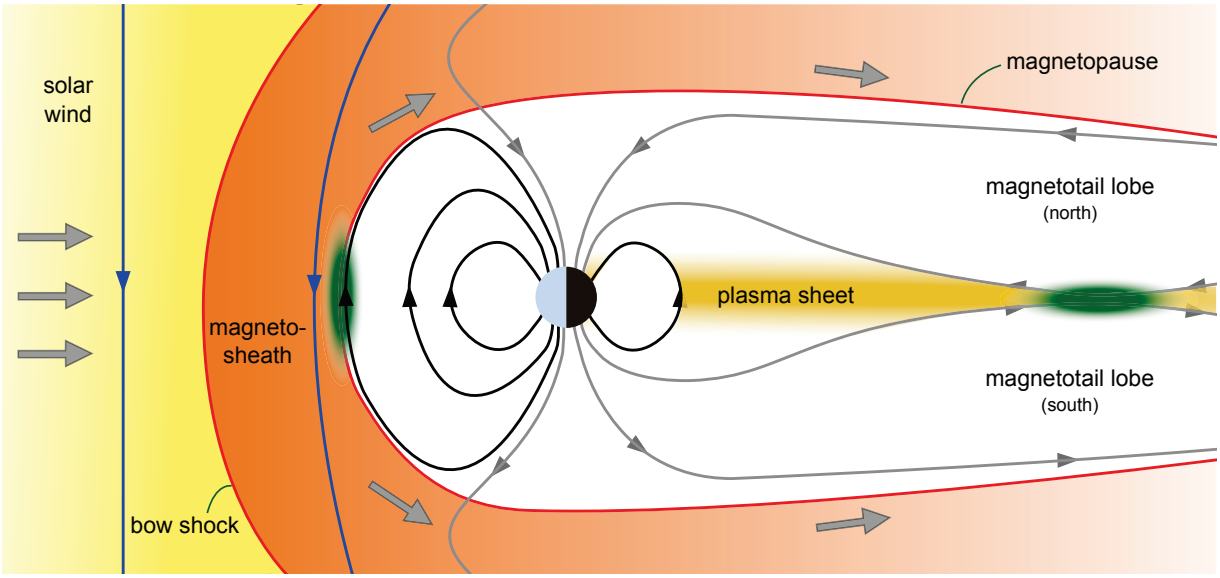


Figure 1.10: The solar wind-magnetosphere interaction, in a meridional cut. The IMF and Earth's magnetic field are shown in blue and black, respectively. Magnetic fields which have undergone reconnection and connect the magnetosphere to the solar wind are shown in grey. The magnetosphere is located within the magnetopause boundary. Reconnection sites are shown in green. Solar wind flow around the magnetosphere is indicated with grey arrows.

magnetosheath is filled with current sheets, and reconnection exhausts are observable (e.g., Phan *et al.*, 2007a; Retinò *et al.*, 2007; Øieroset *et al.*, 2016). Reconnection here is similar to solar wind reconnection, occurring across a range of guide fields and with relatively symmetric inflow conditions.

The magnetopause marks the boundary between the shocked solar wind in the magnetosheath and Earth's magnetosphere. The shape of the magnetopause surface is determined by a balance between the pressure of the solar wind and the pressure of the magnetosphere, and is in constant motion due to fluctuations in the solar wind (Hughes, 1995). Typically, the magnetopause is located at a distance of $\sim$10 R_E from Earth. On the dayside the magnetosphere is compressed, whereas on the nightside it stretches out to in excess of 100 R_E to form the magnetotail. The dayside magnetosphere is characterised by hot (1-10 keV) but tenuous plasma ($n < 1$ cm^{-3}), which is mainly composed of protons and electrons. There are small quantities of He^+ and O^+ which are sourced from lower down in the magnetosphere, as well as He^{2+} which enters the magnetosphere through coupling to the solar wind via reconnection (Hughes, 1995).

On the dayside Earth's magnetic field is dipole-like, whereas in the magnetotail the magnetic field is drawn back. In the northern hemisphere these field lines point towards Earth and in the southern hemisphere they point away from Earth, forming a region of

oppositely directed magnetic fields between them which is the magnetotail current sheet (Figure 1.10).

In the system described, the solar wind and magnetospheric plasmas do not mix. Coupling between them was postulated by Dungey (1961), who invoked magnetic reconnection to explain how the solar wind and magnetosphere interact in a model that became known as the Dungey cycle. When the IMF points southward, magnetic reconnection occurs at the magnetopause between the southward IMF and the northward planetary magnetic field (Figure 1.10). This connects Earth's magnetic field to the IMF. The solar wind flows anti-sunward, convecting the IMF with it. The planetary field lines are stretched back into the magnetotail, where reconnected field lines from the northern pole (directed towards Earth) and southern pole (directed away from Earth) can meet. These oppositely directed field lines reconnect with each other, disconnecting the Earth's field from the IMF. The IMF is rarely directed purely southward, however magnetic reconnection frequently occurs at the magnetopause (where the reconnection site location strongly depends on the direction of the IMF (e.g., Trattner *et al.*, 2012)) and the magnetotail.

Reconnection at the magnetopause occurs between very different plasmas. Plasma in the magnetosheath is typically much denser and contains a weaker magnetic field than plasma in the magnetosphere. Reconnection at the magnetopause was first observed by Paschmann *et al.* (1979) and has since been measured with many spacecraft. The ion diffusion region has been encountered at the magnetopause (Mozer *et al.*, 2002), providing strong evidence for the collisionless reconnection model. Hall signatures in the ion diffusion region also appear to be distorted in a manner expected for asymmetric reconnection (Mozer *et al.*, 2008). More recently, high resolution measurements from the Magnetospheric Multiscale mission (Burch *et al.*, 2016b) have been used to provide evidence for the electron diffusion region at the magnetopause (Burch *et al.*, 2016a). In addition to the asymmetric inflow conditions, magnetopause reconnection often occurs with a guide field as large as $B_G \sim 0.7$ (Pu *et al.*, 2007; Trenchi *et al.*, 2008). Whilst reconnection at the magnetopause is often steady state, the presence of flux-transfer-events indicates that reconnection at the magnetopause can be transient and patchy, and may occur simultaneously at multiple X-lines (e.g., Fear *et al.*, 2008).

The magnetotail is composed of an $\sim$10 R_E thick region called the plasma sheet with a density of $n \sim 1$ cm^{-3} (Figure 1.10). Above and below this are the magnetotail lobes which have an extremely low density of $n \lesssim 0.1$ cm^{-3} (Hughes, 1995). Field lines in the lobes are often open and connect to the solar wind. Reconnection in the magnetotail typically occurs between this low β plasma which has high Alfvén speeds (Table 1.1), often producing reconnection exhausts with outflow speeds in excess of 1000 km s^{-1} (e.g., Hietala *et al.*, 2015). Field lines in the north and south lobes are typically anti-parallel

and plasmas in these two regions are usually very similar. Magnetotail reconnection is therefore usually symmetric with very weak guide fields. In-situ observations have shown magnetotail reconnection to occur in two preferred locations. Quasi-steady and continuous reconnection occurs in the distant magnetotail, with an X-line location of $\sim$140 R_E down tail (Nishida *et al.*, 1997). Reconnection also occurs closer to Earth, which tends to be brief and unsteady, and is associated with magnetospheric substorms (e.g., Baker *et al.*, 1985; Angelopoulos *et al.*, 1992). Near-Earth reconnection X-lines are found at distances of $10 - 30$ R_E (Nishida & Nagayama, 1973). As Earthward fast flows produced by near-Earth reconnection approach denser plasma nearer to Earth, they can compress the Earth's magnetic field to form dipolarization fronts. These dipolarization fronts can be the site of complex interactions between the reconnection outflow and the plasma sheet, and result in particle energisation and heating (e.g., Khotyaintsev *et al.*, 2011; Eastwood *et al.*, 2015). Observations of ion diffusion regions in the magnetotail have shown the Hall current systems and magnetic fields that are expected from collisionless reconnection (e.g., Nagai *et al.*, 2001; Eastwood *et al.*, 2010b).

The magnetopause often moves at speeds of tens of km s^{-1} due to variations in the solar wind pressure (e.g., Dunlop *et al.*, 2001). The magnetotail can also flap and have wave modes which causes it to move at similar speeds (e.g., Sergeev *et al.*, 2003; Volwerk *et al.*, 2003). Spacecraft motion relative to the exhaust structures is therefore slow, and the relative velocity can vary whilst spacecraft are within the exhausts. Spacecraft may therefore move in and out of exhausts, often making partial crossings over several minutes. In comparison, exhaust structures in the solar wind and magnetosheath move at speeds of hundreds of km s^{-1} relative to spacecraft. The spacecraft therefore rapidly traverse the exhausts, and these measurements correspond to straight cuts through the exhaust structures.

In the solar wind the relative speeds are very high and the time that the spacecraft spends inside the reconnection exhaust is shorter than for exhausts at the magnetosheath, magnetopause and magnetotail. This means that fewer data points can be collected, making it more difficult to probe the exhausts in detail. Additionally, the exhaust structures are much larger in the solar wind (hundreds of R_E) than in other environments (tens of R_E). This makes it far more likely for the exhaust region to be encountered in the solar wind rather than the diffusion region.

We note that reconnection has been observed at other planets, and is not unique to Earth's magnetosphere. Reconnection signatures have been observed at Mercury which has a weak planetary magnetic field (Slavin *et al.*, 2009), as well as at Jupiter which has the largest magnetic field and magnetosphere within the solar system (Russell *et al.*, 1998). The diffusion region has also been directly encountered in the magnetotails of Mars (Eastwood *et al.*, 2008) and Saturn (Arridge *et al.*, 2016).

1.7 Outstanding questions

A large amount of observations have suggested that reconnection exhausts are generally two dimensional and planar, and that reconnection occurs in a steady manner in the solar wind. This has been concluded from observations of the same exhausts using multiple spacecraft. Such in-situ measurements are only able to determine the extent to which the exhausts are planar on the spatial scales of the spacecraft separation, however, and smaller scale structure cannot be probed. Some solar wind observations (Gosling *et al.*, 2007a,b) and simulations (Lapenta & Brackbill, 2002; Yin *et al.*, 2008) have indicated that reconnection exhausts and current sheets may sometimes have non-planar structure. Studies with more closely spaced spacecraft would allow these structures to be probed on smaller scales. This is possible with Cluster, which has not been widely used to study reconnection in the solar wind. Cluster measurements allow for multi-point analysis methods, which may provide more accurate measurements of exhaust structures.

Measurements of different reconnection exhausts in the solar wind often differ considerably, the reasons for which are often not immediately clear. In particular, although many exhausts show increases in densities and temperatures within the exhaust, these signatures are not common to all exhausts (e.g., Gosling, 2007; Gosling *et al.*, 2007d) and an understanding of why this is the case has not emerged. Statistical surveys would be helpful in addressing these questions, however they have typically focussed on addressing other questions, namely: the occurrence rate and detection of exhausts (Gosling *et al.*, 2006a,b; Gosling, 2007), the size of reconnection exhausts (Phan *et al.*, 2009), ion heating (Drake *et al.*, 2009a; Enžl *et al.*, 2014) and reconnection onset (Phan *et al.*, 2010).

The general structure of reconnection exhausts is also difficult to determine given that they display a large degree of variability. A determination of this general structure would be helpful for comparisons with models of reconnection exhausts, and allow us to better determine how reconnection accelerates and heats plasma. Observations of solar wind exhausts are ideal for this as they are in general not affected by other processes such as the formation of dipolarization fronts in the magnetotail, and spacecraft are located much further downstream of the reconnection X-line where the exhausts are fully developed. Such distances downstream are difficult to model using simulations as they require vast computing resources, and solar wind observations therefore present an ideal method of probing the exhausts that form as a result of reconnection. Given that these exhausts are observed so far downstream of the reconnection site, it may also be possible to use spacecraft measurements to measure how the exhaust structure evolves with increasing distance from the reconnection site, which is again difficult to approach using numerical simulations.

The majority of observations indicate that reconnection exhausts are well described by

fluid physics (i.e., the accelerated flows are consistent with rotational discontinuities (see Section 2.5)). Kinetic physics is thought to be important in the diffusion region, however the kinetic physics of ions streaming along field lines has been observed far downstream of the X-line (Gosling *et al.*, 2005). It is therefore important to ask what physics processes are required to explain reconnection exhausts and whether it is appropriate to model reconnection exhausts using fluid physics, as is often the case. Furthermore, are other signatures of kinetic processes observable within reconnection exhausts?

1.8 Thesis overview

In Chapter 2 the instruments and analysis methods used in this thesis are introduced, along with the Cluster, Wind and ACE spacecraft. This is followed by a survey for reconnection exhausts in the solar wind using Cluster.

The results of a statistical analysis of 188 solar wind exhausts measured using Wind are presented in Chapter 3, in which the average properties of reconnection exhausts in the solar wind are determined. These data are shown to be consistent with fluid treatments of exhausts. The extent to which the plasma density and temperature increase within reconnection exhausts is found to be dependent upon the inflow region plasma β and guide field, and the reconnection guide field is also found to be important in controlling whether or not ion heating is dependent upon the inflow region Alfvén speed, as has previously been suggested (Drake *et al.*, 2009a).

In Chapter 4 multi-spacecraft observations of three different reconnection exhausts are used to determine how reconnection exhausts change with distance downstream of the X-line. For all events the reconnection current sheet becomes bifurcated with increasing distance downstream, indicating that bifurcated reconnection current sheets are observed when spacecraft are sufficiently far downstream of the reconnection X-line.

The presence of kinetic signatures within reconnection exhausts is presented in Chapter 5. For this study we use the same 188 events as in Chapter 3, finding clear evidence of Hall signatures in several exhausts. We also compare these observations to the results of a fully kinetic PIC simulation in order to better understand the measurements. These signatures persist thousands of d_i downstream of the reconnection X-line, indicating that kinetic processes are not confined to the reconnection X-line and can persist far downstream. These signatures are only evident in a small subset of events, however, and in general reconnection exhausts appear to be well described using fluid physics, as found in Chapter 3.

Another exception to the general properties of reconnection exhausts is found in Chapter 6. Cluster multi-point measurements are used to measure the small-scale three dimensional structure of a reconnection exhaust. This case study indicates that although reconnection generally forms planar exhausts in large open systems, these may also exhibit smaller scale structure. Finally, this thesis is summarised and conclusions from it are presented in Chapter 7.

2 Instrumentation, methods & data survey

2.1 Introduction

In-situ spacecraft measurements have been made since the early days of the space age and have provided major contributions to our understanding of the heliosphere, Earth's magnetosphere and the other planets of the solar system. In this thesis we use measurements acquired in the solar wind with three different spacecraft to investigate the physics of magnetic reconnection exhausts. The spacecraft missions which we use (Cluster, Wind and ACE) are introduced in Section 2.2. The instruments onboard these spacecraft which we use to measure fields and particles are described in the following section. In Section 2.4 we describe four methods which are used to determine appropriate coordinate systems in which to analyse the data. In Section 2.6 we conduct a survey for reconnection exhausts using Cluster measurements of the solar wind to demonstrate how reconnection exhausts are identified using in-situ measurements. Results from this survey are discussed, and three of the events identified during the course of this survey are studied in Chapter 4.

2.2 Spacecraft

2.2.1 Cluster

The Cluster mission was proposed to the European Space Agency in 1982 as a four-spacecraft mission which would allow for detailed studies of plasma physics in key regions of the magnetosphere including the magnetotail, polar cusp and auroral zone, as well as providing measurements of the solar wind and the bow shock (Taylor *et al.*, 2015). Following an unsuccessful launch in 1996, it was decided that the mission was of such high importance that the spacecraft should be re-built. The four identical Cluster spacecraft were then successfully launched in 2000 (Escoubet *et al.*, 2001). We refer to each of the four spacecraft as C-1, C-2, C-3, C-4.

The four spacecraft are spin stabilised with a spin period of 4 s, and each carry a suite of 11 identical scientific instruments. These include electron/ion particle detectors and fluxgate magnetometers (introduced in Section 2.3), as well as instruments for measuring high frequency electric and magnetic fields, plasma waves, and energetic particles (Escoubet *et al.*, 2001). The spacecraft were initially launched into a highly elliptical polar orbit around Earth with apogee at 19.6 R_E and perigee at 4 R_E. This orbit is fixed in inertial space and therefore rotates with respect to the Sun-Earth line throughout the year, allowing different regions of the magnetosphere, magnetotail, magnetosheath and solar wind to be sampled. Cluster enters the solar wind from approximately December to May. By using simultaneously acquired data from four closely spaced spacecraft, the Cluster mission allows for detailed analysis of plasma structures and allows for the separation of temporal and spatial variations in measurements, which is not possible with single spacecraft measurements (Dunlop *et al.*, 1988). The spacecraft orbits are such that the four spacecraft frequently form a regular tetrahedral formation during each orbit, which, through careful manoeuvres, has varied in size (with spacecraft separations of between 20 km and 36,000 km), allowing various spatial scales to be probed (Escoubet *et al.*, 2013).

Measurements from the Cluster mission are available from the Cluster Science Archive[1] (CSA). Cluster measurements are used in Section 2.6 and Chapters 4 and 6.

2.2.2 Wind

The Wind spacecraft was launched in 1994 to accurately measure the plasma environment of the near-Earth solar wind (Acuña *et al.*, 1995). Wind was initially placed in a large orbit with an apogee of 250 R_E before being placed in an orbit of the L1 point. The L1 point is the Lagrange point between the Earth and Sun where the gravitational forces of the Earth and Sun are such that a body at L1 will orbit the Sun with the same angular velocity as Earth, allowing the body to maintain a constant position in Earth's frame of reference. The L1 point is $\sim 1.5 \times 10^6$ km upstream of Earth.

Measurements from Wind are available from Coordinated Data Analysis Web[2] (CDAWeb). Wind measurements are used in Chapters 3, 4, 5 and 6.

2.2.3 ACE

The Advanced Composition Explorer (ACE) was launched in 1997 into an orbit of the L1 point (Stone *et al.*, 1998). ACE is equipped with a range of instruments to study

[1] http://www.cosmos.esa.int/web/csa
[2] http://cdaweb.gsfc.nasa.gov

the solar wind, its elemental and isotopic composition, and energetic populations of the interplanetary medium and more distant sources.

Measurements from ACE are available from Coordinated Data Analysis Web (CDAWeb). ACE measurements are used in Chapters 4 and 6, and ACE measurements of the solar wind speed are used in Section 2.6.3.

2.3 Instruments

In this section we introduce the instruments used to collect data in this thesis. The general designs of these instruments are outlined. The specific details of each instrument's design are customised to meet the science goals of its spacecraft mission.

2.3.1 Fluxgate magnetometer

Fluxgate magnetometers measure local vector magnetic fields, and are the most common magnetometer used for space applications (Balogh, 2010). This is because they are sensitive to a large range of magnetic fields, are stable over the long duration of spacecraft missions, and have low power and mass requirements which are scarce resources on spacecraft. Magnetometers designed for magnetospheric and solar wind research are typically required to measure magnetic fields in the ranges of ∼0.1 nT to in excess of 10,000 nT. Fluxgate magnetometers measure magnetic fields from ∼0 Hz to ∼60 Hz; the upper limit is determined by the response of the electronics. Search coil magnetometers are used where measurements of higher frequency magnetic fields are required.

Fluxgate magnetometers typically employ a ring shaped core of a highly magnetically permeable alloy which exhibits magnetic hysteresis. The drive winding is wrapped around the core. A sense winding is wrapped around the outside (Figure 2.1). The magnetometer works by first applying a current through the drive winding, which induces a magnetic field in the core (Balogh, 2010). In the presence of no external magnetic field, the field induced by the drive winding is symmetric throughout the core. When the drive current is turned off the core comes out of saturation. Since the two sides of the core shown in Figure 2.1 come out of saturation at the same time and their magnetic fields are oppositely directed, the flux through the sense winding is zero and no voltage is induced. In the presence of an external field, the total field in the side of the core where the induced and external field are aligned (shown in green) will be greater than the side where the external field is opposed to the induced field (shown in blue). The side with the weaker total field will come out of saturation first, and differences in the time of different parts of the core to come

out of saturation results in a net flux through the sense winding. The change in this flux induces a voltage in the sense winding, due to Faraday's law. The process is repeated with an AC current in the drive winding (causing the direction of the core's induced magnetic field to reverse), such that the side of the core which came out of saturation first reaches total saturation before the other side. This results in two peaks in the voltage measured from the sense winding, and this signal has twice the frequency of the AC current applied to the drive winding. The size and phase of the induced voltage in the sense winding can be used to determine the magnitude and direction of the external magnetic field along one direction.

Three orthogonally mounted fluxgate magnetometers are used to measure the three components of the magnetic field (a tri-axial fluxgate magnetometer) (e.g., Balogh *et al.*, 2001). These magnetometers are usually located on the end of long booms attached to the spacecraft, such that they are located away from the main spacecraft. This is to reduce electromagnetic interference, allowing the magnetometer to measure the magnetic field of its plasma environment rather than that which is generated by the spacecraft itself. Typically a spacecraft will have two fluxgate magnetometers mounted at different locations on the spacecraft boom(s). This allows the spacecraft magnetic field to be calculated using gradiometry (Ness *et al.*, 1971) and provides a backup in case one magnetometer should fail.

Magnetic field measurements are obtained in the coordinates of the three fluxgate magnetometers. In the case of a spinning spacecraft, the measurements must be transformed from a spinning frame of reference to a despun frame of reference of the spacecraft. They can then be transformed into more useful coordinate systems such as GSE.

The Cluster Fluxgate Magnetometer instrument (Balogh *et al.*, 2001) consists of an outboard fluxgate magnetometer which is located at the end of a 5.2 m boom which extends from the spacecraft, and an inboard fluxgate magnetometer located 1.5 m from the end of the boom. The outboard magnetometer is the primary instrument under normal operation. The instrument measures each component of the magnetic field with an accuracy of $\sim$0.1 nT. We use magnetic field vectors available at 22.416 s^{-1} (normal telemetry mode).

The Wind Magnetic Field Investigation (Lepping *et al.*, 1995) consists of an outboard fluxgate magnetometer which is located on the end of a 12 m boom which extends from the spacecraft, and an inboard fluxgate magnetometer which is located 1/3 of the distance from the end of the boom. The instrument measures each component of the magnetic field with an accuracy of < 0.006 nT. We use magnetic field vectors which are available at 10.9 s^{-1} (normal telemetry mode).

The ACE magnetic field experiment has two fluxgate magnetometers which are located

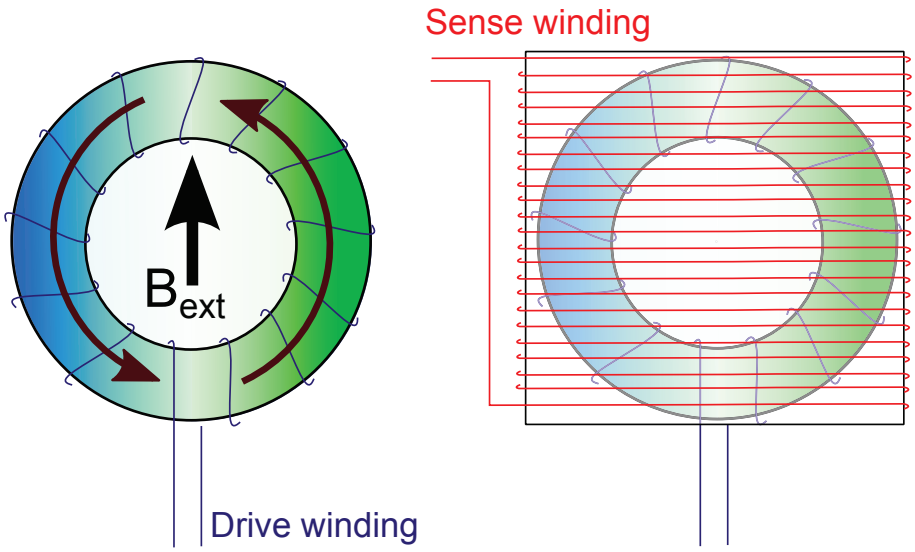


Figure 2.1: Fluxgate magnetometer. The core is shown in blue and green, where arrows indicate the direction of the induced field. An externally applied field is indicated by B_{ext}. The drive winding is shown in dark blue, and the sense winding is shown in red on the right.

at the ends of two 4.2 m booms placed on opposing sides of the spinning spacecraft (Smith *et al.*, 1998). Magnetic fields are measured to within 0.1 nT and we use measurements with 1 s resolution.

2.3.2 Electrostatic analyser

Electrostatic analysers (ESA) are used to measure the plasma populations around spacecraft. They may be designed to measure either ions or electrons. The particles enter the ESA through a narrow opening, allowing the electrons/ion populations to be sampled (e.g., Rème *et al.*, 2001). The direction and speed of the incoming particles is measured, from which a three dimensional velocity distribution is constructed. The particle density, speed, temperature and higher order moments may be calculated from this distribution function.

The opening of the ESA typically has a 180° or 360° field of view in the polar plane (Figure 2.2). This opening is narrow in the azimuthal direction, such that the field of view covers a narrow slice of the sky. Electrostatic deflectors deflect incoming particles through $\sim 90°$ in the azimuthal direction. Only particles with a specific energy per charge (E/q) will be deflected by the correct amount by the voltage between the walls of the electrostatic deflector to reach the microchannel plates (MCPs) which detect them (Fazakerley *et al.*, 1998). Particles with higher E/q or lower E/q will hit the walls of the electrostatic deflectors and not reach the MCPs.

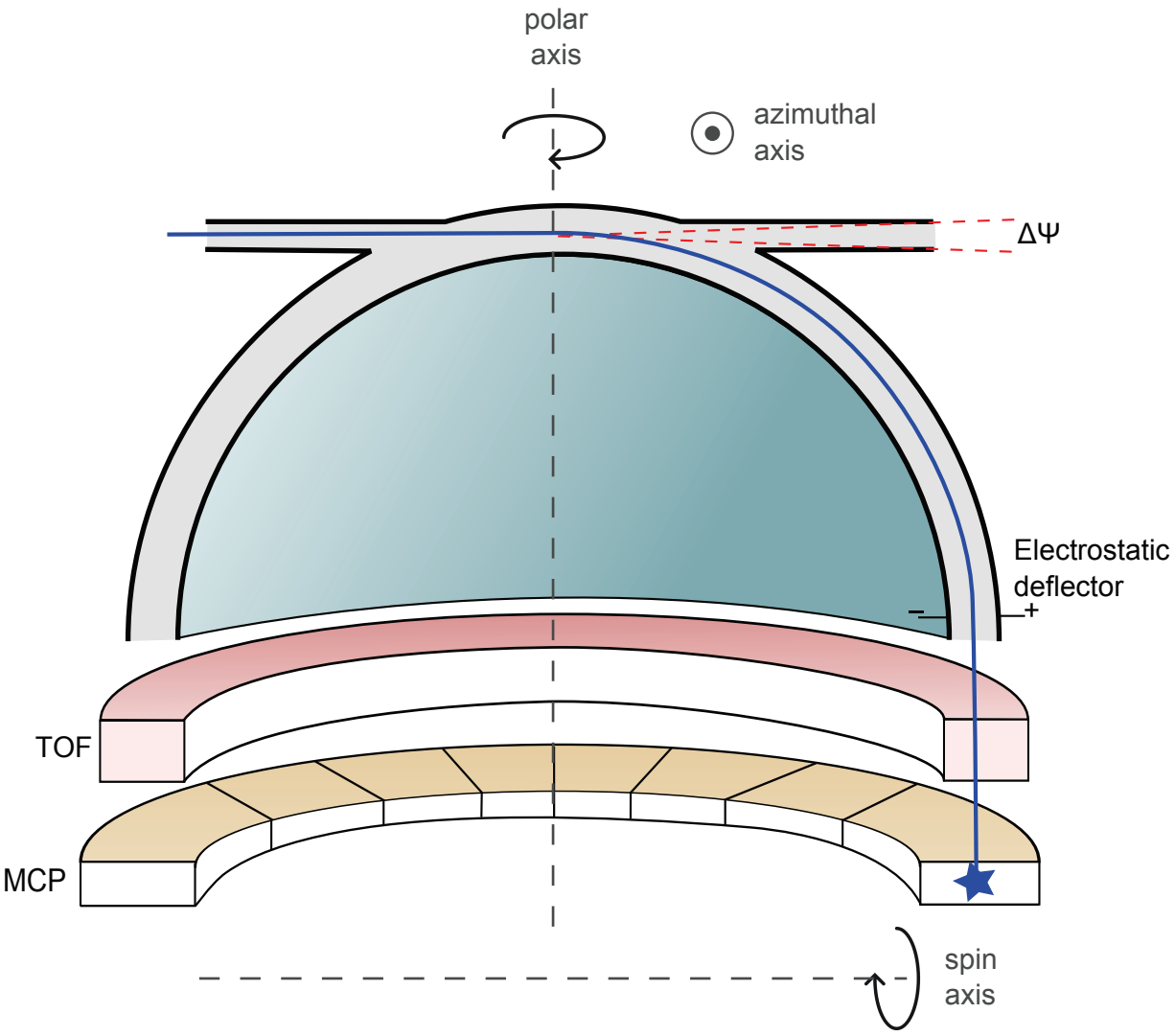


Figure 2.2: Electrostatic analyser with a 180° field of view in the polar plane and a opening of $\Delta\Psi$ in the azimuthal plane. The path of a positively charged ion which is detected at the MCP is shown in blue. A TOF detector is also shown (although they are not included in all electrostatic analysers). The directions of the azimuthal, polar and spacecraft spin axes are shown.

Particles which reach the bottom of the deflectors strike one of many MCPs which are arranged around the device. Once a particle strikes an MCP it causes a cascade of electrons which are detected by an anode. The azimuthal direction in which the opening was pointing at the time of the measurements indicates the azimuthal directional in which the particle was moving, and the MCP which it strikes indicates its polar angle. These measurements provide information of the particles' direction (Fazakerley *et al.*, 1998). If the instrument does not have a time of flight detector (TOF) it is unable to determine the particle mass and the particle is usually assumed to be of a certain species to calculate its speed from its known E/q. The particle speed may be independently measured by placing a TOF detector between the electrostatic deflector and the MCPs. This measures the time that it takes for a particle to move through the TOF detector to determine its speed. This allows the particle mass per charge to be determined from measurements of E/q and its speed, such that distribution functions can be constructed for different species (Fazakerley *et al.*, 1998).

The ESA is usually mounted on the spacecraft such that as the spacecraft spins the detector opening moves through 360° in the spin plane, allowing particles to be measured across the full 4π steradians of the sky. Particles of different E/q are measured by rapidly varying the voltage which is applied between the two walls of the electrostatic deflectors throughout the course of the spacecraft spin.

Once a three dimensional velocity distribution function $f(\mathbf{v})$ has been constructed, moments of the distribution function can be calculated (Paschmann *et al.*, 1998). In this thesis we typically used the particle density, bulk velocity and temperature.

The zeroth order moment (density) is

$$n = \int f(\mathbf{v}) d^3v. \tag{2.1}$$

The first order moment (bulk velocity) is

$$\mathbf{V} = \frac{1}{n} \int \mathbf{v} f(\mathbf{v}) d^3v. \tag{2.2}$$

The second order moment (pressure tensor) is

$$\mathbf{P} = m \int (\mathbf{v} - \mathbf{V})(\mathbf{v} - \mathbf{V}) f(\mathbf{v}) d^3v. \tag{2.3}$$

The temperature components $T_{1,2,3}$ are determined from the pressure tensor by either diagonalising $\mathbf{P}$ or rotating $\mathbf{P}$ according to the magnetic field. The isotropic temperature of the distribution function is calculated as $T = (T_1 + T_2 + T_3)/3$. For a Maxwellian distribution, T represents the distribution's temperature. If the distribution is non-Maxwellian, T may have a different interpretation. Nevertheless, measurements of T may still be useful for

characterising the plasma.

Moments of the distribution function can be determined by processing measured distributions onboard the spacecraft. Alternatively, the distribution function may be downlinked to ground. In this case corrections can be made to the distribution function before calculating moments. This may be necessary to account for effects which are not included when moments are calculated onboard, such as spacecraft charging as a result of solar photons, which can prevent low energy particles from entering ESAs. Downlinking distribution functions requires a greater bandwidth than downlinking moments. Moments calculated from downlinked distributions are therefore available at a lower cadence than onboard moments.

The Cluster Ion Spectrometry experiment (CIS) experiment onboard Cluster consists of two instruments (Rème *et al.*, 2001). The COmposition and DIstribution Function (CODIF) analyser has a TOF detector to provide three dimensional distributions of H^+, He^{2+} and O^+ ions. CODIF has an angular resolution of 22.5° in the polar direction. This resolution is insufficient to resolve the distribution function of particles in the solar wind and is not used in this thesis. The Hot Ion Analyser (CIS-HIA) does not have a TOF detector and cannot distinguish between species. 3D distributions are acquired over one spacecraft spin (4 s) and onboard calculated moments are available at this cadence. CIS-HIA has a 360° field of view in the polar plane, however it is split into two halves, each with a 180° field of view. One side (the high sensitivity side) has an 11.3° angular resolution in the polar direction. The other side (the low sensitivity side) has a higher resolution of up to 5.6°, which is used to measure ions in the solar wind. CIS-HIA has several operation modes which specify which side of the instrument is used to take measurements and the E/q range which is swept through, allowing CIS-HIA to take measurements across a range of environments in which ion densities and energies can differ substantially. Modes can be grouped into solar wind, magnetospheric and magnetosheath modes, which are selected based on Cluster's anticipated orbit. Use of a mode which uses the low angular resolution side when Cluster is located in the solar wind can lead to underestimates of the density and poor measurements of the temperature (see Section 6.2). CIS has not operated since launch on C-2 and CIS-HIA has been switched off on C-4. Cluster also carries an electron ESA instrument (Plasma Electron and Current Experiment (Johnstone *et al.*, 1997)) for the measurement of electrons, however data from this instrument is not used in this thesis as we do not require electron measurements in our analysis of Cluster data.

The 3D Plasma Analyzer (3DP) experiment onboard Wind is composed of several instruments (Lin *et al.*, 1995). We use data from the ion electrostatic analysers and electron electrostatic analysers. These ESAs do not have time of flight detectors. 3D distributions are acquired over one spacecraft spin (3 s) and onboard calculated moments are available at this cadence. 3DP has a polar angular resolution of up to 5.6°. On-board calculated

electron moments tend to be unreliable due to effects such as spacecraft charging (T. D. Phan, private communication). This affects the measurements, however distributions sent to ground can be corrected for such effects. We therefore use moments calculated on-ground for electrons. These are available at a lower cadence than onboard moments. We use onboard moments for ions.

The Solar Wind Electron Proton Alpha Monitor (SWEPAM) onboard ACE has an electron ESA and ion ESA (McComas *et al.*, 1998). We use data from the ion ESA which measures 3D distributions acquired over one spacecraft spin (64 s). Moments are available at this cadence. SWEPAM has a high polar resolution of $2.5 - 5°$. Moments are calculated separately from distributions of H^+ and He^{2+} ions; only moments of H^+ ions are used in this thesis.

2.3.3 Probing of electron density using high frequency waves

The Waves of HIgh frequency and Sounder for Probing of Electron density by Relaxation (WHISPER) experiment (Décréau *et al.*, 1999) onboard Cluster provides a secondary method of determining the electron density using multiple electric field and wave instruments. This may be required when density measurements from CIS-HIA are not available. WHISPER emits radio pulses with a frequency range of $4 - 82$ kHz over a period of $\sim$1 ms and measures radio signals $\sim$5 ms after. The electron plasma frequency is found from the peak of the measured radio spectra, and is available as a data product. The electron plasma frequency, ω_e, is related to the electron density, n_e, by

$$\omega_e = \sqrt{\frac{n_e e^2}{m_e \epsilon_0}}.$$

2.4 Current sheet normal determination techniques

Current sheets and reconnection exhausts in the solar wind have arbitrary orientations. For observations to be compared to reconnection models, it is helpful to use similar coordinate directions for the observations and models. It is extremely unlikely that a reconnection exhaust will be aligned with geocentric coordinate systems which are typically used to examine spacecraft data. It is therefore necessary to determine a coordinate system specific to the reconnection exhaust under consideration, which is comparable to coordinate systems that are more conducive to understanding reconnection models.

An LMN current sheet normal coordinate system is typically used (see Section 1.1.1) which is aligned with the current sheet. In the following sections we outline two methods

used to determine LMN coordinates from single spacecraft data, and two methods to determine the current sheet normal using data from multiple spacecraft.

2.4.1 Minimum variance analysis

The Minimum Variance Analysis (MVA) method (Sonnerup & Cahill, 1967) was initially developed to determine the direction normal to current sheets from single spacecraft measurements. Its working principle is that spacecraft measure hundreds of magnetic field vectors as they cross a reconnection exhaust. The current sheet normal direction is the direction in which these vectors change the least, since the normal component of the field is assumed to be constant across the current sheet. This is because the magnetic field is divergence free (i.e., $\nabla \cdot \mathbf{B} = 0$), which means that across a thin interface (e.g., a current sheet) the normal component of the magnetic field must be constant. The method also finds the directions in which the field varies the most, and a direction of intermediate variance. The maximum, intermediate and minimum variance directions form an orthogonal coordinate system.

In an LMN coordinate system the L component of the magnetic field will vary the most as B_L changes from positive on one side of the exhaust to negative on the other side. The N component of the magnetic field should remain constant across the current sheet. The M component of the magnetic field will vary in the presence of Hall magnetic fields, and in Section 3.4 we show that in general B_M is observed to increase within the exhaust region. LMN coordinates can therefore be determined from MVA where the L, M, N directions correspond to the directions of maximum, intermediate and minimum variance of the magnetic field, respectively.

In order to find the direction in which the magnetic field vectors vary the least, the vector N is chosen such that the standard deviation of the difference between each field vector ($\mathbf{B_i}$) and their mean values ($\langle \mathbf{B} \rangle$) in the N direction is minimised, i.e., through the minimisation of the quantity

$$\sigma^2 = \frac{1}{S} \sum_{i=1}^{S} \left[(\mathbf{B_i} - \langle \mathbf{B} \rangle) \cdot \hat{\mathbf{N}} \right], \tag{2.4}$$

where

$$\langle \mathbf{B} \rangle = \frac{1}{S} \sum_{i=1}^{S} \mathbf{B_i} \tag{2.5}$$

and S is the number of field vectors. The minimisation of Equation 2.4 is achieved through solving the eigenvalue equation of matrix $\mathbf{M}$, the matrix of covariance between the components of the magnetic field. The eigenvector associated with the smallest eigenvalue is the

vector $\hat{\mathbf{N}}$. Elements of matrix $\mathbf{M}$ are given by

$$M_{\mu\nu} = \langle B_\mu B_\nu \rangle - \langle B_\mu \rangle \langle B_\nu \rangle. \tag{2.6}$$

where $\mu, \nu = 1, 2, 3$ (components of the magnetic field) and

$$\langle B_\mu \rangle = \frac{1}{S} \sum_{i=1}^{S} B_{i,\mu}, \qquad \langle B_\mu B_\nu \rangle = \frac{1}{S} \sum_{i=1}^{S} B_{i,\mu} B_{i,\nu}. \tag{2.7}$$

The eigenvector associated with the largest/intermediate/smallest eigenvalue of the eigenvalue equation of matrix $\mathbf{M}$ corresponds to the maximum/intermediate/minimum variance direction of the magnetic field. Further details of the MVA method are provided in Sonnerup & Scheible (1998).

The out-of-plane component of the magnetic field may vary within reconnection exhausts (e.g., as a result of rotational discontinuities at the exhaust boundaries (Section 3.4.3) or Hall fields (Chapter 5)). If this variation is substantial, the directions of intermediate and minimum variance of the magnetic field are well defined, and the M and N directions can be reliably determined from MVA. In practice, however, the variations in the out-of-plane direction are often not significantly large enough compared to variations in the current sheet normal direction for the intermediate and minimum variance directions to be well defined. In such cases the intermediate and minimum variance directions do not correspond directly to the M and N directions. This is discussed further in Section 3.3.2, in which LMN coordinates derived from MVA and hybrid-MVA (outline in the next section) using Wind magnetometer data are compared.

2.4.2 Hybrid-minimum variance analysis

Although MVA estimates of the M and N directions may in some cases be unreliable, MVA does very reliably determine the direction of maximum variance as B_L changes much more significantly than either B_M or B_N. Gosling & Phan (2013) used hybrid-MVA to combine the L direction from MVA with an alternative estimate for the N direction to derive an LMN coordinate system more accurately aligned with the reconnection exhaust. B_N is expected to be small and constant across the current sheet. Hybrid-MVA assumes that the normal component of the magnetic field across the reconnection current sheet is zero, effectively treating it as a tangential discontinuity. Strictly, this is not true, and hybrid-MVA may not be appropriate when accurate measurements of the normal magnetic field are required. This method does, however, successfully differentiate between the M and N directions and is useful for determining the orientation of reconnection current sheets.

When treating the current sheet as a tangential discontinuity, the magnetic field vectors on either side of the reconnection current sheet should have no normal component and should be parallel to the current sheet. Additionally, their cross product should be orthogonal to the current sheet (i.e., parallel to the current sheet normal). Their cross product is therefore used as the current sheet normal direction, which is given by

$$\hat{\mathbf{N}} = \frac{\mathbf{B_1} \times \mathbf{B_2}}{|\mathbf{B_1} \times \mathbf{B_2}|}, \tag{2.8}$$

where $\mathbf{B_1}$ and $\mathbf{B_2}$ are magnetic field vectors on either side of the current sheet. This is combined with the maximum variance direction from MVA (here referred to as L') to determine the M direction,

$$\hat{\mathbf{M}} = \frac{\hat{\mathbf{N}} \times \hat{\mathbf{L}}'}{|\hat{\mathbf{N}} \times \hat{\mathbf{L}}'|}. \tag{2.9}$$

The L direction is then found from the cross product of the M and N directions, to form an orthogonal coordinate system,

$$\hat{\mathbf{L}} = \hat{\mathbf{M}} \times \hat{\mathbf{N}}. \tag{2.10}$$

The L directions and L' (maximum variance direction) are often very closely aligned.

2.4.3 3-spacecraft determination of solar wind current sheet normals

The normal to a planar discontinuity can also be determined from combining observations from multiple spacecraft. This requires accurate knowledge of the relative time delays between the arrival of the discontinuity at the respective spacecraft, which can be found from magnetic field and plasma measurements.

In the solar wind measurements from a minimum of three spacecraft may be used. This requires assumptions that the discontinuity is planar and that it convects with the solar wind (i.e., it is stationary in the plasma frame of reference). This is discussed in Horbury *et al.* (2001), and we use this method in Section 6.3 to determine the normal of a current sheet using observations from Cluster, Wind and ACE.

The separation between spacecraft on the plane of the discontinuity needs to be found, however they may observe the discontinuity at different times. To calculate the separation between spacecraft ν and a reference spacecraft μ in this plane, one can apply a transformation of $\mathbf{V_{SW}} t_{\mu,\nu}$ to the position of spacecraft ν, as shown in Figure 2.3. $\mathbf{V_{SW}}$ is the solar wind bulk velocity and $t_{\mu,\nu}$ is the difference between the time at which the discontinuity was observed at spacecraft ν and μ. This assumes that the velocity of the discontinuity is given by the measured solar wind velocity.

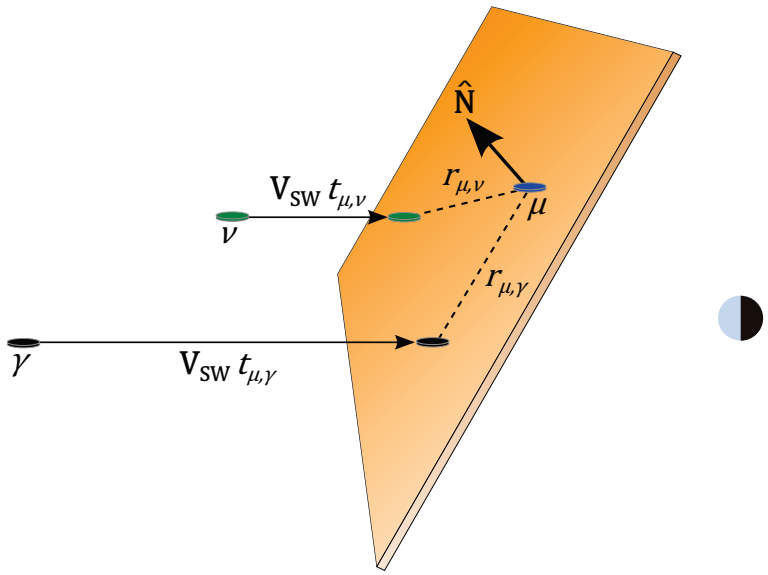


Figure 2.3: A planar discontinuity observed by spacecraft μ, ν, γ is shown, with Earth to the right. The positions of spacecraft ν and γ are transformed by $\mathbf{V_{SW}} t_{\mu,\nu}$ and $\mathbf{V_{SW}} t_{\mu,\gamma}$, respectively, to give their relative positions from spacecraft μ in the plane of the discontinuity (relative positions are given by the vectors $\mathbf{r}_{\mu,\nu}$ and $\mathbf{r}_{\mu,\gamma}$). $\hat{\mathbf{N}}$ is given by Equation 2.11.

Once this transformation has been applied the spacecraft all lie within the plane of the discontinuity. Their relative positions, $\mathbf{r}_{\mu,\nu}$, must lie in this plane, and the cross product of these vectors is perpendicular to the plane. The normal vector can therefore be determined as,

$$\hat{\mathbf{N}} = \frac{\mathbf{r}_{\mu,\nu} \times \mathbf{r}_{\mu,\gamma}}{|\mathbf{r}_{\mu,\nu} \times \mathbf{r}_{\mu,\gamma}|}, \tag{2.11}$$

where $\mu, \nu, \gamma = 1, 2, 3$ indicate the three spacecraft.

This method makes several assumptions. The discontinuity is assumed to be planar over scales of the spacecraft separations. If the discontinuity has non-planar features on scales smaller than the spacecraft these will not be detected using this method. The discontinuity is also assumed to be stationary in the plasma frame of reference, such that its velocity is equal to the measured solar wind velocity. This must be the same at each spacecraft. If these assumptions are not true, this method is unlikely to provide a reliable estimate of the discontinuity normal. This may occur when the spacecraft are separated over large enough scales that the solar wind bulk velocity may differ at each spacecraft, or when they are separated over very small distances such that the time delays $t_{\mu,\nu}$ are small and the uncertainties on this measurement become significant.

2.4.4 Multi-spacecraft discontinuity timing analysis

The three-spacecraft technique described in the previous section relies upon the fact that the velocity of the discontinuity relative to the spacecraft is known (this is the measured solar wind velocity). In this section we outline a more general technique (multi-spacecraft discontinuity timing analysis) for determining the normal to a planar discontinuity moving with an unspecified velocity. Multi-spacecraft discontinuity timing analysis also allows the normal speed of the discontinuity to be estimated. This technique is described in detail in Dunlop & Woodward (1998).

Multi-spacecraft discontinuity timing analysis requires a minimum of four spatially separated measurements of the discontinuity. The technique can be extended to a higher number of measurement points, however here we consider four measurement points as is appropriate for the application of multi-spacecraft discontinuity timing analysis to the four spacecraft Cluster mission.

The technique uses the relative positions of the spacecraft and the time delays between observations of the same discontinuity. If the spacecraft are separated by displacements of $\mathbf{r}_{\mu,\nu}$ and observe the same boundary at differences in time of $t_{\mu,\nu}$, the boundary normal N and its velocity $\mathbf{V_B}$ can be related by the equation

$$(\mathbf{V_B} t_{\mu,\nu}) \cdot \hat{\mathbf{N}} = \mathbf{r}_{\mu,\nu} \cdot \hat{\mathbf{N}}. \tag{2.12}$$

Using spacecraft μ as a reference spacecraft, the relative positions of the other three spacecraft and their relative time differences in observing the discontinuity can be used to solve for the boundary speed in the normal direction ($V_B = \mathbf{V_B} \cdot \hat{\mathbf{N}}$) and $\hat{\mathbf{N}}$ by solving the equation,

$$\begin{pmatrix} \mathbf{r}^{\mathbf{t}}_{\mu,\nu} \\ \mathbf{r}^{\mathbf{t}}_{\mu,\gamma} \\ \mathbf{r}^{\mathbf{t}}_{\mu,\epsilon} \end{pmatrix} \cdot \frac{1}{V_B} \begin{pmatrix} N_1 \\ N_2 \\ N_3 \end{pmatrix} = \begin{pmatrix} t_{\mu,\nu} \\ t_{\mu,\gamma} \\ t_{\mu,\epsilon} \end{pmatrix} \tag{2.13}$$

for the quantity $\frac{1}{V_B} \cdot \hat{\mathbf{N}}$, where $\mu, \nu, \gamma, \epsilon = 1, 2, 3, 4$ specify the spacecraft and 't' indicates the transpose of a column vector. This is solved by multiplying Equation 2.13 by the inverse of the matrix of position vectors, allowing the discontinuity normal, $\hat{\mathbf{N}}$, and the speed of the discontinuity in the N direction (in the spacecraft frame of reference), V_B, to be determined. The velocity of the planar discontinuity can only be calculated in the direction of N. The discontinuity is assumed to be planar and therefore uniform in the plane that defines it, and it is not possible to resolve any motion parallel to this plane.

The ability of this method to estimate N is affected by the relative locations of the spacecraft. The optimum locations are such that the four spacecraft lie at the vertices of a

regular tetrahedron, in which case the normals of discontinuities with arbitrary orientations can be estimated. As an extreme example, if the four spacecraft are instead positioned in a line and the discontinuity normal lies in a plane perpendicular to this line, there is no way of determining the normal's direction within that plane. Although it is difficult to estimate N in such cases, in Section 6.4 we nevertheless use the relative timing of observations between Cluster spacecraft which are in a straight line configuration to apply certain constraints on the structures which are observed. The length of time delays between spacecraft, $t_{\mu,\nu}$, relative to the time that it takes for the discontinuity to pass over each spacecraft are also important. N can be most accurately determined when $t_{\mu,\nu}$ are large with respect to the duration of the discontinuity at each spacecraft, whereas the uncertainty in N becomes large when the discontinuity is comparable to $t_{\mu,\nu}$. This is explored further in Section 4.4.3 where we compare the uncertainties in estimates of N for different discontinuities.

2.5 Walén relation

The Walén relation was derived to test whether observed flows at the magnetopause were consistent with the flows expected for magnetopause reconnection, where the exhaust boundaries are composed of rotational discontinuities (Sonnerup *et al.*, 1981). It can also be used to test whether flows observed in the solar wind in association with current sheets are consistent with reconnection outflows (e.g., Phan *et al.*, 2006). The derivation of the velocity across the discontinuities uses conservation of the tangential electric field at a discontinuity, conservation of mass flux through the discontinuity, and conservation of tangential momentum. Using this, it has been shown that the change in velocity of the plasma across these structures equals the change in Alfvén velocity (using B_L and corrected for anisotropy) so that

$$V_{L2} = V_{L1} \pm \left[\sqrt{\frac{1-\alpha_2}{\mu_0 \rho_2}} B_{L2} - \sqrt{\frac{1-\alpha_1}{\mu_0 \rho_1}} B_{L1} \right], \tag{2.14}$$

where subscripts '1' and '2' are reference points across a rotational discontinuity (Hudson, 1970; Blagau *et al.*, 2015). α is given by

$$\alpha = \frac{(P_{\parallel} - P_{\perp})\mu_0}{B^2} \tag{2.15}$$

where $P_{\parallel}$ and $P_{\perp}$ are the plasma pressures parallel and perpendicular to the magnetic field, respectively. The sign in Equation 2.14 depends on whether V_N and B_N have the same sign (Sonnerup *et al.*, 1981; Paschmann *et al.*, 1986). They have the same sign on one side of the reconnection exhaust and opposite signs on the other side. It is therefore common to calculate the predicted velocity using two reference points (one on either side of the

exhaust). $V_{L,2}$ is calculated from one reference point using the positive sign in Equation 2.14 and from the other point using the negative sign, and is calculated for multiple points within the exhaust.

In the solar wind the temperature anisotropy is difficult to measure at sufficient cadence to calculate the predicted velocity at multiple points in the exhaust. Furthermore, differences between B_{L2} and B_{L1} are typically much greater than those between $\sqrt{(1-\alpha_2)/(\mu_0\rho_2)}$ and $\sqrt{(1-\alpha_1)/(\mu_0\rho_1)}$, and α_1 and α_2 therefore have minimal effects on V_{L2} in Equation 2.14. We therefore often assume solar wind plasma at a reconnection exhaust to be isotropic (i.e., $\alpha_1 = \alpha_2 = 0$) and use Equation 2.14 to calculate the predicted outflow speed. An example of this is shown in Figure 2.6 and discussed in the next section.

Although the Walén relation has often been found to over-estimate the observed exhaust velocity at the magnetopause and in the solar wind (e.g., Sonnerup *et al.*, 1981; Paschmann *et al.*, 2005; Phan *et al.*, 2006; Blagau *et al.*, 2015), the Walén velocity and observed velocity qualitatively agree for a reconnection exhaust. In simulations, Liu *et al.* (2012) showed the Walén velocity to exceed the simulation exhaust velocity in the center of reconnection exhausts, but found that it under-estimated the simulation velocity at the exhaust boundaries.

2.6 Survey for solar wind reconnection exhausts using Cluster

2.6.1 Introduction

Many observations of exhausts in the solar wind have used data from individual spacecraft. Observations of the same exhaust from multiple spacecraft located in the solar wind have also been combined, indicating that exhausts can extend over hundreds of R_E and that they typically have a planar and two dimensional structure over this extent (e.g., Phan *et al.*, 2006, 2009).

The Cluster spacecraft frequently enter the solar wind. The relatively small constellation (maximum separation ∼36,000 km (∼6 R_E)) allows small spatial scales to be studied, in addition to the large scales that are accessible when measurements from widely spaced spacecraft are combined (e.g., Cluster with ACE/Wind). Cluster also allows for the use of multi-spacecraft analysis techniques such as discontinuity timing analysis (Dunlop & Woodward, 1998), which can provide a more reliable determination of a reconnection current sheet normal than single spacecraft techniques such as MVA (see Sections 2.4 and 4.4.3).

Although a single Cluster spacecraft has been used to study a solar wind reconnection exhaust (Phan *et al.*, 2006), the benefits of using the four Cluster spacecraft to investigate solar wind reconnection exhausts have not been exploited. This may in part be because (a) reconnection exhausts were first observed in the solar wind almost 5 years after the launch of Cluster, (b) Cluster's orbits allow the spacecraft to excurse into the solar wind during approximately only four months of the year, and (c) because of the emphasis of Cluster science on magnetospheric research.

In this section reconnection exhausts are identified from Cluster solar wind data acquired during 2004 and 2009 to demonstrate how reconnection exhausts are identified in the solar wind and to identify events which could be studied in detail using the four Cluster spacecraft. Statistical properties of the 39 identified events are presented, and three of these events are studied in detail with the aid of measurements from Wind and ACE in Chapter 4.

2.6.2 Survey methodology

Figure 2.4 shows Cluster inter-spacecraft distances from launch to late 2013. The Cluster spacecraft had equal inter-spacecraft distances from launch to 2005, after which there were extended periods when the separation between C-3 and C-4 was small compared to that between C-1/C-2/C-3. We surveyed Cluster data between the months of January to May as the spacecraft regularly entered the solar wind during these times (near orbit apogee). These months were chosen in the years of 2004 and 2009 because the spacecraft were in a regular tetrahedral formation when in the solar wind during these periods and inter-spacecraft distances differed significantly between the two years; in 2004 and 2009 the spacecraft were separated by ∼280 km and ∼10,000 km, respectively. These years were chosen to provide the possibility of studying different exhausts on very different spatial scales.

The survey was performed by initially inspecting 2 hour plots (generated from CSA) of measurements of the magnetic field magnitude and components in GSE coordinates, and CIS-HIA measurements of the density and ion velocity (in GSE coordinates) from C-1 (or C-3 if C-1 data was not available). Solar wind reconnection exhausts are identified by rotations in the magnetic field (current sheets) which occur at the same time as deflections in the ion velocity (exhaust outflows), such that changes in the magnetic field and ion velocity components are correlated on one side of the ion velocity deflection and anti-correlated on the other side (Gosling *et al.*, 2005). The plots were inspected (by eye) for significant discontinuities or rotations in at least one magnetic field component, accompanied by a perturbation of the ion velocity in the same component such that the magnetic field and

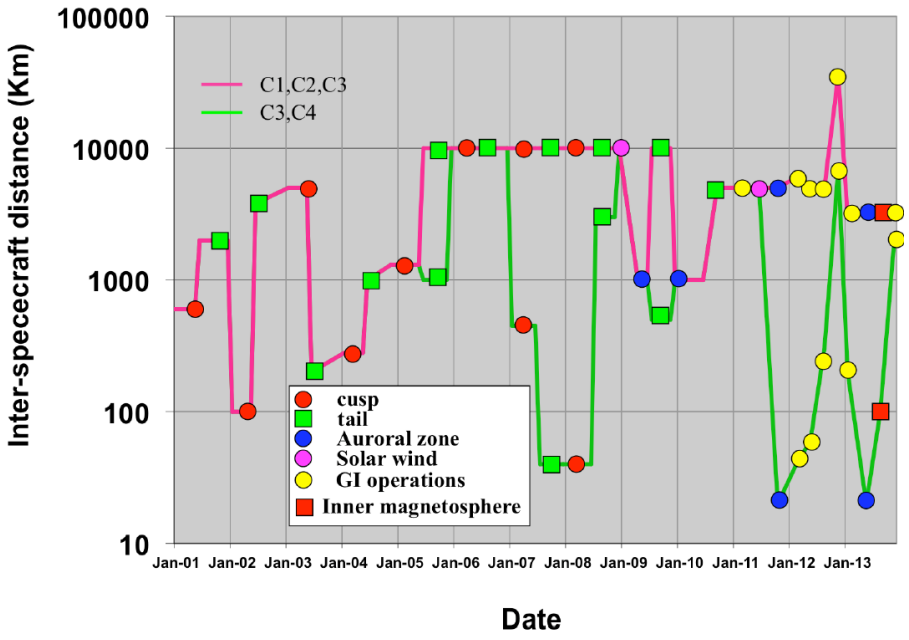


Figure 2.4: Cluster inter-spacecraft distances from launch to late 2013. Distances between C-3 and C-4 are shown in green when they differ to distances between other Cluster spacecraft. Inter-spacecraft distances are shown at the point along the orbit indicated by the legend. Taken from Escoubet *et al.* (2013).

ion velocity changes were correlated on one side of the perturbation and anti-correlated on the other side. The purpose of this survey was to identify multiple events that could be studied either as case studies or in small sets, and not to identify every single event within the data. 2 hour plots of data were inspected (which were found to be sufficient for identifying multiple events) to reduce the time required to conduct the survey. An example of a 2 hour plot with three potential events is shown in Figure 2.5.

Reconnection exhausts and current sheets can have any orientation in the solar wind. Magnetic field and ion velocity changes can therefore occur in multiple GSE components, making it difficult to determine whether these signatures correspond to a reconnection exhaust. Cluster measurements for each potential event were downloaded from CSA and rotated into LMN coordinate systems determined from MVA and hybrid-MVA analyses using MATLAB. It was found that current sheet normal coordinates are more reliably determined from hybrid-MVA (see Section 3.3.2 where this is discussed in more detail for a larger data set). Events that fulfilled the following conditions in LMN coordinates determined from hybrid-MVA were selected as reconnection exhausts.

- change in sign of B_L across the event
- B_N is small and approximately constant (<2 nT fluctuations)

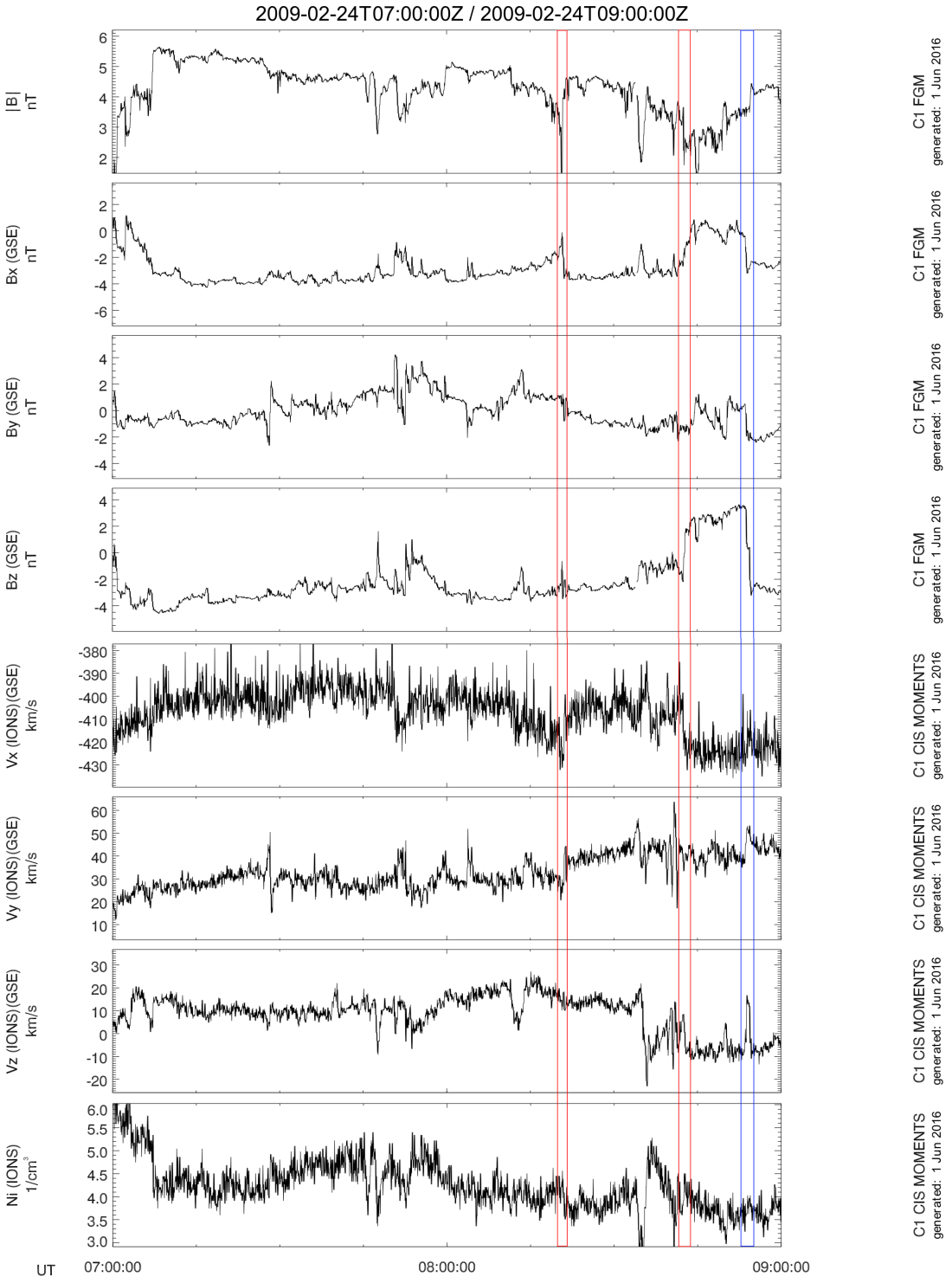


Figure 2.5: 2 hour plot generated by CSA of C-1 measurements of the magnetic field magnitude, magnetic field in GSE coordinates, ion velocity in GSE coordinates and ion density. Vertical lines indicate three potential events. Blue vertical lines indicate a reconnection exhaust that was subsequently identified, and is shown in Figure 2.6.

- changes in V_L and B_L are correlated on one side of the current sheet and anti-correlated on the other side
- changes in V_M and V_N are small with respect to changes in V_L

$|B|$ was not required to decrease across the current sheet as the guide field is often considerable at solar wind reconnection exhausts, in which case $|B|$ may not change significantly. As a further check, the exhaust outflow was then compared to the Walén velocity. These were found to be in reasonable qualitative agreement for all of the 39 events which met the above criteria.

Figure 2.6 shows data from the event indicated in blue in Figure 2.5, rotated into an LMN coordinate system determined using hybrid-MVA, and a diagram indicating how these measurements correspond to Cluster's encounter with the reconnection exhaust. The spacecraft motion relative to the solar wind is predominantly in $+\mathrm{X_{GSE}}$. The N vector is [0.46, -0.87, 0.17] in GSE coordinates, therefore the spacecraft motion was in $+N$ relative to the reconnection exhaust, as indicated in the diagram in Figure 2.6. B_L is positive in the inflow region measured before the exhaust, and negative in the inflow region measured after the exhaust. B_L changes from positive to negative within the interval, indicating the presence of a current sheet. Fluctuations in B_N are relatively small. The ion velocity increases in the $+L$ direction within the bounds of the current sheet such that changes in B_L and V_L are first anti-correlated and then correlated. Changes in V_M and V_N are small with respect to changes in V_L, as expected within a reconnection exhaust. The Walén velocity is shown alongside measurements of V_L. Although the predicted changes in V_L are larger than the observed changes (as has previously been found, see Section 2.5), there is a clear qualitative agreement between them. These measurements therefore indicate that the spacecraft intercepted a reconnection exhaust in the manner illustrated by the diagram in Figure 2.6. B_L starts to change at the second vertical line and stops changing at the third line. We consider the region between these lines to be the exhaust region. Note that $B_L \sim 0$ within the exhaust, indicating that the current sheet is bifurcated. The formation of bifurcated current sheets at reconnection exhausts is studied further in Chapter 4. Additionally, B_M increases within the reconnection exhaust. We investigate increases in the out-of-plane field within reconnection exhausts in Section 3.4.

When rotated into an LMN coordinate system the events shown in red in Figure 2.5 do not have changes in V_L that are bound by changes in B_L (i.e., a current sheet). They consequently did not meet the criteria which we use to identify reconnection exhausts.

We use C-1 measurements for the 39 identified events (with the exception of two events where C-3 measurements are used as C-1 measurements were unavailable). The exhaust interval was defined as the interval during which B_L changes. A period before the exhaust

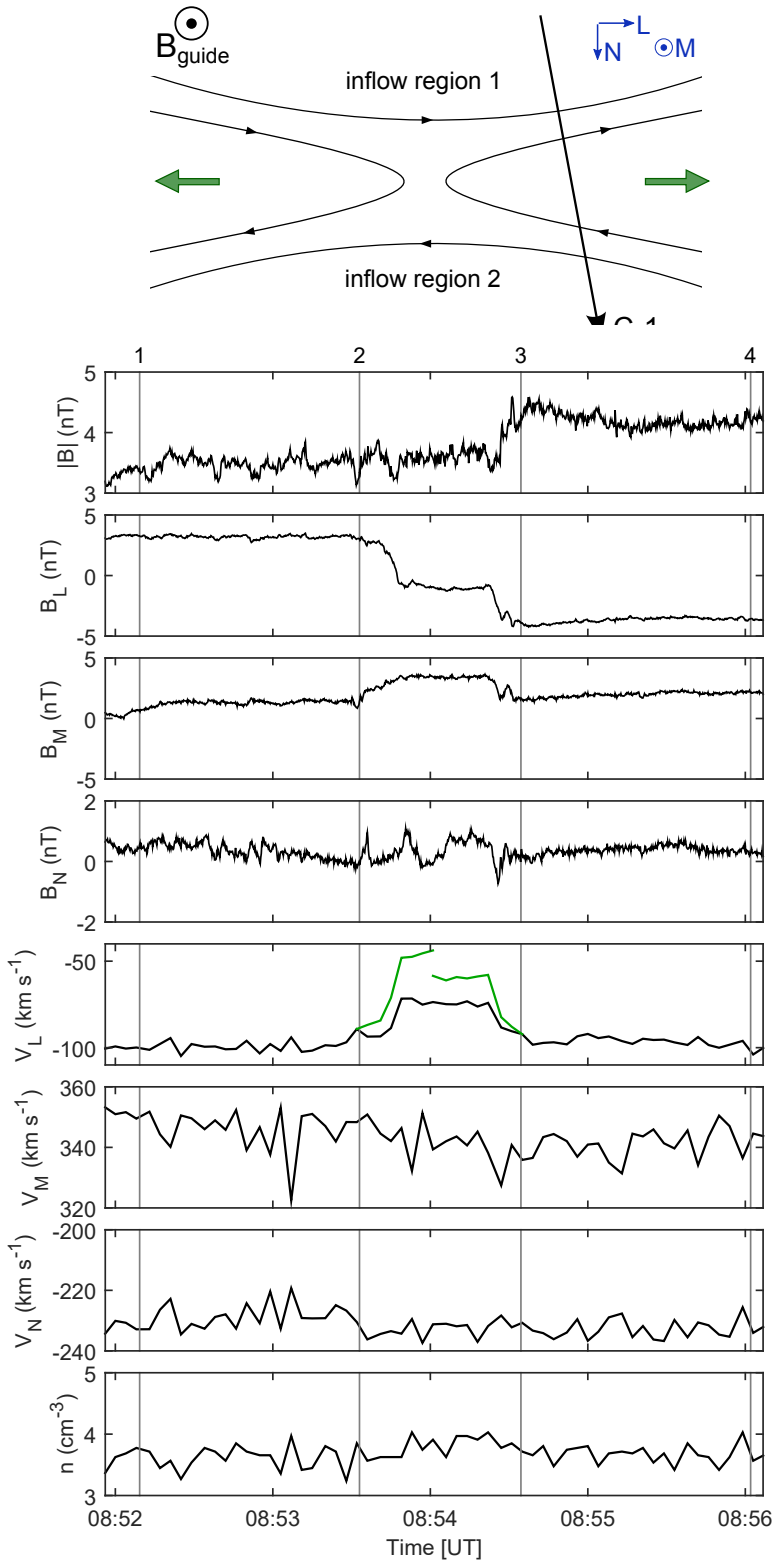


Figure 2.6: Data from the event highlighted in blue in Figure 2.5, in an LMN coordinate system. A diagram illustrating how these measurements correspond to C-1 intercepting the reconnection exhaust is shown above. The Walén velocity is shown in green. Inflow region 1 is between the first and second vertical lines. The exhaust region is between the second and third vertical lines. Inflow region 2 is between the third and fourth vertical lines.

where the magnetic field, density and velocity where relatively stable was identified as inflow region 1. A period after the exhaust where the magnetic field, density and velocity were relatively stable was identified as inflow region 2. The duration of intervals 1 and 2 vary between 18 s and 8 min depending on how stable measurements were in the inflow regions. In Figure 2.6, inflow region 1 is the interval between vertical lines 1 and 2, the exhaust region is between lines 2 and 3, and inflow region 2 is between lines 3 and 4. Averages of measurements within the three regions are used to characterise them. The average of combined data from inflow regions 1 and 2 are used to characterise the inflow region of each event. These measurements are discussed in Section 2.6.4.

2.6.3 Event detection rate

39 events were identified during the course of this survey, 6 events in 2004 and 33 events in 2009. Cluster was located in the solar wind for a total of 3.3 months and 3.5 months during the surveyed periods in 2004 and 2009, respectively, corresponding to detection rates of 1.8 month^{-1} and 9.3 month^{-1}. Gosling (2012) reports a detection rate of 40-80 month^{-1} for Wind data surveyed at solar activity minimum. Confirmation of both a current sheet and accelerated plasma flow are required for the detection of a reconnection exhaust, which requires multiple data points from measurements of the magnetic field and plasma velocity. Magnetic field measurements are acquired at a much higher cadence (22 Hz and 11 Hz for Cluster and Wind, respectively) than plasma moments (4 s and 3 s for Cluster and Wind, respectively). It is therefore the cadence of plasma moments that determines the duration of the shortest event which can be identified. Cluster CIS-HIA produces plasma moments at a similar cadence to Wind 3DP, therefore they should be able to resolve the same reconnection exhausts. The large discrepancy in occurrence rates between this survey and that conducted by Gosling (2012) is likely, therefore, to be due to the selection criteria rather than differences in data used. Since our events were first identified from 2 hour data plots, very short duration events are likely to be missed. Furthermore, it is possible that events with small changes in magnetic field or plasma velocity could have been missed (e.g., events with low Alfvén speeds). It is very difficult to identify all of the reconnection events in an extended period of solar wind data, and the intention of this survey was not to find all of the events, but to find a large set of well defined events. Indeed, no surveys of solar wind reconnection exhausts claim to have found all of the reconnection exhausts that may be present in the data, yet important results have still been found (Gosling *et al.*, 2006a,b; Phan *et al.*, 2009, 2010; Enžl *et al.*, 2014).

The detection rate of events is much higher in 2009 than 2004. The high sunspot number in 2004 (Figure 2.7) indicates that the Sun was in an active stage of the solar cycle in 2004, and the minima in sunspot number in 2009 indicates that the Sun was near solar

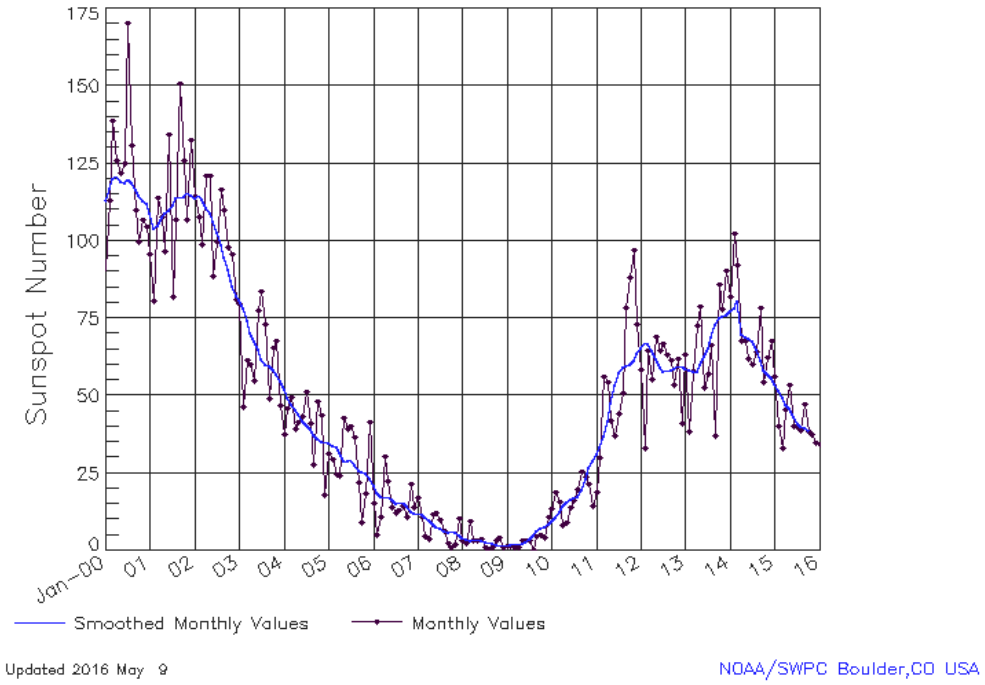


Figure 2.7: Monthly sunspot number from January 2000 to December 2015. Taken from http://www.swpc.noaa.gov/products/solar-cycle-progression.

minimum. In general, the solar wind is therefore expected to be slower and more steady in 2009 than in 2004, when it is likely to be be faster and more turbulent. Figure 2.8 shows ACE SWEPAM measurements of the solar wind velocity during the periods surveyed. The solar wind speed was typically higher in 2004. Additionally, speeds of less than 400 km s^{-1} (typically considered as 'slow' solar wind) were far more common in 2009, as shown by the horizontal bars. For a given exhaust width, the time which it takes for an exhaust to convect over a spacecraft decreases as the solar wind speed increases. The minimum width of exhausts which can be detected (which corresponds to an interval of the order 4 s) is therefore higher in 2004, and it is likely that thin reconnection exhausts were not resolved by CIS-HIA. This is important as thin reconnection exhausts are more abundant in the solar wind than relatively thick exhausts (see Figure 2.9(b)). Figure 2.8 additionally shows that in both years the vast majority of events that were identified were actually in solar wind with speeds of less than 400 km s^{-1}, further demonstrating that this is the likely cause of the difference in detection rates between the two years. The low detection rate of reconnection exhausts in the higher speed solar wind is consistent with previous findings that the detection rate of reconnection exhausts is reduced in the high speed solar wind as compared to slower solar wind (Gosling, 2007).

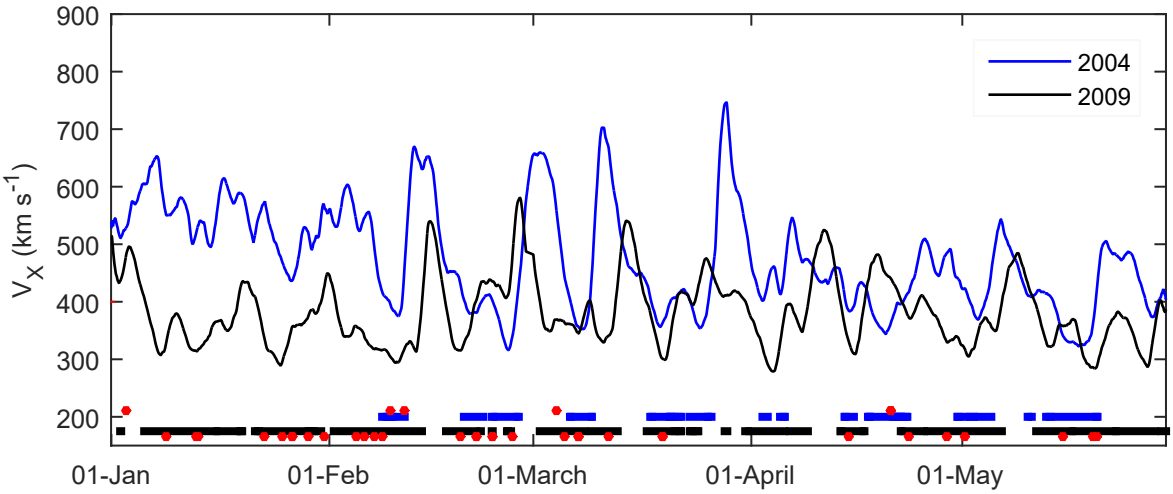


Figure 2.8: Hourly ACE SWEPAM measurements of the X_{GSE} component of the solar wind velocity during surveyed periods. Solid bars indicate when the velocity is less than 400 km s^{-1}. Red circles against the blue and black horizontal bars indicate the events identified in 2004 and 2009, respectively.

2.6.4 Current sheet and reconnection exhaust properties

An overview of the properties of the identified events is given in this section, with reference to measured properties of the reconnecting plasmas, the reconnection current sheets, and the exhaust outflows. A summary of the results discussed below is provided in Table 2.1.

Figure 2.9(a) shows the distribution of the duration over which each event was detected by Cluster. This duration is principally affected by the solar wind speed, the width of the exhaust in N, and the angle between Cluster's motion relative to the current sheet and the N direction. The minimum duration was 11.9 s. Events with lower durations are unlikely to have been detected using 2 hour overview plots. The majority of events are observed with durations of less than 100 s, and the median duration is 47 s.

The exhaust width in the N direction is calculated as $(\mathbf{V_{SW}}.\hat{\mathbf{N}})T$, where T is the event duration. Figures 2.9(b) and 2.9(c) show this width in km and d_i, respectively, where d_i is calculated for each event using the average of the density in inflow regions 1 and 2 (see Figure 2.9(e)). Figures 2.9(b-c) show that low width events are more frequently detected, and that very wide reconnection exhausts are less common. One exceptionally wide reconnection event is not shown in these plots, for which the measured width was 15.2×10^4 km (3100 d_i). The median exhaust width in units of d_i is 145. Assuming a reconnection rate of 0.1, would place Cluster at a median distance of 728 d_i downstream of the X-line.

Table 2.1: Summary of distributions shown in Figures 2.9 and 2.10.

	median	mean	minimum	maximum
Duration (s)	47.3	81.6	11.9	613.7
Width (km)	12,099	19,904	2,969	152,300
Width (d_i)	145	287	34	3,058
$\|B\|$ (nT)	4.7	5.7	1.8	15.2
n (cm^{-3})	8.3	9.8	1.6	21.9
T_i (eV)	9.5	13.0	4.2	44.4
normalised $\|B\|$ asymmetry	0.09	0.16	0.00	0.77
normalised n asymmetry	0.15	0.15	0.01	0.55
normalised T_i asymmetry	0.10	0.12	0.01	0.47
B_G	0.7	1.0	0.07	3.3
Shear angle (°)	111	105	33	172
Solar wind speed(X_{GSE}) (km s^{-1})	347	363	283	571
Exhaust outflow speed (km s^{-1})	21	25	11	55
$\|V_{L,2} - V_{L,1}\|/(2C_{AS})$	0.08	0.10	0.00	0.40

The magnetic field magnitude, ion density and ion temperature from averages in inflow regions 1 and 2 are shown in Figures 2.9(d-f). The minimum and maximum measured values are 1.8 nT and 15.2 nT for $|B|$, 1.6 cm^{-3} and 21.9 cm^{-3} for n, and 4.2 eV and 44.4 eV for T_i.

Plasma in the two inflow regions are generally considered to be fairly similar for solar wind reconnection current sheets, which is in contrast to some other reconnection environments such as the magnetopause (where reconnection occurs between the magnetosheath which has a low magnetic field strength and high density, and the magnetosphere which has a high magnetic field strength and low density). Figure 2.10(a) shows the distribution of differences between T_i, n and $|B|$ measured in the two inflow regions, normalised by the mean of the two inflow regions. Although these differences are typically small (< 0.2), there are cases where differences between the two inflow regions are non-negligible.

Figure 2.10(b) shows the exhaust outflow speed. The mean value of V_L in the two inflow regions is found. The exhaust outflow speed shown here is the greatest departure of V_L within the exhaust region from this mean value. These outflow speeds (with a median of 21 km s^{-1}) are far lower than those typically found at the magnetopause (> 100 km s^{-1}) and magnetotail (of the order 1000 km s^{-1}) where the inflow region Alfvén speeds are higher. The minimum measured value was 11 km s^{-1}. Exhausts with lower outflow speeds may exist within the surveyed data set, however events were first identified by searching for changes in the ion velocity within 2 hour time windows. Exhausts with low outflow speeds may be difficult to identify on these scales as these speeds may be lower than other velocity fluctuations within a 2 hour window.

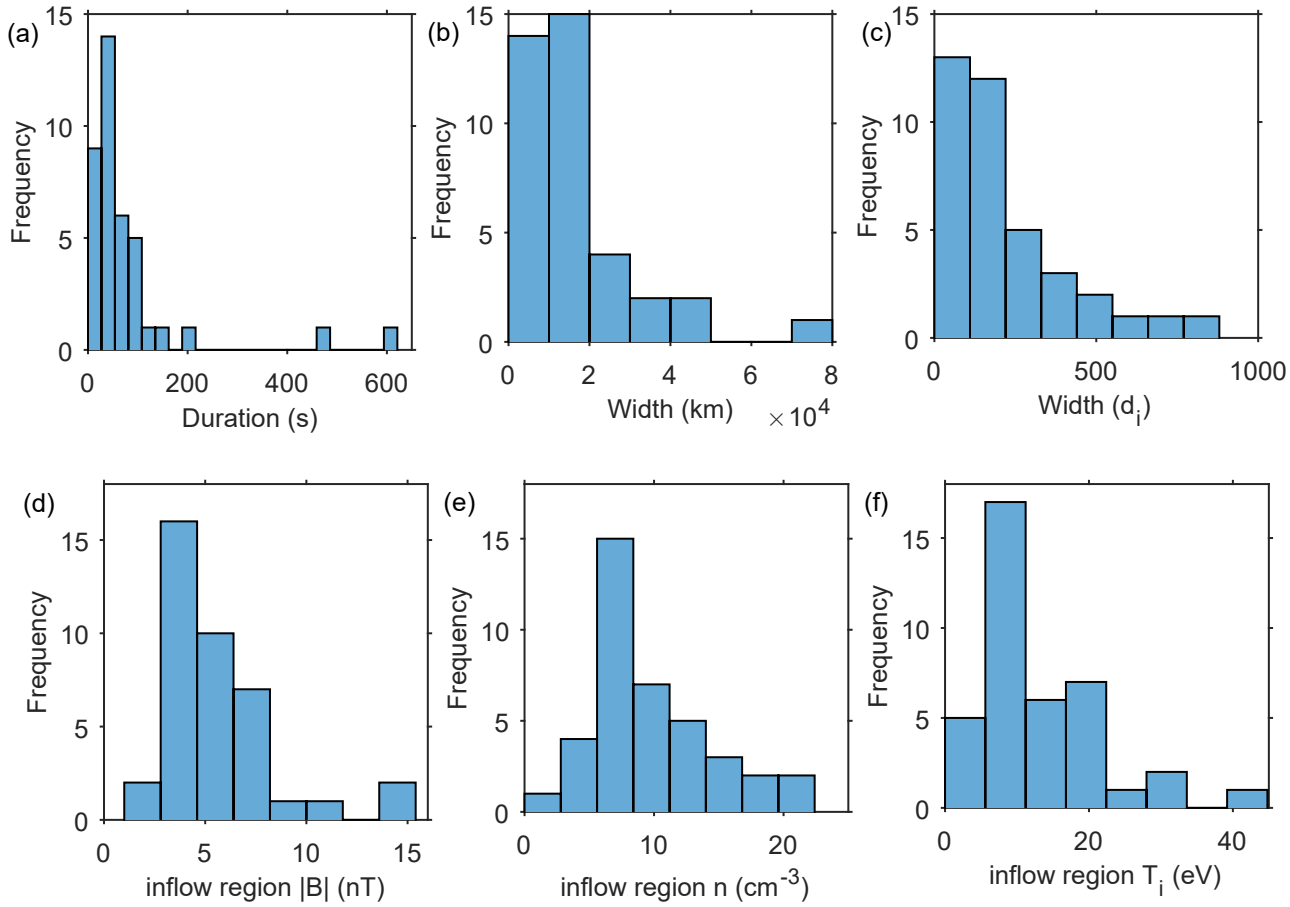


Figure 2.9: Histograms of (a) the interval over which the event was detected, (b-c) the measured exhaust width in km and d_i, and average values of the (d) magnetic field, (e) density and (f) ion temperature from the two inflow regions. One event with a width of 15.2×10^4 km (3100 d_i) is not shown in panels (b) and (c).

Reconnection of anti-parallel magnetic fields between symmetric plasmas has been studied the most extensively as it is the simplest reconnection configuration to study theoretically and to simulate, and because it is often applicable to reconnection in the magnetotail. In addition to asymmetries between plasmas in the two inflow regions, this configuration can be complicated by flow shears between the inflow regions and a non-reconnecting component of the field (the 'guide field'). Figure 2.10(c) shows the velocity shear in the L direction between the two inflow regions, which is half of the difference in V_L between the two inflow regions, normalised by C_{AS} (the Alfvén speed as determined for reconnection between asymmetric plasmas, using the L component of the magnetic field (Cassak & Shay, 2007)). C_{AS} is given by

$$C_{AS} = \sqrt{\frac{B_{L1}B_{L2}}{\mu_0}\frac{(B_{L1}+B_{L2})}{(\rho_1 B_{L2}+\rho_2 B_{L1})}}, \tag{2.16}$$

where subscripts '1' and '2' refer to measurements in inflow regions 1 and 2, respectively. This velocity shear is typically much smaller than the Alfvén speed, and is therefore unlikely to have a significant affect on the reconnection dynamics (Doss *et al.* (2015) and references therein). Figure 2.10(d) shows the distribution of reconnection guide fields, which results in a relatively flat distribution of magnetic shear angles between 33° and 172° (Figure 2.10(e)). Enžl *et al.* (2014) similarly found a relatively flat distribution of magnetic shear angles for solar wind reconnection exhausts. Lower shear angle exhausts would reduce the exhaust outflow speed, making such events difficult to identify within the survey.

2.6.5 Conclusions

Cluster solar wind data from 2004 and 2009 has been surveyed with the aim of identifying well defined solar wind reconnection exhausts. Since events were first identified from 2 hour data plots, very short duration events within the data may not have been detected. Furthermore, variations in measurements within 2 hour intervals can be large enough that small changes which are associated with reconnection exhausts are not readily identifiable. Events where the inflow region Alfvén speed is low, the magnetic shear is high or which are short in duration are therefore unlikely to have been detected.

These results clearly show a preference for the detection of reconnection exhausts in the slow solar wind. Gosling (2007) exclusively surveyed the high-speed solar wind, finding lower rates of exhaust detection than those found in other surveys where the data included various solar wind conditions. These various surveys, however, sometimes used different spacecraft and methodologies. We have used the same spacecraft instruments and methodology to detect events throughout the surveyed data in both fast and slow solar wind, showing more reliably the relationship between the solar wind speed and rates at which reconnection exhausts can be detected.

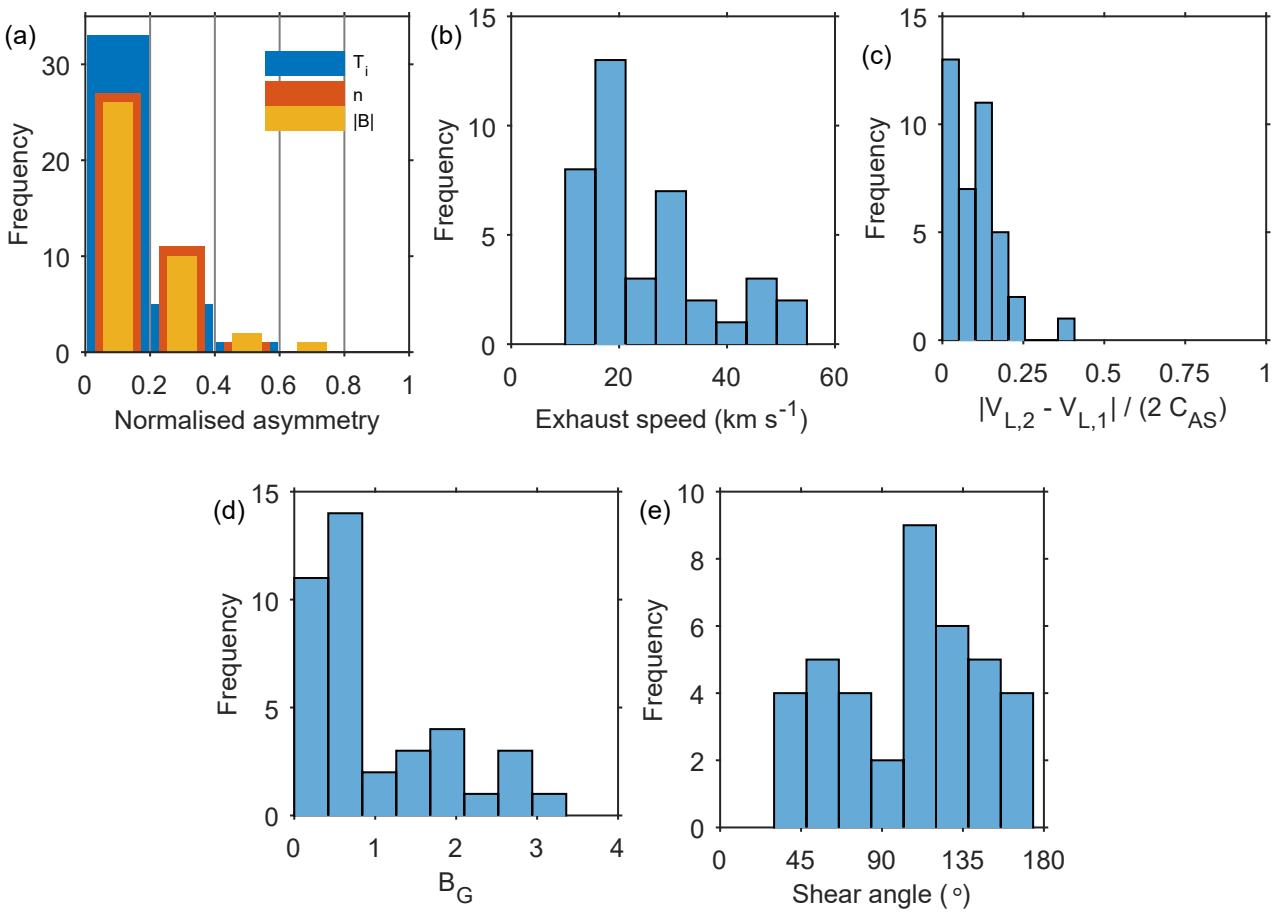


Figure 2.10: Histogram of (a) the difference in T_i, n and $|B|$ between each inflow region, normalised by their mean value. Histograms of the (b) exhaust outflow speed, (c) velocity shear across the current sheet in the L direction (normalised to C_{AS}), (d) reconnection guide field and (e) magnetic shear across the current sheet.

The identified events show that reconnection in the solar wind can occur over a broad range of magnetic shear angles and that the reconnecting plasmas are generally symmetric, although small differences between the two inflow regions are sometimes observed. Furthermore, flow shears between the two inflow regions are generally weak and we do not observe any super-Alfvénic flow shears. The solar wind therefore provides an ideal opportunity to study collisionless symmetric guide field reconnection using in-situ measurements. 39 reconnection exhausts were identified in this survey. Three of these events are studied in detail using multi-point Cluster measurements in Chapter 4, in combination with complimentary measurements from ACE and Wind. In order to determine the statistical properties of exhausts in the solar wind we use a more extensive list of 188 reconnection exhausts identified by Phan *et al.* (2010). This does not require multi-point measurements, therefore we use single spacecraft measurements from Wind for this analysis in Chapter 3.

3 Statistical properties of reconnection exhausts in the solar wind

3.1 Introduction

Reconnection exhausts in the solar wind are typically observed in excess of hundreds of d_i downstream of the X-line (Section 2.6.4 and 3.3), in some cases many thousands of d_i (Davis *et al.*, 2006 and Chapter 4 of this thesis). In-situ observations this far downstream are crucial to understanding the exhausts that form as a result of reconnection, as these distances are far beyond the range of what is routinely modelled in two and three dimensional simulations. Furthermore, the solar wind is an ideal environment in which to study these systems, where exhausts generally form two dimensional planar structures and where the exhaust regions are not affected by interactions with other structures, in contrast to reconnection in the magnetosphere.

Despite the fact that reconnection in the solar wind occurs with almost symmetric inflow conditions and that the exhausts are planar structures, observations show that there is a huge amount of variability between different reconnection exhausts. For example, reconnection exhausts have been observed where the current layer is bifurcated (e.g., Gosling *et al.*, 2005, 2006b; Phan *et al.*, 2006) and where the current has a single more broad layer (e.g., Gosling, 2007; Gosling *et al.*, 2007c and Chapter 6 of this thesis). Although they are often observed with enhancements in density and temperature within the exhaust region (e.g., Gosling *et al.*, 2005), exhausts have been observed with the absence of such signatures (Gosling, 2007; Gosling *et al.*, 2007d).

Forming an understanding of the general characteristics of solar wind exhausts is therefore difficult, given the large degree of variability between individual events and their inflow conditions. Furthermore, although hundreds of events have been identified in the solar wind, few events have been published in detail. In-situ observations have not been systematically compared to address the average properties of reconnection exhausts at large distances from the X-line, which could be used to constrain theories and models of the exhaust structure.

In addition to the problem of the general characteristics of reconnection exhausts, the

reasons for the observed variability between events have not been addressed. The guide field significantly affects reconnection dynamics by perturbing the Hall current system, electron dynamics and the current sheet structure (e.g., Pritchett, 2001; Pritchett & Coroniti, 2004; Huba, 2005; Eastwood *et al.*, 2010a; Goldman *et al.*, 2011). The plasma beta also affects reconnection dynamics as it controls the proportion of pressure contained within the magnetic field and the plasma, affecting the behaviour of the field and plasma within the exhaust region. It is therefore pertinent to ask whether such parameters affect the observed characteristics of reconnection exhausts, and if so, how? A large set of events with a range of parameter values would be required to test this statistically, and the few surveys of reconnection exhausts with a large number of events have not focussed on this problem (Gosling *et al.*, 2006a,b, 2007d; Gosling, 2007; Phan *et al.*, 2009, 2010; Enžl *et al.*, 2014).

The exhausts formed in solar wind reconnection are collisionless in nature, and indeed counterstreaming ions (a kinetic process which can only occur in collisionless media) have been observed along field lines within a reconnection exhaust (Gosling *et al.*, 2005). The ion temperature increase associated with these counterstreaming beams is expected to be 33% of the magnetic energy available to each proton-electron pair (Drake *et al.*, 2009a), however observations have shown this temperature increase to be only 13%. These observations used a small number of solar wind reconnection exhausts (22) (Drake *et al.*, 2009a) and a larger number of magnetopause reconnection exhausts (87) (Phan *et al.*, 2014). Few events with large guide fields were included in these studies.

In this chapter we determine the *average* characteristics of reconnection exhausts far downstream of the X-line in the solar wind through an analysis of 188 events. The data set is introduced in Section 3.2, and general properties of the data set are outlined in Section 3.3. This data set is first compared to the events collected from the Cluster survey (Section 2.6). We confirm that velocity shears and asymmetries between inflow regions are weak in this data set, indicating that the events may be considered as exhausts that result from symmetric guide field reconnection. The 188 events are used to determine the *average* properties of solar wind reconnection exhausts through a superposed epoch analysis in Section 3.4. Once the average properties are determined and the variability of the events characterised, we compare the average properties of these exhausts to exhaust structures that are expected in the Petschek model and from other studies of the boundaries of reconnection exhausts. This is particularly helpful as individual events often have a degree of variability in the measured signals, whereas the means from superposed epoch analyses do not suffer from this problem. The amounts by which the thermal pressure, density and ion temperature increase within reconnection exhausts are investigated in terms of the guide field strength in Section 3.5, and we show that this depends specifically upon the combination of reconnection guide field and plasma beta. The exhaust region temperature is further examined in Section 3.6, in which we expand upon the previous surveys and assess

the variability of the amount of ion heating between events. The occurrence of current sheet bifurcations is investigated separately in Chapter 4.

3.2 Data set

For this study we use a large set of events observed by the Wind spacecraft at 1 AU. These events were studied by Phan *et al.* (2010) to show that these events satisfied the reconnection onset condition for the magnetic shear angle and difference in plasma beta across the current sheet (see Section 1.5.6).

Phan *et al.* (2010) used a set of 197 events. These events were composed of a set of 50 events that were observed by both ACE and Wind between 1997 and 2004 and studied in Phan *et al.* (2009), and 147 events found from a detailed survey of solar wind data collected by Wind during the year 2002. This data set was selected for analysis in this chapter on the basis that it is one of the largest sets of solar wind reconnection exhausts that has been published. These events were identified by manually searching for reconnection exhausts using criteria similar to those in Section 2.6.2, and events were individually verified as reconnection exhausts. Although this survey contains fewer events than the survey by Enžl *et al.* (2014) which used an algorithm to find reconnection exhausts, the event list of Phan *et al.* (2010) was readily accessible. Furthermore, the solar wind often has significant fluctuations, and it is possible that algorithms may incorrectly identify these as reconnection events.

Phan *et al.* (2010) were principally concerned with the inflow conditions for these events, and several events had gaps in either Wind magnetometer or 3DP data within the exhaust interval. In this chapter we are concerned with both the inflow regions and the internal exhaust region, therefore we do not consider events with missing data. The following analysis uses the remaining 188 solar wind reconnection exhausts.

In analysis of the data we use 11 Hz magnetic field data and ion moments calculated onboard Wind using 3DP, at 3 s cadence. Onboard 3DP electron moments have considerable uncertainties. To measure electron temperatures we use moments calculated on ground from three dimensional distributions acquired over 3 s intervals and transmitted to ground every 100 s. These distribution functions are corrected on ground for effects such as spacecraft charging. As per Chapter 2, three regions are identified for each exhaust: inflow region 1, exhaust region, inflow region 2. We define these three regions to be the same as those used by Phan *et al.* (2010) in their analyses of the inflow conditions for these events. In the next section we provide a statistical overview of the events in this data set.

Table 3.1: Summary of distributions shown in Figures 3.1-3.4 and 3.6.

	median	mean	minimum	maximum
Duration (s)	41.9	106.9	3.7	1,610
Width (km)	9,630	28,780	41	478,000
Width (d_i)	121	355	1	7,680
$\|B\|$ (nT)	8.9	9.5	2.5	24.6
n (cm^{-3})	7.5	9.4	0.8	35.4
T_i (eV)	7.2	11.3	1.9	77.4
T_e (eV)	12.4	13.1	5.5	41.1
β_i	0.4	0.5	0.03	2.4
β_e	0.5	0.8	0.08	5.6
$\beta_i + \beta_e$	0.9	1.3	0.1	6.6
normalised $\|B\|$ asymmetry	0.05	0.08	0.00	0.37
normalised n asymmetry	0.10	0.19	0.00	1.40
normalised T_i asymmetry	0.11	0.21	0.00	0.93
normalised T_e asymmetry	0.03	0.07	0.00	0.97
B_G	1.2	1.7	0.06	10.0
Shear angle (°)	82	86	11	173
Solar wind speed(X_{GSE}) (km s^{-1})	396	412	282	689
Exhaust outflow speed (km s^{-1})	32	40	7	169
$\|V_{L,2} - V_{L,1}\|/(2C_{AS})$	0.25	0.32	0.01	1.20

3.3 Statistical overview of data set

In this section we summarise statistical properties of the 188 reconnection exhausts used in this chapter. This provides context for the subsequent analysis, and additionally acts to confirm the findings of Section 2.6.4 in which a much smaller set of events observed by Cluster were used to identify statistical properties of solar wind reconnection exhausts. A summary of the histograms discussed below (Figures 3.1-3.4, 3.6) is provided in Table 3.1. The following analysis is similar to that in Section 2.6 and data for each event are analysed in LMN coordinates derived from hybrid-MVA analysis of magnetic field data within the exhaust interval.

3.3.1 Current sheet and exhaust properties

The duration of the exhausts are shown in Figure 3.1(a), and the exhaust widths in terms of km and inflow region d_i are shown in Figures 3.1(b-c). These show similar shaped distributions to those in Section 2.6.4, with a strong preference for thinner current sheets. There are, however, a small number of particularly wide reconnection exhausts. These are the type of exhausts that were first observed in the solar wind when only low cadence plasma instruments (e.g., ACE SWEPAM) were used to identify reconnection exhausts

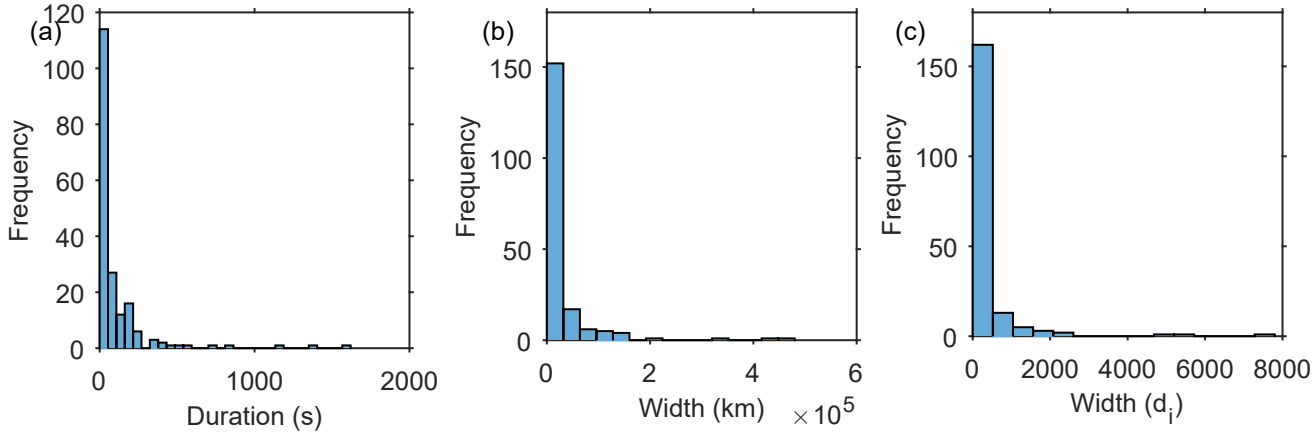


Figure 3.1: Histograms of (a) the interval over which the event was detected, and the measured exhaust width in (b) km and (c) d_i.

(e.g., Gosling *et al.*, 2005, 2006a,b). The median exhaust width in d_i (using the mean inflow region density) is 121, which is comparable to the median width observed in the Cluster survey (145 d_i).

The magnetic field magnitude, ion density, ion temperature and electron temperature from averages of inflow regions 1 and 2 are shown in Figure 3.2. The electron temperature is slightly higher than that of the ions, which is also evident in the distributions of plasma beta, where β_e is generally higher than β_i (Figures 3.2(e-f)). The distributions of inflow region parameters for these currents sheets shown in Figure 3.2 are similar to distributions of background solar wind conditions measured at 1 AU (e.g., Wolfe, 1972). The median total plasma beta is 0.9, and in general the plasma beta of solar wind reconnection exhausts is of the order 1 (the maximum total plasma beta is 6.6).

Distributions of differences in the ion temperature, density, magnetic field strength and electron temperature between the two inflow regions (normalised by their mean value) are shown in Figure 3.3. These differences are typically small (< 0.2), as was the case for the events identified in Section 2.6.4. We again use the asymmetric Alfvén speed, C_{AS}, (Cassak & Shay, 2007) to determine the Alfvén speed of the inflow regions.

The range of guide fields ($B_G = B_M/B_L$, where B_M and B_L are measured in the inflow region) for events included in this survey is significantly greater than those in Section 2.6.4, and the maximum guide field strength is 10 (Figure 3.4(a)). Such large guide fields may have been missed in the survey of Cluster data as C_{AS} and the exhausts outflow speeds tend to be low for strong guide fields (the outflow speed of the event where $B_G = 10$ is 7.3 km s^{-1}, for example), however the more extensive survey of Phan *et al.* (2010) was able to detect such events. Although these guide fields are considered very high, reconnection exhausts with shear angles as low as 4° have been observed in the solar wind (Gosling &

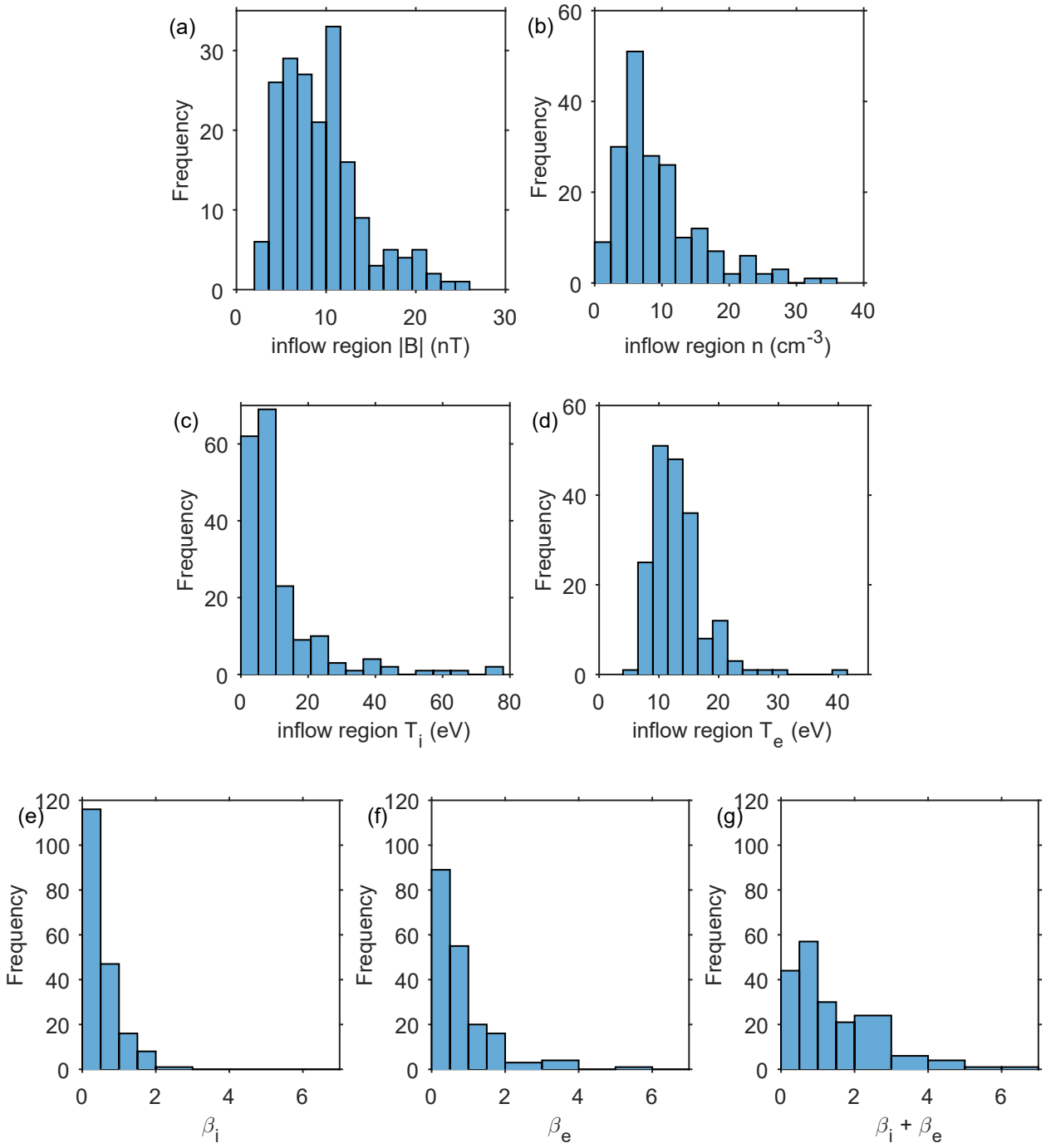


Figure 3.2: Histograms of (a) the magnetic field, (b) density, (c) ion temperature, (d) electron temperature, (e) ion β, (f) electron β and (g) total β. These are averages from the two inflow regions.

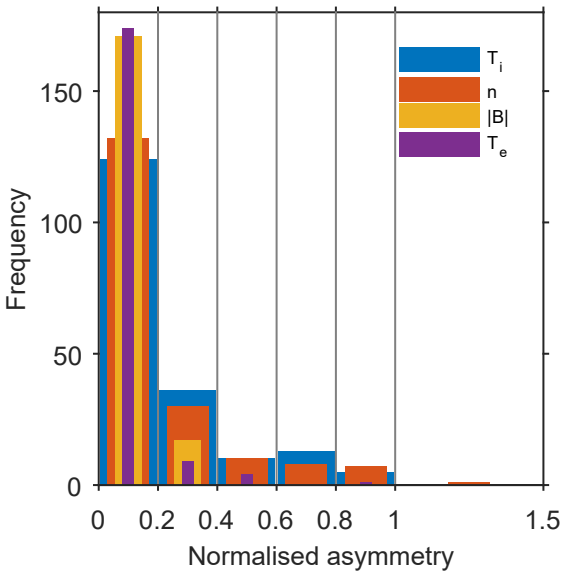


Figure 3.3: Histograms of of the difference in ion temperature, density, magnetic field magnitude and electron temperature between each inflow region, normalised by their mean value.

Phan, 2013). The distribution of magnetic shear angles is again approximately flat (Figure 3.4(b)).

3.3.2 Current sheet normal coordinates

The LMN vectors determined from MVA and hybrid-MVA analysis of Wind magnetometer data during the exhaust interval are compared in Figure 3.5. As has been noted, we find that the current sheet normal coordinate system is more reliably determined from

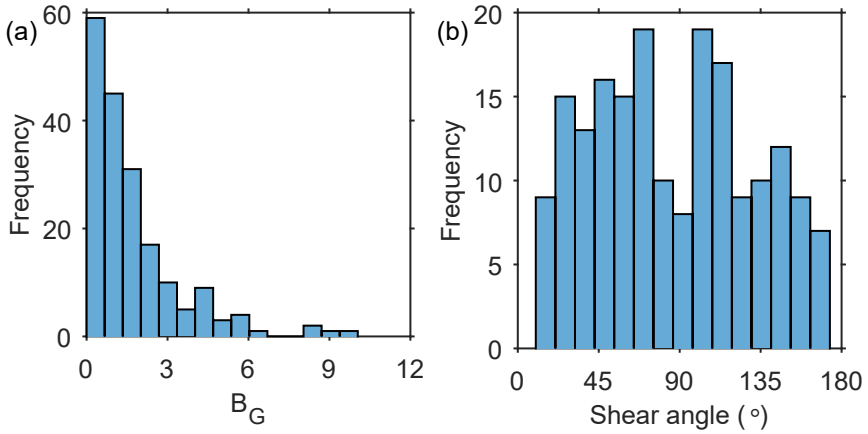


Figure 3.4: Histograms of the (a) reconnection guide field, (b) magnetic shear angle.

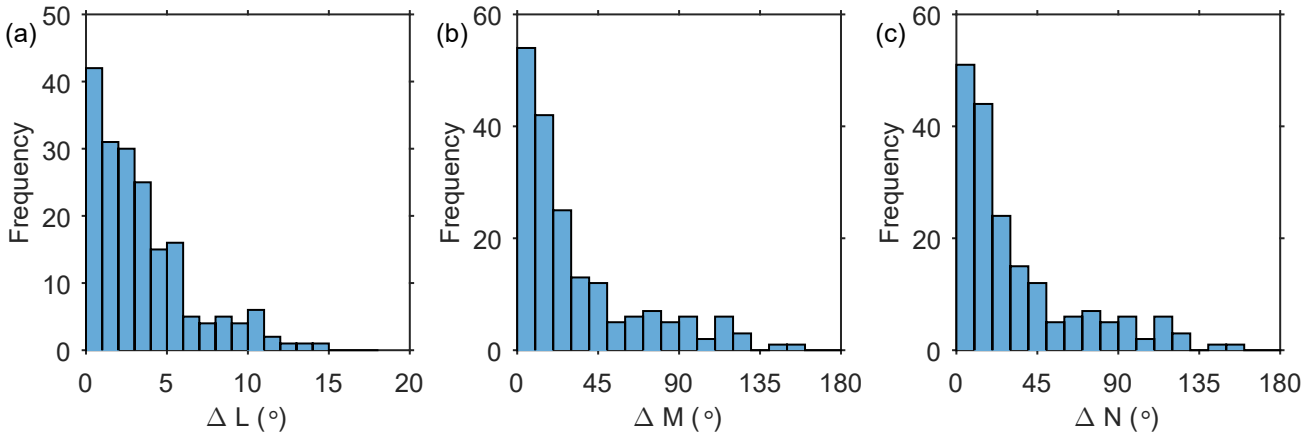


Figure 3.5: Angular differences between the LMN vectors determined from MVA and hybrid-MVA.

hybrid-MVA; the normal component of the magnetic field determined from MVA is often unrealistically large indicating that the current sheet normal coordinates have not been accurately determined. Figure 3.5(a) shows that the L directions from the two methods are generally consistent (mean difference is 3.5°). This is to be expected as the L direction is the maximum variance direction in the MVA method, whereas L in hybrid-MVA is the maximum variance direction with a small adjustment to ensure that the final coordinate system is orthogonal. The M and N directions differ more considerably; the mean differences between the M and N vectors from the two methods are 33.0° and 33.6°, respectively, however they can be considerably larger than this.

Hybrid-MVA determines N from the cross product of the field vectors on either side of the exhaust interval, effectively forcing B_N to be zero. The normal direction in MVA is the direction of minimum variance of the magnetic field. Whilst the maximum variance direction is always well defined because of the large change in the reconnecting component of the field, it is often difficult to distinguish the directions of intermediate and minimum variance. More importantly, the degree of variance in the two directions seems to be comparable to the extent that the MVA technique is unable to distinguish them sufficiently well, so that the minimum and intermediate directions actually correspond to some combination of the current sheet normal and out-of-plane directions.

3.3.3 Exhaust outflow speeds

The solar wind speed (as measured using Wind) at the time of each reconnection exhaust observation is shown in Figure 3.6(a). The majority of events are observed in solar wind speeds of less than 400 km s^{-1}, consistent with the findings in Section 2.6.4. Reconnection

exhausts are found in solar wind speeds of up to 689 km s^{-1}, however such events are infrequent. The range of exhaust outflow speeds is much larger than those measured in Section 2.6.4, and the maximum outflow speed measured here is 169 km s^{-1}. This is still significantly slower than outflow speeds observed at the magnetopause and magnetotail. The difference in V_L between the two inflow regions is generally small and the majority of velocity shears are significantly less than the inflow region Alfvén speed. There are a small number of events (4) where the flow shear is greater than half of C_{AS}.

It is possible that these flow shears can begin to affect the reconnection dynamics. Specifically, Doss *et al.* (2015) found that velocity shears in the L direction can cause the X-line to drift in the reconnection outflow direction. Consequently the X-line would not be stationary in the solar wind frame of reference, but would drift with respect to the solar wind. This implies that the reconnection exhaust velocity measured in the solar wind frame would not be the velocity of the exhaust in the X-line frame of reference. This is important if the exhaust velocity is to be compared to the Alfvén speed or Walén velocity, for example. Doss *et al.* (2015) show that the X-line drift in the presence of a velocity shear across the reconnection exhaust (and generalised for the case of asymmetric inflow conditions) is given by

$$V_{drift} = \frac{n_1 B_2 V_{L,1} + n_2 B_1 V_{L,2}}{n_1 B_2 + n_2 B_1}. \tag{3.1}$$

This drift velocity was derived for the case of anti-parallel reconnection, and ignored the effects of guide fields. The presence of a guide field can cause the X-line to drift as a consequence of other effects (as discussed in Section 1.5.6). These various drifts, however, are expected to sum in a non-linear way. It is therefore difficult to assess how the X-line is expected to drift in the presence of both a guide field and velocity shear, and this is an area of active research.

Although these solar wind exhausts have significant guide fields, we calculate V_{drift} using Equation 3.1 to provide a rough estimate of the order of magnitude X-line drift that may be expected as a result of velocity shears. This estimate of V_{drift} is shown as a function of the exhaust velocity in Figure 3.7. The standard deviations of B_L, n and V_L in inflow regions 1 and 2 have been found and used in standard error propagation formulae to calculate the standard deviation of V_{drift}. The exhaust velocity is calculated as the difference between the mean value of V_L in the inflow regions and the maximum departure from this within the exhaust region. Its standard deviation is calculated using the standard deviations of V_L in inflow regions 1 and 2 and standard error propagation formulae. Figure 3.7 shows that V_{drift} is often negligible. The maximum value of V_{drift} for these events is estimated to be 43 km s^{-1}, however for the vast majority of solar wind reconnection exhausts we do not expect velocity shears in the L direction to cause substantial X-line drifts. This effect is likely to be more important at the magnetopause flanks where reconnection can occur

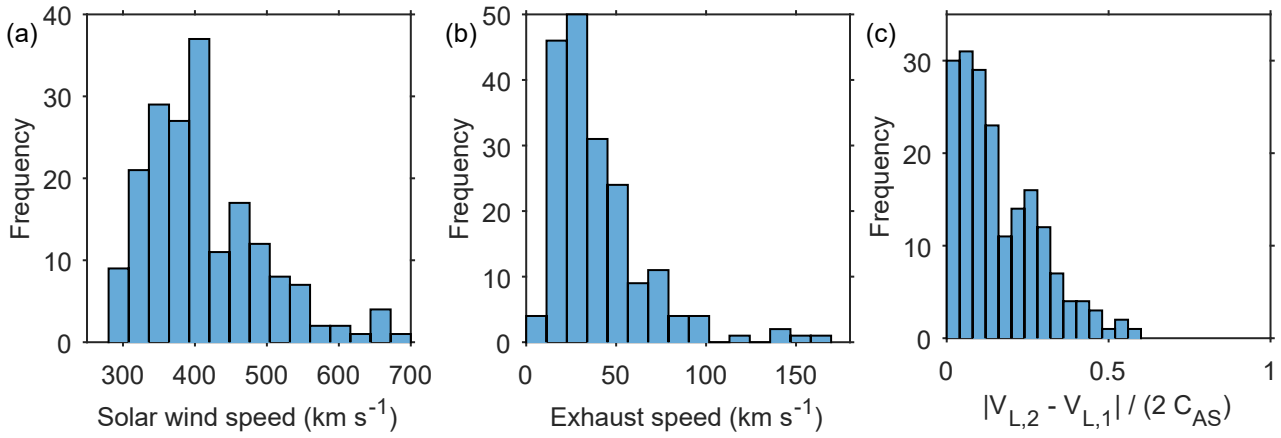


Figure 3.6: Histograms of the (a) X_{GSE} component of the solar wind speed, (b) exhaust outflow speed, (c) velocity shear across the current sheet in the L direction (normalised to C_{AS}).

with substantial velocity shears between the inflow regions.

The asymmetric Alfvén speed has been used as the inflow region Alfvén speed for these events, given that some events have non-negligible differences between the two inflow regions. A comparison between C_{AS} and the Alfvén speed calculated using mean values of B_L and n from the two inflow regions (i.e., $V_{A,L,mean} = \frac{(B_{L,1}+B_{L,2})/2}{\sqrt{\mu_0 m_i (n_1+n_2)/2}}$) is made in Figure 3.8. The standard deviations of B_L and n in inflow regions 1 and 2 have been found and used in standard error propagation formulae to calculate the standard deviations of C_{AS} and $V_{A,L,mean}$. Figure 3.8 shows that in the solar wind, asymmetries between the inflow regions tend to be small enough that corrections to the inflow region Alfvén speed for asymmetric inflow conditions tend to be minor, although they can differ by up to 22 km s^{-1}.

In Figure 3.9, C_{AS} is compared to the maximum measured exhaust velocity. The data show that there is a good agreement between the exhaust velocity and the inflow region Alfvén speed, however the scatter shows that there are events where the exhaust velocity is less than C_{AS} and events where it exceeds C_{AS}. There is a very slight trend for C_{AS} to be greater than the maximum observed exhaust velocity. These outflow speeds are discussed further in Section 3.4.2.

3.4 Average properties of reconnection exhausts far downstream of the X-line: Superposed epoch analysis

In-situ observations have been used to study reconnection at the magnetopause and magnetotail for some time. The spacecraft used are often not significantly far downstream of

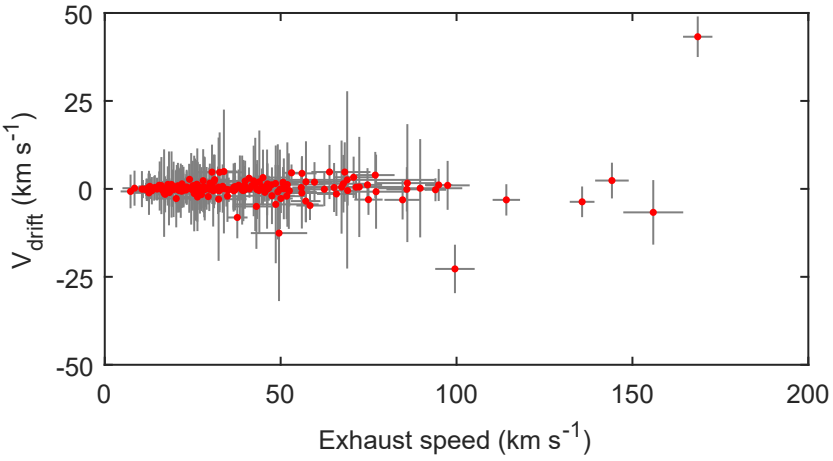


Figure 3.7: Estimated X-line velocity drift as a result of velocity shears between the inflow region, as a function of the exhaust outflow speed.

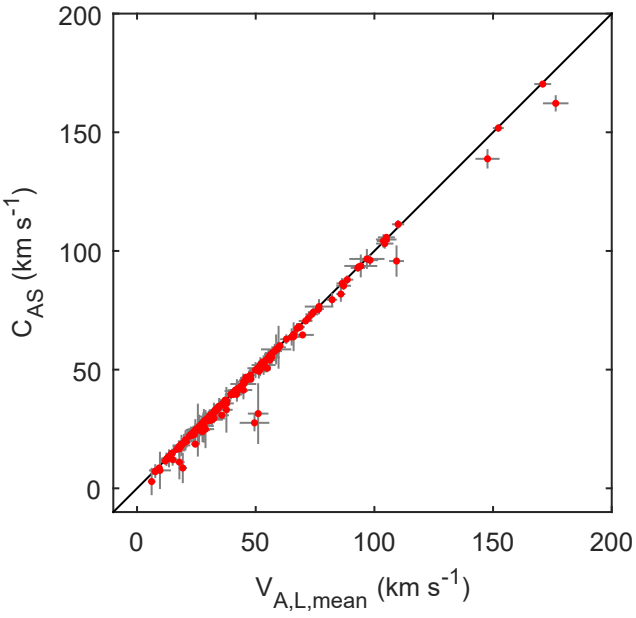


Figure 3.8: Inflow region Alfvén speed calculated using the mean values of B_L and n in inflow regions 1 and 2, and using the Alfvén speed for reconnection between asymmetric plasmas, C_{AS}, (Cassak & Shay, 2007). The black line shows where they are equal.

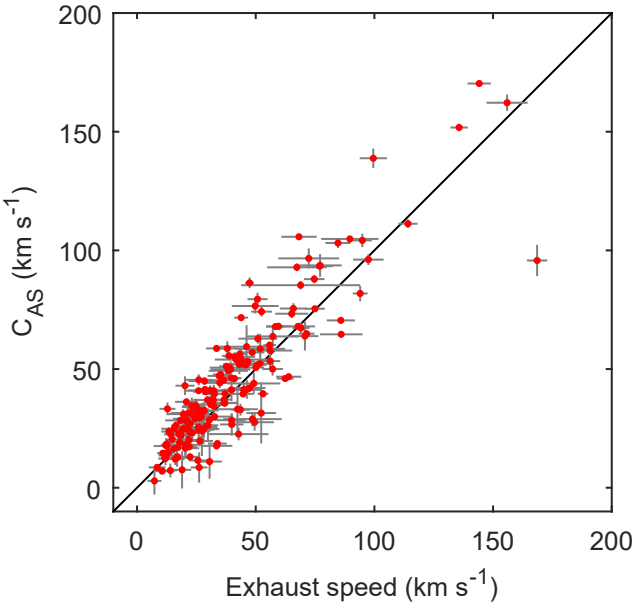


Figure 3.9: Inflow region Alfvén speed calculated using the Alfvén speed for reconnection between asymmetric plasmas, C_{AS}, (Cassak & Shay, 2007) against measured exhaust outflow speed. The black line shows where they are equal.

the diffusion region and several encounters have been made with the diffusion region itself. Similarly, two dimensional kinetic simulations are currently able to simulate as far as $\sim$100 d_i (where d_i is normalised to the inflow region density) downstream of the diffusion region (e.g., Liu *et al.*, 2012), and these simulations are often more suited to studying the reconnection process itself rather than exhaust structures far downstream of the X-line.

Spacecraft which observe reconnection exhausts in the solar wind are typically located far downstream of the X-line. The median exhaust width of the 188 events studied in this chapter is 121 d_i. Assuming a reconnection rate of 0.1, a spacecraft which measures this width would be located 605 d_i downstream of the X-line. These observations are therefore crucial to understanding the exhausts that form as a result of collisionless reconnection at distances downstream of the X-line where it is often considered that spatial gradients are weak enough that the plasma can be described using MHD. Solar wind observations show a large amount of variability between events and forming an understanding of the general characteristics of solar wind exhausts is therefore difficult. In order to understand the average characteristics of reconnection exhausts in the solar wind we perform a superposed epoch analysis of the events studied in this chapter.

3.4.1 Method

When comparing these events the large degree of variability between current sheet and plasma parameters should be considered. As shown in Figures 3.2(a-d) the inflow region magnetic field, density and temperature can vary significantly. Furthermore, although the spacecraft are located much further downstream of the X-line than at the magnetopause/magnetotail, the measured width of the exhausts (Figures 3.1(a-c)) shows a large degree of variability, suggesting that the spacecraft distance downstream of the X-line also varies considerably. Perhaps most importantly, these events exhibit a large range of guide fields, which are likely to affect the exhaust region structure. The effects of this variability are considered in Section 3.5.

Measurements made across relatively wide exhausts and relatively narrow exhausts may show variations on different temporal scales. In order to compare such events we normalise the time axis such that 0 and 1 correspond to the spacecraft crossing the exhaust boundaries. Since the exhausts are frozen to the solar wind, time series measurements can be considered as measurements along a line in the solar wind in the direction of the negative solar wind vector. Consequently, a normalised time axis also corresponds to an axis along the spacecraft path relative to the exhaust, where 0 is one side of the exhaust and 1 is the other side. We may therefore consider the time axis to be the *distance* through the reconnection exhaust. This normalisation allows spacecraft measurements from different events to be directly compared. Furthermore, if the exhaust structure is assumed to be invariant in the L and M directions, this corresponds directly to a cut through the reconnection exhaust in the N direction.

We normalise each parameter that is plotted against the *distance* axis by its mean value in inflow regions 1 and 2. Without such normalisation in density, for example, the superposed data would include densities over the range $0.8 - 35.4$ cm^{-3}, in which case underlying trends in changes in the density from the inflow region to exhaust region would be masked by the variability of inflow region densities.

Reconnection exhausts in the solar wind have arbitrary orientations. In order to compare events, consistent coordinate systems must be used. In the absence of a guide field it is possible to define coordinate systems in which all events should show the same changes in fields and velocities. For example, one may define the $+L$ direction to be the direction of exhaust outflow and the $+N$ direction to be in the direction that the spacecraft is moving (i.e., with a negative X_{GSE} component), in which case similar qualitative changes would be measured in B_L, B_M, B_N and V_L (Figure 3.10(a)). The presence of a guide field breaks the symmetry of the system, and one cannot find coordinate systems for all events in which changes in fields and velocities are the same. For example, we may define coordinate

systems such that the exhaust outflow is in the $+L$ direction and the guide field is in the $+M$ direction. If two exhausts with opposite guide fields but otherwise the same reconnection geometry are compared, many signatures using these coordinate systems would appear the same. B_N, however, would be opposite for the two events (as illustrated in Figures 3.10(b) and (c)).

In this analysis we use the coordinate systems shown in Figures 3.10(b) and (c), i.e., where the exhaust outflow is in the $+L$ direction and the guide field is in the $+M$ direction. Because these exhausts can have any orientation in the solar wind, the spacecraft trajectory may take it either from the side where B_L is positive to the side where it is negative, or from the negative side to the positive side. Time series measurements are therefore reversed in time if B_L changes from negative to positive. In this way, all measurements in the superposed epoch analysis are such that $B_L > 0$ is measured at $distance = 0$ and $B_L < 0$ is measured at $distance = 1$.

3.4.2 Results

Figure 3.11 shows a superposed epoch analysis of 188 exhausts. Panels (a-c) show magnetic field measurements normalised by the average of B_L measured in inflow regions 1 and 2 ($B_{L,in}$). The out-of-plane field shown is the measured field (B_M) minus the average out-of-plane field measured in the inflow regions ($B_{M,in}$), and normalised by ($B_{L,in}$). Panels (d-f) show ion velocity measurements with mean measurements from the inflow regions subtracted (which is equivalent to a transformation from the spacecraft frame of reference to the reconnection exhaust frame of reference), normalised by C_{AS}. Magnetic field magnitude, ion density and ion temperature measurements, normalised by their respective mean values in the inflow regions are shown in panels (g-i). The thermal (ion and electron) pressure, normalised by its inflow region value is shown in (j). We use electron temperature measurements with a cadence of 100 s. Measurements of the electron temperature in inflow regions 1 and 2 contain at least one data point; for most events measurements of the electron temperature within the exhaust are not available. The electron contribution to the thermal pressure is calculated by linearly interpolating the electron temperature between $distance = 0$ and $distance = 1$, and by considering the electron temperature for $distance < 1$ and $distance > 1$ to be the value used in that inflow region. The magnetic pressure and total pressure (calculated by averaging the magnetic field pressure to the cadence of thermal pressure measurements prior to summing them) are shown in panels (k) and (l), respectively, each normalised to their values in the inflow regions.

Individual event measurements are shown in grey. The number of data points measured for each exhaust interval varies depending on the duration that it is observed for. Mean

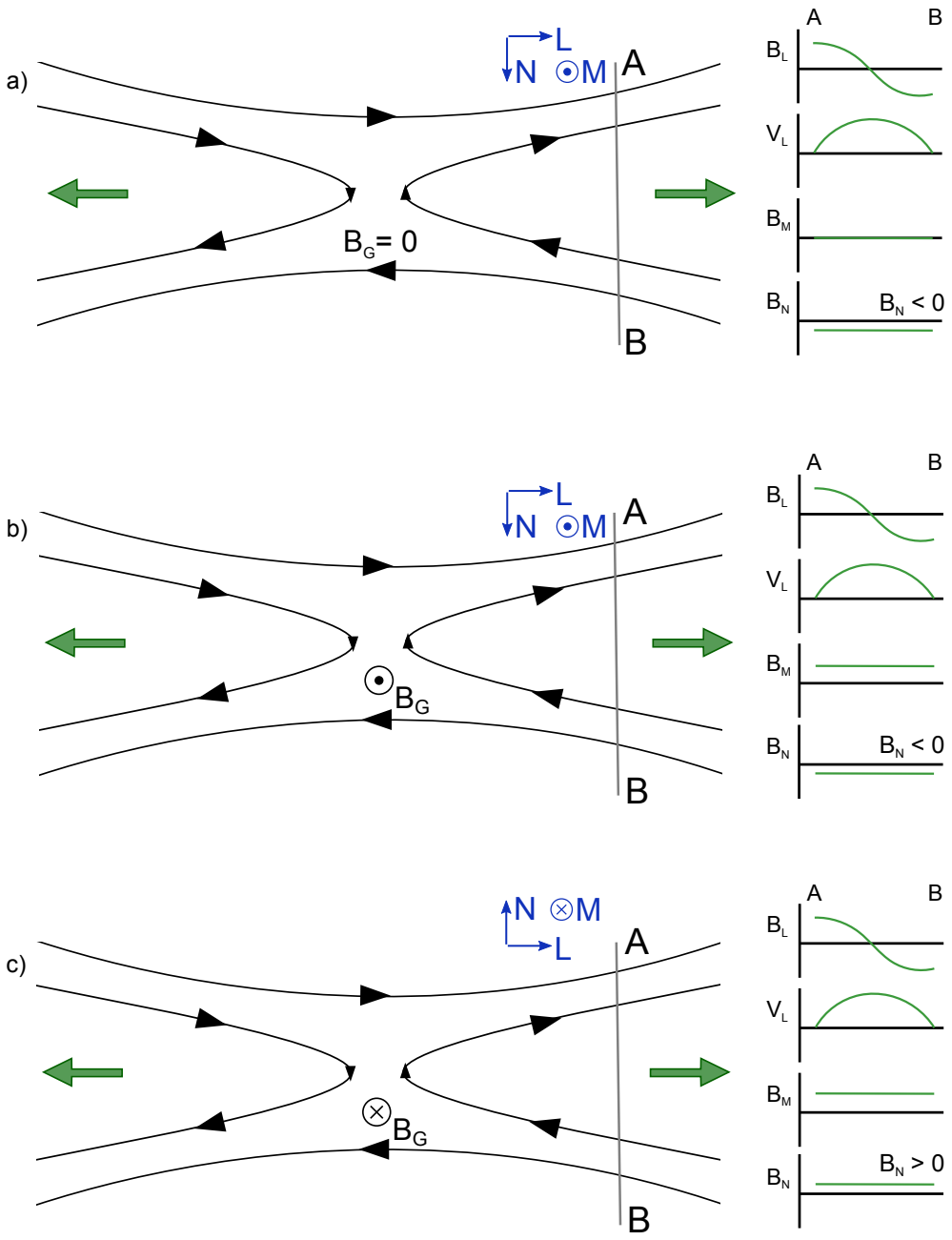


Figure 3.10: Three events with the same reconnection geometries but with (a) zero guide field, (b) a guide field directed out of the page, and (c) a guide field directed into the page. In (b) and (c) the coordinate system is such that the exhaust outflow is in $+L$ and the guide field is in $+M$. In (a) the coordinate system is such that the exhaust outflow is in $+L$ and $+N$ is from A to B (as $B_G = 0$). B_N in these coordinates is negative in (a) and (b), and positive in (c).

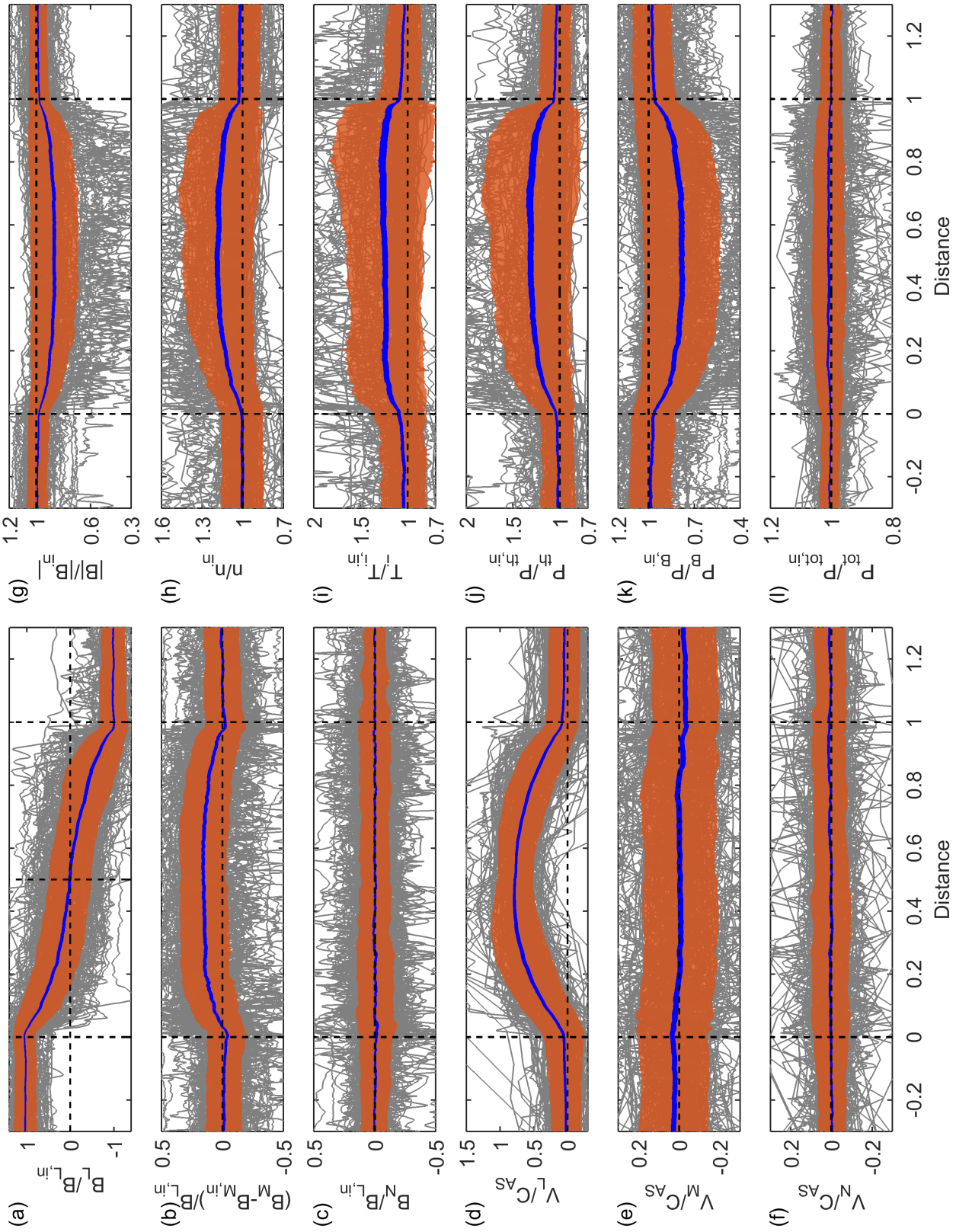


Figure 3.11: Superposed epoch analysis of 188 events. Individual events are shown in grey. The standard deviation of the measurements are shown in orange and the mean values are shown in blue, where the width of the line is the ±1 standard deviation range of the mean value.

values (shown in blue) are calculated by re-sampling data for each event so that 375 data points are used between $distance = 0$ and $distance = 1$. This requires linear interpolation of measurements where less than 375 data points were measured between $distance = 0$ and $distance = 1$, and averaging of measurements where there are more than 375 data points. The standard deviation of the quantities from measurements of the 188 events are shown in orange and the ± 1 standard deviation of the mean value is indicated by the thickness of the blue line.

In all panels measurements for each event are normalised by the measured inflow region values. If there are differences between the two inflow regions, measurements in each inflow region will differ from this mean. Consequently, for many events the measurements in the inflow regions are not equal to the value used for normalisation. The standard deviation of measurements within the inflow region is non-zero because of these asymmetries.

An exception to this is B_N, which, due to symmetry breaking of the guide field, can take positive or negative values for each event. Consequently, the average value of B_N is zero. For a canonical reconnection rate of 0.1 the ratio $B_N/B_{L,in}$ is expected to be 0.1.

The average B_L rotates smoothly from positive to negative. The large standard deviation of B_L (within the exhaust region) is evidence of the large variability of B_L profiles between events. Traces for individual events more clearly show that some events undergo large changes in B_L very close to the exhaust boundary (i.e., near $distance = [0, 1]$). These events are likely to have bifurcated current sheets. It is worth noting that the thickness of the changes in B_L is affected by the time normalisation. If large changes in B_L occur over a fixed spatial scale, they will appear to be very thin in Figure 3.11 if the exhaust is particularly thick, and wider if the exhaust is thin. The mean B_L is therefore affected by the measured B_L profile as well as the exhaust width. With such a large set of events, however, the mean trace is still expected to be representative of the average B_L profile within a reconnection exhaust far downstream of the X-line.

The out-of-plane magnetic field, on average, increases within the reconnection exhaust (Figure 3.11(b)). The extent to which this happens varies considerably within the exhaust; at $distance = 0.5$ the ± 1 standard deviation range of B_M is $-0.02 < B_M < 0.34$. Individual event traces show that B_M can vary considerably between events and can increase by up to 71% of the inflow region reconnecting field, but may decrease in some cases. Increases in B_M within reconnection exhausts have not previously been noted in observations, however these data clearly show that such increases are common in solar wind exhausts.

$|B|$ decreases within the reconnection exhausts, however the extent to which this occurs varies significantly (Figure 3.11(g)). This is largely dependent upon the guide field. For anti-parallel reconnection $|B|$ is expected to be zero within the exhaust, whereas in the

presence of a guide field it should be at least the magnitude of the guide field.

The exhaust outflow is shown in Figure 3.11(d). The mean value of V_L reaches a maximum of 79±34% of C_{AS} (where the quoted uncertainty is the standard deviation of all events), indicating that on average the exhaust outflow speed is less than the inflow region Alfvén speed. This has been noted previously (e.g., Enžl *et al.*, 2014). Figure 3.9 shows that the *peak* exhaust velocity is more comparable to C_{AS}, however the ion velocity within the exhaust can be variable, and Figure 3.11(d) therefore shows that in general the exhaust velocity tends to be less than C_{AS}. On average the ion velocity in the out-of-plane direction (V_M) and in the current sheet normal direction (V_N) are zero (Figures 3.11(e-f)).

The ion density and temperature increase within reconnection exhausts, on average (Figures 3.11(h-i)). This has been noted in several previous case studies (e.g., Gosling *et al.*, 2005), as well as the statistical survey of Enžl *et al.* (2014). In Enžl *et al.* (2014) data were not normalised between events. The observed increases in density and temperature were therefore strongly affected by the variability between events and the standard deviations were larger than the mean increases. Enžl *et al.* (2014) measured average increases in density of 1.3 ± 2.6 cm^{-3} and ion temperatures of 1.8 ± 2.0 eV. Our superposed epoch analysis show a maximum increase in density of $19 \pm 26\%$ and ion temperature of $28 \pm 57\%$ (where the quoted uncertainty is the standard deviation of all events). Although the standard deviations are also larger than the mean values, we attribute this to effects related to the guide field, as discussed in Section 3.5. Scaling the measured fractional increases in density and ion temperature to the median inflow region density and ion temperatures of the events used in this survey (Table 3.1) corresponds to increases of 1.4 ± 1.9 cm^{-3} and 2.0 ± 4.1 eV, respectively, which are compatible with the results of Enžl *et al.* (2014).

The thermal pressure increases within the exhausts and the magnetic pressure decreases (Figures 3.11(j) and (k)). This occurs in such a way that the total pressure remains remarkably constant throughout the exhaust (the mean total pressure is $\sim 1.00 \pm 0.05$ within the exhaust region, where the quoted uncertainty is the standard deviation of all events) as shown in Figure 3.11(l). The electron thermal pressure within the reconnection exhausts was assumed to vary linearly between inflow regions 1 and 2. Assuming that the electron temperature does not increase within the exhaust is reasonable considering that ion heating within reconnection exhausts has been measured to be ∼8 times larger than electron heating (Phan *et al.*, 2014), and increases in electron temperature are ∼1.7% of the available magnetic energy for each proton-electron pair (Phan *et al.*, 2013b). The available magnetic energy is the kinetic energy of a proton moving at the inflow region Alfvén speed ($m_i C_{AS}^2$). For the median inflow region Alfvén speed of the events in this survey (35.6 km s^{-1}) this corresponds to an increase in temperature of 0.22 eV, which is negligible with respect to the median electron temperature in the inflow regions (12.4 eV). Electron heating has been

observed in the solar wind for an unusually high Alfvén speed event, however in general electron heating is not observable in solar wind reconnection exhausts (Pulupa *et al.*, 2014). The thermal pressure and magnetic pressure within the exhaust region are investigated further in Section 3.5.

3.4.3 Discussion

This superposed epoch analysis is used to demonstrate the average properties of reconnection exhausts at large distances downstream of the X-line. In general we find that within the exhaust region:

- B_L changes sign
- B_M, density and ion temperature increase
- thermal pressure increases and magnetic pressure decreases
- total pressure is constant

Of key importance here is that the density and ion temperature remain increased throughout the exhaust region, and that this occurs in conjunction with an increase in B_M. This is surprising given that systematic increases in B_M within the exhaust region have not been reported before. These increases in B_M are not an artefact of the superposed epoch analysis and can be seen in a large proportion of individual events, however this does not seem to have drawn attention in previous studies which have focussed on aspects other than the structure of the exhaust boundaries.

In Petschek's MHD reconnection model the density and temperature are enhanced at slow mode shocks which form at the exhaust boundaries. These shocks also reduce B_L to zero (and B_M remains unchanged from its initial value of zero), and the changes in B_L, n, T and pressures are coincident. Whilst this model is often cited with relation to observed enhancements to the density and temperature, strictly it is only applicable to reconnection of anti-parallel fields.

The boundaries of reconnection exhausts far downstream of the X-line were explored more extensively with the aid of one dimensional MHD and hybrid simulations in the 1990s. For symmetric reconnection with zero guide field, Lin & Lee (1993) found that the exhaust boundaries in MHD simulations are composed of slow shocks which reduce B_L to zero, in agreement with Petschek's model. With the introduction of a guide field rotational discontinuities propagate ahead of the slow shocks. The reconnection exhaust is therefore composed of rotational discontinuities on the outside which rotate the magnetic

field, reducing B_L and increasing B_M, and increasing the plasma velocity. Downstream of the rotational discontinuities are slow shocks which decrease B_M (to a level comparable to that upstream of the rotational discontinuity) and increase n and T. The points at which the magnetic field and velocity change are therefore not coincident with where the density and temperature changes and B_M does not remain increased throughout the exhaust region. With increasing guide field the strength of the slow shocks is decreased, reducing the extent by which B_M decreases (and n and T increase) at the slow shock.

In these MHD simulations the rotational discontinuities and slow shocks form infinitely thin discontinuities. Later one dimensional hybrid simulations (Lin & Lee, 1995) show that the ability for ions to acquire a temperature anisotropy modifies the structure of the exhaust boundaries. With anisotropy the Rankine-Hugoniot jump relations are modified and changes in plasma temperature and density can occur at the rotational discontinuity (Hudson, 1971). Simulation results show that the density and temperature increase at the rotational discontinuities. Furthermore, their decrease at the slow shocks is considerably weaker with respect to the MHD case, due to temperature anisotropy modifications to the slow shocks (Lin & Lee, 1993). An additional change is that the rotational discontinuities and slow shocks are no longer infinitely thin, but are of a finite extent. This was explored further in Lin & Swift (1996), where, with a guide field of $B_G = 0.5$, the strength of the slow shocks was reduced to the extent that they were almost undetectable. The rotation of the magnetic field and increase in plasma density, temperature and exhaust velocity were achieved via the anisotropic rotational discontinuities entirely. Consequently, changes in B_L, B_M, n, T and the corresponding pressures were almost coincident (Figure 3.12). Furthermore, the rotational discontinuity decreased B_L and increased B_M, and B_M was not decreased by the (weak) slow shocks, causing B_M to remain enhanced within the reconnection exhaust. These results are not an artefact of using one dimensional simulations; similar structures were found in two dimensional simulations (Lin & Swift, 1996).

The superposed epoch analyses show that changes in the magnetic field, velocity, density and temperature occur simultaneously. Further within the exhaust there are no points where B_M is reduced or n and T are notably further enhanced, which would be indicative of a slow shock. Changes in the field, velocity, n and T are most evident at $0 < distance < 0.2$ and $0.8 < distance < 1$. Within these regions the magnetic field rotates such that B_L is reduced and B_M is increased. These regions are very similar to the rotational discontinuities formed in 1D hybrid simulations for symmetric guide field reconnection (Lin & Lee, 1995; Lin & Swift, 1996), suggesting that the exhaust region far downstream of the X-line can be modelled as one dimensional. It is perhaps unsurprising that these results do not show evidence for slow shocks downstream of the rotational discontinuity-like region as the median and mean guide field for the events used in this analysis were $B_G = 1.2$ and $B_G = 1.7$, respectively. Identification of slow shocks and rotational discontinuities in individual events

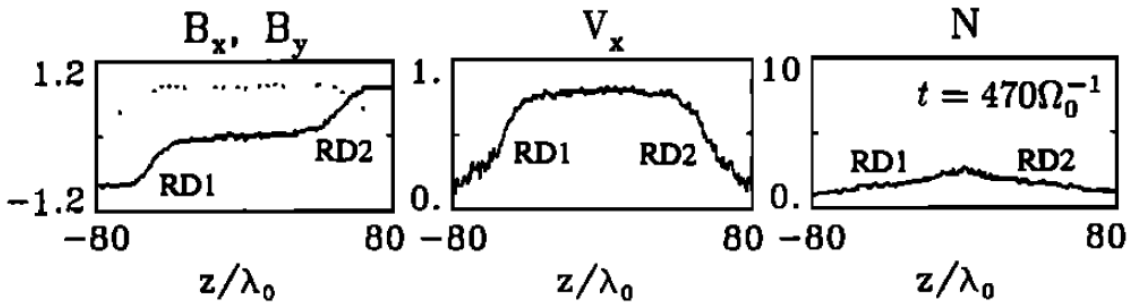


Figure 3.12: Results from a 1D hybrid simulation with $B_G = 0.5$. The first panel shows B_X (which corresponds to B_L) in solid and B_Y (which corresponds to B_M) with a dotted line. The second and third panels show V_X (which corresponds to V_L) and n, respectively. The simulation results are shown at a time of 470 inverse ion gyroperiods, when the rotational discontinuities (labelled 'RD1' and ''RD2') are well separated. Figure adapted from Lin & Swift (1996).

is difficult as the measured parameters vary far more than the mean values shown in Figure 3.11. The exhaust boundaries most evidently resemble the rotational discontinuities that form in simulations when multiple events are analysed together (as per Figure 3.11) to reduce the variation in these measurements.

The Wind 3DP instrument is unable to provide reliable ion temperature anisotropies at the required cadence to test whether events used in these analyses fulfil the anisotropic Rankine-Hugoniot relations which such rotational discontinuities should satisfy. It is therefore difficult to fully assess the extent to which these boundaries are consistent with those found in Lin & Lee (1995) and Lin & Swift (1996), however the superposed epoch analysis results of Figure 3.11 strongly resemble the 1D simulation of reconnection with a guide field of $B_G = 0.5$ (Lin & Swift, 1996) (shown in Figure 3.12). Liu *et al.* (2012) and Innocenti *et al.* (2015) have used two dimensional simulations to show that compound structures of rotational discontinuities and slow shocks form at the exhaust boundaries, however higher resolution measurements are also required to test these hypotheses.

This superposed epoch analysis shows the average properties of reconnection exhausts in the solar wind, far downstream of the X-line. These average properties have not been revealed in previous studies, in which either only a handful of events were studied or in which large differences between their inflow regions concealed features that were common to the events. The analysis has shown that increases in the out-of-plane magnetic field are common at reconnection exhausts, and that the changes in B_L, B_M, n and T_i are qualitatively consistent with 1D simulations where the ions gain a self-generated temperature anisotropy. This indicates that one dimensional simulations may be sufficient to describe basic features of reconnection exhaust far downstream of the X-line. In Chapter 5, however, we show that there are a small number of cases where this is not true, and the exhaust region can have

Hall magnetic field signatures which are related to a two dimensional current system within the exhaust region, supported by differential electron and ion flows. Our analysis here has also shown that the exhaust region is in pressure balance, which, although is expected, has not been previously measured. As we shall see in the next section, this has important implications for changes in n and T_i in the exhaust region, which show a large degree of variability between events.

3.5 Thermal and magnetic pressure within reconnection exhausts: the effects of guide fields and plasma beta

In Section 3.4 we showed that on average the plasma density, ion temperature, thermal pressure and out-of-plane magnetic field increase within reconnection exhausts, and that the magnetic pressure decreases. There was, however, significant variability between events. This is not surprising given that whilst many previously studied events show evidence of increases in ion density and temperature within the exhaust region, events have also been observed with a clear absence of these signatures. In this section we determine how the guide field and the plasma beta of the inflow regions affects the changes in pressures, densities and temperatures within reconnection exhausts, which provides an explanation of the different signatures that have emerged from previous observations. Such a study of how the guide field and plasma beta affect observed reconnection exhausts has not been previously conducted.

In Figure 3.13 the 188 events have been grouped into four guide field bins which each contain 47 events. The values shown are the means from superposed epoch analyses of the events in each bin. This shows that the extent by which parameters change from the inflow region to the exhaust region depends on the guide field strength. At weak guide fields the decrease in $|B|$ (and corresponding magnetic pressure) and the increases in n, T_i and thermal pressure are substantial. The profiles of these parameters vary across the reconnection exhaust in a similar manner for all guide fields, however as the guide field decreases the amplitude of the changes increases. Changes in the out-of-plane magnetic field (normalised by $B_{L,in}$) and the total pressure do not seem to depend as significantly on the guide field.

90% quantiles of the density, ion temperature and thermal pressure and the 10% quantiles of the magnetic field and magnetic field pressure were found for the exhaust region of each event in each bin. The mean of these quantiles for all events in each bin and their standard deviation are shown as a function of guide field in Figure 3.14, to determine how they depend on the guide field. These quantiles were used instead of the minimum or maximum

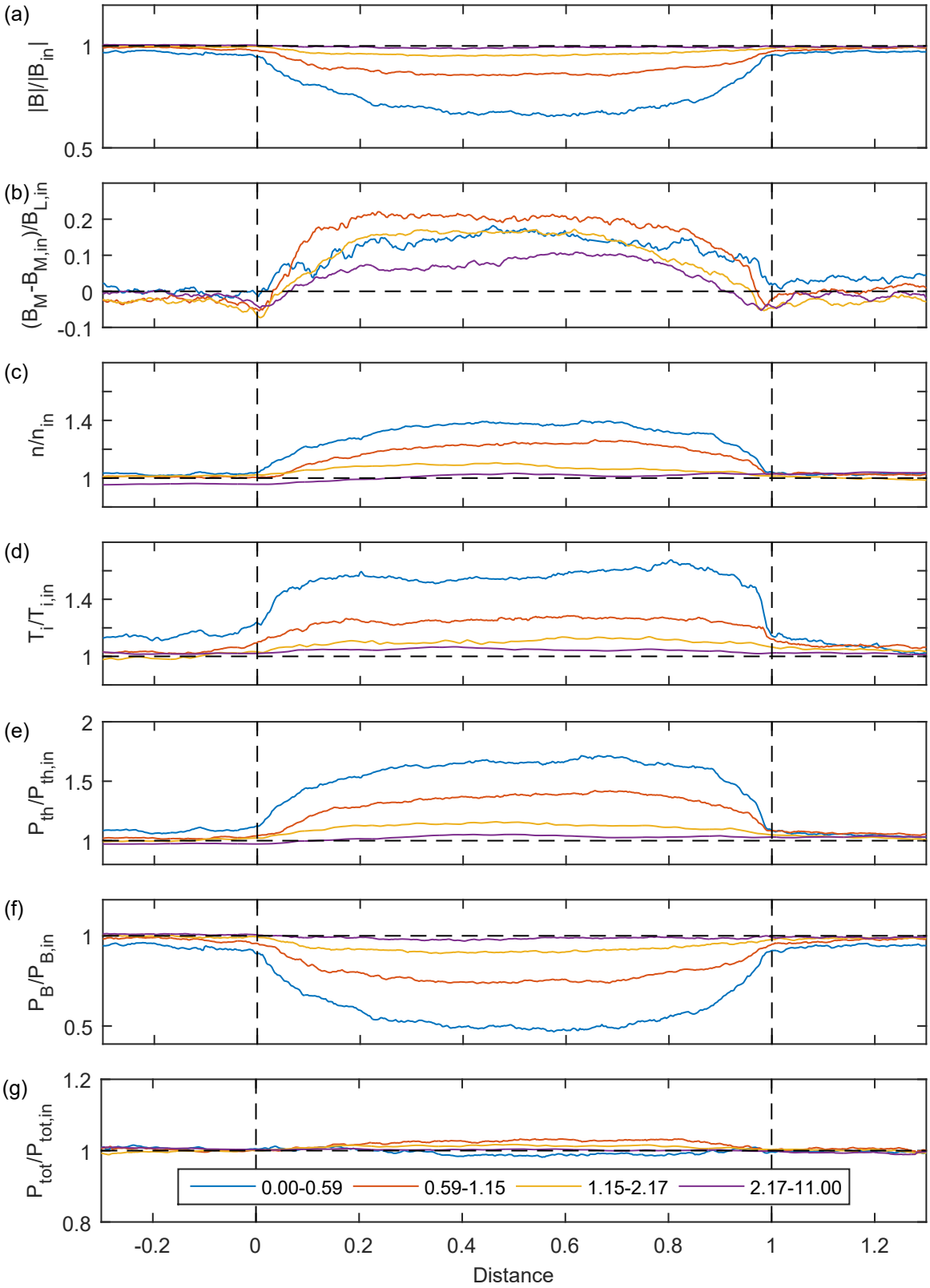


Figure 3.13: Mean values from superposed epoch analysis of 188 events binned by guide field (see legend).

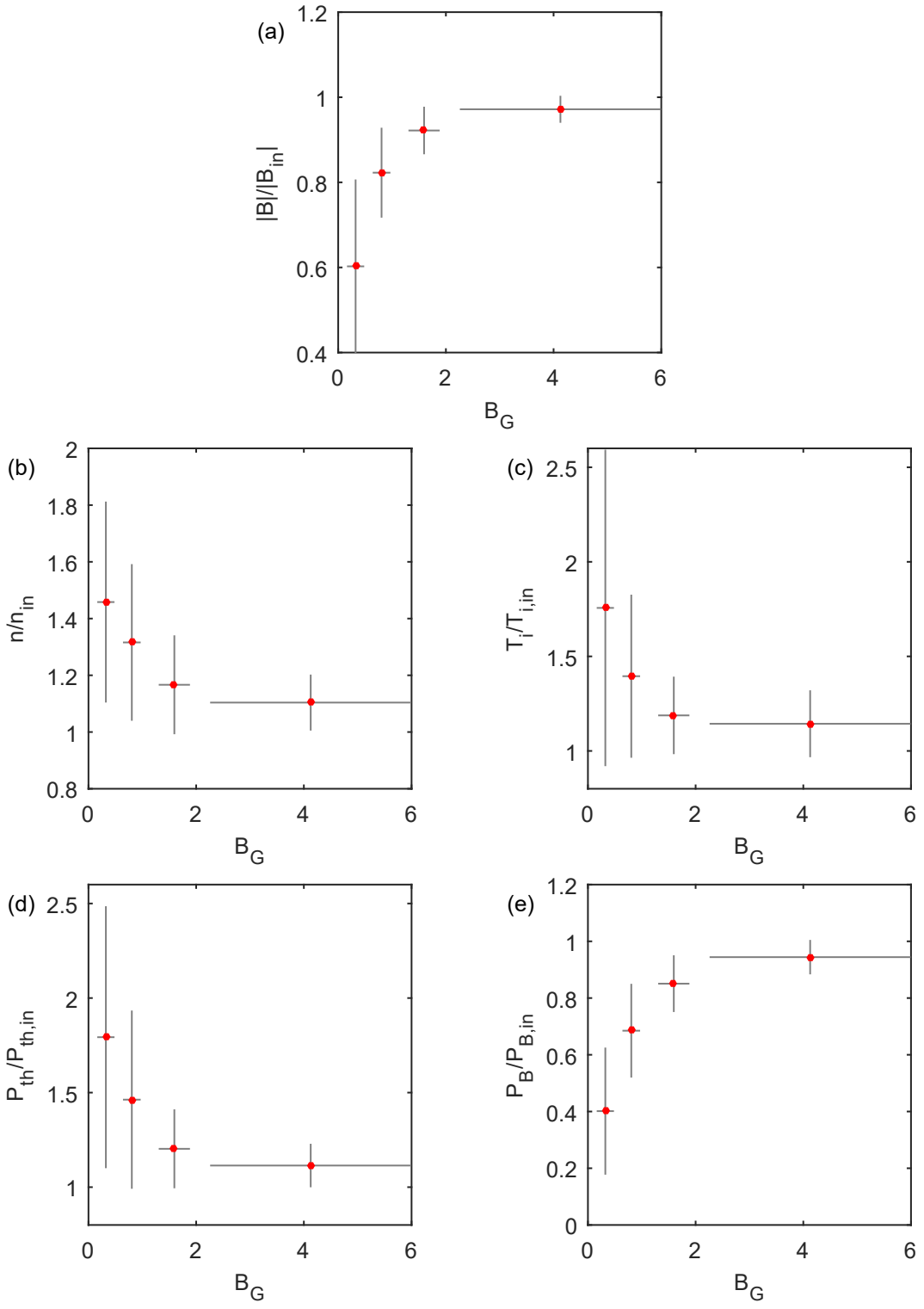


Figure 3.14: (a) minimum $|B|$, (b) maximum n, (c) maximum T_{in}, (d) maximum thermal pressure and (e) minimum magnetic pressure from within the exhaust region (calculated from 10% and 90% quantiles) as a function of guide field. Guide field bins are the same as in Figure 3.13. Error bars for B_G show the standard deviation of the guide field for events in each bin and are centred on the mean guide field value within that bin.

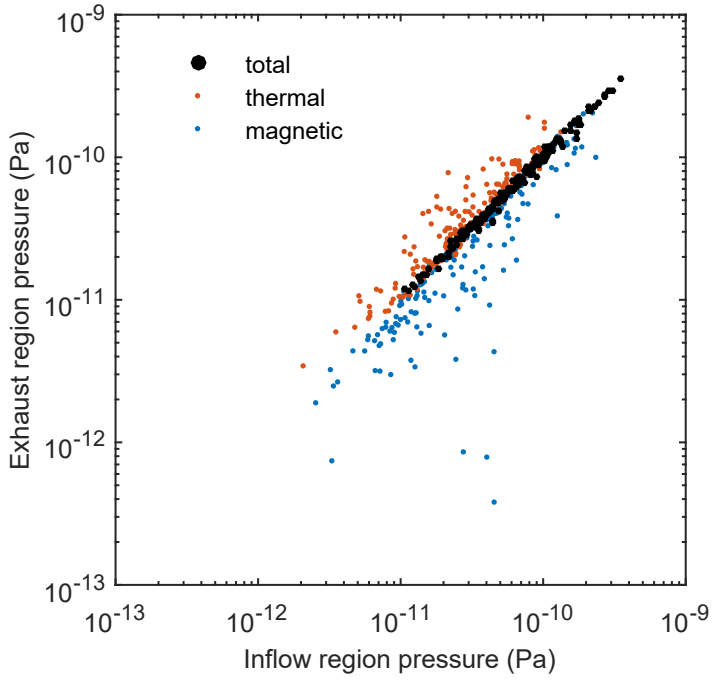


Figure 3.15: Pressures in the inflow regions and exhaust regions of 188 reconnection exhausts. Inflow region pressures are means from inflow regions 1 and 2. Exhaust regions pressures are calculated at the midpoint of the exhaust region.

values within the exhaust region to reduce the effects of any erroneous extreme data points, however in most cases the quantiles are extremely similar to the minimum/maximum values. At low B_G these parameters change within the exhaust region considerably, and at large guide fields these changes are reduced in amplitude. The standard deviations are larger at low guide fields, indicating that the maximum density/ion temperature/thermal pressure and minimum magnetic field/magnetic pressure vary more considerably between events with low guide fields.

These signatures can be understood by considering that these events are in pressure balance. This is shown in the superposed epoch analyses of Figures 3.11 and 3.13, but is shown more explicitly for each event in Figure 3.15 where the magnetic pressure, thermal pressures and total pressure in the inflow regions and at the mid-point of the exhausts are compared. The inflow regions have lower magnetic pressures and higher thermal pressures than the exhaust regions. The total pressure, however, is the same in both regions for all events, to a remarkable extent. Note that these pressures are isotropic pressures as we are unable to resolve the pressure anisotropy at sufficient resolution for these events.

The contribution of the magnetic pressure and thermal pressure to the total pressure is dictated by the plasma beta. For $\beta >> 1$, for example, the thermal pressure will contribute to almost all of the total pressure, and the magnetic pressure will be negligible. This means

that as the magnetic field and magnetic pressure decrease within the exhaust, only small increases in the thermal pressure are required to maintain pressure balance. Increases in the density and ion temperature are expected to be small in such cases.

To understand how this affects the density and temperature within reconnection exhausts more specifically, we first consider reconnection with zero guide field. In this case the sum of the thermal pressures (P_{th}) and magnetic pressures (P_B) in the inflow region (subscript 'in') and exhaust region (subscript 'exh') will be equal, however the exhaust region magnetic pressure will be zero as the magnetic field strength decreases to zero at the field reversal. This can be expressed as

$$P_{th,in} + P_{B,in} = P_{th,exh}, \tag{3.2}$$

which may be re-arranged to

$$1 + \beta_{in}^{-1} = \frac{P_{th,exh}}{P_{th,in}}, \tag{3.3}$$

where β_{in} is the plasma beta of the inflow region. In the case of zero guide field the relative increase in thermal pressure in the exhaust region ($P_{th,exh}/P_{th,in}$) is therefore dictated by the inflow region plasma beta.

Figures 3.14(d-e) show that the guide field also plays a key role in determining exhaust region pressures. Furthermore, Figure 3.13(b) shows that B_M is enhanced in the exhaust region. The standard deviations of these measurements are large, and it is not clear how B_M in the exhaust region depends upon the guide field. An analytical expression for the ratio of the exhaust region to inflow region thermal pressure or magnetic pressure, such as Equation 3.3, cannot be written in the case of a guide field as both the exhaust region thermal and exhaust region magnetic pressure are unknown.

To understand how both the inflow region plasma beta and guide field affect the relative changes in pressure, we plot the relative change in thermal pressure as a function of β_{in} and B_G in Figure 3.16(a). The thermal pressure in the inflow regions is the mean from inflow regions 1 and 2. The thermal pressure in the exhaust region is the maximum pressure measured during the exhaust region. Events with the lowest guide fields are close to the line given by Equation 3.3. This indicates that the thermal pressure increase within the exhaust is dictated by the plasma beta according to Equation 3.3 when $B_G \sim 0$, as expected.

Given that in the case of zero guide field $P_{th,exh}/P_{th,in}$ follows Equation 3.3, an equation of the following form was fitted to the data to derive an empirical relation between $P_{th,exh}/P_{th,in}$, the guide field and the inflow region plasma beta,

$$P_{th,exh}/P_{th,in} = \beta_{in}^{a} + B_G^{b} + c, \tag{3.4}$$

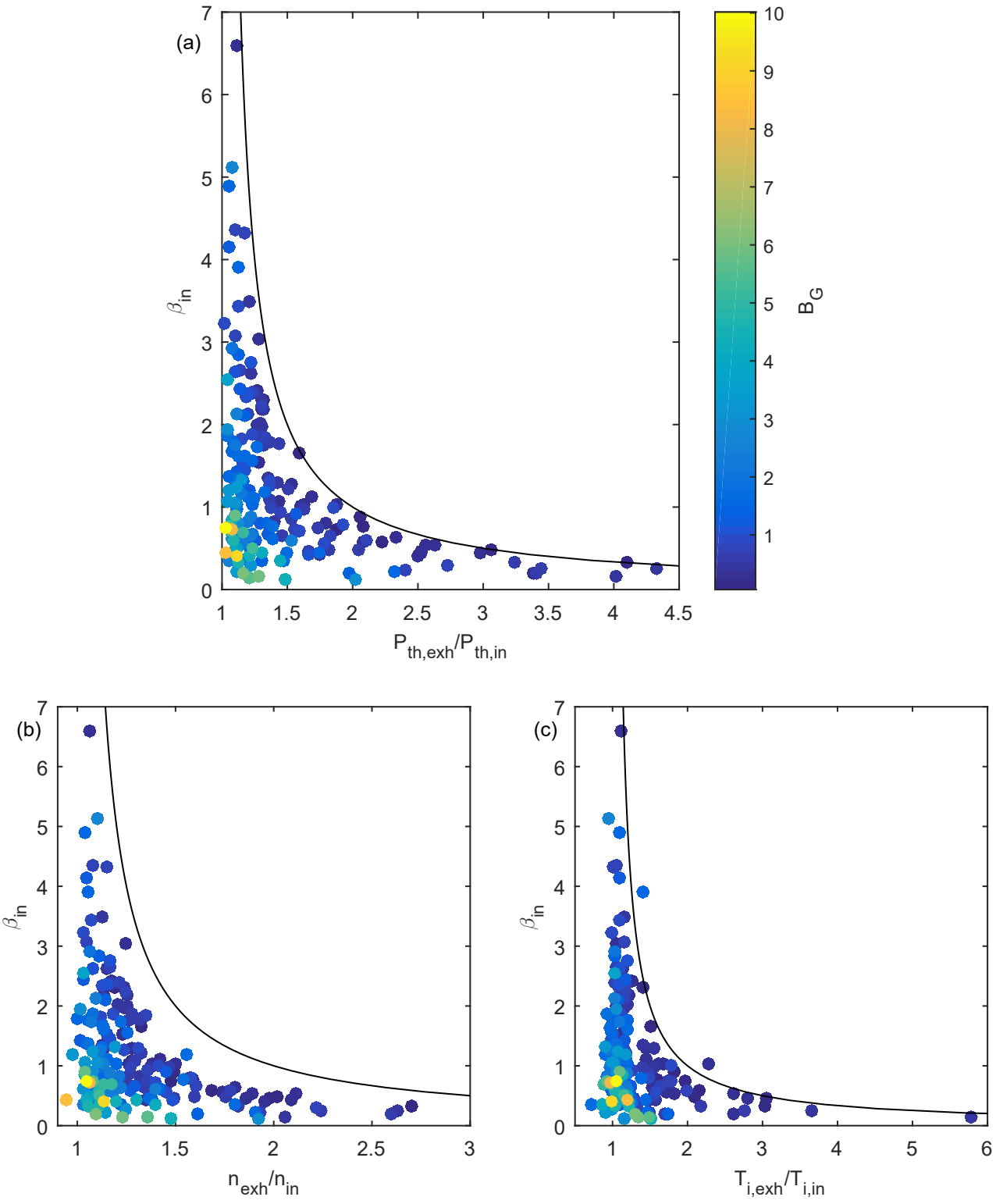


Figure 3.16: (a) Ratio of exhaust region to inflow region thermal pressure, as a function of inflow region plasma beta and guide field. The case for zero guide field (Equation 3.3) is shown by the line. The ratio for density and ion temperature are shown in (b) and (c), where the lines are Equation 3.3 using the ratios n_{ex}/n_{in} and $T_{i,ex}/T_{i,in}$, respectively, instead of $P_{th,ex}/P_{th,in}$.

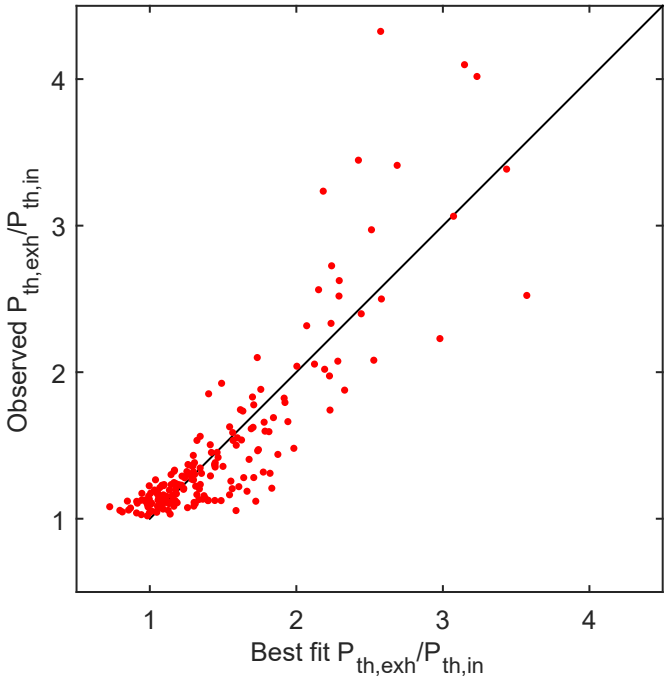


Figure 3.17: Observed thermal pressure increase, and thermal pressure increase according to a best fit to the data (Equation 3.6).

as well as an equation of the form

$$P_{th,exh}/P_{th,in} = \beta_{in}^{a} \times B_G^{b} + c, \tag{3.5}$$

where the β and B_G terms are multiplied instead of summed. The best fit to the data using a least squares fit was found with the equation

$$P_{th,exh}/P_{th,in} = \beta_{in}^{-0.44} \times B_G^{-0.29} + 0.36. \tag{3.6}$$

There is a good correlation between the fit and the data, with a R^2 value of 0.75. The value of $P_{th,exh}/P_{th,in}$ found using Equation 3.6 and measured values of β_{in} and B_G is shown in Figure 3.17, plotted against observed values of $P_{th,exh}/P_{th,in}$. These values agree fairly well for most events, indicating that Equation 3.6 describes $P_{th,exh}/P_{th,in}$ well, however there is poorer agreement for some events at large $P_{th,exh}/P_{th,in}$ (corresponding to events with low values of β_{in} and B_G). Additionally, $P_{th,exh}/P_{th,in}$ in Equation 3.6 does not tend to 1 at large values of β or B_G. We would expect it to tend to 1 in this limit (as is the case for the observed data) as the thermal pressure in the exhaust region should be almost unchanged from the inflow region at large β or B_G. The equation is therefore only valid where it is greater than 1.

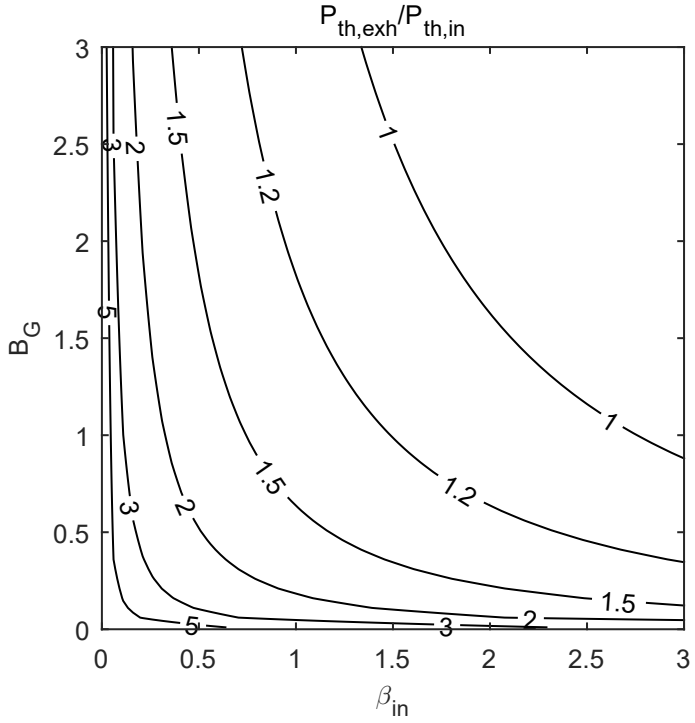


Figure 3.18: Ratio of exhaust region to inflow region thermal pressure, as a function of inflow region plasma beta and guide field, as given by Equation 3.6.

A contour plot of $P_{th,exh}/P_{th,in}$ according to Equation 3.6 is shown in Figure 3.18. The dependence of $P_{th,exh}/P_{th,in}$ on β_{in} and B_G is fundamentally a result of pressure balance. The magnetic pressure within the exhaust decreases as B_L tends to zero. Consequently, the thermal pressure must increase (facilitated by increases in the density and ion temperature). The magnetic pressure is low for large β_{in}, therefore the necessary increase in thermal pressure (i.e., $P_{th,exh}/P_{th,in}$) is small. If there is a large guide field only a small component of the magnetic field will reconnect and the decrease in magnetic pressure will be small, therefore the increase in $P_{th,exh}/P_{th,in}$ will be even smaller. The relative thermal pressure increase is therefore a function of both the inflow region plasma beta and the guide field. These together control the decrease in magnetic pressure within the exhaust region and, therefore, the necessary increase in thermal pressure.

Figures 3.16(a) and 3.18 show that at low guide fields the range of possible thermal pressure increases is large, and that this is sensitive to β_{in}. This explains why the standard deviation of increases in n, T and thermal pressure are large for low B_G in Figure 3.14. At low B_G these increases can take a broad range of values depending on β_{in}, whereas at high B_G the increases occur over a lower range of values and are far less sensitive to β_{in}.

The relative increases in the constituents of the thermal pressure (density and temperature) show similar trends (Figures 3.16(b-c)). The density and temperatures shown in

Figures 3.16(b) and (c) were measured at the same time as the data shown in Figure 3.16(a). Increases in temperature tend to be larger than density (as shown in the superposed epoch analyses), which is why there is a gap between the data and the line in Figure 3.16(b), and why some data are to the right of the line in Figure 3.16(c). There are also some events where the exhaust region density or ion temperature is reduced with respect to the inflow region, however the product of the density and temperature is such that the exhaust region relative thermal pressure is always greater than 1.

In this section we have shown, for the first time, that the guide field and inflow region plasma beta control the increase in the thermal pressure within the exhaust region, which also affects the increase in density and ion temperature. This analysis sheds light on why n and T_i vary so much between events in the analysis of Section 3.4, and why some reconnection exhausts in the solar wind have been observed with the absence of density and ion temperature enhancements. The most extensive surveys where a lack of these enhancements were noted had large guide fields (Gosling *et al.*, 2007d) or large plasma beta (Gosling, 2007). In both cases this analysis shows that densities and ion temperatures within such exhausts should be comparable to the inflow regions.

3.6 Ion heating as a function of inflow region Alfvén speed

In the fluid description of magnetic reconnection, plasma is heated by slow shocks at the exhaust boundaries (Petschek, 1964). In collisionless reconnection, however, plasma can flow into the exhaust from the two inflow regions and mix along field lines. Counterstreaming ion beams have been observed in the solar wind (Gosling *et al.*, 2005), the magnetosheath (Phan *et al.*, 2007b) and magnetotail (Hoshino *et al.*, 1998), and result in an increase in the ion temperature from the inflow region to the exhaust region. These temperature increases have been observed at many reconnection exhausts, however the amount by which the ion temperature increases can vary considerably. In the previous section we showed that the relative increase in thermal pressure is dependent upon the plasma beta and the guide field. In this section we build upon previous surveys of heating of ions within reconnection exhausts with respect to the inflow region Alfvén speed by expanding upon the number of events studied, studying how guide fields affect the observed heating, and quantifying the uncertainty in these measurements.

In a study of the ion temperature increase at 22 reconnection exhausts in the solar wind with magnetic shear angles of more than 120° ($B_G < 0.6$), Drake *et al.* (2009a) found that the increase in ion temperature and the speed of the exhaust outflow were correlated. Specifically, they found that $\Delta T_i = 0.13 m_i V_{exhaust}^2$, where ΔT_i is the difference between the ion temperatures in the exhaust region and inflow region, m_i is the ion mass and $V_{exhaust}$

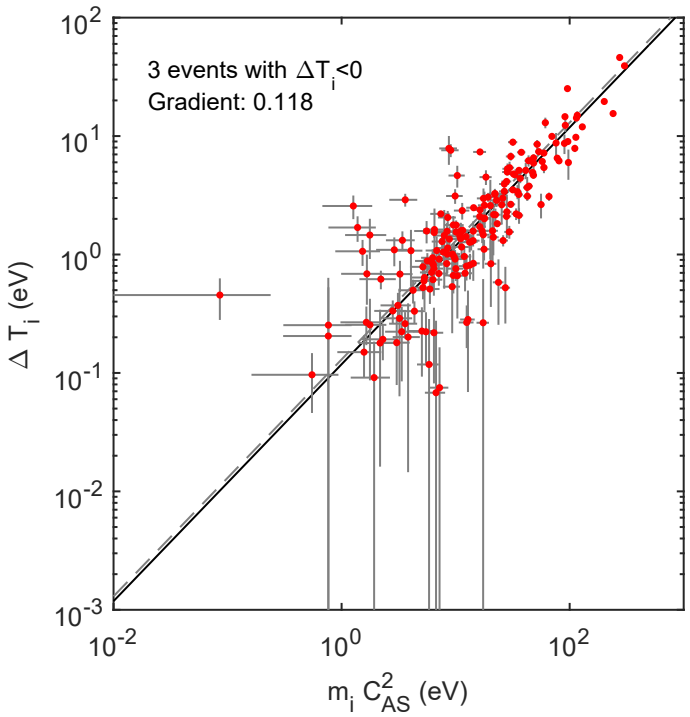


Figure 3.19: Increase in ion temperature within the reconnection exhausts as a function of $m_i C_{AS}^2$ for 188 events. The solid lines shows the best fit to the data. The dashed lines shows $\Delta T_i = 0.13 m_i C_{AS}^2$, as reported by Phan *et al.* (2014). ΔT_i was calculated to be negative for 3 events (not shown).

is the measured exhaust outflow speed. Similarly, Phan *et al.* (2014) measured the increase in ion temperature at 87 exhausts formed from reconnection between asymmetric plasmas at the magnetopause, and found that 13% of the available magnetic energy went to heating of ions, i.e., $\Delta T_i = 0.13 m_i C_{AS}^2$. These events had magnetic shear angles of 40° to 177° ($0 < B_G < 2.7$), and Phan *et al.* (2014) found that of events with the same C_{AS}, those with guide fields had lower increases in ion temperatures.

The ion heating rates found in these studies (13%) are substantially less than the ion heating rates predicted to occur as a result of ions entering the exhaust along field lines (33%) (Drake *et al.*, 2009a), and an understanding of the observed heating rate has not emerged. In this section we calculate the ion heating rates for 188 solar wind reconnection exhausts to extend upon the scope of these previous studies and more accurately characterise the variability of heating rates between events.

Ion heating within reconnection exhausts is measured as the difference between the ion temperature within the inflow regions and the exhaust region. The difference in the ion temperature within the two inflow regions is non-negligible for many of these events (Figure 3.3). In order to more accurately determine the ion heating rate we define the inflow region

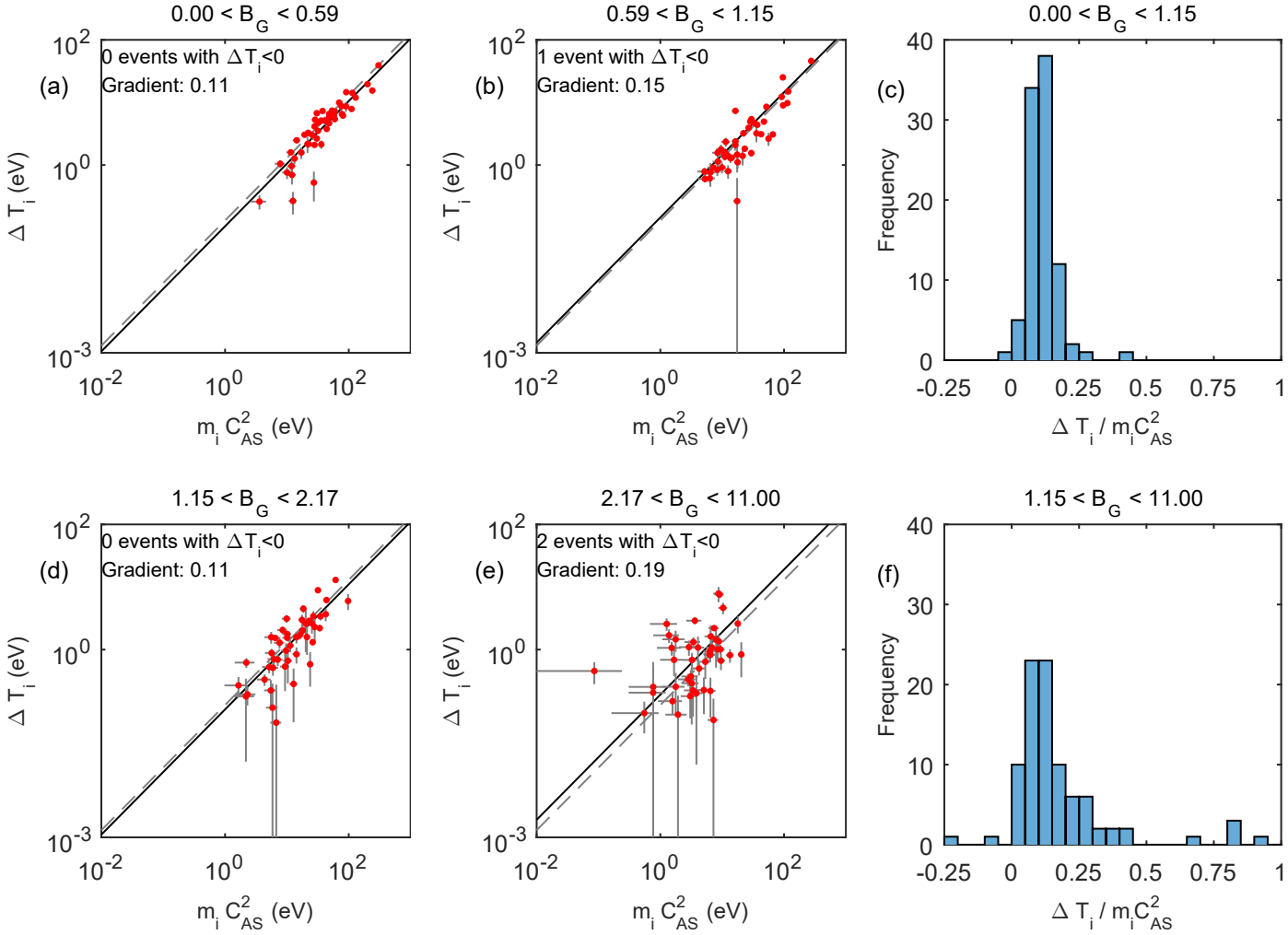


Figure 3.20: Increase in ion temperature within the reconnection exhausts as a function of $m_i C_{AS}^2$. Scatter plots show events binned by guide field (47 events per bin). Solid lines show best fits to the data. Dashed lines show $\Delta T_i = 0.13 m_i C_{AS}^2$, as reported by Phan *et al.* (2014). The number of events where ΔT_i was calculated to be negative (the data of which are not shown) are given in each scatter plot. (c) and (f) are histograms of the fraction of magnetic energy available that goes to ion heating for the combined events in (a,b) and (d,e), respectively.

temperature to be the effective inflow temperature as used by Phan *et al.* (2014) for reconnection at the magnetopause where the two inflow region temperatures differ substantially. This is given by,

$$T_{i,eff} = \frac{n_1 T_{i,1}/B_{L,1} + n_2 T_{i,2}/B_{L,2}}{n_1/B_{L,1} + n_2/B_{L,2}}. \tag{3.7}$$

The maximum difference between this inflow temperature and the inflow temperature defined as the average of T_i in inflow regions 1 and 2 is 26%, but it is less than 4% for three quarters of the events. The ion temperature within the exhaust region can vary considerably, and is often not uniform across the exhaust region. To measure the amount by which ions are heated within the exhaust region we use the 90% quantile of the ion temperature within the exhaust region. We do not use the maximum measured ion temperature, so as to avoid the use of possible erroneous measurements. We define ΔT_i as the 90% quantile exhaust region temperature minus $T_{i,eff}$.

Figure 3.19 shows ΔT_i as a function of $m_i C_{AS}^2$. The standard deviation of C_{AS}^2 measurements are calculated using the standard deviations of B_L and n in inflow regions 1 and 2, and standard error propagation formulae. The standard deviation of ΔT_i measurements are calculated using the standard deviations of B_L, n and T_i in inflow regions 1 and 2 and standard error propagation formulae. We are unable to attribute a standard deviation to the exhaust region temperature for each event as it is taken as the 90% quantile. There is considerable scatter of the data, indicating substantially different rates of ion heating as a function of $m_i C_{AS}^2$. Additionally, 3 out of the 188 events had higher ion temperatures in the inflow region than the exhaust region, and are not shown. A best fit to the data (including events where $\Delta T_i < 0$) shows that $\Delta T_i = 0.118 m_i C_{AS}^2$ (i.e., 11.8%), which is marginally lower than the rate reported by Phan *et al.* (2014). This data set contains a larger number of events across a broader range of guide fields, and we have additionally shown the standard deviations of each measurement (which has not been shown in previous studies). These new measurements show that the heating rates of specific events can be considerably different from the mean of the distribution and that the standard deviation of each measurement can be substantial, indicating the large uncertainty in these types of measurements.

To investigate the variability of heating rates between events, they are binned by guide field in Figure 3.20. There is a clear difference in the correlation between ΔT_i and $m_i C_{AS}^2$ for the case of weak guide fields (panels (a,b)) and stronger guide fields (panels (d,e)). For weak guide fields the data are well correlated. The distribution of heating rates ($\Delta T_i / m_i C_{AS}^2$) for the 96 events with $B_G < 1.15$ is shown in Figure 3.20(c). The distributions in Figures 3.20(d-e) are weakly correlated and the distribution of heating rates for the 96 events with $B_G > 1.15$ (Figure 3.20(f)) is much more spread than that for events with $B_G < 1.15$. These data show that although the mean heating rate determined from high guide field

events is similar to that determined for low guide field events, there is considerably more scatter and uncertainty. Phan *et al.* (2014) found weaker ion heating rates for events where $B_G > 1$, however this was based on only 7 out of 87 events. We do not find any clear evidence that the ion heating rates are lower at large guide fields, only that they are more variable.

PIC simulations and observations from MMS have shown that the guide field also affects the ion temperature profile across the reconnection exhaust (Øieroset *et al.*, 2016). The presence of a guide field affects the Hall electric field and ion motion, which creates strong perpendicular ion heating on one side of the exhaust. The parallel ion temperature peaks on the other side (the reasons for which remain unclear) and an asymmetric ion temperature profile is produced across the exhaust. Observations confirming this were made $\sim$12 d_i downstream of the X-line, however a comparative simulation produced similar asymmetries which filled the exhaust region. In Chapter 5 we show that Hall magnetic fields can persist extremely far downstream of the X-line, therefore one might expect that these asymmetric temperature profiles may also exist far downstream. This implies that, in the presence of a guide field, the ion temperature profile may vary across the exhaust region. The ion temperature from this variable profile may therefore not follow a simple scaling with $m_i C_{AS}^2$ as the exhaust is no longer characterised by a single ion temperature. This could explain why our data show that the temperature increase is considerably variable for large B_G. Furthermore, Wind 3DP measures ion temperatures averaged over 3 s. Ion temperature variations across the exhaust may occur on sub-3 s timescales, in which case they would not be resolved with Wind. In order to identify this type of asymmetry in the ion temperature and whether the ion temperature anisotropy (which cannot be measured sufficiently well with Wind for these events) reported by Øieroset *et al.* (2016) persists far downstream, faster plasma instrumentation is required, such as the 150 ms cadence Fast Plasma Investigation on MMS (Pollock *et al.*, 2016).

In this section we show that the maximum increase in ion temperature (not normalised) is proportional to the square of the inflow region Alfvén speed, and that this relationship is more tenuous for large guide fields. In Section 3.5, however, we showed that the increase in ion temperature within the exhaust region is a function of the inflow region plasma beta and the guide field. Although we used normalised temperatures in the analysis, this does not appear to affect the conclusions, and a plot of the unnormalised temperature increase (i.e., ΔT_i) as a function of β_{in} and B_G shows a similar relationship to Figure 3.16(c). We specifically found that T_{exh}/T_{in} decreases for large guide fields and for large plasma beta. This is qualitatively consistent with the scaling of ΔT_i with C_{AS}^2 which we have investigated in the present section. For large guide fields B_L (and therefore C_{AS}^2) tends to be small, which will cause a small temperature increase. If we now consider the plasma beta, this is proportional to $(T_{i,in} + T_{e,in})/V_A^2$, where V_A^2 is the Alfvén speed of the inflow region plasma

(which is a function of $|B|$). An increase in β_{in} will decrease V_A^2 and C_{AS}^2, also resulting in a small temperature increase.

3.7 Conclusions

In this chapter we have used 188 reconnection exhausts observed by the Wind spacecraft to study the average properties of solar wind reconnection exhausts far downstream of the X-line. The aim of this was to better characterise the exhaust region, given that comparisons between events can show large differences, and to understand what determines the observed differences between events. The variability between events means that exhaust region structure and characteristics are not obvious from observations of a small number of events, and a large statistical study was required.

Analysis of the events used in this study show that in general the velocity shears across reconnection exhausts are not substantial enough to cause significant drifts of the X-line. Furthermore, differences between the two inflow regions tend to be relatively weak, and any corrections to the Alfvén speed and inflow region temperatures to correctly account for this asymmetry (as used at the magnetopause where asymmetries tend to be far more substantial) tend to be small. The guide fields, however, can vary significantly and reconnection occurs across a broad range of magnetic shear angles. This is partly because the asymmetries between the inflow region tend to be small, such that reconnection at large guide fields is not suppressed by diamagnetic drifts of the X-line that occur in the presence of large asymmetries (Swisdak *et al.*, 2010; Phan *et al.*, 2010). Reconnection in the solar wind can therefore generally be considered to occur with symmetric inflow conditions and with non-zero guide fields, with negligible affects from asymmetries and flow shears.

The analysis of 188 events shows that increases in B_M are very common in reconnection exhausts far downstream of the X-line, which has not been previously reported. This occurs in conjunction with decreases in B_L. Additionally, these changes occur with increases in n and T_i, and are qualitatively consistent with rotational discontinuities that form in 1D and 2D simulations of the exhaust region where ion temperature anisotropy is permitted (Lin *et al.*, 1995; Lin & Swift, 1996). The fact that exhaust boundaries do not show clear evidence for slow shocks is not surprising, given that previous studies have shown that shocks tend to be weakened at guide field strengths comparable to those commonly found at solar wind reconnection current sheets (Lin & Lee, 1993; Lin *et al.*, 1995; Lin & Swift, 1996). The exhaust structure does not, therefore, resemble that predicted by the Petschek model.

At low guide fields where the slow shocks are stronger, the exhaust boundaries may more

strongly resemble the Petschek configuration or the compound structures reported by Liu *et al.* (2012) and Innocenti *et al.* (2015). A detailed and quantitative study of the exhaust boundaries is beyond the scope of this study and requires higher resolution measurements such as those taken by MMS. These observations suggest, however, that reconnection exhausts may be sufficiently described with one dimensional simulations. This is important given that two and three dimensional simulations are significantly more computationally expensive, and it is currently not possible to simulate significantly further than $\sim$100 d_i downstream of the X-line in such configurations using PIC codes. One dimensional simulations, in conjunction with solar wind observations (where spacecraft are typically hundreds of d_i downstream), could provide significant insight into these structures. In Chapter 5, however, we show that there are a small number of cases where this is not true and the exhaust contains Hall magnetic fields which are generated from two dimensional effects. The conditions under which the exhaust region exhibits this phenomenon are not clear, and it may not always be appropriate to model exhausts as one dimensional structures.

These events have also demonstrated the huge amount of variability in the density and ion temperature between different solar wind reconnection exhausts. This variability seems to be strongly related to the guide field, however the density and ion temperature can still vary significantly between events with comparable guide fields. We have shown (using empirical evidence that the exhausts are in pressure balance) that the combination of guide field and plasma beta controls how much the thermal pressure changes from the inflow region to exhaust region, and that this explains the previously unaddressed problem of why the density and ion temperature increase at some exhausts but not others.

The increase in ion temperature within reconnection exhausts has previously been shown to be related to the inflow region Alfvén speed/exhaust speed. We have shown that these events agree with previous observations; the increase in ion temperature is of the order of 13% of $m_i C_{AS}^2$. This scaling is in qualitative agreement with the increase in thermal pressure being a function of the plasma beta and guide field. We have shown that the increase in ion temperature is very variable at large guide fields, indicating that the scaling of the ion temperature increase with the inflow region Alfvén speed is more tenuous in such regimes.

4 Current sheet bifurcations: dependence on distance downstream of the X-line

Material in this chapter has been published in *Geophysical Research Letters* in Mistry *et al.* (2015b).

4.1 Introduction

Fast reconnection is achieved in MHD reconnection with the Petschek model. In this model slow shocks propagate away from the dissipation region and are crucial in facilitating fast reconnection, as the majority of exhaust plasma actually enters the exhaust across the shocks rather than through the dissipation region. These slow shocks also affect the magnetic field, reducing the in-plane tangential magnetic field (B_L) from its inflow region value to zero within the exhaust; the downstream field is comprised of only the unchanged normal component of the field (B_N). In contrast to Sweet-Parker reconnection the current is not concentrated at the current sheet mid-plane, but rather splits or *bifurcates* into two current layers, which are each localised to the boundaries of the exhaust where the field changes (i.e., near the slow shocks in Figure 1.3).

It is important to note that MHD simulations only form a Petschek configuration when a enhanced localised resistivity is imposed (Sato, 1979; Biskamp, 1986; Scholer, 1989). A similar open-outflow exhaust structure is formed in collisionless reconnection; the exhausts are bound by abrupt transitions between the upstream region and the downstream accelerated plasma of the reconnection exhaust (e.g., Hesse *et al.*, 2001). Since collisionless reconnection could effectively provide the localised dissipation required for Petschek's model, it is pertinent to ask whether exhausts formed in collisionless reconnection have the same structure as in Petschek's model, and therefore whether the current sheet bifurcates.

The majority of hybrid collisionless reconnection simulations do not produce bifurcated current sheets (Krauss-Varban & Omidi, 1995; Lottermoser *et al.*, 1998; Nakamura *et al.*, 1998; Arzner & Scholer, 2001), although they do form in the simulations of Lin & Swift (1996). It is more clear, however, that slow shocks and resulting current sheet bifurcations

are more likely to form further downstream of the reconnection site where slow mode waves can steepen, and the downstream regions of the back-to-back shocks are well separated (Krauss-Varban & Omidi, 1995; Lin & Swift, 1996).

The exhaust structure downstream of the reconnection site has been studied more recently with large-scale collisionless PIC simulations. Liu *et al.* (2012) showed that in a simulation of anti-parallel reconnection the exhaust boundary consists of multiple compound discontinuities, and the current sheet does not bifurcate. With the introduction of a weak guide field ($B_G = 0.3$), however, the boundary structure changes and the current sheet bifurcates far downstream of the X-line (130 simulation units $\sim$ 58 d_i) (Innocenti *et al.*, 2015).

Bifurcated current sheets have been observed in collisionless reconnection. Hoshino *et al.* (1996) and Asano *et al.* (2005) observed bifurcated magnetotail current sheets in association with magnetotail reconnection. Bifurcated magnetotail current sheets have also been suggested to be associated with wave-like transients (e.g., Runov *et al.*, 2003a) and instabilities (e.g., Daughton *et al.*, 2004; Ricci *et al.*, 2004). The formation mechanism of bifurcated current sheets in the magnetotail therefore remains unclear. Additionally, slow shocks have been observed in the near/mid-Earth magnetotail (Eriksson *et al.*, 2004; Øieroset *et al.*, 2004), however most of these observations are from the mid/deep tail using the ISEE-3 and Geotail spacecraft (e.g., Feldman *et al.*, 1985; Saito *et al.*, 1995; Smith *et al.*, 1984).

In Chapter 3 we investigated the variability between different solar wind reconnection exhausts. We found that the average properties of these exhausts are consistent with fluid treatments of the exhaust, and that differences in density and temperature increases between different exhausts can be attributed to pressure balance across these structures. In addition to this variability, the current sheet structure may also differ. There have been multiple observations of bifurcated reconnection current sheets (e.g., Gosling *et al.*, 2005, 2006b; Phan *et al.*, 2006) and it has become common to associate bifurcated solar wind current sheets with reconnection. There are, however, examples of solar wind reconnection current sheets which are not bifurcated (e.g., Gosling, 2007; Gosling *et al.*, 2007c and Chapter 6 of this thesis). An understanding of why some solar wind reconnection current sheets are bifurcated and others are not has not yet emerged.

There has been little observational evidence to suggest that the current sheet structure changes with distance downstream of the X-line, partly because it is extremely difficult to reliably estimate a spacecraft's distance from the X-line using single spacecraft solar wind observations. In this chapter we use multiple spacecraft to observe both of the reconnection exhausts formed from a reconnection site and we estimate each spacecraft's distance from the X-line using a new method. This information is subsequently used to study how the current sheet structure depends on distance from the X-line, and we show with observations

that bifurcations become more developed further downstream.

4.2 Observations

39 reconnection exhausts were identified in the solar wind using Cluster data in Chapter 2. We have also examined ACE and Wind measurements to identify whether the same reconnection exhausts were also observed at these spacecraft. For three events Wind observed an exhaust in the opposite direction to that at Cluster and was located on the opposite side of the X-line. Observations of both of the oppositely directed exhausts are rare in the solar wind. This is because the exhausts extend over much larger distances than the spacecraft separations, therefore it is likely that spacecraft would be located on the same side of the reconnection X-line rather than the X-line being located between them. One of these three events was observed at ACE, in addition to Wind and Cluster. For the three events the data have been rotated into an LMN co-ordinate system (Table 4.1) defined from hybrid-MVA applied to C-1 during the exhaust interval identified in Section 2.6. Observations from the four Cluster spacecraft are very similar, therefore only observations from C-1 are presented (although measurements from the four Cluster spacecraft are used in Section 4.4.3). The events are presented in an order which aids the explanation and interpretation of the results. A summary of key information for each event is provided in Table 4.1.

4.2.1 Event 1

Figure 4.1 shows observations from 24 February 2009. Wind measurements have been time-shifted for comparison with C-1. The current sheet at C-1 is clearly bifurcated; at 08:53:47 UT and 08:54:25 UT there are sudden changes in B_L. B_L is approximately constant in between these times. The current sheet is accompanied by an increase in the ion velocity in the $+L$ direction, indicating a reconnection exhaust. In comparison, Wind data show a smooth change in the magnetic field between 08:54:00 UT and 08:54:07 UT; the current sheet is clearly not bifurcated. This current sheet is accompanied by an increase in the ion velocity in the $-L$ direction. This event could not be found in ACE data.

Measurements of the field magnitude and density from the two spacecraft in the inflow regions (i.e., before and after the exhaust interval) are very similar (see Figure 4.1 and Table 4.1). Furthermore, the magnetic field and ion velocity vectors are similar, indicating that the spacecraft may have observed the same reconnection event. A comparison of the time delay between observations at the two spacecraft and the expected delay for a planar structure in the solar wind (with the same normal vector as the observed current sheet) provides a further test of whether this is the same event. This assumes that the reconnection

Table 4.1: Spacecraft measurements, their position relative to C-1 in the reconnection exhaust rest frame, differences between hybrid-MVA vectors from analysis at each spacecraft, and estimations of distance downstream of the X-line and reconnection rate. LMN coordinates derived from hybrid-MVA applied to C-1 are also given for each event.

	Event 1		Event 2			Event 3	
	C-1	Wind	C-1	Wind	ACE	C-1	Wind
Magnetic shear (°)	138	121	59	60	55	150	145
B_G	0.38	0.57	1.77	1.73	1.92	0.27	0.32
$V_{A,L}$ (km s^{-1})	39.3	34.9	21.1	24.3	21.1	29.6	33.5
Inflow region density (cm^{-3})	3.6	3.0	4.6	3.3	3.9	14.4	10.8
Duration (s)	61.5	6.0	28.2	55.9	120.4	141.5	21.9
Exhaust width (d_i)	119	12	36	71	269	715	111
L position relative to C-1 (d_i)	-	-1295	-	613	1754	-	-5726
M position relative to C-1 (d_i)	-	-1092	-	-3655	-4984	-	-6679
Hybrid-MVA $\hat{\mathbf{L}}$ vs. C-1 (°)	-	17	-	12	5	-	8
Hybrid-MVA $\hat{\mathbf{M}}$ vs. C-1 (°)	-	27	-	12	9	-	5
Hybrid-MVA $\hat{\mathbf{N}}$ vs. C-1 (°)	-	22	-	8	10	-	6
L distance from X-line (d_i)	1180	-116	-206	408	1548	4958	-768
θ (°)	5.8		9.9			8.3	
Reconnection rate	0.05		0.09			0.07	
L (GSE)	(0.25, 0.31, 0.92)		(0.05, 0.79, 0.61)			(0.45, 0.58, 0.68)	
M (GSE)	(-0.86, -0.38, 0.36)		(0.91, -0.29, 0.30)			(0.03, -0.77, 0.63)	
N (GSE)	(0.46, -0.87, 0.17)		(0.42, 0.53, -0.73)			(0.89, -0.26, -0.37)	

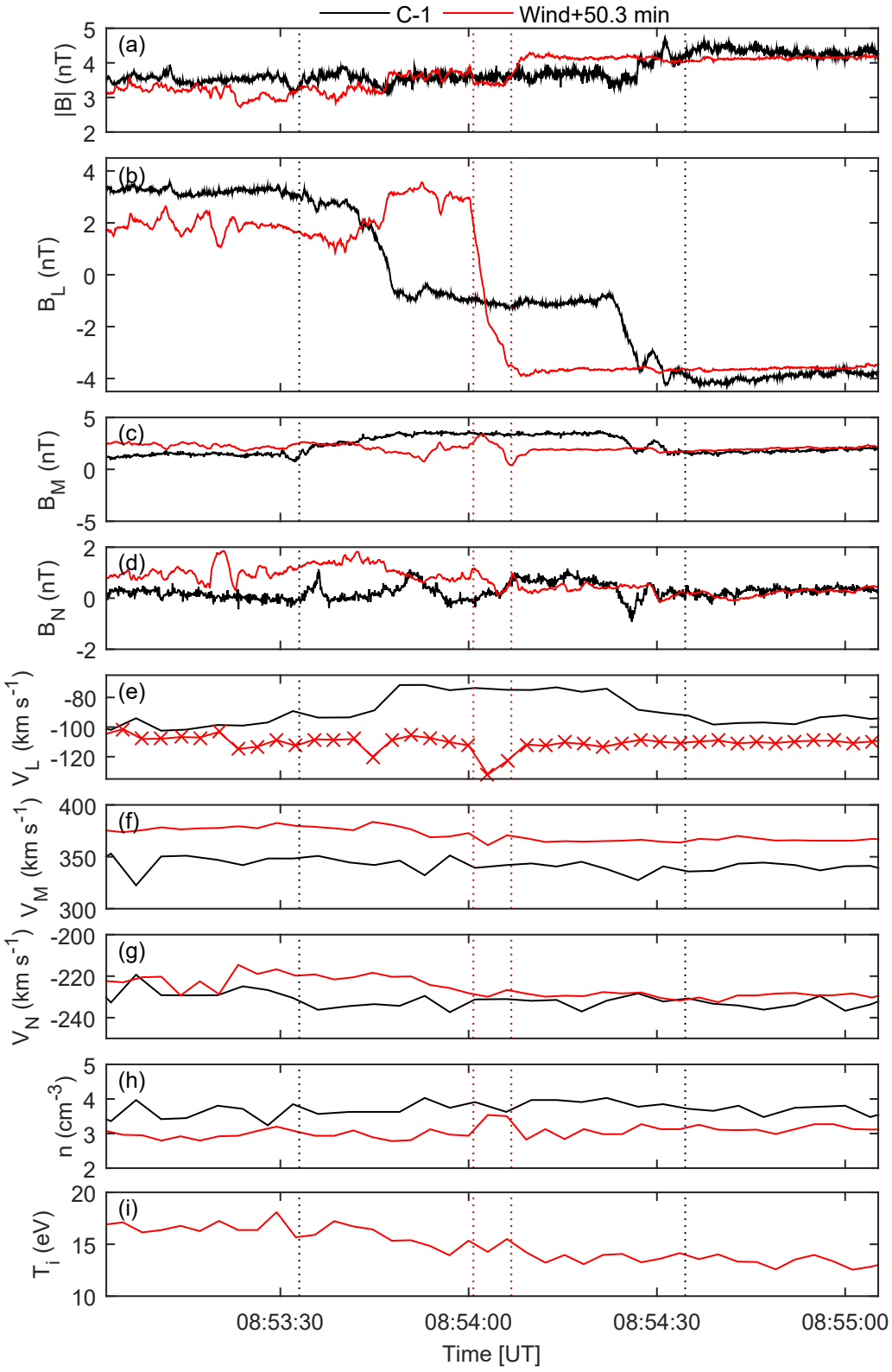


Figure 4.1: C-1 and Wind measurements of Event 1. (a-d) magnetic field and (e-g) ion velocity, in LMN coordinates. (h) Ion density, and (i) ion temperature. Vertical lines indicate the time at which the exhaust is observed by each spacecraft.

current sheet is two dimensional, which is generally the case in the solar wind on such large spatial scales (Phan *et al.*, 2006, 2009). Wind is located at $\mathbf{r} = [179.2, -40.0, -10.4]$ R_E (GSE coordinates) relative to C-1, which is a separation in the normal direction of $\Delta N = |\mathbf{r} \cdot \hat{\mathbf{N}}| = 114.8$ R_E. The solar wind propagates at a speed of $\mathbf{V_{SW}} \cdot \hat{\mathbf{N}} = 230.7$ km s^{-1} in the N direction. The planar structure is therefore expected to take a time $\Delta t_{exp} = \Delta N/(\mathbf{V_{SW}} \cdot \hat{\mathbf{N}}) = 3{,}174$ s to travel the distance of ΔN between the spacecraft. The delay between observations of the current sheets at C-1 and Wind is $\Delta t_{obsv} = 3{,}016$ s (5% difference from expected delay), indicating that the spacecraft did indeed observe the same event. Hybrid-MVA data was also performed on Wind data. The difference between LMN vectors determined from hybrid-MVA at C-1 and Wind were were not significantly large (Table 4.1), indicating that the current sheet orientation was similar at C-1 and Wind.

The position of Wind relative to C-1 in the solar wind/reconnection exhaust rest frame can be found by a coordinate transformation of Wind's position by $\mathbf{V_{SW}}\Delta t_{obsv}$, which gives a relative position of [-24.2, -20.4, -5.7] R_E in LMN coordinates. Since C-1 observed an exhaust in the $+L$ direction and Wind observed an exhaust in the $-L$ direction and was located in the $-L$ direction with respect to C-1, this indicates that the X-line was located between the two spacecraft.

4.2.2 Event 2

Figure 4.2 shows observations from 6 March 2009 from C-1, Wind and ACE. The current sheet at C-1 is not bifurcated, and is associated with an exhaust in the $-L$ direction. At Wind the magnetic field undergoes several sharp changes and has a complex profile. Although there are sharp changes in B_L, B_L is not constant across the exhaust and we conclude that the current sheet is not clearly bifurcated. Ion velocity data indicate an exhaust in the $+L$ direction. At ACE the current sheet is clearly bifurcated. A plasma measurement within the current sheet shows accelerated flow in the $+L$ direction, consistent with the expected exhaust direction given the spacecraft locations (as illustrated in Figure 4.4(b)). Following the same methods as described in Section 4.2.1, we confirm that C-1, Wind and ACE all observed the same reconnection current sheet, and that the X-line was located between C-1 and Wind, with ACE being further away from the X-line than Wind (and on the same side of the X-line).

4.2.3 Event 3

Figure 4.3 shows observations from 26 January 2009 from C-1 and Wind. C-1 observed a clearly bifurcated current sheet and an exhaust in the $+L$ direction. The Wind obser-

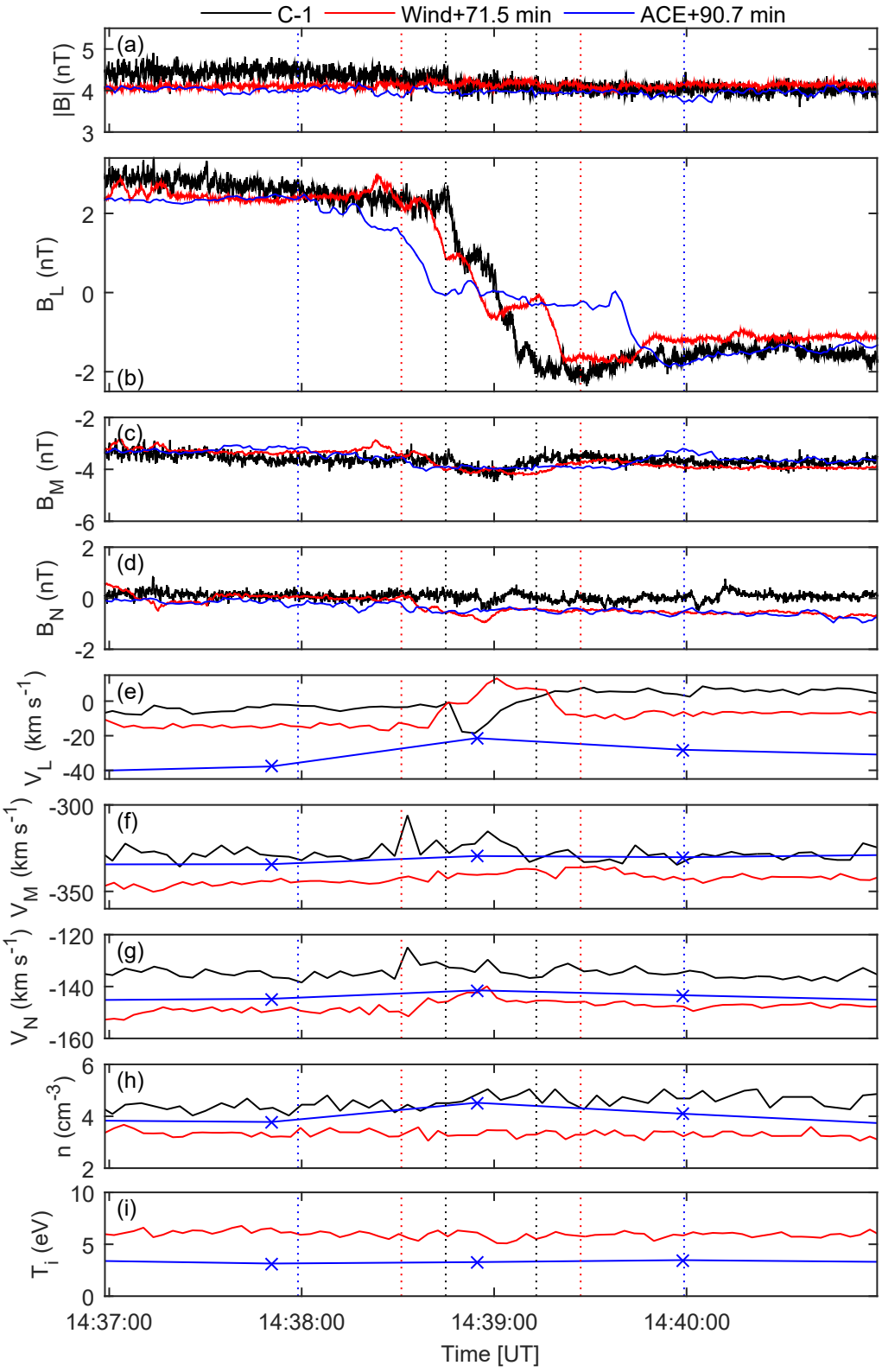


Figure 4.2: C-1, Wind and ACE measurements of Event 2. (a-d) magnetic field and (e-g) ion velocity, in LMN coordinates. (h) Ion density, and (i) ion temperature. Vertical lines indicate the time at which the exhaust is observed by each spacecraft.

vations are more complex. There are abrupt changes in B_L at 17:47:25 UT and 17:47:47 UT, however in between these times B_L is not constant and gradually increases. Therefore, although the current sheet displays bifurcated characteristics, we conclude that the bifurcation is not fully developed. Ion velocity data indicate an exhaust in the $-L$ direction. Following the same methods as described in Section 4.2.1, we confirm that the spacecraft observed the same reconnection current sheet, and that the X-line was located in between them. The presence of this event in ACE data was ambiguous as the event duration was less than the temporal resolution of plasma measurements, and we therefore do not include ACE data in the analysis of this reconnection current sheet.

4.3 Distance downstream from the X-line: macroscopic reconnection geometry

The relative distances between spacecraft in the reconnection exhaust rest frame can be estimated (Section 4.2.1). Furthermore, the width of the exhaust in the normal direction at the spacecraft location can be measured from $(\mathbf{V_{SW}} \cdot \hat{\mathbf{N}})\Delta t$, where Δt is the duration over which the exhaust was observed at that spacecraft. For Event 1, the exhaust was observed for 61.5 s and 6.0 s at C-1 and Wind, respectively, corresponding to widths of 1.42×10^4 km and 1.39×10^3 km, at C-1 and Wind, respectively, or 119 d_i and 12 d_i, where d_i is calculated from the average ion density in inflow regions 1 and 2 at C-1 (3.6 cm^{-3}). The reconnection rate cannot vary on either side of the X-line, therefore the exhaust opening angle (θ) is expected to be the same on either side. For Event 1, C-1 and Wind are separated by a distance of 1,295 d_i (24.2 R_E) in the L direction in the rest frame of the reconnection exhaust. Since the relative separation of the spacecraft in L is known, θ and each spacecraft's distance from the X-line (along L) can be determined from basic trigonometry. This analysis indicates that C-1 and Wind are located at a distance of 1,180 d_i and 116 d_i from the X-line in the L direction, respectively, and $\theta = 5.8°$ (Figure 4.4(a)).

Since this method uses information from spacecraft located at opposite sides of the X-line, θ for Event 2 can be estimated from observations of the exhaust widths and relative spacecraft separations between either C-1 and Wind or C-1 and ACE. Once θ is determined, the distance of all three spacecraft from the reconnection X-line can be estimated. Using data for C-1 and Wind, we determine distances from the X-line of 206 d_i, 408 d_i and 1,548 d_i for C-1, Wind and ACE, respectively, and $\theta = 9.9°$. Using data for C-1 and ACE, we determine distances from the X-line of 333 d_i, 280 d_i and 1,421 d_i for C-1, Wind and ACE, respectively, and $\theta = 6.1°$. In both cases ACE is found to be significantly further from the X-line than C-1 and Wind. There is some evidence from simulations that the exhaust may begin to collimate at large distances from the X-line in guide field reconnection (Cassak

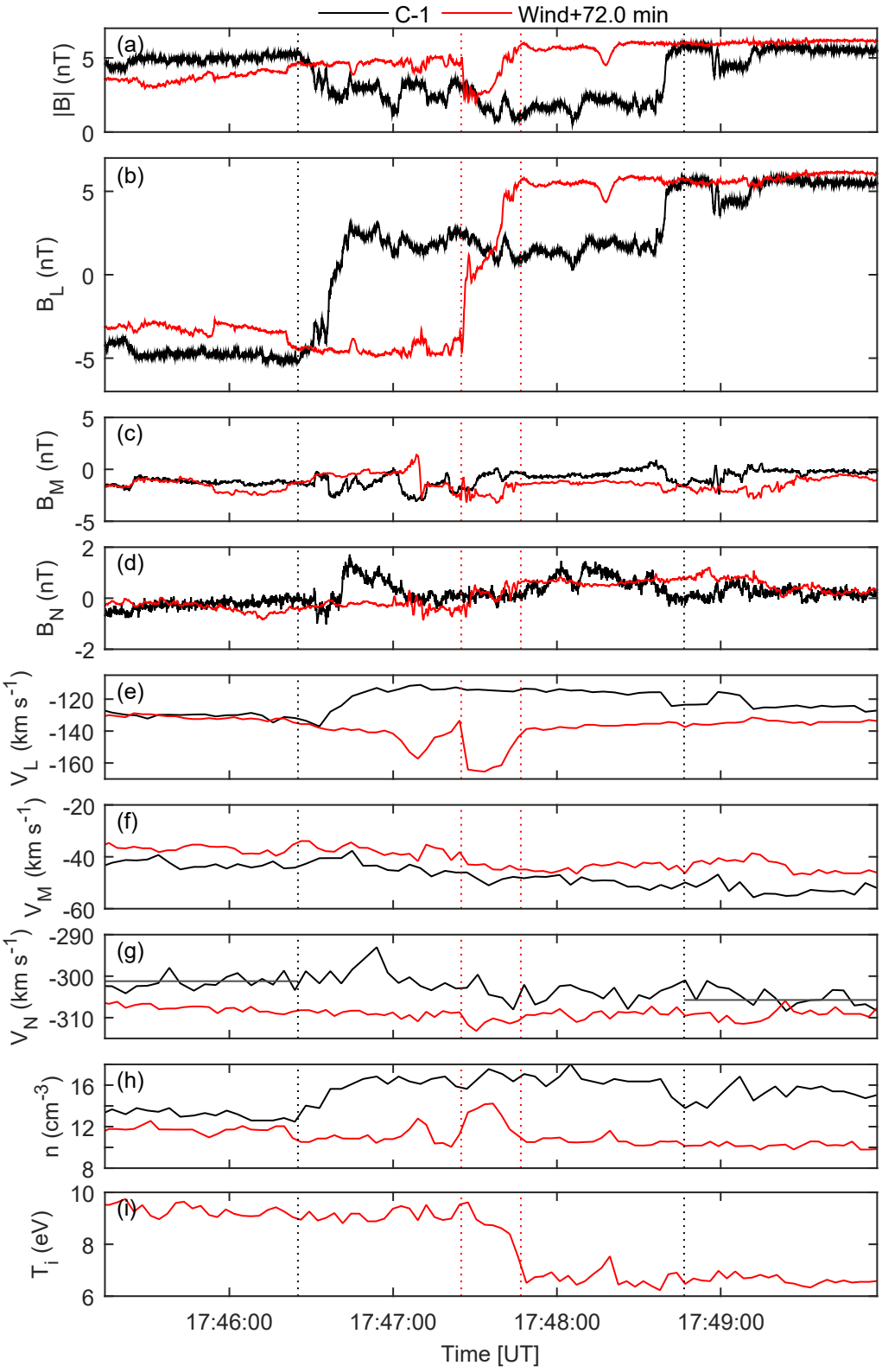


Figure 4.3: C-1 and Wind measurements of Event 3. (a-d) magnetic field and (e-g) ion velocity, in LMN coordinates. (h) Ion density, and (i) ion temperature. Vertical lines indicate the time at which the exhaust is observed by each spacecraft.

et al., 2013). If the exhaust begins to collimate, the exhaust would spread less at large distances from the X-line, and the opening angle would not be constant with increasing distance downstream. The analysis using C-1 and Wind data is therefore likely to be more reliable, and we use this. The estimated distances are shown in Figure 4.4(b).

For Event 3, C-1 and Wind were separated by a distance of 5,726 d_i in the L direction in the rest frame of the reconnection exhaust. We determine that C-1 and Wind were located at a distance of 4,958 d_i and 768 d_i downstream from the X-line, respectively, and $\theta = 8.3°$ (Figure 4.4(c)).

Each spacecraft's distance downstream of the X-line in the outflow (L) direction has been found using measurements of the macroscale reconnection geometry. This assumes that θ is constant with increasing distance downstream of the X-line and also along the X-line. In the observations presented in this chapter the spacecraft detect oppositely directed exhausts from a reconnection site located between them and are therefore relatively close to the X-line. In general, reconnection exhausts form extremely extended structures in the solar wind and it is far more common for multiple spacecraft to be located on the same side of the X-line (and therefore observe only one of the the reconnection exhausts). This technique can in principal be modified to apply to events where the spacecraft are located on the same side of the X-line, however it is more likely that the exhaust opening angle is reduced at such large distances downstream (e.g., Cassak *et al.*, 2013), possibly making the technique unreliable.

Figure 4.5 shows the spacecraft separations along the X-line and their estimated distance from the X-line in the LM plane (calculated from the method described in Section 4.2.1). Spacecraft separations along the X-line are relatively small for Event 1, however they are larger for Event 2 (4,984 d_i) and Event 3 (6,679 d_i). Over such large distances it is possible that the reconnection rate and therefore the exhaust opening angle may vary along the X-line, however it is not possible to measure such effects.

4.4 Estimates of the exhaust opening angle from local measurements

In Section 4.3 the exhaust angle and reconnection rate are determined using observations of oppositely directed exhausts from both sides of the X-line. This method uses the macroscale geometry of the reconnection exhaust encounters. The exhaust opening angle can also be independently estimated from other methods using local spacecraft measurements of the magnetic field and plasma velocity, and Cluster multi-spacecraft timing analysis.

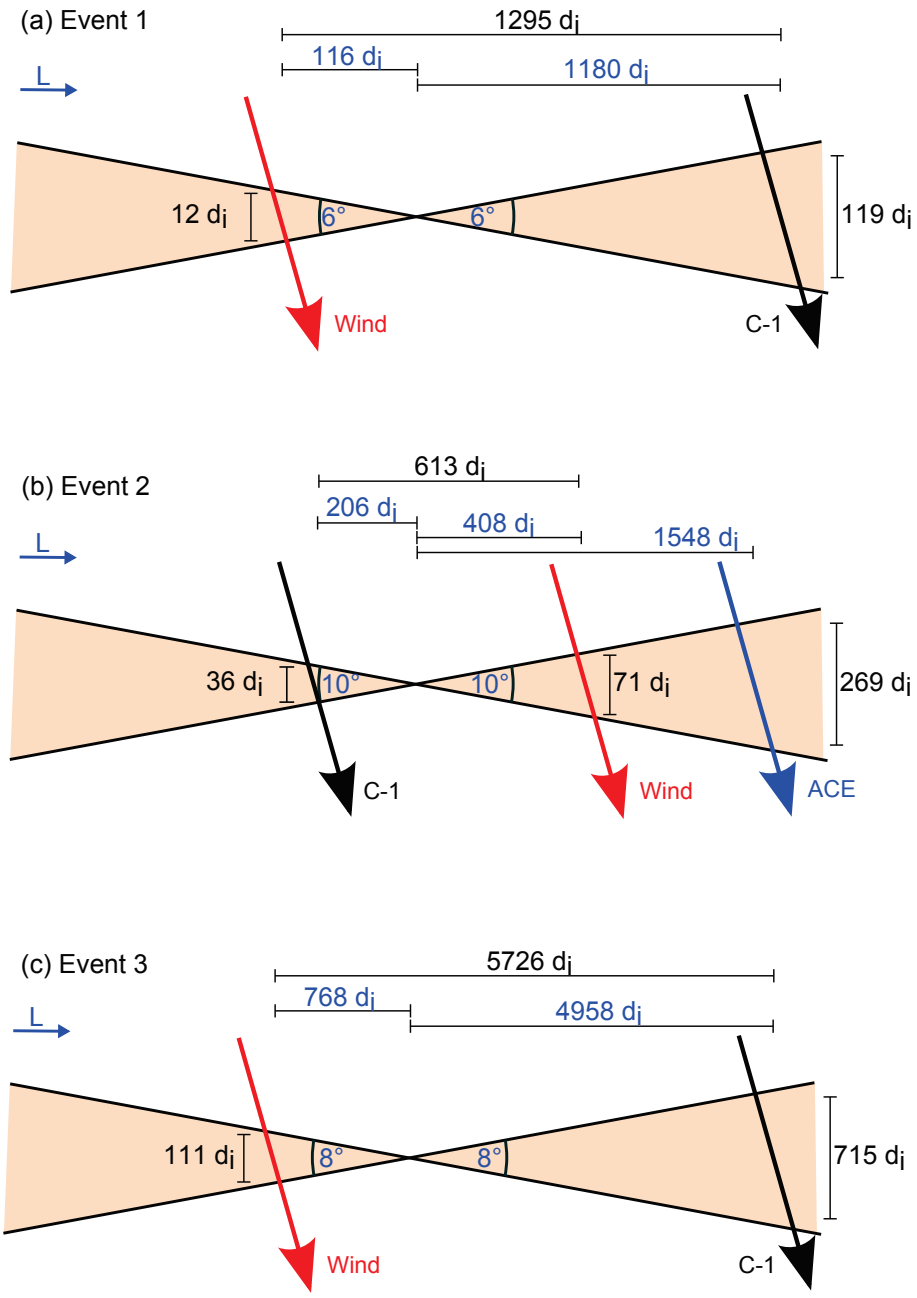


Figure 4.4: Estimated distance of C-1, Wind and ACE (for Event 2) from the X-line (not to scale). Distances determined from spacecraft measurements are in black. Estimated spacecraft separations from the X-line and the exhaust opening angle are in blue.

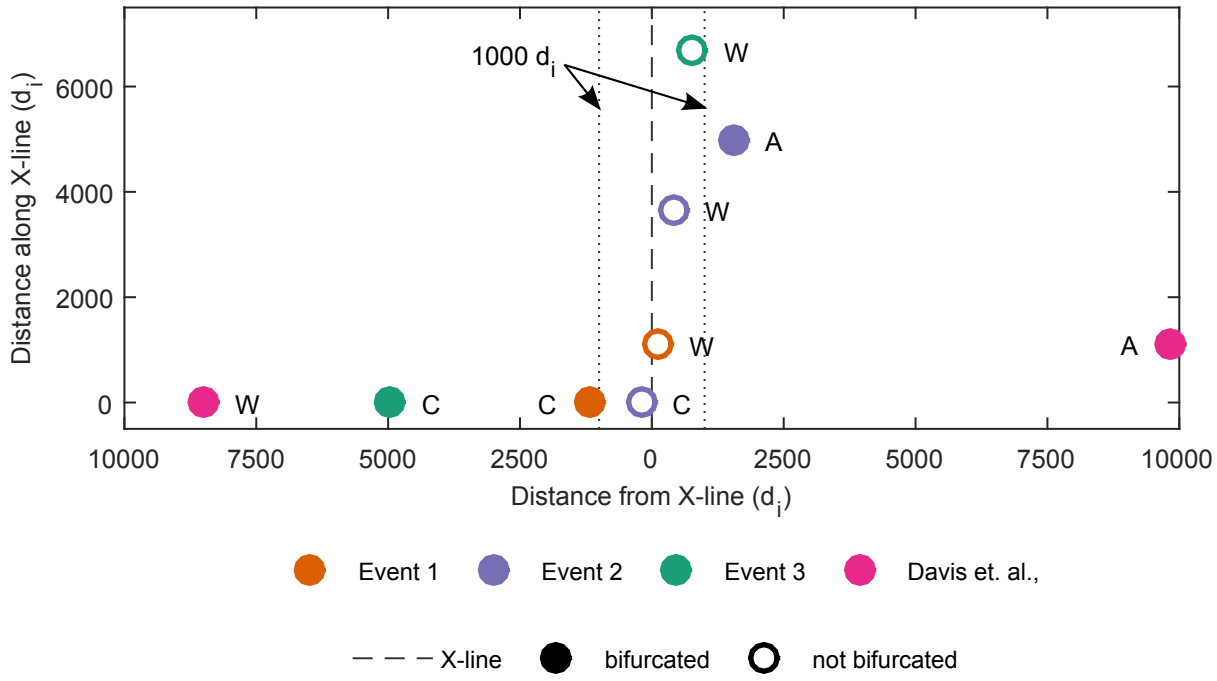


Figure 4.5: Spacecraft's estimated distance from the X-line along L (x-axis) and separation along the X-line from other spacecraft that observed the same event (y-axis). The Davis *et al.* (2006) event is also shown. Cluster (C) (and Wind (W) for Davis *et al.* (2006) event only) are shown on the left of the X-line. Spacecraft on the opposing side of the X-line are placed on the right hand side. Solid circles indicate observations of clearly bifurcated current sheets.

4.4.1 Normal component of the magnetic field

The reconnection rate is equal to the ratio of the normal component of the magnetic field (B_N) to the reconnection component (B_L) (Section 1.1.1). Within the solar wind B_L is easily measured in the inflow regions, and is often relatively constant (see, for example, Figure 4.3(b) where B_L is constant on either side of the exhaust at both C-1 and Wind). The magnetic field magnitude, however, is typically of the order 10 nT, which is much smaller than at the magnetopause or magnetotail. B_N is therefore very small within solar wind reconnection exhausts, and difficult to measure (whereas B_N has been more successfully measured at the magnetopause (Sonnerup *et al.*, 1981)). Furthermore, the value of B_N is very sensitive to the coordinate system used. The minimum and intermediate variance directions are often unreliably determined from MVA (as discussed in Section 2.4), and B_N estimates are consequently unreliable. Hybrid-MVA defines the current sheet normal as the cross product of the magnetic field vectors on either side of the exhaust, and therefore forces the normal component of the field to be zero. Estimating the normal component in such a coordinate system is therefore not possible, and other methods are usually used to estimate the reconnection rate at solar wind exhausts such as using the normal component of the inflow velocity (e.g., Davis *et al.*, 2006; Phan *et al.*, 2006).

4.4.2 Normal component of inflow velocity

The reconnection rate is also equal to the velocity of plasma flowing into the exhaust divided by the Alfvén velocity in the inflow region (Section 1.1.1). For these events the N directions are defined to point sunward. Since the exhausts move in the anti-sunward direction with the solar wind, V_N is negative. Plasma flows into the exhaust from both inflow regions, which should cause a decrease in V_N as a spacecraft intercepts the exhaust, as illustrated in Figure 4.6. Such a change in the ion velocity has been measured in previous solar wind observations and used to estimate the reconnection rate (Davis *et al.*, 2006; Phan *et al.*, 2006). In most observations, however, this measurement is difficult to make as the change in V_N (i.e., ΔV_N) is very small and therefore very sensitive to the coordinate system used.

For Event 3, C-1 observes a decrease in V_N of 4.6 km s^{-1} across the reconnection exhaust, indicated by horizontal bars in Figure 4.3(g). This corresponds to a plasma inflow velocity of 2.3 km s^{-1}. The L component of the Alfvén speed in the inflow region is 29.6 km s^{-1}, giving a reconnection rate of 0.08. This agrees with the measurements of the reconnection rate from the macroscale geometry (0.07) in Section 4.3. For this same event there is no measurable change in V_N across the reconnection exhaust at Wind, and we are unable to determine the reconnection rate from Wind using this method. For Events 1 and 3 we are also unable to measure a change in V_N at any of the spacecraft.

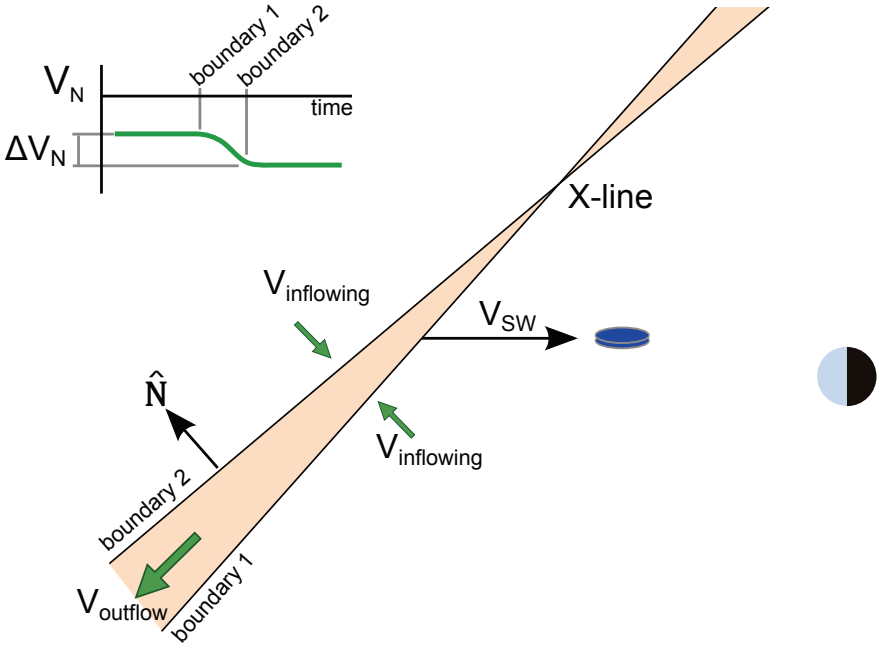


Figure 4.6: A spacecraft should measure a change in the normal component of the velocity of ΔV_N (due to plasma flowing into the exhaust from the inflow regions ($V_{inflowing}$)) as the exhaust propagates over the spacecraft with the solar wind. Earth is shown to the right and the N direction (which is defined to be sunward) is shown.

4.4.3 Cluster multi-spacecraft timing analysis

The events presented in this chapter were observed by all four Cluster spacecraft. The two sudden changes in magnetic field across bifurcated current sheets can be treated as distinct planar discontinuities, and we can therefore apply four point multi-spacecraft timing analysis to the Cluster measurements to determine the normal of each discontinuity. The discontinuities are expected to converge at the X-line (see Figure 4.6), and their angular difference corresponds to the exhaust opening angle.

To estimate the uncertainty in the normal direction and our estimate of θ, we developed a Monte Carlo approach to timing analysis. A time interval during which each Cluster spacecraft crossed one of the discontinuities was identified. For each of the four spacecraft, a time was randomly selected from each spacecraft's identified interval, and timing analysis was performed using these four time stamps to calculate a boundary normal. This process was repeated 1000 times.

Time intervals selected for Event 1 are shown in Figure 4.7. In Figure 4.8, we show (for both boundaries) each normal vector generated from the Monte Carlo method, their mean, and the vector determined from hybrid-MVA applied to C-1 using the same time

interval. The normal calculated from 1000 vectors for the first boundary crossing has a larger standard deviation than that of the second crossing because it occurs over a longer interval. Using the mean and standard deviation for both boundaries, we find that $\theta = 2.4 \pm 12.1°$. The discontinuity normals are such that the exhaust boundaries converge in the $-L$ direction relative to Cluster's location, which is in the direction of the X-line location, as expected. This measurement has a large uncertainty because the identified interval at each spacecraft ($\sim$ 4 s) is not significantly smaller than the delay between observations at each spacecraft ($\sim$38 s). The uncertainty in θ is significantly larger than the mean value, indicating that the measurement is unreliable.

Time intervals selected for Event 3 are shown in Figure 4.9 and the normal vectors generated for each boundary are shown in Figure 4.10. We find that $\theta = 10.6 \pm 5.6°$. The uncertainty in the measurement is lower than for Event 1 as the identified interval at each spacecraft ($\sim$2 s) is significantly smaller than the delay between observations at each spacecraft ($\sim$120 s). This can be seen in Figures 4.7 and 4.9 which both span a 4 minute interval (for both events inter-spacecraft separations were $\sim$10,000 km). The boundary normals, however, are such that they converge in the $+L$ direction relative to Cluster's location. This is in the opposite direction to the X-line location, therefore the identified boundary normals are inconsistent with the macroscale reconnection geometry. This local measure is therefore unable to reliably estimate the exhaust opening angle which is a macroscale property. Additionally, the direction in which the boundaries converge differs from the expected direction of the X-line, despite the fact that the uncertainty on θ is less than the value of θ itself. This may indicate that the exhaust has non-planar structure, which is investigated in detail for a different event in Chapter 6.

Our inability to estimate the reconnection rate using local measurements of the normal component of the magnetic field, inflow velocity and multi-spacecraft timing analysis suggests that the reconnection rate may be more reliably determined from the macroscale geometry using spacecraft on opposite sides of the X-line, as per Section 4.3, rather than local measurements which may have considerable uncertainty. Additionally, such local measurements may be affected by local small scale structure of the reconnection exhaust, such as that presented in Chapter 6.

4.5 Discussion

In all three events presented in this chapter, despite observing the same reconnection event, different spacecraft observe characteristically different magnetic field profiles. Specifically, in each event the spacecraft located furthest from the reconnection site observe fully developed bifurcations of the current sheet, while those closer to the reconnection site do

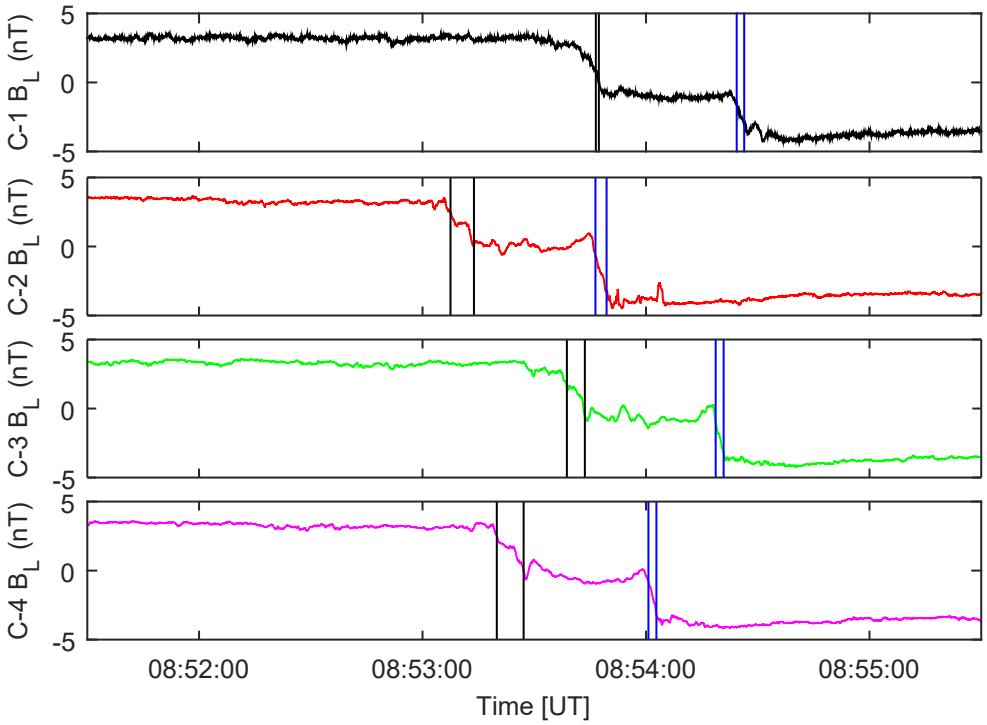


Figure 4.7: Cluster measurements of B_L for Event 1 during a 4 minute interval. Time intervals used for timing analysis are marked in black for the first discontinuity and blue for the second discontinuity.

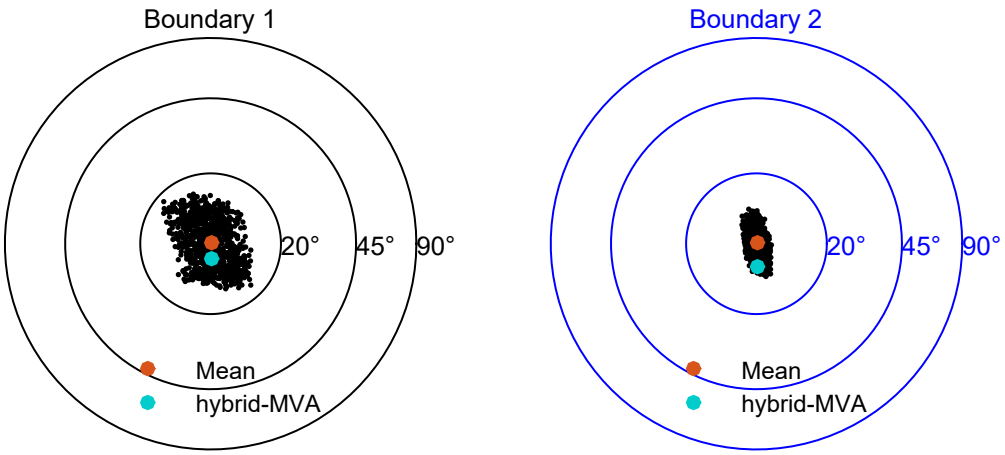


Figure 4.8: 1000 normal vectors generated from multi-spacecraft timing analysis for Event 1, in a plane perpendicular to the mean vector. 90°, 45°, and 20° differences from the mean vector are marked. The normal vector determined from hybrid-MVA applied to C-1 is also shown.

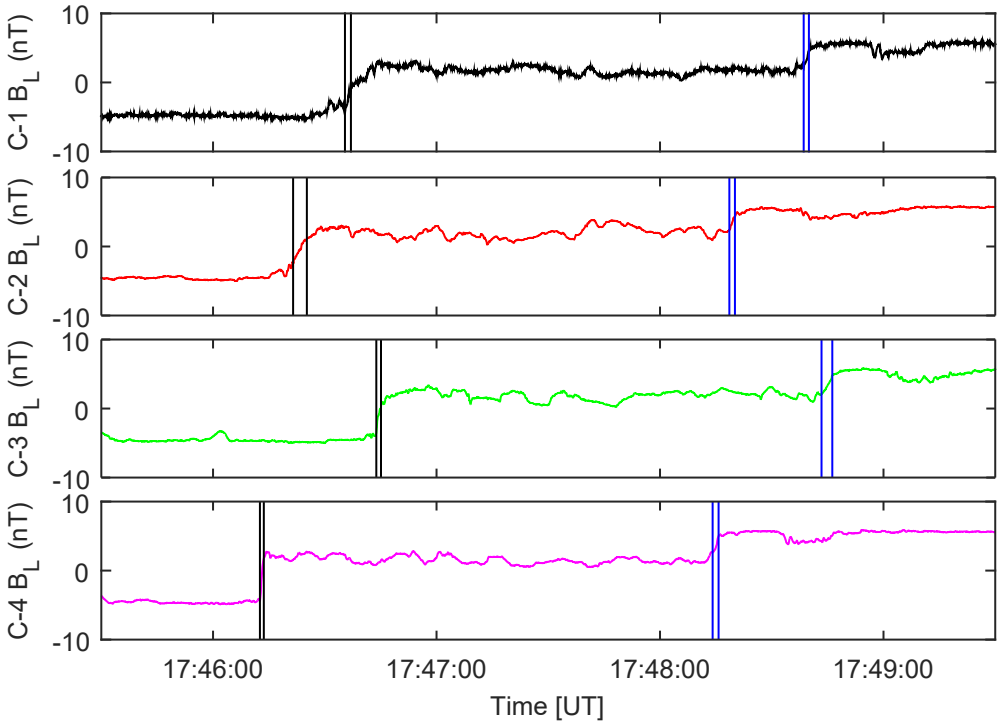


Figure 4.9: Cluster measurements of B_L for Event 3 during a 4 minute interval. Time intervals used for timing analysis are marked in black for the first discontinuity and blue for the second discontinuity.

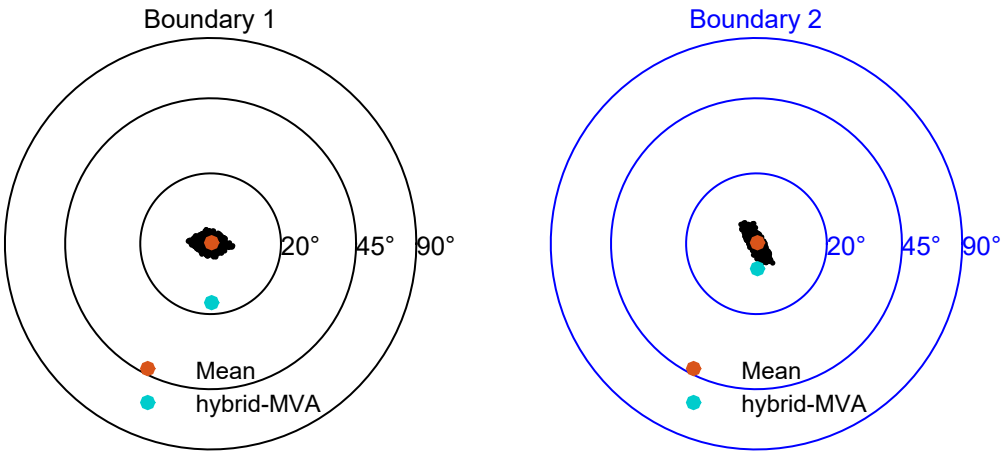


Figure 4.10: 1000 normal vectors generated from multi-spacecraft timing analysis for Event 3, in a plane perpendicular to the mean vector. 90°, 45°, and 20° differences from the mean vector are marked. The normal vector determined from hybrid-MVA applied to C-1 is also shown.

not. This indicates that bifurcations of reconnection current sheets form with increasing distance from the X-line, and become more developed further downstream. Davis *et al.* (2006) studied an event where ACE and Wind were located on opposite sides of the X-line. Using measurements of the inflow velocity of the plasma (as in Section 4.4.2), Davis *et al.* (2006) estimated that Wind was 8,500 d_i from the X-line (with ACE located at a similar distance on the opposing side of the X-line) and that $\theta = 3.7°$. Using the method in Section 4.3, we estimate that Wind and ACE were 12,900 d_i and 9,400 d_i downstream of the X-line, respectively, and that $\theta = 2.7°$, which is largely consistent with the estimates made by Davis *et al.* (2006). Both spacecraft observed a bifurcated current sheet (data are shown in Figure 5.9) and were significantly further downstream of the X-line than the spacecraft in the present study (maximum of 4,958 d_i). The fact that ACE and Wind observed bifurcated current sheets at such large distances from the X-line is consistent with our results, as shown in Figure 4.5.

The Petschek model of reconnection has slow shocks located at the exhaust boundaries and a bifurcated current sheet. Slow shocks should increase the plasma density and temperature from the inflow regions as the plasma is shocked and enters the exhaust. We do not observe ion temperature enhancements for any of the events presented in this chapter, and weak density enhancements are observed at both bifurcated reconnection current sheets (at ACE for Event 2, and at C-1 for Event 3) and non-bifurcated reconnection current sheets (at Wind for Events 1 and 3). In Section 3.5 we found that the magnitude of density and temperature enhancements actually depends on the plasma beta and guide field. Using Wind measurements of the plasma beta and guide field in the empirically derived relationship of Equation 3.6, we estimate relative increases in the thermal pressure of 1.1, 1.1 and 1.3 for Event 1, 2 and 3, respectively. It is therefore not surprising that we observe weak increases in density and no increase in ion temperature for these events. Without higher cadence plasma measurements we are unable to test whether the transitions at the boundaries of these reconnection exhausts fulfil the conditions of slow shocks.

At each event fully developed bifurcated current sheets are observed at the spacecraft furthest downstream from the reconnection site. Figure 4.5 shows the distance of each spacecraft from the X-line, and whether or not that spacecraft observed a bifurcated current sheet. All observations beyond 1,000 d_i have fully developed bifurcations, while those at less than 1,000 d_i do not.

In the magnetotail, a distance of 1,000 d_i corresponds to $50 - 160$ R_E for a plasma density of $0.05 - 0.5$ cm^{-3} (typical of the lobes). This suggests that fully developed bifurcations of large-scale exhausts should not develop in the near-Earth magnetotail, as spacecraft would be well within 1,000 d_i of the X-line. Spacecraft in the mid/deep-magnetotail, however, may be sufficiently far from the X-line to observe bifurcated reconnection current sheets.

Interestingly, most reports of slow shocks in the magnetotail are from ISEE-3 and Geotail observations where the spacecraft were located in the mid/deep magnetotail (e.g., Feldman *et al.*, 1985; Saito *et al.*, 1995; Smith *et al.*, 1984). It is possible that these were associated with current sheet bifurcations (which may therefore agree with the result that bifurcations are expected at distances greater than 1000 d_i downstream). The current sheet structure could not be examined with these observations, however, due to the variable and slow motion of the spacecraft relative to the magnetotail current sheet.

The reconnection exhausts studied in this chapter have guide fields of $0.3 \leq B_G \leq 1.8$ and $\beta \sim 1$. Magnetotail reconnection, however, typically has near anti-parallel magnetic fields ($B_G \lesssim 0.3$) and low plasma beta ($\beta \lesssim 0.1$). The reconnection current sheet has been shown to bifurcate in a 2.5D PIC simulation with $B_G = 0.3$ and $\beta = 0.2$ (Innocenti *et al.*, 2015). Conversely, in a purely anti-parallel reconnection simulation with the same β the current sheet did not bifurcate (Liu *et al.*, 2012). The effects of plasma inflow region parameters such as B_G and β on bifurcations of reconnection current sheets and the distance downstream at which this occurs are not known, and it is possible that the distance at which bifurcations become fully developed may differ between the solar wind and other space plasmas. Furthermore, the effects of unrealistic mass ratios and plasma temperatures are not known. The effects of these parameters on the development of bifurcations of reconnection current sheets may be best addressed with more extensive simulation studies across a wide region of parameter space.

4.6 Conclusions

In this chapter a new multi-spacecraft technique has been used to determine spacecraft's distance downstream of the X-line. Additionally, the reconnection rate was estimated for each event, and these rates were found to be consistent with expected reconnection rates for collisionless reconnection ($\sim$0.1). Estimates of the reconnection rate from local measurements were found to be unreliable, demonstrating that the reconnection rate and geometry can be better measured using macroscale observations.

More importantly, we have used this multi-spacecraft technique to experimentally show, for the first time, that reconnection current sheets become bifurcated with increasing distance downstream of the X-line, which is consistent with expectations from hybrid simulations (Krauss-Varban & Omidi, 1995; Lin & Swift, 1996) and a large-scale guide field PIC simulation (Innocenti *et al.*, 2015). Collisionless reconnection can therefore produce bifurcated current sheets, but only far downstream of the X-line where the back-to-back exhaust boundaries are likely to be well separated. The variability of density and temperature enhancements between different events was explained in Chapter 3, and the results

of this chapter further contribute to our understanding of the differences between different reconnection exhausts by showing that whether or not reconnection current sheets are observed as bifurcated is a function of the distance downstream of the X-line at which they are observed.

The effects of inflow region plasma properties (e.g., B_G, β, T) on whether or not the current sheet bifurcates and the distance downstream of the X-line at which this occurs are not known. These effects would be better addressed with large-scale simulations. It should be noted that current PIC simulations are only able to extend to a few hundred d_i downstream due to computational constraints. It is possible that for certain inflow region parameters this is not sufficiently far downstream for bifurcations to become well developed, which presents a challenge for simulations.

5 Hall physics far downstream of the X-line

Material in this chapter has been published in *Physical Review Letters* in Mistry *et al.* (2016).

5.1 Introduction

In Chapter 3 we used a set of 188 solar wind reconnection exhausts to investigate the average properties of reconnection exhausts far downstream of the X-line. These events show that the out-of-plane magnetic field increases within the exhaust region, which is also evident in one dimensional simulations with a guide field, where rotational discontinuities form at the exhaust boundaries (Lin *et al.*, 1995; Lin & Swift, 1996).

In collisionless plasmas the reconnection regions are not composed of fluid structures everywhere, and one dimensional descriptions become inadequate. These two factors are perhaps most important at the diffusion region, where reconnection occurs on kinetic scales. The diffusion region takes on a two-scale structure for proton-electron plasmas (Sonnerup, 1979). In the small inner electron diffusion region, ions and electrons decouple from the magnetic field because the field changes over smaller scales than the particles' gyro-orbits. Outside of this is the larger ion diffusion region where the field no longer varies on the electron scale. Electrons therefore gyrate around the field whilst the ions remain decoupled from the field. This results in differential motion between the de-coupled ions and magnetised electrons which produces an in-plane Hall current system in the two dimensional ion diffusion region. Associated with this is a Hall electric field (Sonnerup, 1979; Terasawa, 1983) and an out-of-plane Hall magnetic field which takes on a quadrupolar structure for symmetric inflow conditions with zero guide field (Figure 5.1(a)) (Mandt *et al.*, 1994; Hesse *et al.*, 2001).

Reconnection at the magnetotail generally occurs between symmetric plasmas and anti-parallel magnetic fields. Out-of-plane Hall magnetic fields near the ion diffusion region have been observed in the magnetotail (e.g., Øieroset *et al.*, 2001; Runov *et al.*, 2003b; Eastwood

et al., 2007). In these cases proximity to the diffusion region was confirmed by observations of reversals of the ion exhaust outflow. A statistical study of flow reversal events at the magnetotail has also shown the full quadrupolar structure of the Hall magnetic field in ion diffusion regions (Eastwood *et al.*, 2010b).

Although the Hall magnetic field is thought to be generated from dynamics within the ion diffusion region, Hall signatures have been detected in the magnetotail where spacecraft did not observe flow reversals, indicating that the spacecraft may not have been in the immediate vicinity of the diffusion region (Nagai *et al.*, 2001; Manapat *et al.*, 2006). Furthermore, field-aligned electron flows consistent with Hall current systems have been observed along reconnection separatrices in the magnetotail (Fujimoto *et al.*, 1997; Nagai *et al.*, 2003; Manapat *et al.*, 2006). Although these observations were made at some distance from the diffusion region, the measurements do not indicate that the spacecraft would have been more than a few hundred d_i from the diffusion region.

The addition of a guide field disrupts the quadrupolar structure of the Hall magnetic field. Simulations have shown that the electron current in the ion diffusion region is deflected from the mid-plane by the $\mathbf{J} \times \mathbf{B}$ Lorentz force of the electron current and the out-of-plane guide field (Horiuchi & Sato, 1997; Huba, 2005). This deflection results in the positive Hall field occupying a greater proportion of the exhaust and having a larger magnitude than the negative Hall field (Karimabadi *et al.*, 1999; Rogers *et al.*, 2003), where positive is defined to be parallel to the guide field. This is shown in Figure 5.1(b). There have been few in-situ observations of the effects of guide fields on Hall fields in symmetric reconnection. This is because (a) the guide field in magnetotail reconnection is typically very weak, (b) plasma inflow at the magnetopause is rarely symmetric and (c) diffusion regions have not been observed in the solar wind. Despite this, with the presence of a weak guide field ($B_G = 0.2$), the Hall magnetic and electric fields in a magnetotail diffusion region have been shown to be distorted in a manner consistent with simulations (Eastwood *et al.*, 2010a).

The effects of guide fields on particle dynamics can also be seen outside of the ion diffusion region. With a guide field there is always a component of the reconnection electric field parallel to the magnetic field. This parallel electric field introduces electron motion along the field at the separatrices (Ricci *et al.*, 2004), accelerating electrons towards the diffusion region along one pair of opposing separatrices and pushing them away from the diffusion region along another pair. The parallel electric field is sustained by a density gradient (Kleva *et al.*, 1995). The electron motion produces a large current along two opposing separatrices, which extends far beyond the ion diffusion region in simulations (Pritchett, 2001; Ricci *et al.*, 2004; Drake *et al.*, 2009b; Goldman *et al.*, 2011), and an associated Hall magnetic field. Although these Hall magnetic fields appear to extend entirely along the separatrices in simulations, these simulations are limited to a few hundred d_i from the

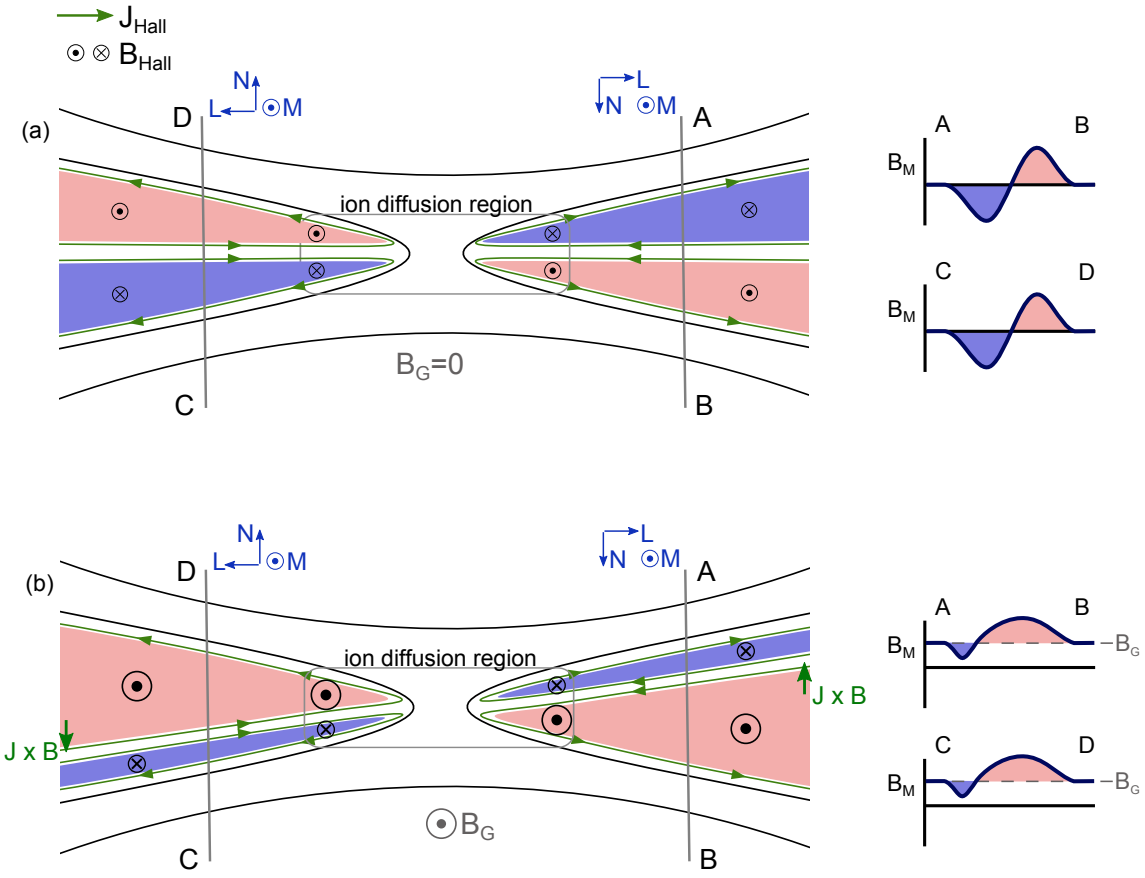


Figure 5.1: Hall magnetic fields in the ion diffusion region and how they can extend in to the exhaust in the case of (a) anti-parallel reconnection and (b) guide field reconnection. The Hall current system is shown in green. In the presence of a guide field (panel (b)) the current towards the X-line (due to electrons flowing away from the X-line) is deflected from the mid-plane by the $\mathbf{J} \times \mathbf{B}$ force. B_M along the paths AB and CD are shown on the right. The background guide field is shown in grey for (b). The directions of the in-plane magnetic field are not shown as Hall signatures are insensitive to the direction of B_L above/below the current sheet. The coordinate systems shown for AB and CD are such that L is the direction of positive exhaust outflow and M is in the direction of the out-of-plane field (i.e., $B_G > 0$).

diffusion region, and it is not known how far downstream these electron motions and Hall fields may persist. In contrast, simulations of anti-parallel reconnection show that the out-of-plane magnetic field becomes highly variable downstream of the X-line, making the Hall magnetic field difficult to observe (e.g., Hietala *et al.*, 2015; Higashimori & Hoshino, 2015).

Diffusion regions have not been observed at solar wind reconnection exhausts. This is likely to be because the diffusion region size is of the order of several d_i, whereas the exhaust regions can extend over thousands of d_i, making it far more likely for spacecraft to intercept the exhaust region far downstream. Reconnection exhausts far downstream are often described using MHD which does not include kinetic physics (e.g., Petschek, 1964; Vasyliunas, 1975). In Chapter 3 we also showed that the *average* properties of 188 reconnection exhausts are consistent with fluid descriptions of the exhaust region. Despite this, the kinetic process of ions counterstreaming along magnetic field lines has been observed far downstream of the X-line in the solar wind using ACE (Gosling *et al.*, 2005). It is therefore important to understand where non-MHD effects are important in the reconnection process, and whether MHD can sufficiently capture the physics of the exhaust region.

Given that Hall fields appear to extend beyond the X-line in guide field reconnection simulations, one may expect Hall effects to be observable downstream of the X-line in solar wind exhausts. Such Hall effects have not previously been observed in the solar wind (although Hall fields have been observed at a magnetic island in the solar wind (Eriksson *et al.*, 2014)). If present, these effects are likely to be most evident in the Hall magnetic field as the cadence of solar wind particle measurements are too low to be able to measure effects associated with particle dynamics at exhaust boundaries.

In this chapter we seek to identify whether Hall magnetic fields are present and observable in solar wind reconnection exhausts. We survey the 188 reconnection exhausts used in Chapter 3 for Hall magnetic field signatures. Although there are a large number of events where the presence of these signatures is ambiguous, we find 8 events with clear bipolar perturbations to the out-of-plane magnetic field. One of these events is sufficiently close to the X-line to compare the observations with a numerical simulation. An appropriately-scaled two-dimensional fully kinetic PIC simulation shows that the observed signatures are consistent with Hall magnetic fields generated downstream of the X-line. Furthermore, for one of these events Wind was located $\sim$9,000 d_i downstream of the X-line, indicating that Hall signatures and kinetic processes can persist extremely far downstream and well into regimes where the exhaust has previously been described using MHD.

5.2 Identification of Hall magnetic fields

In order to identify Hall magnetic fields in the data set we use LMN coordinate systems for each event, determined from hybrid-MVA analysis of magnetic field data within the exhaust region (see Section 3.3). The LMN coordinates are defined such that the exhaust outflow is in $+L$, and M is such that $B_G > 0$ (as per Figure 5.1). In the solar wind observations are made as a spacecraft rapidly traverses the exhaust region. Time series measurements therefore correspond to spatial cuts across the reconnection exhaust. Observationally, in the case of zero guide field, one would expect to observe a bipolar perturbation to B_M within the exhaust region, with $B_M = 0$ outside of the exhaust region. In the coordinates we use, this bipolar perturbation is expected to be negative and then positive in the direction of increasing N (Figure 5.1). With a guide field, one would expect a bipolar perturbation to B_M where the increase in B_M due to the Hall field is larger in magnitude than the decrease in B_M (Karimabadi *et al.*, 1999; Rogers *et al.*, 2003). Additionally, the increase is expected to be longer in duration than the decrease as the Hall current is shifted from the mid-plane (Figure 5.1(b)). These perturbations will be on top of a background out-of-plane guide field.

To identify Hall magnetic fields within this data set we sought to identify bipolar perturbations to B_M within the exhaust region. We did not impose requirements on the magnitude of these changes or their duration within the exhaust region. The data often show considerable variations in the observations and it is often difficult to determine whether a perturbation to the out-of-plane magnetic field is consistent with a Hall field, and to justify the perturbation as being bipolar. As an example, we show an event in Figure 5.2 where there is clearly no bipolar perturbation to B_M. Within the exhaust region B_M shows a unipolar increase, which is consistent with findings from the superposed epoch analysis in Chapter 3. In another event (Figure 5.3) B_M increases in the exhaust region, and there is a small decrease in B_M below the inflow region value towards the end of the exhaust. This suggests a bipolar perturbation to B_M, however there is also a small decrease in B_M towards the beginning of the exhaust interval. The presence of a bipolar perturbation to B_M is therefore ambiguous and we do not categorise this event as having an unambiguous bipolar signature in B_M.

We also do not consider events where differences in V_L between the inflow regions exceeds 75% of the exhaust outflow speed. This is because a high velocity shear can affect the current sheet structure, making bipolar perturbations to B_M difficult to determine. From the 188 Wind events considered, we identify 8 events with unambiguous bipolar perturbations to B_M within the exhaust region. These are presented in Section 5.4. In this process we did not impose any requirements on the polarity of the perturbation i.e., whether B_M decreases and then increases with increasing distance along N (consistent with the polarity

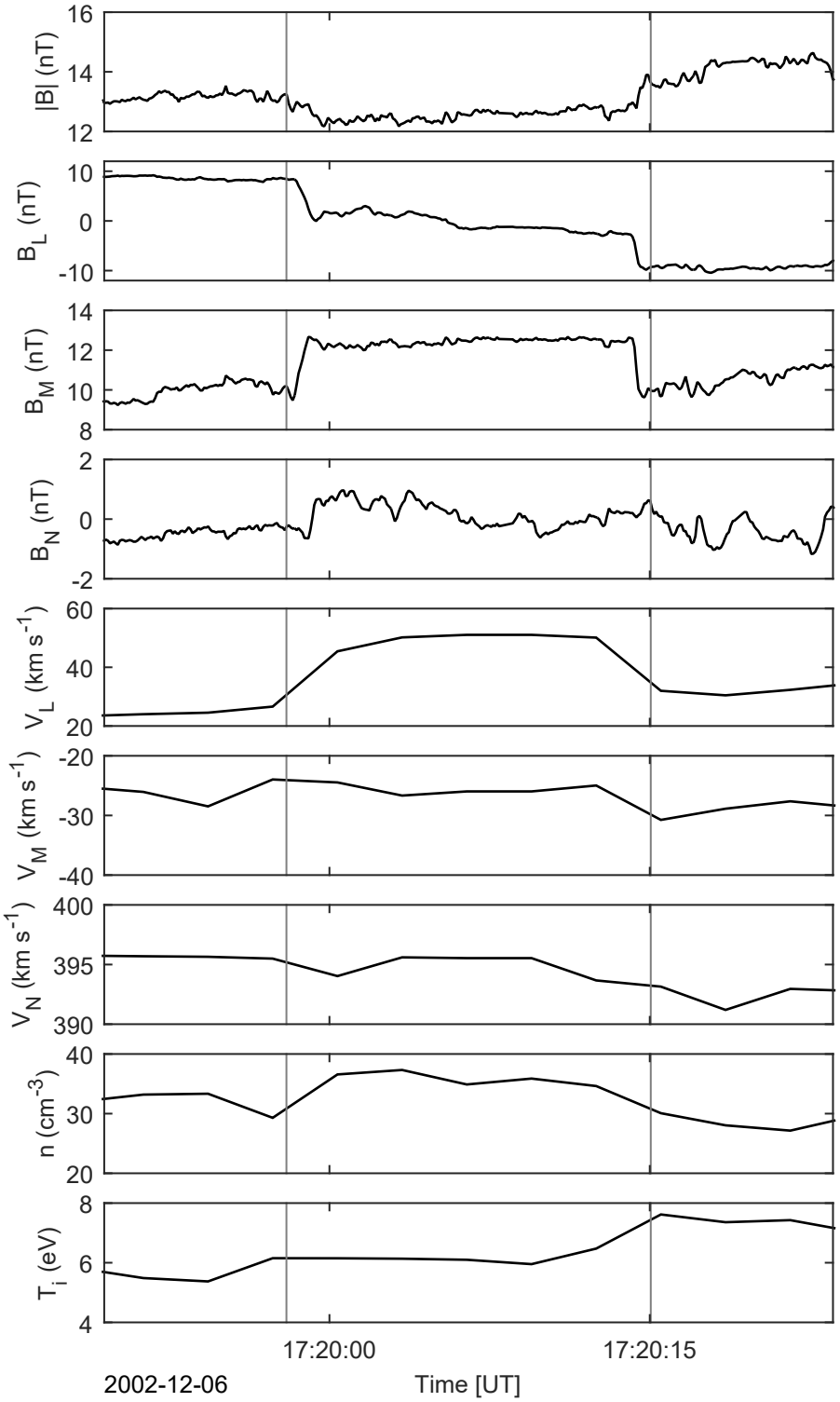


Figure 5.2: An event with a clear unipolar increase in B_M within the exhaust region. The exhaust region is indicated by vertical lines.

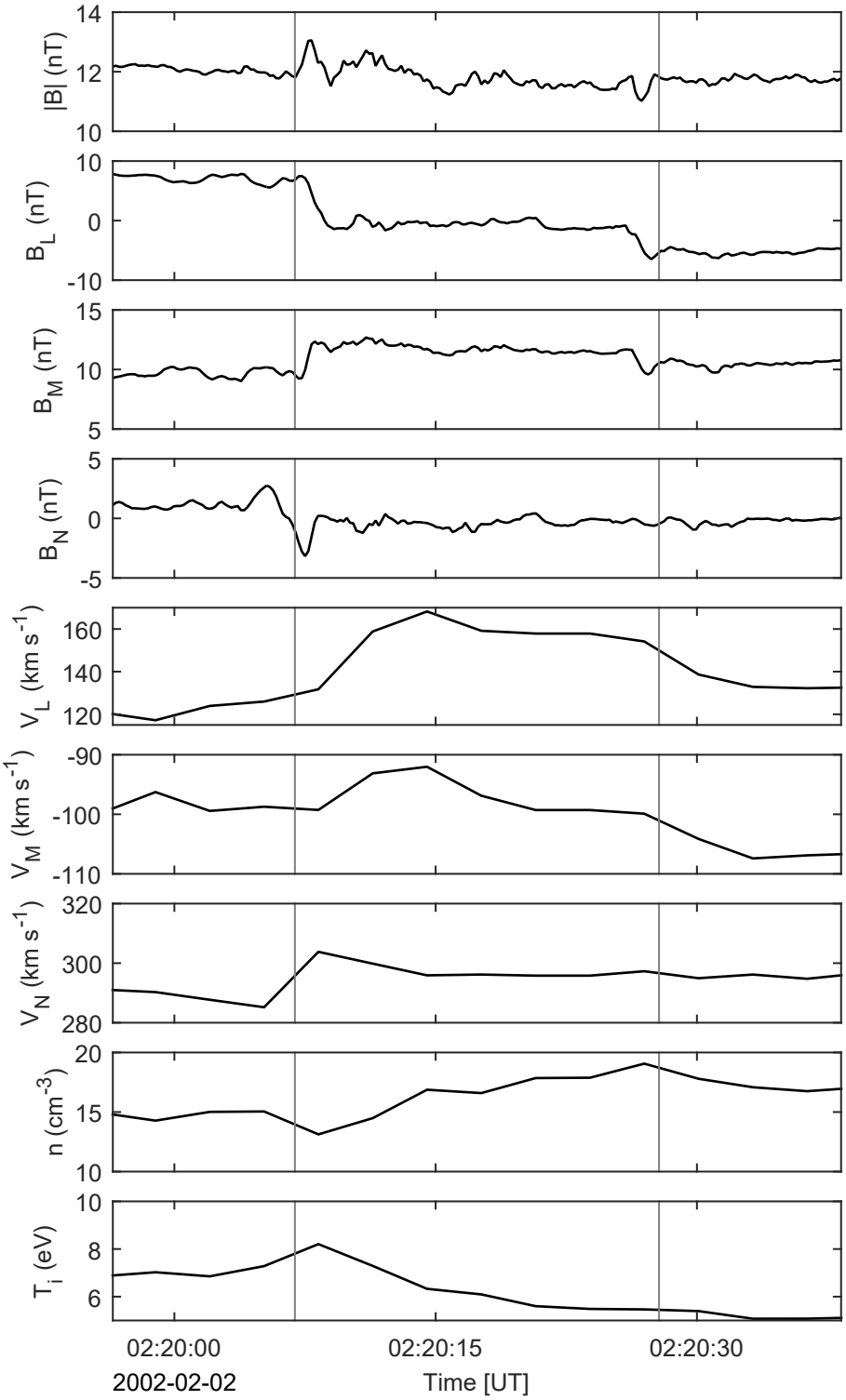


Figure 5.3: An event with multiple changes in B_M within the exhaust region. The exhaust region is indicated by vertical lines.

of Hall fields) or whether B_M increases and then decreases with increasing distance in N (inconsistent with the polarity of Hall fields). Despite this, for all 8 events the polarity of the perturbation was consistent with the presence of Hall fields. One of these events is presented in detail and compared to a fully kinetic PIC simulation in Section 5.3. The 8 identified events are presented in Section 5.4, and in Section 5.5 we use measurements from ACE and Wind to reveal Hall fields on both sides of the X-line for one of these events.

5.3 Comparison of observed data and a PIC simulation

In order to verify whether the observed signatures were consistent with Hall magnetic fields and to better explain the observations, we compare the observed data to a reconnection simulation. The self-generated temperature anisotropy at the boundaries of reconnection exhausts has been shown to affect the exhaust structure (Karimabadi *et al.*, 1995; Liu *et al.*, 2011). Plasma in Hall-MHD simulations have isotropic temperatures, and as such Hall magnetic fields within reconnection exhausts are not well reproduced by Hall-MHD simulations (e.g., Shay *et al.*, 2004). We therefore use a kinetic simulation which is better able to reproduce the structure of reconnection exhausts.

The minimum exhaust width of the 8 events for which we identify bipolar perturbations to B_M is 25 d_i (Event 1), and the next smallest width is 80 d_i (Event 2). For a canonical reconnection rate of 0.1, this would place the spacecraft at 125 d_i and 400 d_i downstream of the X-line, respectively. To compare the observations to a simulation, a cut should be made across the simulation at a similar distance downstream of the X-line as where the spacecraft intercepted the exhaust. Kinetic simulations are currently unable to simulate distances of 400 d_i downstream of the X-line due to computational constraints. It is possible to simulate distances of $\sim$125 d_i downstream of the X-line, and we therefore are able to compare Event 1 with a numerical simulation to better understand the observed signatures.

Figure 5.4 shows observations from Event 1 in black. The data are plotted as a function of time (top axis) and distance through the reconnection exhaust in the N direction (bottom axis), calculated as $(\mathbf{V_{SW}} \cdot \hat{\mathbf{N}})\delta t$, where δt is the time between the observations and when the spacecraft crossed the first exhaust boundary. The rotation in B_L (panel (b)) indicates the current sheet, which is accompanied by an exhaust (panel (f)). B_M has a bipolar perturbation within the exhaust region; B_M first decreases (shaded blue) and then increases (red) relative to its value in the inflow regions. In the inflow regions B_M is 1.3 times B_L i.e., $B_G = 1.3$. With increasing N, B_M decreases and then increases, indicating that the polarity of the bipolar signature is consistent with Hall magnetic fields. Furthermore, the increase in B_M is larger in duration and magnitude than the decrease, which is qualitatively consistent with the distortion of the quadrupole structure of the Hall field in symmetric

reconnection reported in guide field simulations (Huba, 2005; Eastwood *et al.*, 2010a).

We compare these observations to a kinetic PIC simulation run using the P3D code (Zeiler *et al.*, 2002). Particles have two dimensions in real space and three dimensions in velocity space. Both electrons and ions are treated as particles. In the simulation the magnetic field strength and density are normalised to inflow region values, which we denote as $|B_0|$ and n_0, respectively. Lengths are normalised to the ion inertial length d_i based on n_0. Velocities are normalised to the Alfvén speed based on $|B_0|$ and n_0. Simulations are performed in a periodic domain with a system size of $\mathrm{S_L} \times \mathrm{S_N} = 366.4\ d_i \times 183.2\ d_i$. The system was initialised with 100 particles per grid in the inflow region and with two Harris current sheets superimposed on an ambient population. The ion to electron mass ratio is 25.

The inflow region plasma parameters were chosen to match Wind observations of the inflow region. The guide field was $B_G = 1.3$, $\beta_i = 1.15$ and $\beta_e = 1.68$. The simulation coordinate system is the same as that used for the observations. This simulation was run by C. C. Haggerty and M. A. Shay (University of Delaware), who provided outputs of the simulation. I have performed analyses of these outputs, which are presented in this section.

We show results from one of the two current sheets in the simulation at a time when reconnection reached a steady state (57 ion gyroperiods). At this time there is a single dominant X-line located at the origin. The ion velocity shows the oppositely directed exhausts which extend away from the reconnection X-line (Figure 5.5(a)). Due to the periodic boundary conditions a large island forms where the two exhaust outflows meet. Additionally, small islands form at earlier times as a result of how reconnection is initiated in the simulation. Remnants of these can be seen in the exhaust at $L < 0$. The exhaust at $L > 0$ does not show these islands and we use this side of the exhaust for comparisons with observations. Figure 5.5(b) shows B_L which is positive at $N < 0$ and negative at $N > 0$. Magnetic field lines are also shown which indicate the large and small islands. Figure 5.5(c) shows B_M. Relative to the inflow regions, B_M is increased within the majority of the exhaust. Distinct regions of decreased B_M can be seen (in blue) along two opposing separatrices (at $N < 0$ for $L > 0$ and at $N > 0$ for $L < 0$, ignoring the regions near the large island), which is in agreement with the Hall fields depicted in Figure 5.1(b).

In order to quantitatively compare the observations to the simulation we take a cut across the simulation domain at a point where the simulation exhaust width is equal to the exhaust width measured by Wind. This is a cut along N at $L = 80\ d_i$ (vertical line in Figure 5.5). At this location the reconnection exhaust does not appear to be affected by the magnetic island downstream of it (i.e., the cut shows similar structure to cuts taken closer to the X-line). Data from the simulation is converted to real units and shown alongside Wind observations in Figure 5.4. There is a shear in V_L across the exhaust in the observations

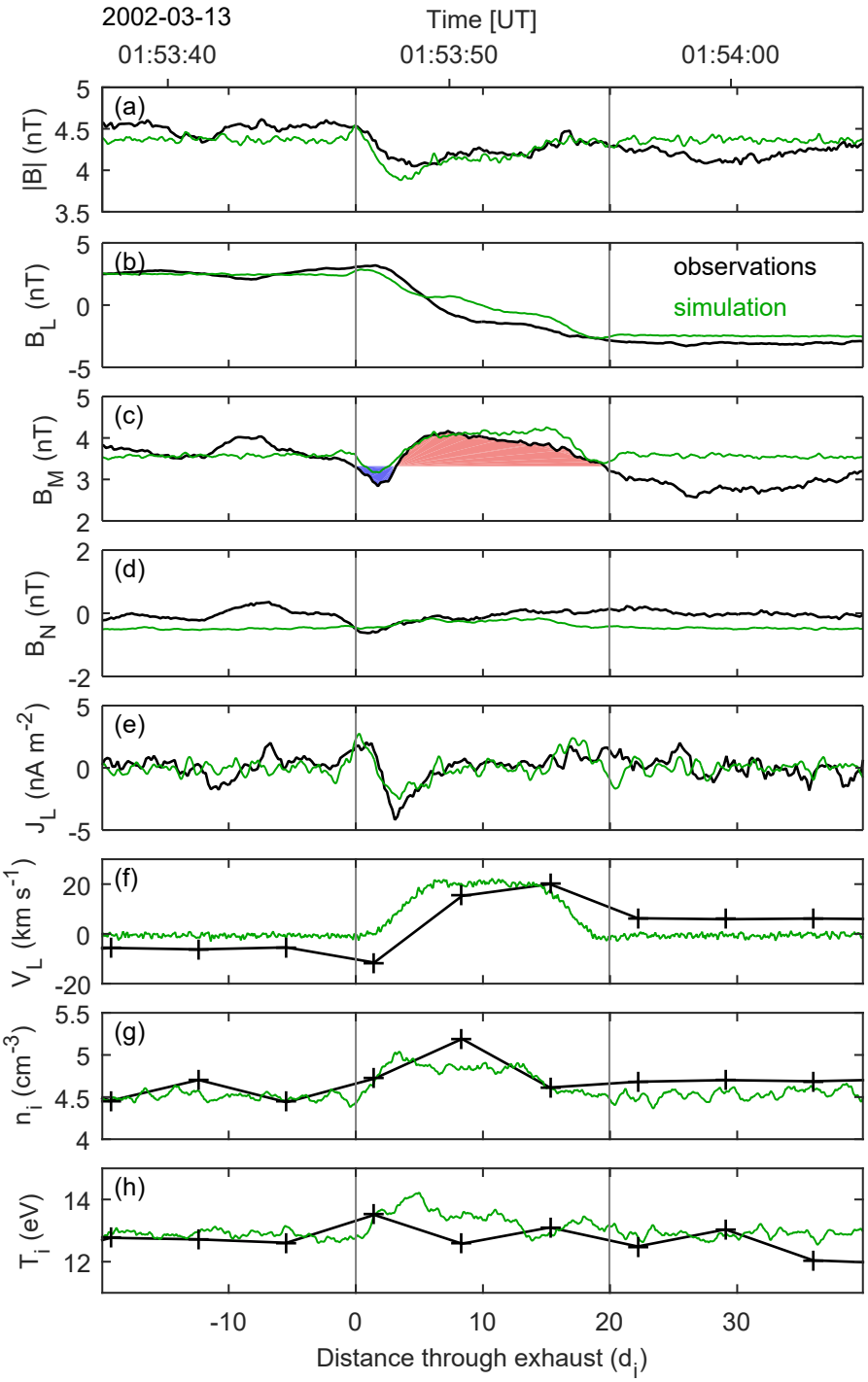


Figure 5.4: Observations are shown in black and simulation data from a cut at $L = 80$ d_i are shown in green. Panels show (a) magnetic field magnitude, (b-d) magnetic field components, (e) L component of the current density (calculated as $J_L = -(\partial B_M/\partial N)/\mu_0$ for observed data), (f) L component of the ion velocity (observed data has been offset by -274 km s^{-1}), (g) ion density and (h) ion temperature. Positive and negative perturbations to B_M within the exhaust region are shaded in blue and red, respectively. Times of observations are indicated at the top. Vertical lines mark the exhaust region.

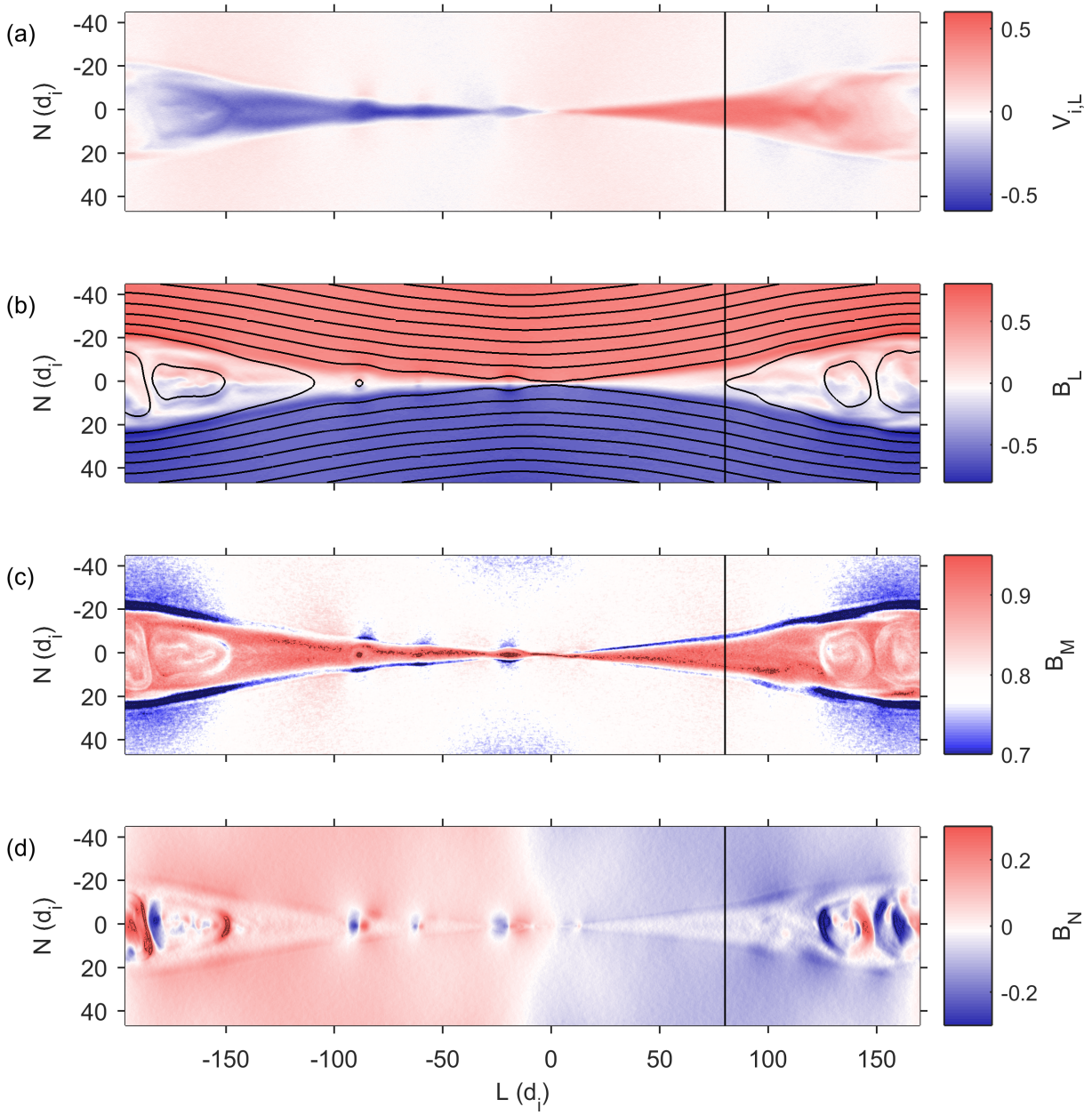


Figure 5.5: 2D plots of PIC simulation at a time of 57 ion gyroperiods. (a) $V_{i,L}$, (b) B_L (c) B_M, (d) B_N.The X-line is located at the origin and results are shown in simulation units. Magnetic field lines are shown in (a). The cut at $L = 80\ d_i$ is indicated in black.

which is not included in the simulation. Despite this, we find excellent agreement between the simulated and observed data across all measured quantities. Most importantly, there is excellent agreement between the simulated and observed out-of-plane magnetic field, indicating that the observed out-of-plane magnetic field is consistent with the Hall field generated in the simulation. The width of the exhaust increases with distance from the X-line, making it difficult to compare cuts at other locations to the observations. We therefore compare magnetic field hodograms from cuts at $25 \leq L \leq 110$ d_i at 5 d_i intervals to the observed data in Figure 5.6. There is excellent agreement in magnetic structure at all cut locations.

The B_M Hall magnetic field is associated with a J_L Hall current density. L components of the ion and electron velocities at $L = 80$ d_i are shown in Figure 5.7(a). $V_{i,L}$ is positive throughout the exhaust region. $V_{e,L}$, however, is negative at $-11 < N < -9$. Since $V_{i,L} > V_{e,L}$, the J_L current density is positive. This causes a decrease in B_M which generates the negative Hall magnetic field (Figure 5.7(b)). In this region the electron velocity is almost anti-parallel to the magnetic field, corresponding to electron flow towards the X-line.

At $-8 < N < 9$ the electron velocity is shifted in the $-N$ direction relative to the ion velocity (Figure 5.7(a)), which also affects J_L and B_M. At $-8 < N < 4$ this causes the electron velocity to exceed the ion velocity, resulting in $J_L < 0$. B_M therefore increases in this region from its minima ($B_M \sim 0.7$) to $B_M \sim 0.9$ (simulation units). At $5 < N < 8$ the shift in electron and ion velocities causes the ion velocity to exceed the electron velocity, resulting in $J_L > 0$. B_M therefore decreases to its value in the inflow regions. Between these two regions the electron and ion velocities are approximately equal, and B_M does not change significantly. The Hall magnetic fields are therefore generated by current systems associated with an electron flow towards the X-line at one separatrix (shown in Figure 5.1(b)), as well as a relative shift between the ion and electron outflows in the N direction.

In the ion diffusion region the electron current is shifted in the presence of a guide field by a Lorentz force (e.g., Huba, 2005; Eastwood *et al.*, 2010a). The shift of the electron velocity in the $-N$ direction with respect to the ion velocity in our simulation is qualitatively consistent with this, and indicates that the electron current remains significantly deflected from the mid-plane far downstream of the X-line. This deflection results in local differences in the ion and electron velocities far downstream, which generates Hall magnetic fields.

Wind ion and electron velocities cannot be resolved at sufficiently high resolution to determine J_L directly i.e., from $J_L = ne(V_{i,L} - V_{e,L})$. J_L is therefore calculated from Wind magnetic field observations. Using Ampère's Law,

$$J_L = \frac{1}{\mu_0}\left(\frac{\partial B_N}{\partial M} - \frac{\partial B_M}{\partial N}\right). \tag{5.1}$$

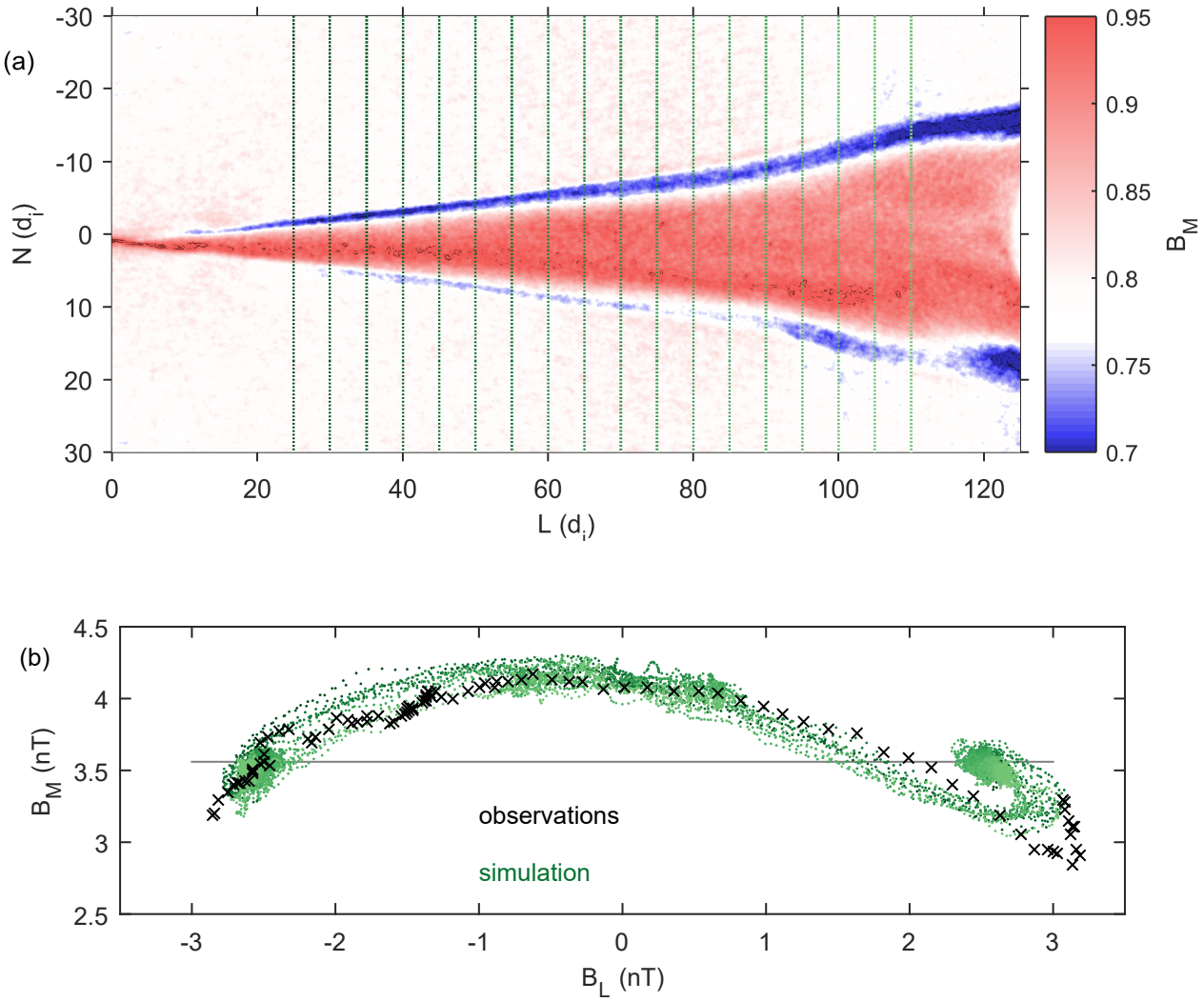


Figure 5.6: (a) B_M within the simulated exhaust for $L > 0$ (in simulation units). (b) Magnetic field hodograms from cuts at $25 \leq L \leq 110$ d_i at 5 d_i in physical units, compared to Wind observations. Lighter points are located further from the X-line and the location of each cut is shown in (a) with vertical lines.

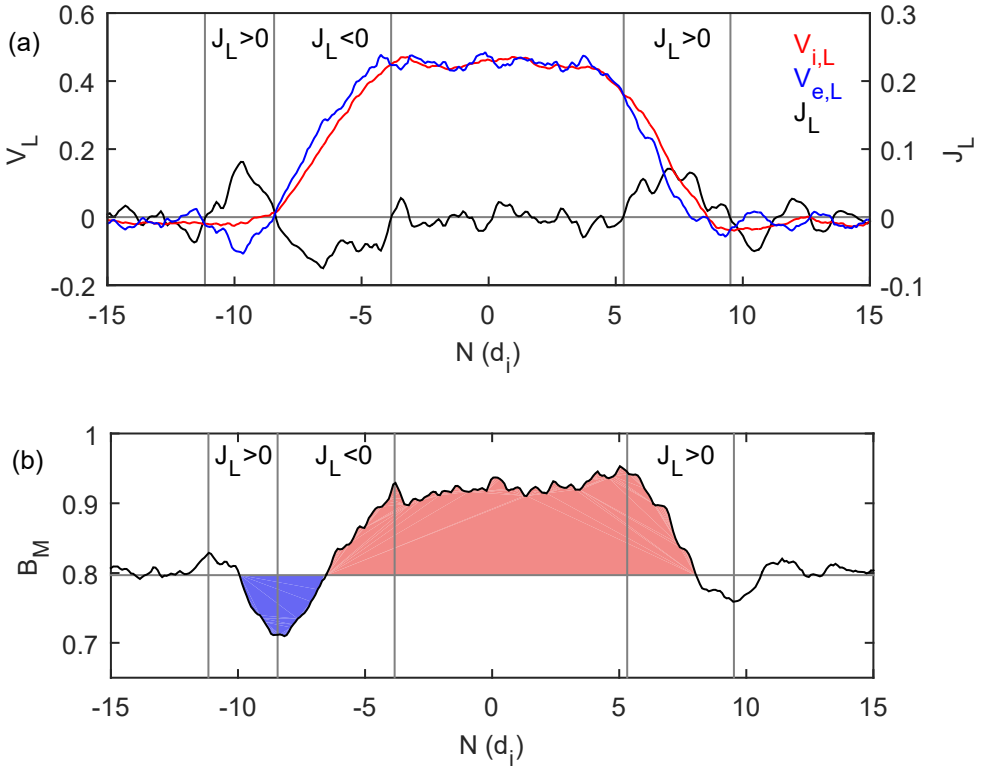


Figure 5.7: PIC simulation cuts at $L = 80\ d_i$ of (a) L components of the ion and electron velocities and L component of the current density. (b) B_M. Three regions are marked in each panel where $J_L > 0$, $J_L < 0$ and $J_L > 0$. All quantities are shown in simulation units.

Table 5.1: Width of reconnection exhaust, guide field, total β in the inflow regions and full-width-at-half-maximum of the current layer between the positive and negative Hall fields.

Event	Width (d_i)	B_G	Total β	J_L FWHM (d_i)
1	25	1.3	2.8	1.1
2	80	0.7	4.3	1.1
3	124	0.3	6.6	0.8
4	177	1.6	0.5	1.3
5	214	0.7	2.2	1.0
6	225	0.7	1.1	4.0
7	558	0.3	1.3	6.0
8	743	0.4	2.0	2.0

$B_N \sim 0$, and we can therefore calculate J_L using measurements of $\partial B_M/\partial N$. This current density shows excellent agreement with that from the simulation (Figure 5.4(e)). Furthermore, from these measurements we determine the current layer between the positive and negative Hall fields to have a full-width-at-half-maximum of 1.1 d_i and 1.3 d_i in the observations and simulations, respectively. MHD is often used to describe reconnection exhausts, however these Hall structures and narrow electron flows far downstream of the X-line indicate that MHD treatments may be unable to sufficiently describe the exhaust region and its structure.

5.4 Hall magnetic fields at 8 reconnection exhausts

We have identified a total of 8 reconnection exhausts with unambiguous bipolar perturbations in B_M. For all of these events the polarity of the perturbations was consistent with the polarity expected for Hall fields. Guide fields for the 8 events are in the range 0.3 to 1.6, whereas the range of all 188 events is 0 to 10. Further details of these events are provided in Table 5.1.

In the coordinate systems used in this chapter (where $+L$ is in the direction of positive exhaust outflow and M is such that $B_G > 0$) a spacecraft which intercepts the right hand side exhaust of Figure 5.1(b) may pass from either A to B or from B to A. In order to compare observations of the out-of-plane field we plot B_M as a function of distance through the reconnection exhaust in Figure 5.8. Events where the spacecraft motion relative to the exhaust corresponds to the path B to A in Figure 5.1(b) are plotted in reverse time (i.e., points located at large N in Figure 5.8 were measured at earlier times than points at $N = 0$) so that the plotted data corresponds to measurements from A to B for all events.

B_M shows similar features at all 8 events. The decrease in B_M is narrow and confined to

the edge of the exhaust, whilst B_M is increased throughout the remainder of the exhaust. On the right of Figure 5.8 we show the relative distance of Wind from the X-line for each event, under the assumption of a constant reconnection rate for all events. This shows that the narrow negative Hall field is observed even at very large distances downstream of the X-line, and that it remains near the exhaust boundary. From full-width-at-half-maximum measurements of J_L, we determine the current layers between the negative and positive Hall fields to have widths in the normal direction of $0.8 - 6.0\ d_i$ for these 8 events.

5.5 Observations of Hall fields on both sides of the X-line: dual spacecraft observations

In single spacecraft observations in the solar wind the Hall field is observed as a bipolar perturbation to B_M as the spacecraft crosses one of the exhausts (as shown in Figure 5.1). In order to identify the full quadrupolar structure both reconnection exhausts must be observed (e.g., Eastwood *et al.*, 2010b). In the solar wind it is very difficult to reliably estimate a spacecraft's distance from the reconnection X-line; this distance is often crudely estimated using the measured exhaust width and a canonical reconnection rate of 0.1. Observations of both reconnection exhausts can additionally provide a much more reliable estimate of the spacecraft's distance from the X-line, as shown in Section 4.3.

Event 7 was previously studied by Davis *et al.* (2006). This reconnection event was observed by both Wind and ACE. The spacecraft were located on opposite sides of the X-line and observed oppositely directed exhausts. Spacecraft measurements are overlaid in Figure 5.9 in the LMN coordinate system defined in the above analysis of Wind data. The passage of a current sheet is detected at Wind (ACE) at 09:25:36 - 09:28:47 UT (08:24:24 - 08:26:54 UT), and is accompanied by an outflow in the $+L$ ($-L$) direction.

Having identified bipolar changes in B_M in Wind data, we carefully re-examined ACE data. B_M is increased within the exhaust at both spacecraft, however at 09:25:37.7 - 09:28:41.2 UT and 08:24:27.3 - 08:24:33.5 UT it is decreased at Wind and ACE, respectively (shaded regions in panel (c)). These decreases correspond to regions near opposing pairs of separatrices. These measurements are consistent with the expected directions and location of the Hall fields shown in Figure 5.1(b), with Wind intercepting the exhaust along the path BA and ACE intercepting the exhaust along the path CD.

In guide field reconnection the deflection of the electron current means that the reversal in the bipolar perturbation to B_M does not occur at $B_L = 0$ (e.g., Rogers *et al.*, 2003; Eastwood *et al.*, 2010a). This is shown in Figure 5.6 for both the observations and simulation. The value of B_L at which this occurs differs at the two opposing exhausts because the electron

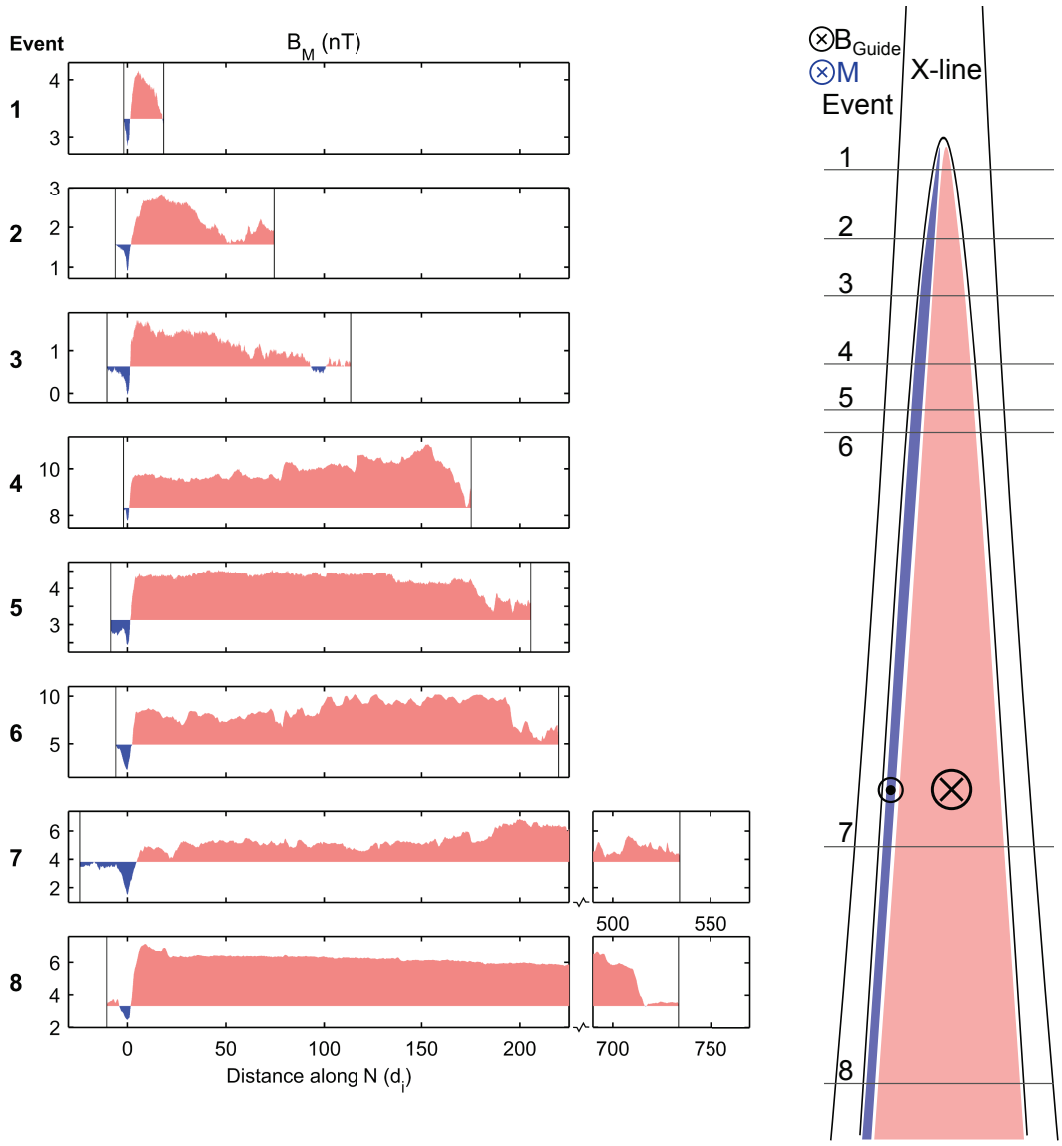


Figure 5.8: B_M for 8 events, as a function of distance in the normal direction. Positive and negative Hall magnetic field regions are coloured in red and blue, respectively. The x-axis origin is located at the minima in B_M. Vertical lines mark the exhausts edges. Data are shown across two panels for Events 7 and 8. Relative distances of observations from the X-line are shown on the right.

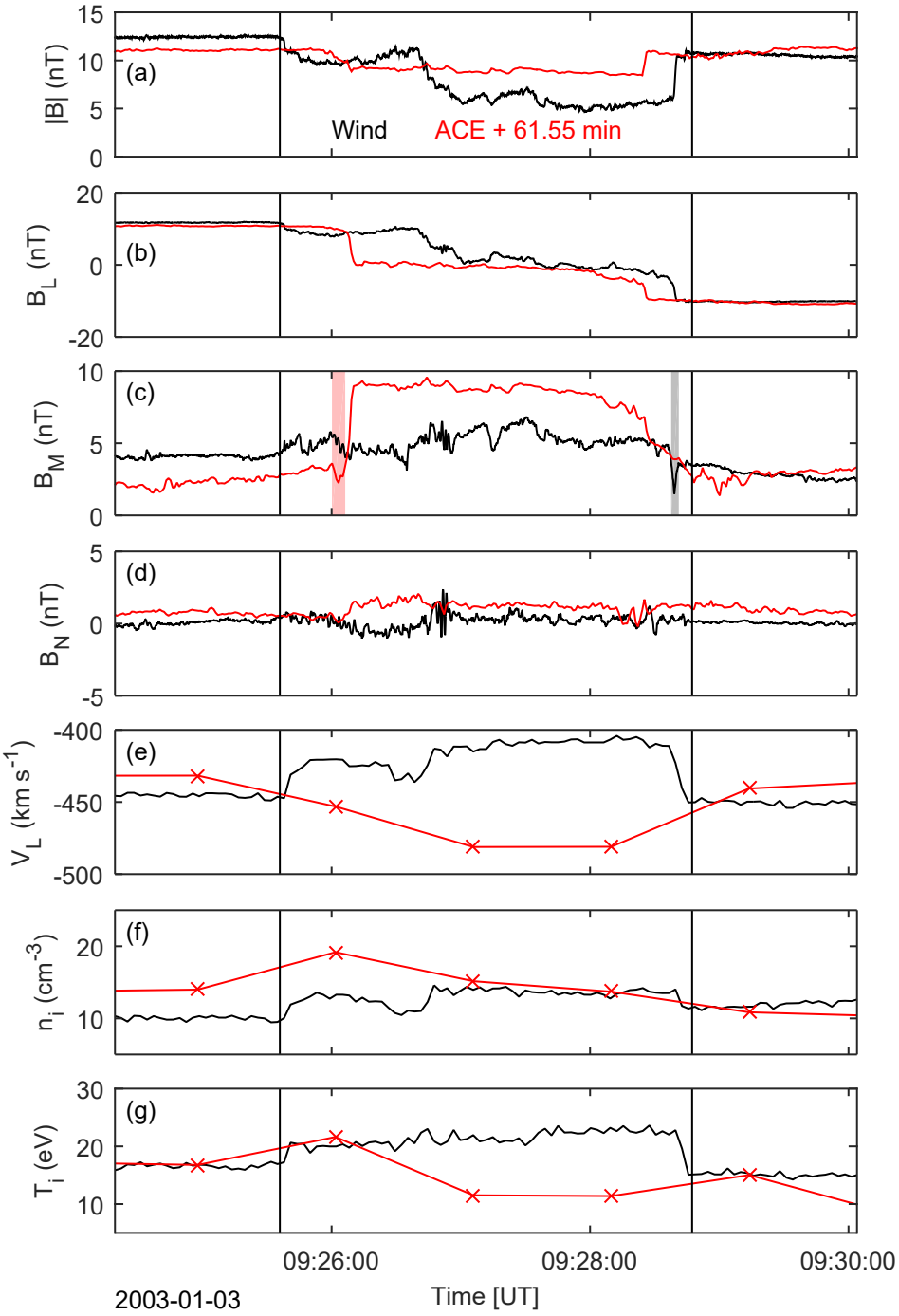


Figure 5.9: Observations from Wind (black) and ACE (red) for Event 7. Vertical lines mark the exhaust region at Wind. Shaded regions in (c) indicate where negative Hall fields are observed at each spacecraft.

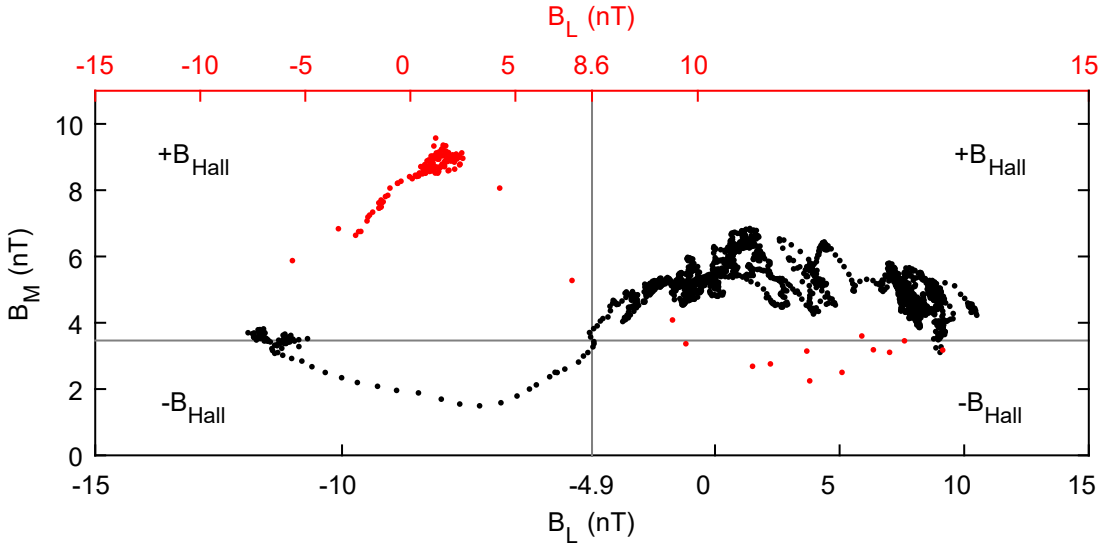


Figure 5.10: $B_L - B_M$ hodograms from the exhaust intervals at Wind (black) and ACE (red) for Event 7. The vertical grey line marks the values of B_L at which bipolar perturbations in B_M reverse at each spacecraft. The B_L axes vary linearly on either side of this line. The horizontal line marks the value of B_M in the inflow regions at Wind.

current is deflected in opposite directions at the two exhausts. Figure 5.10 shows overlaid hodograms from the two spacecraft. The B_L axes have been re-scaled so that the values of B_L at which the bipolar perturbations in B_M reverse are at the centre of the axes and are coincident (and indicated by the vertical line). The B_L axes vary linearly on either side of these values. Wind and ACE measurements in Figure 5.10 clearly show the full quadrupolar pattern of the Hall field, using observations from both sides of the X-line.

Using measurements of the inflow velocity of the plasma, Davis *et al.* (2006) estimated both Wind and ACE to be approximately 9,000 d_i downstream of the reconnection X-line, and determined a reconnection rate of 0.03 (which is lower than the canonical rate of 0.1). From the macroscopic reconnection geometry of this event we estimate that Wind and ACE were located 12,900 d_i and 9,400 d_i downstream of the X-line, and estimate a reconnection rate of 0.02 (following the same method as Section 4.3). These two independent measures indicate that Wind and ACE were both of the order of thousands of d_i downstream of the X-line, and, therefore, that Hall magnetic fields may persist to at least this distance. For Event 8 the exhaust width is 743 d_i and Wind was also likely to be many thousands of d_i downstream (a canonical reconnection rate of 0.1 would imply that Wind was 3,700 d_i downstream).

5.6 Conclusions

In this chapter we have presented 8 events which show strong evidence for Hall magnetic fields. These observations were made far downstream of the X-line, significantly further than previous magnetotail observations that suggested that Hall effects may occur beyond the diffusion region (e.g., Fujimoto *et al.*, 1997; Nagai *et al.*, 2001). Additionally, we have used dual spacecraft observations to show the Hall fields generated on both sides of the X-line. In all cases the Hall magnetic field was found to be distorted by the guide field in a manner qualitatively consistent with simulations (e.g., Huba, 2005; Eastwood *et al.*, 2010a). Furthermore, we have compared one of these observations with a fully kinetic PIC simulation. The simulation shows excellent quantitative agreement with the observations and indicates that the Hall field is generated by differences between the ion and electron exhaust outflows. The electron outflow is deflected from the mid-plane in a manner consistent with the deflection that occurs in the ion diffusion region (e.g., Eastwood *et al.*, 2010a), and this deflection persists far downstream.

In these 8 events the current layer which generates the Hall magnetic field is measured to be of ion-scale ($0.8 - 6.0$ d_i). The exhaust, however, is significantly wider (for these 8 events the exhaust widths were between 25 d_i and 743 d_i). B_M increases throughout the majority of these exhausts, which ensures pressure balance across the structure (as discussed in Section 3.5). In contrast, the negative Hall field occurs across a very narrow region. The negative Hall field is easy to miss unless one is carefully seeking to identify it, which may be why Hall fields have not been previously identified at solar wind reconnection exhausts.

The events presented here are 8 events from the set of 188 events which were studied in Chapter 3. We note that a large number of events had ambiguous signatures and only events with very clear bipolar B_M signatures are presented in this chapter. The 8 events had guide fields of $0.3 < B_G < 1.6$. At larger guide fields the decrease in B_M has been shown to be much weaker (Karimabadi *et al.*, 1999), making Hall fields more difficult to observe (Rogers *et al.*, 2003). At smaller guide fields, fluctuations can develop downstream in the exhaust which obscures Hall fields, also making them difficult to observe (Higashimori & Hoshino, 2015). Furthermore, some of these 188 events have flow shears and weak asymmetries between the inflow regions, and the effects of these may further obscure Hall signatures. Many of the 188 events had guide fields comparable to the 8 events with Hall fields, however any Hall signatures present may have been obscured by the effects listed above. For this reason it is extremely difficult to identify exactly why these 8 events show such clear Hall field signatures while others do not. We have tried to separate these events from the other 180 events in terms of upstream parameters, however this has been unsuccessful. To identify the conditions under which Hall fields persist far downstream in reconnection

exhausts requires a more systematic study which may be aided by multiple simulations across a range of parameter space.

Observations of Hall fields far downstream of the X-line has important implications for our understanding of reconnection exhausts. In Chapter 3 we discussed the exhaust boundaries as MHD discontinuities (albeit with temperature anisotropy), and discussed the exhausts as pressure balanced MHD structures. This is consistent with the frequent presumption that kinetic effects are confined to the diffusion region, and that the exhaust may consequently be described using MHD. Furthermore, the exhaust regions bear resemblance to the results of one dimensional simulations. In this chapter, however, we have shown some exhausts to have narrow regions of kinetic dynamics that can persist thousands of d_i downstream of the diffusion region, which generate Hall magnetic fields. This is caused by a two dimensional current system. MHD and one dimensional models of the exhaust region are therefore inadequate for describing these exhausts and the effects which we observe. Despite this, we are not able to detect Hall signatures at the majority of exhausts and in general it appears as though the exhausts are well described using MHD, as discussed in Chapter 3.

6 Small-scale structure of a reconnection exhaust

Material in this chapter has been published in *Journal of Geophysical Research: Space Physics* in Mistry *et al.* (2015a).

6.1 Introduction

Multi-spacecraft observations of the same reconnection exhausts in the solar wind have allowed them to be probed on the spatial scales over which the spacecraft were separated. In the solar wind the spacecraft used for such studies have typically been separated by tens or hundreds of R_E. For example, observations of the same reconnection exhaust at ACE, Wind and Cluster were used to infer that a reconnection X-line extended over 390 R_E (the distance over which the spacecraft were separated) (Phan *et al.*, 2006). Furthermore, time delays between the observations at each spacecraft indicated that the reconnection exhaust was two dimensional on similar spatial scales.

Further case studies have similarly found reconnection exhausts to span large distances in the solar wind (Davis *et al.* (2006); Gosling *et al.* (2007b) and Chapter 4 of this thesis). A more extensive statistical study of 51 reconnection exhausts observed at both ACE and Wind revealed that in general reconnection X-lines span large distances in the solar wind (tens to hundreds of R_E) and that the exhausts are typically planar and two-dimensional over such extents (Phan *et al.*, 2009).

These observations strongly indicate that reconnection in the solar wind produces planar reconnection exhausts that are two dimensional. Collisionless reconnection is therefore frequently simulated in two spatial dimensions, such that the out-of-plane (i.e., along the X-line) direction is invariant. The assumption of invariance in the out-of-plane dimension reduces the computational demands of simulations, which allows larger domains to be simulated than is possible in three spatial dimensions. These two dimensional simulations produce oppositely directed exhaust outflows from the diffusion region which are consistent with the two dimensional exhaust structures which have been observed in the solar wind.

The importance of the out-of-plane third dimension has been emphasised more recently in reconnection physics, particularly with the advance of larger computational facilities which can be used to simulate larger domains in three spatial dimensions. Yin *et al.* (2008), Fujimoto (2009) and Daughton *et al.* (2011) showed that simulated reconnection current sheets can have additional structure and complexity in three spatial dimensions, which is inhibited in two dimensional systems. The scales over which these fluctuations are generated in simulations are orders of magnitude smaller than the scales which have been probed using multi-spacecraft solar wind observations, and would therefore be difficult to observe. Additionally, these computationally intensive simulations were limited to domain sizes of the order 100 d_i. Simulations are therefore currently unable to be used to investigate whether the complexity that is introduced with the third dimension has implications far downstream.

The magnetic field in the current sheet normal and out-of-plane directions is not expected to fluctuate considerably within a reconnection exhaust. Variability in these components of the magnetic field within multiple reconnection exhausts observed using Ulysses data was used to suggest that the observed exhausts may have had three dimensional structure (Gosling *et al.*, 2006b). Direct observations of non-planar exhausts, however, are rare. In one instance, a reconnection exhaust at the heliospheric current sheet was encountered by five spacecraft (over a 5 hour interval). Three of the spacecraft encountered the exhaust multiple times (Gosling *et al.*, 2007a), indicating that the boundaries of the exhaust were non-planar over length scales of tens of R_E (thousands of d_i). In the other case, multiple spacecraft encounters with an exhaust where the X-line was inferred to be in excess of 670 R_E indicated non-planar length scales of a few R_E (hundreds of d_i) (Gosling *et al.*, 2007b). In both cases the detailed structure of the exhaust and how this resulted in the spacecraft encountering it multiple times was not studied.

In this chapter a rare and fortuitous encounter by the Cluster spacecraft with a reconnection exhaust is presented. C-3 observations in Section 6.2 show a complete exhaust traversal to be followed by two re-entries into the exhaust, indicating that the exhaust has substantial three dimensional structure. Observations of the same current sheet at ACE and Wind are presented in Section 6.3, which indicate that the current sheet is planar on large scales. In Section 6.4, measurements from all four Cluster spacecraft are used to identify the detailed exhaust structure and show that although the current sheet is planar on large scales, the reconnection exhaust is non-planar at Cluster's location, with folds (length scale $\sim$230 d_i) in the out-of-plane direction.

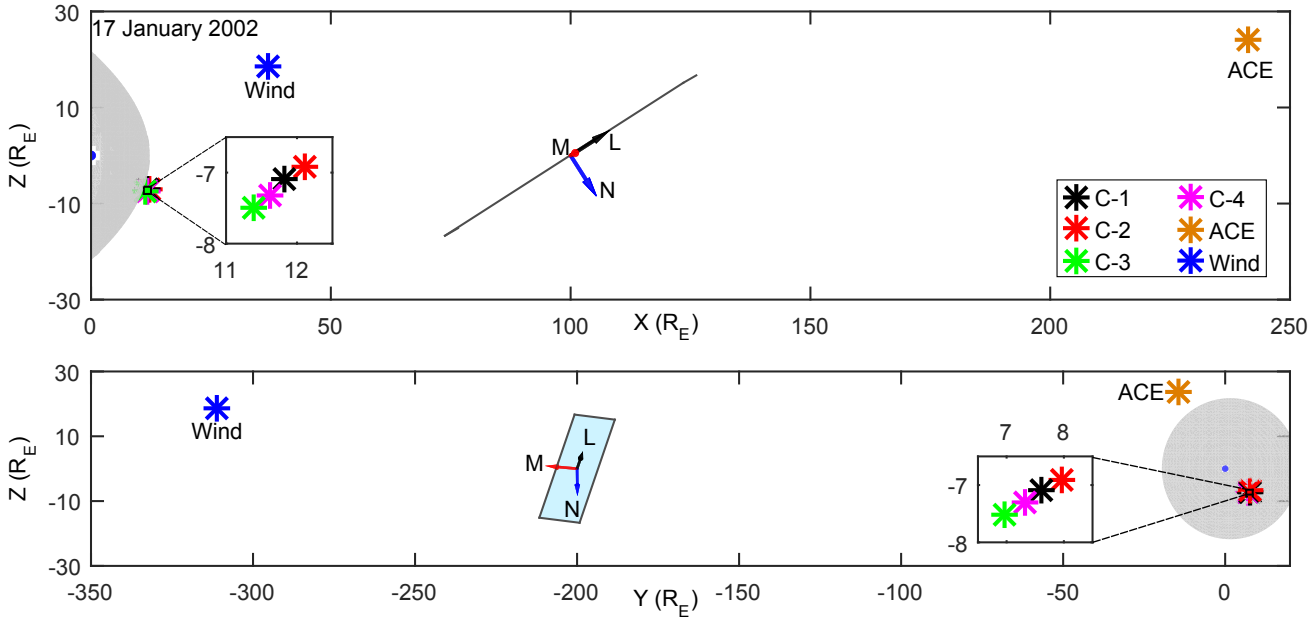


Figure 6.1: Positions of Cluster, ACE and Wind when they observed the current sheet. The bow shock (calculated using the Merka *et al.* (2005) bow shock model and an upstream density of 12.5 cm^{-3}, velocity of 402 km s^{-1} and magnetic field strength of 6.7 nT) is shown in grey. The LMN directions and the associated current sheet are shown, at an arbitrary position. The formation of the Cluster spacecraft is shown in more detail in both panels.

6.2 Overview of Cluster observations

We have identified this event from a brief survey of Cluster solar wind data obtained during January 2002, in a manner similar to the survey conducted in Chapter 2. ACE and Wind measurements show that they also observed this event. On 17 January 2002 the Cluster spacecraft tetrahedron was in the process of being reconfigured to reduce spacecraft separations from ∼2,000 km to ∼100 km. The four spacecraft were arranged in an approximately straight line in the solar wind with inter-spacecraft separations of approximately 0.5 R_E, (see Figure 6.1).

At the time of observations CIS-HIA at C-1 and C-3 was in a magnetospheric operational mode (mode 10), therefore data was collected using the low angular resolution (high sensitivity) section of the detector. The solar wind beam is relatively narrow and can frequently cause the detector counts of the high sensitivity section to saturate, due to the section's high geometric factor. This can result in an underestimate of the ion density. Furthermore, the high sensitivity section has a large polar angular bin width (11.25°). The solar wind beam is relatively narrow and the ions are therefore likely to be collected within only a few bins. The distribution is therefore unlikely to be measured with a sufficient resolution

to reliably calculate temperature moments from the distribution function. For this reason CIS-HIA density and temperature moments are not used for these observations. The location of the peak of the distribution function is affected by count rate saturation and poor angular resolution to much less of an extent. CIS-HIA velocity moments of the distribution function are therefore not strongly affected by the fact that the distribution was measured using the high sensitivity side of the detector. We therefore use CIS-HIA to measure the ion velocity in the solar wind for these observations. Measurements of the plasma density are instead obtained from the WHISPER instrument. WHISPER measurements of the electron density are available at a time cadence of 1.7 s for these observations.

Figure 6.2 shows the magnetic field, electron density and ion velocity observed by C-3 during a 12 minute interval when the spacecraft was located within the solar wind. Between 09:40:10 UT and 09:40:55 UT (interval 1) the magnetic field direction changed considerably (evidenced by the change in sign of B_X and B_Z), indicating the presence of a solar wind current sheet. During the current sheet crossing the field strength decreased, the density increased and there was a deflection of the ion velocity. Changes in the magnetic field direction and changes which are somewhat similar to those seen during interval 1 in the field magnitude, density and ion velocity are also evident between 09:41:12 UT and 09:41:32 UT (interval 2) and between 09:42:19 UT and 09:42:49 UT (interval 3).

Figure 6.3(ii) shows the current sheet encounter in more detail, using an LMN coordinate system derived from hybrid-MVA applied to C-3 magnetic field data during interval 1. Similar magnetic field measurements were made by all Cluster spacecraft. Hybrid-MVA was also applied to magnetic field measurements of the complete current sheet traversal at each Cluster spacecraft. The largest angular difference between the LMN vectors derived from the four spacecraft were 9° in L (between C-2 and C-3), 8° in M (between C-2 and C-3) and 7° in M (between C-1 and C-3). The coordinate systems derived from each spacecraft are largely consistent and all spacecraft observations are shown in the LMN coordinate system derived from C-3. In GSE coordinates the LMN vectors are given by $\hat{\mathbf{L}} = [0.79, 0.25, 0.56]$, $\hat{\mathbf{M}} = [0.24, -0.97, 0.08]$, $\hat{\mathbf{N}} = [0.56, 0.07, -0.82]$. Multi-spacecraft timing analysis cannot be applied to this interval to determine the current sheet normal as the spacecraft were in a straight line configuration.

Magnetic field, WHISPER and CIS-HIA measurements are also available from C-1. These are shown alongside C-3 measurements in Figure 6.3. There is a clear decrease in the field magnitude across interval 1 at both C-1 and C-3. This is accompanied by a rotation in the field in the L component, whilst B_N is small and B_M is approximately constant. B_M increases in magnitude slightly, as expected from the superposed epoch analysis in Chapter 3. The magnetic shear across the current sheet is 122° ($B_G = 0.47$) at both spacecraft. There are density enhancements at both spacecraft within the current sheet,

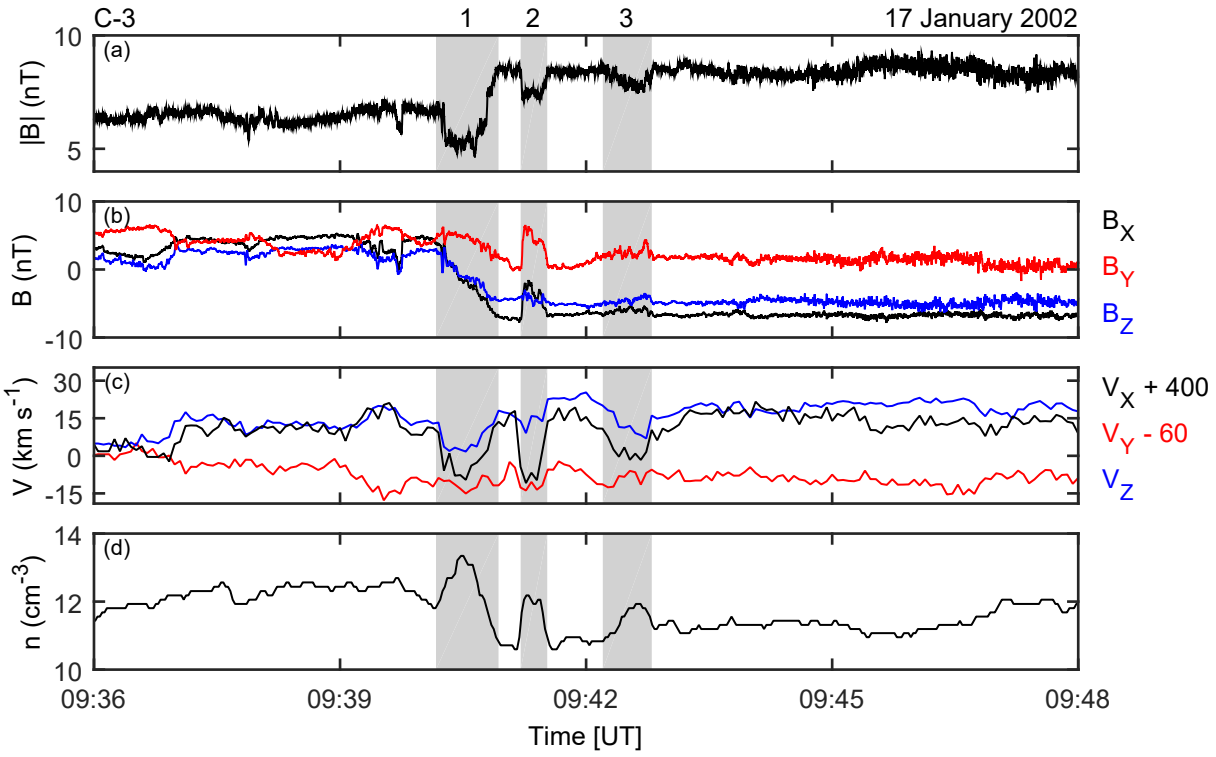


Figure 6.2: C-3 observations of (a) magnetic field magnitude, (b) GSE components of the magnetic field, (c) GSE components of the ion velocity, (d) electron density. Intervals 1-3 are shaded in grey.

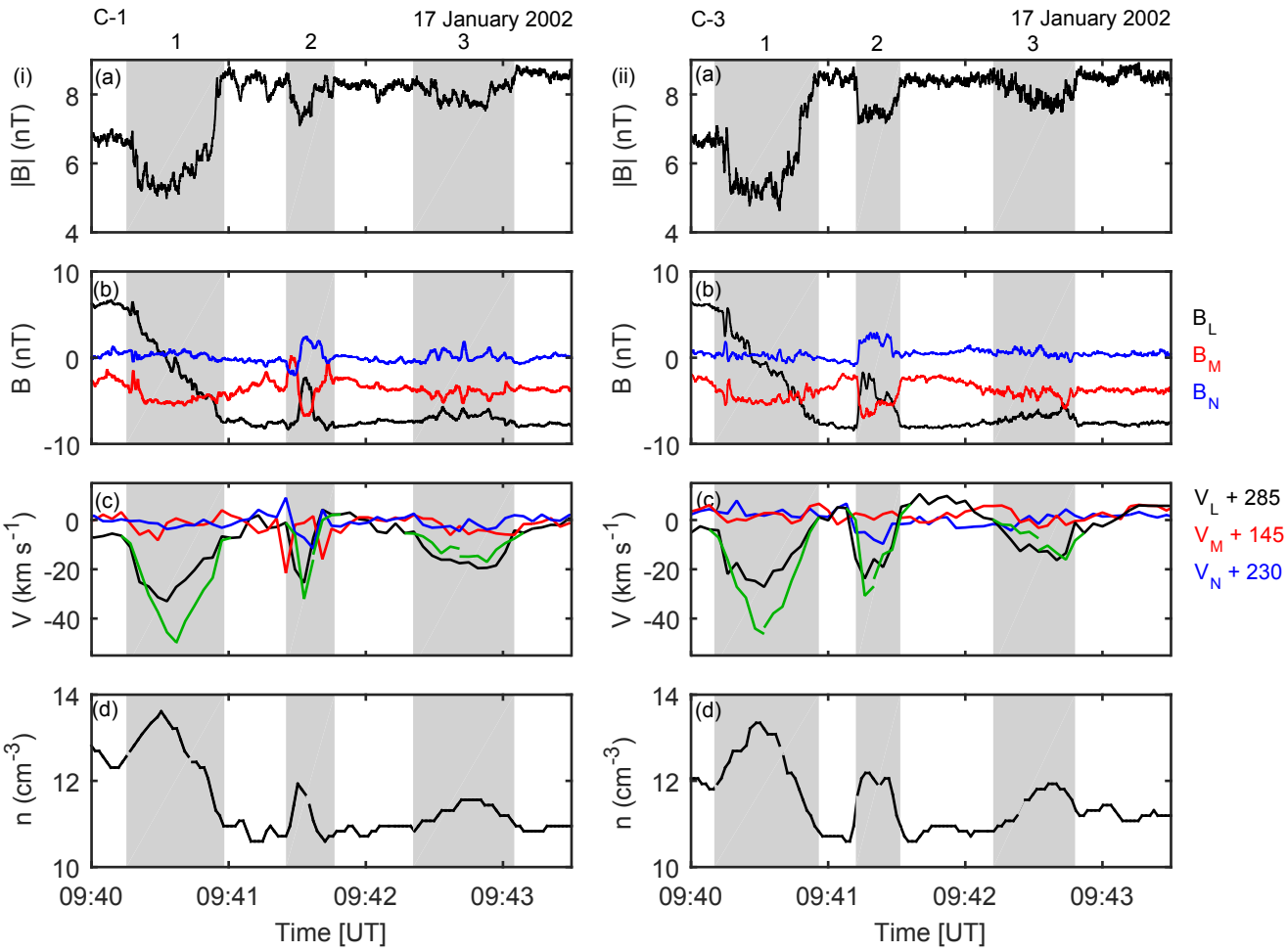


Figure 6.3: C-1 (i) and C-3 (ii) observations of (a) magnetic field magnitude, (b) magnetic field in LMN coordinates. (c) LMN ion velocity components. The L component of the Walén predicted exhaust velocity is shown in green for intervals 1-3. (d) Electron density. Intervals 1-3 are shaded in grey for each spacecraft.

and accelerated ion flow in the $-L$ direction. These observations are consistent with the presence of a reconnection exhaust with the X-line located in the $+L$ direction relative to Cluster. Additionally, the ion flows during interval 1 are compared to the Walén velocity. CIS-HIA could not resolve the ion temperature anisotropy nor accurately measure the ion density, therefore the Walén velocity is calculated assuming the plasma temperature to be isotropic, and using measurements of the electron density from WHISPER. The Walén velocity agrees reasonably well with the observed velocity close to the leading and trailing edges of the exhaust, however the observed velocity only reached 61% and 57% of the maximum predicted velocity at C-1 and C-3, respectively. Intervals 2 and 3 are examined in more detail in Section 6.4.

The current sheet is not bifurcated; the magnetic field rotates smoothly across the current sheet. Although this current sheet is observed by ACE and Wind (Section 6.3), there is no evidence that these spacecraft were located on the opposite side of the X-line to Cluster, and we cannot use the macroscale reconnection geometry to estimate Cluster's distance downstream of the X-line (as was performed in Chapter 4). The complete current sheet traversal has a duration of 46 s at C-3, indicating an exhaust width in the normal direction of 9.5×10^3 km (135 d_i, where d_i is determined from the average electron density in the inflow region at C-3 (11 cm^{-3})). A canonical reconnection rate of 0.1 would imply that Cluster was located 675 d_i downstream of the reconnection X-line. That the current sheet is not bifurcated at Cluster is consistent with findings in Chapter 4, which indicate that solar wind reconnection current sheets should develop clear bifurcations at distances greater than 1000 d_i downstream of the X-line.

6.3 Large scale current sheet structure

The current sheet observed by Cluster during interval 1 was also observed at ACE and Wind. In this section we use Cluster, ACE and Wind measurements to investigate the large scale structure of the reconnection current sheet. ACE was located almost directly upstream of Cluster, whilst Wind was separated by ∼300 R_E from Cluster along the $-Y_{GSE}$ direction (locations are shown in Figure 6.1). Figure 6.4 shows ACE and Wind data in the LMN coordinate system derived from hybrid-MVA applied to C-3 data. These data show that changes in the magnetic field at ACE and Wind were similar to those at Cluster. Comparison of magnetic field and plasma data between ACE, Wind and Cluster over several hours shows that the spacecraft observe similar structures in the solar wind, and that these are observations of the same current sheet.

Hybrid-MVA was also applied to magnetic field data from ACE and Wind across the shaded intervals in Figure 6.4, to identify the local current sheet normal at their locations.

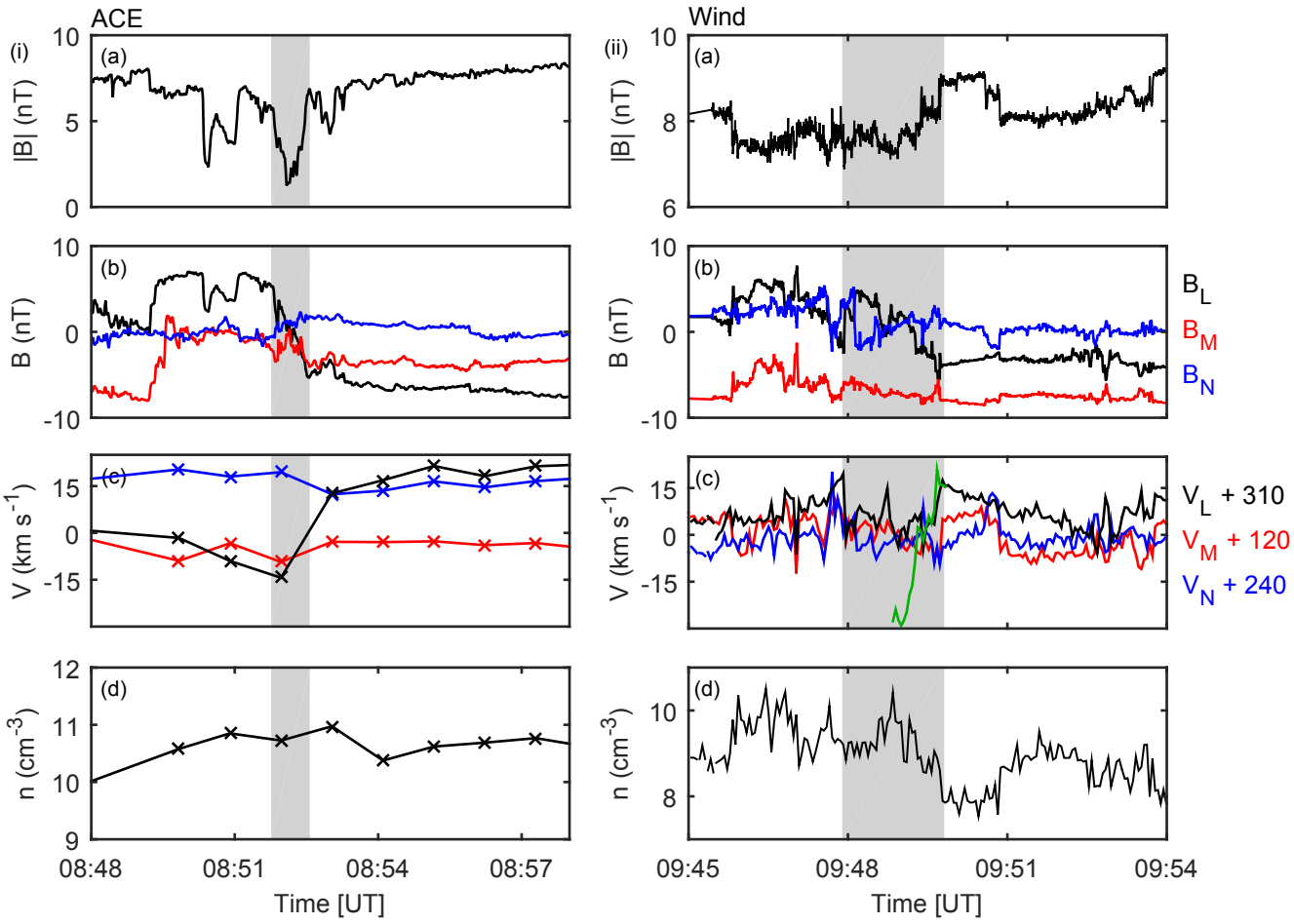


Figure 6.4: ACE (i) and Wind (ii) observations of (a) magnetic field magnitude (b) LMN magnetic field components. (c) LMN ion velocity components. The L component of the Walén predicted exhaust velocity for the second half of the current sheet is shown in green for Wind. (d) Ion density. The shaded interval indicates the current sheet that is associated with interval 1.

Differences between the normal obtained from C-3 and those obtained from ACE and Wind were 17° and 24°, respectively. This local analysis demonstrates that the current sheet has a similar orientation at the locations of Cluster, ACE and Wind. We have also determined the current sheet normal using measurements from C-3, ACE and Wind in the 3-spacecraft technique (Section 2.4.3). The difference between this normal and the normal from hybrid-MVA at C-3 is 4°, indicating that the local current sheet normal at C-3 is closely aligned with the normal of the large-scale current sheet.

The difference between the time lag predicted between observations at ACE and C-3 (based on the solar wind velocity and current sheet normal from C-3) and the observed time lag is 129 s (4.4% of the observed time lag), whilst between ACE and Wind the difference is 274 s (7.8% of the observed time lag). This provides additional evidence that the current sheet is planar on large scales and that the spacecraft did indeed all observe the same current sheet.

ACE SWEPAM measurements are available every 64 s. The current sheet is observed over an interval of 48 s at ACE, therefore the ion velocity within the current sheet cannot be resolved. The ion velocity at Wind is resolved using measurements with a 3 s cadence from 3DP (Figure 6.4(ii)(c)). The ion density is slightly enhanced and there is an increase in the ion velocity in the $-L$ direction. Across the current sheet the decrease in the field magnitude is weak and there is a strong guide field of $\sim$7 nT (the magnetic shear angle is 54°). The magnetic field is relatively stable after the current sheet, however it is varies significantly prior to the arrival of the current sheet. For this reason, a reliable reference point for the Walén relation could not be selected for the leading edge of the exhaust. The Walén velocity is only calculated from the reference point at the trailing edge, assuming the plasma to be isotropic. There is strong agreement between the predicted and observed velocities until $B_L = 0$, after which the Walén velocity and observed velocity do not show good agreement. It is therefore difficult to conclude whether or not a reconnection exhaust was observed in association with the current sheet at Wind. These measurements do indicate, however, that the magnetic field was significantly more variable and the current sheet had a stronger guide field at Wind's location.

The current sheet was encountered for 48 s, 46 s and 115 s at ACE, C-3 and Wind, respectively, indicating that the exhaust was significantly wider at Wind. The positions of ACE and Wind relative to Cluster in the rest frame of the reconnection exhaust are shown in Figure 6.5. The separation of the three spacecraft was not significant along the L direction, however Wind was located a large distance from Cluster and ACE along the M direction. The current sheet at Wind is therefore likely to be wider than at ACE/Cluster because of a varying reconnection rate along the X-line, rather a result of the exhaust widening with increasing distance downstream of the X-line.

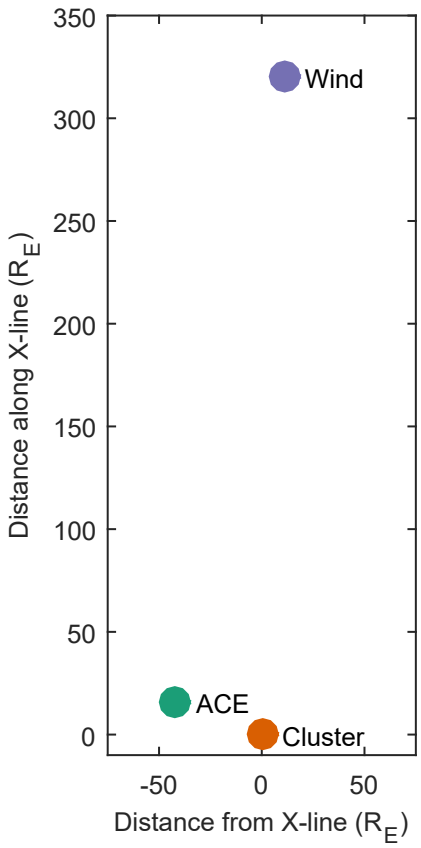


Figure 6.5: Positions of ACE and Wind relative to Cluster along L (x-axis) and along M (y-axis) in the rest frame of the reconnection exhaust.

6.4 Detailed analysis of exhaust structure at Cluster

The Cluster observations are of special interest as the reconnection exhaust was detected by the spacecraft two further times (intervals 2 and 3), despite being rapidly convected past the spacecraft by the solar wind.

During interval 2, Figure 6.3 shows that there is a decrease in the field magnitude and increase in the density at C-1 and C-3. The ion speed is also increased, primarily in the $-L$ direction (although there is variability in V_M at C-1). The maximum observed velocity within the interval is 80% and 81% of the predicted velocity (assuming isotropy) at C-1 and C-3, respectively. At the beginning of interval 2, C-3 observed a change in B_L from -8.4 nT to -2.4 nT, followed by a gradual return to -8.4 nT. At both spacecraft the density, magnetic field strength and magnetic field direction are very similar before and after interval 2, showing that Cluster did not return to the plasma environment which was present prior to interval 1. Indeed, B_L remained negative, indicating that although the spacecraft re-entered the exhaust, they did not cross the current sheet neutral-plane (where $B_L = 0$). The similarity between ion velocity measurements at C-3 during intervals 1 and 2 indicate that C-3 was located within the exhaust during interval 2. The spacecraft therefore traversed the trailing edge of the exhaust to re-enter the exhaust at the beginning of interval 2, and traversed it again to exit the exhaust at the end of the interval. During this interval there were also changes in B_M and B_N, indicating that the orientation of the current sheet was slightly different between intervals 1 and 2. The current sheet orientation at interval 2 cannot be accurately determined using MVA as the current sheet is not completely traversed during the interval and the eigenvalues were not well separated. The variability in the M and N components of the magnetic field and velocity at C-1 may indicate the presence of additional local small-scale structure within the exhaust.

During interval 3 there are weak changes in the magnetic field components. There is a decrease in the field magnitude of $\sim$1 nT at C-1 and C-3, and an increase in the density of 0.6 cm^{-3} and 0.9 cm^{-3} at C-1 and C-3, respectively. There is an increased velocity in the $-L$ direction which is within strong agreement to that predicted for an exhaust by the Walén relation (assuming isotropy). Observed velocities at both spacecraft during interval 3 and the edges of interval 2 are similar to, but slightly less than, the Walén velocities. PIC simulations have similarly noted that the Walén prediction underestimates velocities at exhaust boundaries, and overestimates velocities towards more central regions of the exhaust (as observed here at the centres of intervals 1 and 2) (Liu *et al.*, 2012; Le *et al.*, 2014).

Although changes in individual field components are small, the increased density, decreased field magnitude and observed velocity changes (and their agreement with the pre-

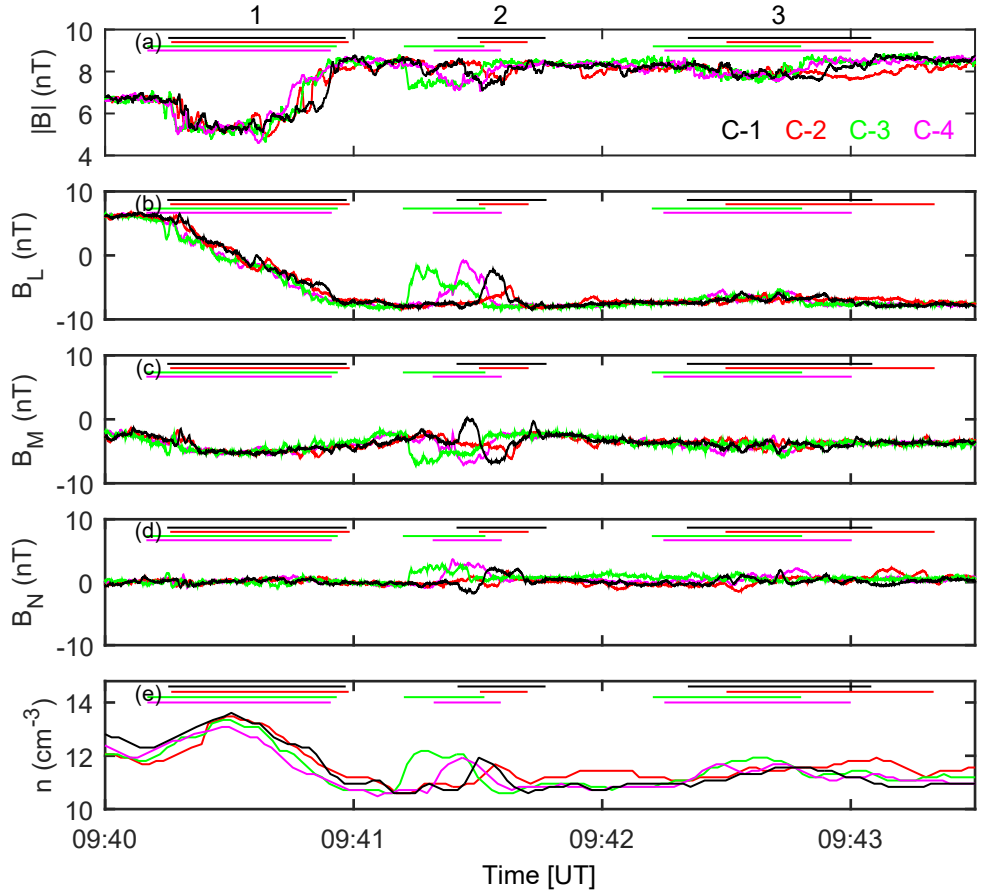


Figure 6.6: Cluster measurements of (a) magnetic field magnitude. (b)-(d) LMN magnetic field components. (e) Electron density. Horizontal lines in each panel indicate intervals 1-3 for each spacecraft.

dicted changes) clearly indicate that the spacecraft have again re-entered the exhaust. During this interval they do not appear to have penetrated very deeply into the exhaust as the change in B_L (+2.3 nT at C-3) is far smaller than for interval 2. The density, field magnitude and field direction on either side of interval 3 are similar to that observed after interval 1 and either side of interval 2, suggesting that interval 3 was again a result of traversals of the trailing edge of the exhaust.

The probability that the spacecraft would intercept a folded current sheet three times in this manner is extremely low, making this event both remarkable and of particular interest. Ion measurements are not available from C-2 and C-4. The exhaust structure is analysed in more detail using high resolution magnetic field measurements and density measurements (from WHISPER) from all four Cluster spacecraft which are shown in Figure 6.6. Magnetic field signatures at all spacecraft are similar during interval 1, whereas during interval 2, C-2 observes a smaller change in the magnetic field than the other three spacecraft, indicating that C-2 did not penetrate as deep into the exhaust.

Large-scale analysis of the current sheet in Section 6.3 revealed that the current sheet is roughly planar on large scales, however re-entries by the four Cluster spacecraft indicate that the trailing edge of the reconnection exhaust at Cluster is not planar at Cluster's location. To constrain the geometry of the reconnection exhaust we consider distortions from a planar geometry. If distortions were confined to the LN plane the exhaust boundaries would not be straight as shown in Figure 6.7, but would have significant distortions. In this case, the magnetic field at the end of interval 1 and the beginning/end of intervals 2 and 3 would be expected to have different directions. Figure 6.3, however shows that the magnetic field at these exhaust boundaries has the same direction. Similarly, the ion velocity would be expected to have a different direction during each interval, however it is observed to be mostly in the $-L$ direction. Furthermore, if the exhaust were distorted in such a way, it is not clear how the flow would interact with the folded exhaust boundaries. The same arguments apply if the distortions were confined to the LM plane.

If the distortions were instead confined to the MN plane the magnetic field at the end of interval 1 and the beginning/end of intervals 2 and 3 would be expected to have the same direction. The ion flow direction during intervals 1-3 would be unaffected by the folds as the exhaust outflow would be perpendicular to the wave vector of the folds. Measurements made by the four spacecraft are consistent with these expectations. We now discuss perturbations in the MN plane in more detail.

The spacecraft traversed the current sheet (interval 1) at approximately the same time, however intervals 2 and 3 are observed at distinctly different times by each spacecraft. Analysis of the time delay between observations of the similar structures by each spacecraft is used to further constrain the geometry of the current sheet and exhaust in the vicinity of the Cluster spacecraft. Spatial distances corresponding to time series measurements are calculated as $(\mathbf{V_{SW}} \cdot \hat{\mathbf{N}})\delta t$, where δt is a time interval. This allows the spacecraft motion relative to the exhaust to be inferred. The spacecraft move in a straight line relative to the reconnection exhaust (at a velocity of $-\mathbf{V_{SW}}$). The spatial extents of intervals 1-3, as observed by each spacecraft, are shown in the MN plane in Figure 6.7(a). B_L measurements from C-3 are also shown, which indicate the magnetic field reversal across interval 1 and the change in the magnetic field during intervals 2 and 3. The schematic in Figure 6.7(b) shows the structure of the reconnection exhaust (assuming the exhaust width to be constant), which is consistent with measurements shown in Figure 6.7(a). The reconstruction of this event in Figure 6.7(a) shows C-2 to penetrate the least into the exhaust during interval 2, which is consistent with C-2 observing the smallest changes in magnetic field and density of the four spacecraft during this interval (Figure 6.6).

A three dimensional visualisation of the local exhaust structure is shown in Figure 6.8, where the positions of the exhaust boundaries are constrained by Figure 6.7(a). The visual-

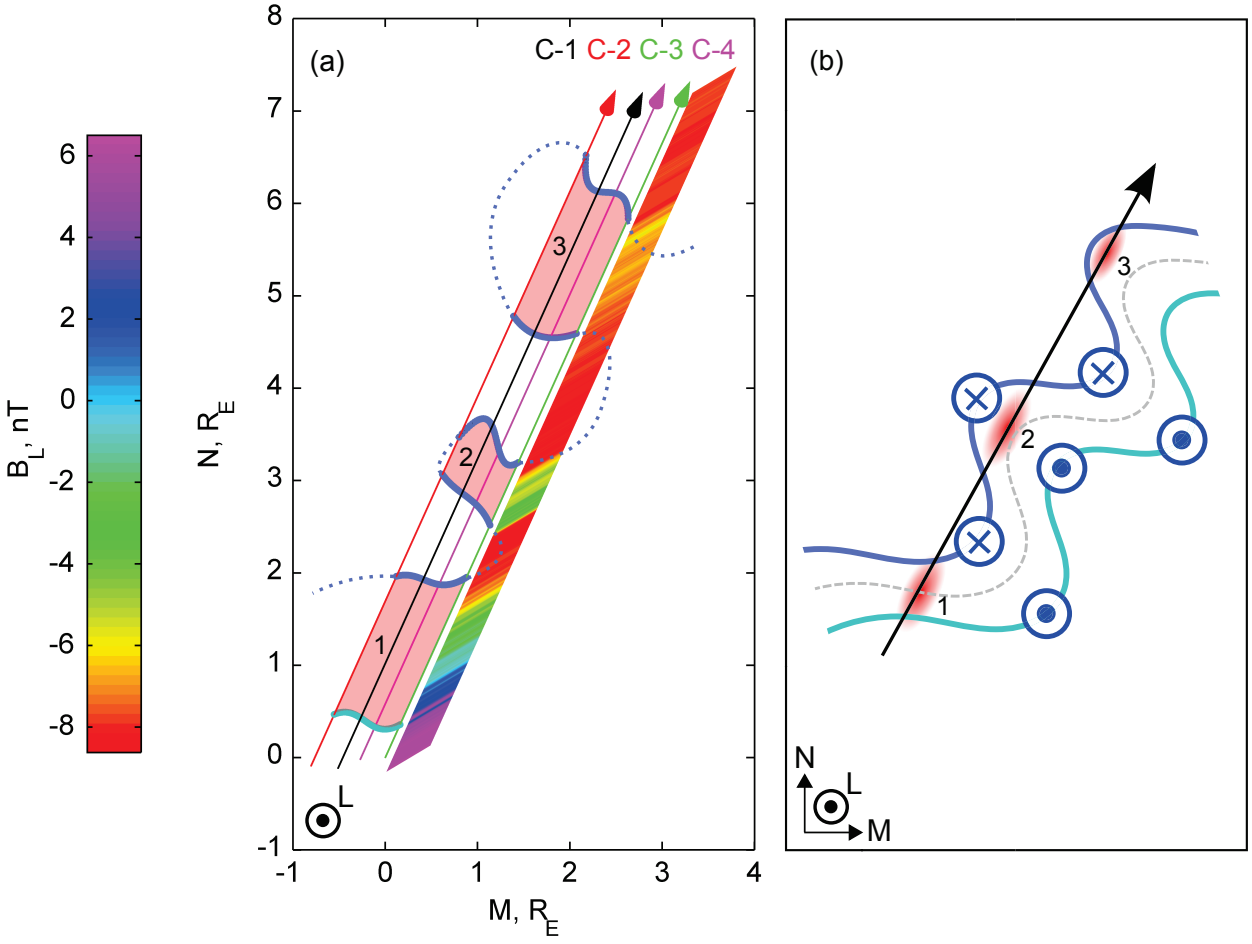


Figure 6.7: (a) Spatial map of observations of the reconnection exhaust and (b) schematic illustration, both shown in the MN plane (the L direction is indicated). Note that the spacecraft also move in the $+L$ direction, as illustrated in Figure 6.8. In (a) spacecraft trajectories relative to the exhaust are shown with coloured arrows. Positions are relative to C-3's position at 09:40:00 UT. C-3 measurements of B_L are shown by the colour bar. Red shading is used to indicate intervals 1-3. The leading edge of the exhaust is shown in turquoise, the trailing edge in light blue. These edges are calculated by spline interpolating between the boundaries of intervals 1-3 at each spacecraft. Dotted lines illustrate how the trailing edge may be connected, for comparison with (b), and are not directly inferred from the data. The schematic illustration (b) shows how intervals 1-3 correspond to distortions in the MN plane. The neutral plane at which $B_L = 0$ is in grey and magnetic field directions are shown in dark blue. The black arrow indicates Cluster's motion relative to the exhaust.

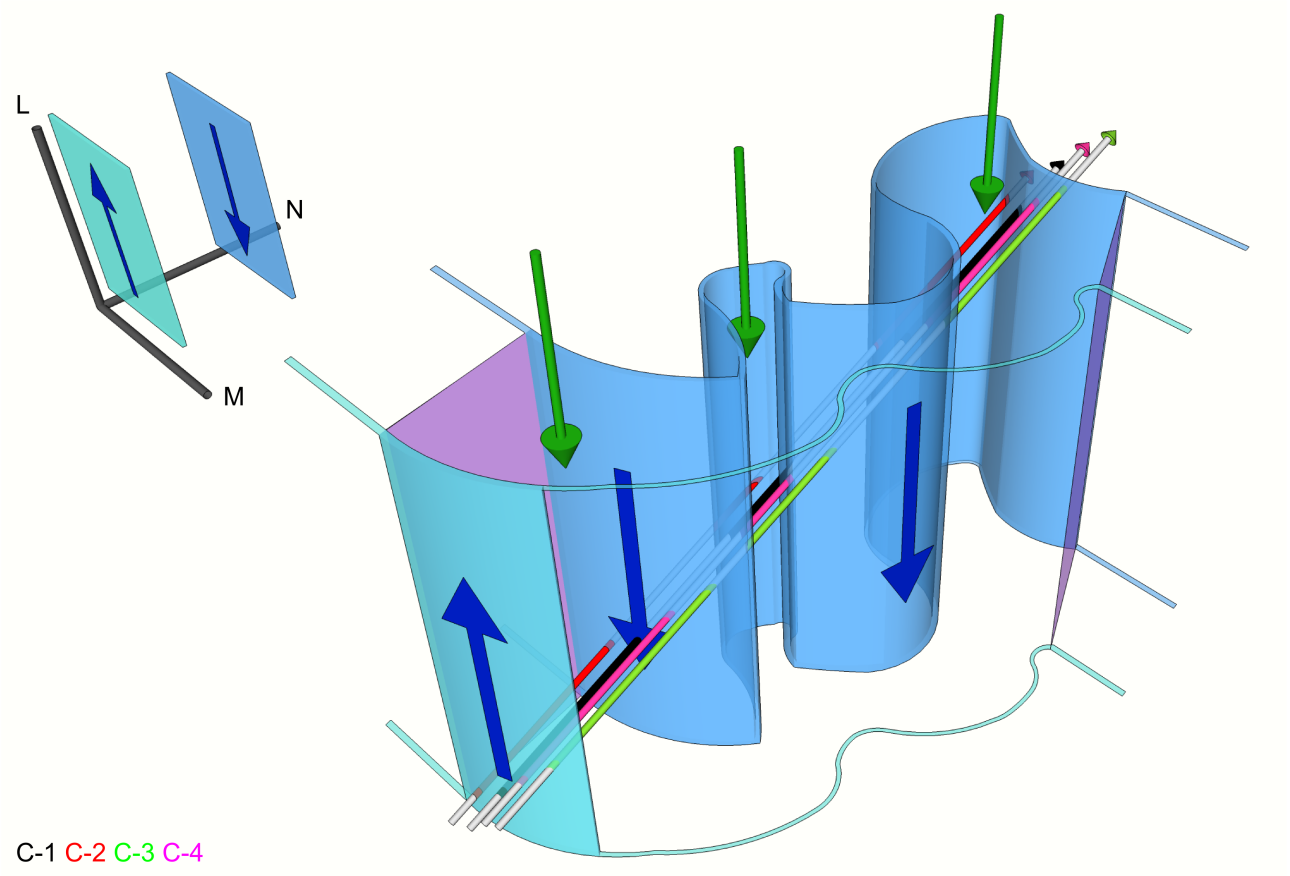


Figure 6.8: Visualisation of the exhaust structure in the vicinity of Cluster, produced using the data from Figure 6.7(a). LMN directions are shown. The leading edge of the exhaust is shown in turquoise and the trailing edge in light blue; dark blue arrows on the exhaust edges indicate the local L component of the magnetic field. Green arrows indicate the direction of exhaust outflow. Extended arrows indicate spacecraft motion relative to the exhaust, which are coloured when the spacecraft are within the exhaust. Purple edges at either end indicate the exhaust thickness. The orientation of the large-scale current sheet which is detected by ACE, Wind and Cluster is shown by the small square current sheet edges. A possible leading edge is shown by the turquoise lines to indicate the extent of the exhaust, however we are unable to constrain its actual shape. Turquoise and light blue lines indicate how this section of the exhaust could connect to the large-scale current sheet.

isation shows a possible geometry of the exhaust which is consistent with the observations and spacecraft trajectories relative to the exhaust, however it is not a unique solution to Figure 6.7(a). The geometry of the leading edge of the exhaust (turquoise) can only be constrained near the beginning of interval 1, however folds in the trailing edge (light blue) are constrained using the end of interval 1 and the beginning/end of intervals 2 and 3. B_M and B_N are not constant during interval 2 which indicates that there is likely to be some degree of distortion in the LN plane, which is not included in the visualisation. The likelihood of similar distortions at interval 3 is difficult to determine because changes in the magnetic field are very small. Figure 6.7 indicates that distortions to the trailing edge of the current sheet have a length scale of approximately 2.5 R_E (230 d_i).

6.5 Discussion

Simulations have shown that plasma instabilities can modify a two dimensional current sheet and cause it to develop three dimensional structure, including perturbations in the out-of-plane direction (e.g., Büchner & Kuska, 1999; Daughton, 1999). Such instabilities, however, are often simulated using small kinetic simulations which do not indicate the effects far downstream in the exhaust region, where solar wind observations are typically made. Although some kinetic instabilities have been shown to seed larger-scale deformations of current sheets, these simulation domains are still small in comparison to length scales relevant to the solar wind (Lapenta & Brackbill, 2002). Furthermore, these simulations typically use thin current sheets and low mass ratios, and for many instabilities the growth rates are expected to decrease for thicker current sheets and more realistic mass ratios. Many simulations are also performed using anti-parallel field configurations, however the presence of a guide field has been shown to stabilise some current sheet kink modes (Pritchett & Coroniti, 2004).

More recent large-scale simulations have studied reconnection current sheets in three dimensions, showing that the current sheet and exhaust can kink significantly (in a manner similar to that indicated in Figure 6.7(b)) (Yin *et al.*, 2008; Fujimoto, 2009; Daughton *et al.*, 2011). Such simulations are still inhibited by the use of low mass ratios and small simulation domains with respect to solar wind length scales. Three dimensional simulations with larger domains, moderate guide fields and realistic mass ratios would be advantageous for more direct comparisons with observations of reconnection exhausts, however this presents a significant challenge for simulations.

C-3 observations from the beginning of interval 1 to the end of interval 3 were measured over a 190 s duration ($t\Omega_i = 128$, where Ω_i is the proton gyrofrequency for $B = 7$ nT). If the trailing edge of the current sheet was not curved and the re-encounters were a result

of a simple harmonic perturbation to the trailing edge of a current sheet (such that the trailing edge could catch up with the spacecraft as the current sheet was convected past them) the perturbation would require a period of ∼60 s and an amplitude of ∼27,000 km (385 d_i). This implies a velocity amplitude of ∼2,800 km s^{-1}; a velocity far greater than the local sound speed. Such a perturbation would be expected to drive shock waves into the surrounding plasma, which we do not observe.

Perturbations to the current sheet structure detected here (∼2.5 R_E) are much smaller than the spatial extent of the large-scale current sheet (hundreds of R_E). It is therefore likely that a spacecraft which observed this current sheet would not encounter the small scale perturbations, although in this rare case they were detected. If previously observed reconnection current sheets had similar perturbations it is likely that they would not have been detected. Furthermore, although multi-spacecraft timing analysis has been used to show that many reconnecting current sheets are planar (e.g., Phan *et al.*, 2009), these studies have used spacecraft which have much larger separations than the scale length of the folds which we detect here. Such methods are unable to resolve variations on smaller scales than the spacecraft separations, and would therefore not be able to detect these perturbations.

6.6 Conclusions

Many previous multi-spacecraft studies have shown that reconnection exhausts in the solar wind are large scale structures which are planar, and that reconnection occurs in two dimensions in the solar wind (i.e., it is invariant in the out-of-plane direction). Such observations have acted as a validation of the two dimensional approaches used to describe reconnection which were introduced at the beginning of this thesis (i.e., the resistive MHD and collisionless reconnection models). Furthermore, they have justified the assumption of invariance in the third spatial dimension in simulations, which has been necessary to simulate large spatial regions.

Using multi-point Cluster observations in conjunction with measurements from ACE and Wind we have identified, for the first time, a solar wind exhaust which is associated with a large-scale planar current sheet and which exhibits significant small-scale three dimensional structure. The folds which we detect are orthogonal to the reconnection plane. Some current sheet simulations have revealed kinetic instabilities which also produce perturbations in the out-of-plane direction, however observational data do not allow us to identify instabilities in the observed exhaust. Three dimensional simulations with large domain sizes, moderate guide fields and large mass ratios may provide further insight into the mechanisms which may cause a reconnection exhaust to develop the structure which we observe.

The observations presented here have important implications for our understanding of solar wind reconnection exhausts and their structure. Whilst reconnection exhausts can often be large-scale, planar and quasi-steady, our observations show that they may also contain additional smaller scale structure and complexity. Since there is a low probability of spacecraft in the solar wind detecting such small scale structure, it is possible that some previously detected large-scale and planar exhausts had small-scale structure at their exhaust boundaries which was left undetected. This possibility invokes the question of how frequently such structuring of reconnection exhausts occurs in the solar wind. This may best be addressed through further simulations which study the dynamics of the exhaust region far downstream, and detailed analysis of further events using multiple closely spaced spacecraft.

7 Conclusions

Previous observations of exhausts in the solar wind have shown reconnection to be quasi-steady, and have shown that the exhausts can extend over distances of hundreds of R_E. There is a large amount of variability between observations of different exhausts, much of which has not been addressed. Over the course of this thesis we have investigated different signatures observed at exhausts in order to understand their presence, as well as determining the average properties and features that are common to exhausts in the solar wind.

A statistical study of 188 reconnection exhausts was performed in Chapter 3, which showed that in general reconnection in the solar wind occurs between symmetric plasmas and with a large range of guide fields. The out-of-plane magnetic field tends to increase within reconnection exhausts, which is apparent in many individual events as well as through a superposed epoch analysis, however this has not been previously shown. These increases show similarities to one-dimensional simulations of reconnection exhausts where rotational discontinuities form at the exhaust boundaries (e.g., Lin & Lee, 1993).

We have shown these reconnection exhausts to be in pressure balance. Furthermore, thermal pressure increases within exhausts have been shown to be a function of the inflow region plasma β and the reconnection guide field. This explains why although density and temperature increases are observed at many exhausts, they are generally very weak at low magnetic shear events and in high β plasmas. Whilst this is a rather simple explanation, it may have been difficult to reach this conclusion without analysing a sufficiently large number of events. This analysis and the results of the superposed epoch analyses indicate that reconnection exhausts at large distances downstream of the reconnection site may be described using fluid physics.

It is difficult to measure ion distribution functions within reconnection exhausts, however counterstreaming beams were observed when they have been measured (Gosling *et al.*, 2005). This is a kinetic signature which is beyond the scope of a fluid physics, and therefore may seem at odds with the fluid description. The increase in temperature expected from this pressure balance argument, however, is qualitatively consistent with increases in the temperature expected from kinetic processes. Specifically, the temperature increase expected from a kinetic treatment is 33% of the inflow region Alfvén speed (Drake *et al.*,

2009a). Observationally, however, the temperature increase has been measured to be ∼13% of the inflow region Alfvén speed in the solar wind (Drake *et al.*, 2009a) and at the magnetopause (Phan *et al.*, 2014). Using a much larger data set than has been used before, we have also measured the ion temperature increase to be ∼13% of the inflow region Alfvén speed. The reasons why the temperature increase is substantially lower than predicted remain unclear. By using events with a large range of guide fields we have shown that correlation between the ion temperature increase and inflow region Alfvén speed is very strong for $B_G < 1$, however at larger guide fields the ion temperature within the reconnection exhaust is extremely variable. Simulations and high resolution measurements from MMS of guide field reconnection show ion temperatures to be non-uniform downstream of the X-line (Øieroset *et al.*, 2016). If the ion temperature within reconnection exhausts remains non-uniform far downstream the exhaust temperature may not be characterised by a single value, and a simple scaling with the inflow region Alfvén speed may not apply.

Bifurcated current sheets have been observed at many solar wind exhausts, although the magnetic field has also been shown to vary more smoothly for other events. The reasons for these differences had not been explored. In Chapter 4 we use measurements from spacecraft located at different distances downstream of the same reconnection X-line to show that the current sheet structure changes with distance downstream. We use a new method to determine the spacecraft's distance downstream of the X-line in the solar wind, when oppositely directed exhausts are observed from a common X-line. The reconnection rate determined using this technique is found to be more reliable than local measurements. For all three events the spacecraft furthest downstream observe a bifurcated current sheet, while those closer to the X-line do not. This indicates that bifurcations of reconnection current sheets may be formed far from the X-line where the downstream regions of the two exhaust boundaries are well separated. Confirmation of whether these exhausts are bound by slow shocks (as is the case in the Petschek model) would require much higher resolution measurements, which may be possible with MMS. It is worth noting, however, that slow shocks may not be expected at exhausts in the solar wind and magnetosheath as these often have a non-zero guide field, and guide fields are expected to significantly suppress the formation of slow shocks (Lin & Lee, 1995; Lin & Swift, 1996).

In Chapter 5 we identify kinetic signatures in 8 of these events in the form of Hall magnetic fields, which is confirmed by comparisons with an appropriately scaled fully kinetic PIC simulation. This indicates that kinetic physics can in fact persist far downstream of the reconnection X-line, where the Hall field is generated in tandem with two dimensional current systems. In such cases the exhaust region cannot be sufficiently described using one dimensional models or with MHD. These signatures were clear in only a small number of events, and as yet it is unclear under which conditions these signatures persist far downstream. In the vast majority of events we are unable to measure such signatures and

the exhaust region appears to be consistent with fluid descriptions, as was found in the superposed epoch analyses in Chapter 3.

Multi-spacecraft observations of exhausts in the solar wind have shown that they are in general planar and can extend over hundreds of R_E. In Chapter 6 we use Cluster to probe smaller scales than has been done before, using a rare case study event. This event shows that even though reconnection exhausts may be planar on very large scales, they can have complex small scale structure. The reasons why this structure may develop are unclear and requires further investigation.

The findings of this thesis have been reached through the analysis of field and particle measurements from single as well as multiple spacecraft, and the use of fully kinetic PIC simulations. In summary, we have shown that in general reconnection exhausts in the solar wind are well described using fluid theory, and show clear enhancements in the out-of-plane field within the exhaust. Increases in the ion temperature are proportional to the inflow region Alfvén speed for low guide field reconnection. The presence of increases in thermal pressure within reconnection exhausts is dependent upon the inflow region β and the reconnection guide field, and whether or not the reconnection current sheet is bifurcated depends on the distance downstream of the X-line at which the exhaust is observed. Whilst these findings are generally common to reconnection exhausts in the solar wind, exceptions clearly exist. In some cases kinetic physics can persist thousands of d_i downstream of the X-line, locally generating Hall magnetic fields. Furthermore, although exhausts in the solar wind are generally planar, it is possible that three dimensional and small scale structure of the exhaust can develop, as has been shown with a single event case study.

A number of questions remain outstanding about solar wind reconnection exhausts and reconnection exhausts in general. We do not know how prevalent small scale structure of reconnection exhausts is, and further surveys of exhausts using closely spaced spacecraft may help to address this issue. Such measurements may also aid our understanding of how and why this small scale structure develops. Additionally, it is unclear exactly why Hall magnetic fields persist far downstream for only a small number of events. In Chapter 5 we only studied events where bipolar Hall magnetic fields were very clear, and future work would include analysing events where these signatures were more ambiguous. Further surveys for Hall signatures may help to identify conditions under which these signatures persist far downstream, and multiple simulations with different initial conditions would also contribute greatly. Higher resolution particle measurements would also enable us to identify other kinetic processes downstream of the X-line, using, for example, MMS particle data of reconnection exhausts in the magnetosheath.

Although our results show variability of the ion temperature at large guide fields, we have been unable to address how non-uniform the ion temperature is across reconnection

exhausts. Higher resolution measurements are required for this, for example, from MMS. Such measurements would also allow us to probe the structure of reconnection exhaust boundaries using ion measurements at 27 times the cadence of those available with Cluster. These measurements would allow us to more accurately identify the nature of the exhaust boundaries and whether they are consistent with rotational discontinuities, and whether slow shocks accompany bifurcated current sheets far downstream of the X-line. Further measurements of bifurcated and non-bifurcated reconnection current sheets may be used to investigate whether the development of current sheet bifurcations is affected by the inflow region conditions. Additionally, further simulations could also help to identify the effects of inflow region conditions on the formation of current sheet bifurcations and slow shocks.

Bibliography

Acuña, M. H., Ogilvie, K. W., Baker, D. N., Curtis, S. A., Fairfield, D. H., & Mish, W. H. 1995. The Global Geospace Science Program and its investigations. *Space Science Reviews*, **71**(1), 5–21.

Angelopoulos, V., Baumjohann, W., Kennel, C. F., Coroniti, F. V., Kivelson, M. G., Pellat, R., Walker, R. J., Lühr, H., & Paschmann, G. 1992. Bursty bulk flows in the inner central plasma sheet. *Journal of Geophysical Research: Space Physics*, **97**(A4), 4027–4039.

Arridge, C. S., Eastwood, J. P., Jackman, C. M., Poh, G-K, Slavin, J. A., Thomsen, M. F., André, N., Jia, X., Kidder, A., Lamy, L., *et al.* 2016. Cassini in situ observations of long-duration magnetic reconnection in Saturn's magnetotail. *Nature Physics*, **12**(3), 268–271.

Arzner, K., & Scholer, M. 2001. Kinetic structure of the post plasmoid plasma sheet during magnetotail reconnection. *Journal of Geophysical Research: Space Physics*, **106**(A3), 3827–3844.

Asano, Y., Nakamura, R., Baumjohann, W., Runov, A., Vörös, Z., Volwerk, M., Zhang, T. L., Balogh, A., Klecker, B., & Rème, H. 2005. How typical are atypical current sheets? *Geophysical Research Letters*, **32**(3), L03108.

Baker, D. N., Fritz, T. A., McPherron, R. L., Fairfield, D. H., Kamide, Y., & Baumjohann, W. 1985. Magnetotail energy storage and release during the CDAW 6 substorm analysis intervals. *Journal of Geophysical Research: Space Physics*, **90**(A2), 1205–1216.

Balogh, A. 2010. Planetary magnetic field measurements: Missions and instrumentation. *Space Science Reviews*, **152**(1), 23–97.

Balogh, A., Carr, C. M., Acuña, M. H., Dunlop, M. W., Beek, T. J., Brown, P., Fornacon, K.-H., Georgescu, E., Glassmeier, K.-H., & Harris, J. 2001. The Cluster magnetic field investigation: Overview of in-flight performance and initial results. *Annales Geophysicae*, **19**(10/12), 1207–1217.

Baumjohann, W., & Treumann, R. A. 1997. *Basic space plasma physics*. Imperial College Press.

Birn, J., & Hesse, M. 2001. Geospace Environment Modeling (GEM) magnetic reconnection challenge: Resistive tearing, anisotropic pressure and Hall effects. *Journal of Geophysical Research: Space Physics*, **106**(A3), 3737–3750.

Birn, J., Drake, J. F., Shay, M. A., Rogers, B. N., Denton, R. E., Hesse, M., Kuznetsova, M., Ma, Z. W., Bhattacharjee, A., Otto, A., & Pritchett, P. L. 2001. Geospace Environmental Modeling (GEM) magnetic reconnection challenge. *Journal of Geophysical Research: Space Physics*, **106**(A3), 3715–3719.

Biskamp, D. 1986. Magnetic reconnection via current sheets. *Physics of Fluids*, **29**(5), 1520–1531.

Biskamp, D. 2005. *Magnetic reconnection in plasmas*. Cambridge University Press.

Blagau, A., Paschmann, G., Klecker, B., & Marghitu, O. 2015. Experimental test of the $\rho(1-\alpha)$ evolution for rotational discontinuities: cluster magnetopause observations. *Annales Geophysicae*, **33**(1), 79–91.

Borovsky, J. E. 2008. Flux tube texture of the solar wind: Strands of the magnetic carpet at 1 AU? *Journal of Geophysical Research: Space Physics*, **113**(A8), A08110.

Bruno, R., & Carbone, V. 2013. The solar wind as a turbulence laboratory. *Living Reviews in Solar Physics*, **10**(1), 1–208.

Büchner, J., & Kuska, J. P. 1999. Sausage mode instability of thin current sheets as a cause of magnetospheric substorms. *Annales Geophysicae*, **17**(5), 604–612.

Büchner, J., Dum, C., & Scholer, M. 2003. *Space plasma simulation*. Vol. 615. Springer Science & Business Media.

Burch, J. L., Torbert, R. B., Phan, T. D., Chen, L.-J., Moore, T. E., Ergun, R. E., Eastwood, J. P., Gershman, D. J., Cassak, P. A., Argall, M. R., Wang, S., Hesse, M., Pollock, C. J., Giles, B. L., Nakamura, R., Mauk, B. H., Fuselier, S. A., Russell, C. T., Strangeway, R. J., Drake, J. F., Shay, M. A., Khotyaintsev, Y. V., Lindqvist, P.-A., Marklund, G., Wilder, F. D., Young, D. T., Torkar, K., Goldstein, J., Dorelli, J. C., Avanov, L. A., Oka, M., Baker, D. N., Jaynes, A. N., Goodrich, K. A., Cohen, I. J., Turner, D. L., Fennell, J. F., Blake, J. B., Clemmons, J., Goldman, M., Newman, D., Petrinec, S. M., Trattner, K. J., Lavraud, B., Reiff, P. H., Baumjohann, W., Magnes, W., Steller, M., Lewis, W., Saito, Y., Coffey, V., & Chandler, M. 2016a. Electron-scale measurements of magnetic reconnection in space. *Science*, **352**(6290).

Burch, J. L., Moore, T. E., Torbert, R. B., & Giles, B. L. 2016b. Magnetospheric Multiscale overview and science objectives. *Space Science Reviews*, **199**(1), 5–21.

Burlaga, L. F. 1968. Micro-scale structures in the interplanetary medium. *Solar Physics*, **4**(1), 67–92.

Cassak, P. A., & Shay, M. A. 2007. Scaling of asymmetric magnetic reconnection: General theory and collisional simulations. *Physics of Plasmas*, **14**(10), 102114.

Cassak, P. A., Drake, J. F., Gosling, J. T., Phan, T. D., Shay, M. A., & Shepherd, L. S. 2013. On the cause of supra-arcade downflows in solar flares. *The Astrophysical Journal Letters*, **775**(1), L14.

Cowling, T. G. 1953. *Solar Electrodynamics*. Page 532.

Daughton, W. 1999. Two-fluid theory of the drift kink instability. *Journal of Geophysical Research: Space Physics*, **104**(A12), 28701–28707.

Daughton, W., Lapenta, G., & Ricci, P. 2004. Nonlinear evolution of the lower-hybrid drift instability in a current sheet. *Physical Review Letters*, **93**(10), 105004.

Daughton, W., Roytershteyn, V., Karimabadi, H., Yin, L., Albright, B. J., Bergen, B., & Bowers, K. J. 2011. Role of electron physics in the development of turbulent magnetic reconnection in collisionless plasmas. *Nature Physics*, **7**(7), 539–542.

Davis, M. S., Phan, T. D., Gosling, J. T., & Skoug, R. M. 2006. Detection of oppositely directed reconnection jets in a solar wind current sheet. *Geophysical Research Letters*, **33**(19), L19102.

Décréau, P. M. E., Fergeau, P., Krasnoselskikh, V., Le Guirriec, E., Lévêque, M., Martin, Ph., Randriamboarison, O., Rauch, J. L., Sené, F. X., Séran, H. C., Trotignon, J. G., Canu, P., Cornilleau, N., de Féraudy, H., Alleyne, H., Yearby, K., Mögensen, P. B., Gustafsson, G., André, M., Gurnett, D. C., Darrouzet, F., Lemaire, J., Harvey, C. C., Travnicek, P., & Whisper, experimenters. 1999. Early results from the Whisper instrument on Cluster: an overview. *Annales Geophysicae*, **19**(10/12), 1241–1258.

Doss, C. E., Komar, C. M., Cassak, P. A., Wilder, F. D., Eriksson, S., & Drake, J. F. 2015. Asymmetric magnetic reconnection with a flow shear and applications to the magnetopause. *Journal of Geophysical Research: Space Physics*, **120**(9), 7748–7763.

Drake, J. F., Swisdak, M., Schoeffler, K. M., Rogers, B. N., & Kobayashi, S. 2006. Formation of secondary islands during magnetic reconnection. *Geophysical research letters*, **33**(13).

Drake, J. F., Swisdak, M., Phan, T. D., Cassak, P. A., Shay, M. A., Lepri, S. T., Lin, R. P., Quataert, E., & Zurbuchen, T. H. 2009a. Ion heating resulting from pickup in magnetic reconnection exhausts. *Journal of Geophysical Research: Space Physics*, **114**(A5), A05111.

Drake, J. F., Cassak, P. A., Shay, M. A., Swisdak, M., & Quataert, E. 2009b. A magnetic reconnection mechanism for ion acceleration and abundance enhancements in impulsive flares. *The Astrophysical Journal Letters*, **700**(1), L16.

Dungey, J. W. 1961. Interplanetary magnetic field and the auroral zones. *Physical Review Letters*, **6**(2), 47–48.

Dungey, J.W. 1953. LXXVI. Conditions for the occurrence of electrical discharges in astrophysical systems. *The London, Edinburgh, and Dublin Philosophical Magazine and Journal of Science*, **44**(354), 725–738.

Dunlop, M. W., & Woodward, T. I. 1998. Multi-spacecraft discontinuity analysis: Orientation and motion. *Pages 271–306 of:* Paschmann, G., & Daly, P. W. (eds), *Analysis methods for multi-spacecraft data*. Noordwijk, Netherlands: ESA Publication Division.

Dunlop, M. W., Balogh, A., Cargill, P., Elphic, R. C., Fornaçon, K.-H., Georgescu, E., & Sedgemore-Schulthess, F. 2001. Cluster observes the Earth's magnetopause: coordinated four-point magnetic field measurements. *Annales Geophysicae*, **19**(10/12), 1449–1460.

Dunlop, M.W., Southwood, D.J., Glassmeier, K.-H., & Neubauer, F.M. 1988. Analysis of multipoint magnetometer data. *Advances in Space Research*, **8**(9), 273 – 277.

Eastwood, J. P., Phan, T. D., Mozer, F. S., Shay, M. A., Fujimoto, M., Retinò, A., Hesse, M., Balogh, A., Lucek, E. A., & Dandouras, I. 2007. Multi-point observations of the Hall electromagnetic field and secondary island formation during magnetic reconnection. *Journal of Geophysical Research: Space Physics*, **112**(A6).

Eastwood, J. P., Brain, D. A., Halekas, J. S., Drake, J. F., Phan, T. D., Øieroset, M., Mitchell, D. L., Lin, R. P., & Acuña, M. 2008. Evidence for collisionless magnetic reconnection at Mars. *Geophysical Research Letters*, **35**(2).

Eastwood, J. P., Shay, M. A., Phan, T. D., & Øieroset, M. 2010a. Asymmetry of the ion diffusion region Hall electric and magnetic fields during guide field reconnection: Observations and comparison with simulations. *Physical Review Letters*, **104**(20), 205001.

Eastwood, J. P., Phan, T. D., Øieroset, M., & Shay, M. A. 2010b. Average properties of the magnetic reconnection ion diffusion region in the Earth's magnetotail: The 2001-2005 Cluster observations and comparison with simulations. *Journal of Geophysical Research: Space Physics*, **115**(A8), A08215.

Eastwood, J. P., Goldman, M. V., Hietala, H., Newman, D. L., Mistry, R., & Lapenta, G. 2015. Ion reflection and acceleration near magnetotail dipolarization fronts associated with magnetic reconnection. *Journal of Geophysical Research: Space Physics*, **120**(1), 511–525.

Enžl, J., Přech, L., Šafránková, J., & Němeček, Z. 2014. Statistical study of reconnection exhausts in the solar wind. *The Astrophysical Journal*, **796**(1), 21.

Eriksson, S., Øieroset, M., Baker, D. N., Mouikis, C., Vaivads, A., Dunlop, M. W., Rème, H., Ergun, R. E., & Balogh, A. 2004. Walén and slow-mode shock analyses in the near-Earth magnetotail in connection with a substorm onset on 27 August 2001. *Journal of Geophysical Research: Space Physics*, **109**(A10), A10212.

Eriksson, S., Newman, D. L., Lapenta, G., & Angelopoulos, V. 2014. On the signatures of magnetic islands and multiple X-lines in the solar wind as observed by ARTEMIS and WIND. *Plasma Physics and Controlled Fusion*, **56**(6), 064008.

Escoubet, C. P., Fehringer, M., & Goldstein, M. 2001. Introduction: The Cluster mission. *Annales Geophysicae*, **19**(10/12), 1197–1200.

Escoubet, C. P., Taylor, M. G. G. T., Masson, A., Laakso, H., Volpp, J., Hapgood, M., & Goldstein, M. L. 2013. Dynamical processes in space: Cluster results. *Annales Geophysicae*, **31**(6), 1045–1059.

Fazakerley, A. N., Schwartz, S. J., & Paschmann, G. 1998. Measurement of Plasma Velocity Distributions. *Pages 91–124 of:* Paschmann, G., & Daly, P. W. (eds), *Analysis Methods for Multi-Spacecraft Data*. Noordwijk, Netherlands: ESA Publication Division.

Fear, R. C., Milan, S. E., Fazakerley, A. N., Lucek, E. A., Cowley, S. W. H., & Dandouras, I. 2008. The azimuthal extent of three flux transfer events. *Annales Geophysicae*, **26**(8), 2353–2369.

Feldman, W. C., Baker, D. N., Bame, S. J., Birn, J., Gosling, J. T., Hones, E. W., & Schwartz, S. J. 1985. Slow-mode shocks: A semipermanent feature of the distant geomagnetic tail. *Journal of Geophysical Research: Space Physics*, **90**(A1), 233–240.

Fujimoto, Keizo. 2009. Fast magnetic reconnection in a kinked current sheet. *Physics of Plasmas*, **16**(4).

Fujimoto, M., Nakamura, M. S., Shinohara, I., Nagai, T., Mukai, T., Saito, Y., Yamamoto, T., & Kokubun, S. 1997. Observations of earthward streaming electrons at the trailing boundary of a plasmoid. *Geophysical Research Letters*, **24**(22), 2893–2896.

Furth, H. P., Killeen, J., & Rosenbluth, M. N. 1963. Finite resistivity instabilities of a sheet pinch. *Physics of Fluids (1958-1988)*, **6**(4), 459–484.

Giovanelli, R. G. 1946. A theory of chromospheric flares. *Nature*, **158**(4003), 81–82.

Goldman, M. V., Lapenta, G., Newman, D. L., Markidis, S., & Che, H. 2011. Jet deflection by very weak guide fields during magnetic reconnection. *Physical Review Letters*, **107**(13), 135001.

Goldman, M. V., Newman, D. L., & Lapenta, G. 2016. What can we learn about magnetotail reconnection from 2D PIC Harris-sheet simulations? *Space Science Reviews*, **199**(1), 651–688.

Gopalswamy, N. 2009. The CME link to geomagnetic storms. *Proceedings of the International Astronomical Union*, **5**(Symposium S264), 326–335.

Gosling, J. T. 2007. Observations of magnetic reconnection in the turbulent high-speed solar wind. *The Astrophysical Journal Letters*, **671**(1), L73.

Gosling, J. T. 2012. Magnetic reconnection in the solar wind. *Space Science Reviews*, **172**(1-4), 187–200.

Gosling, J. T., & Phan, T. D. 2013. Magnetic reconnection in the solar wind at current sheets associated with extremely small field shear angles. *The Astrophysical Journal Letters*, **763**(2), L39.

Gosling, J. T., & Szabo, A. 2008. Bifurcated current sheets produced by magnetic reconnection in the solar wind. *Journal of Geophysical Research: Space Physics*, **113**(A10), A10103.

Gosling, J. T., Thomsen, M. F., Bame, S. J., Elphic, R. C., & Russell, C. T. 1990. Cold ion beams in the low latitude boundary layer during accelerated flow events. *Geophysical Research Letters*, **17**(12), 2245–2248.

Gosling, J. T., Skoug, R. M., McComas, D. J., & Smith, C. W. 2005. Direct evidence for magnetic reconnection in the solar wind near 1 AU. *Journal of Geophysical Research: Space Physics*, **110**(A1).

Gosling, J. T., Eriksson, S., & Schwenn, R. 2006a. Petschek-type magnetic reconnection exhausts in the solar wind well inside 1 AU: Helios. *Journal of Geophysical Research: Space Physics*, **111**(A10), A10102.

Gosling, J. T., Eriksson, S., Skoug, R. M., McComas, D. J., & Forsyth, R. J. 2006b. Petschek-type reconnection exhausts in the solar wind well beyond 1 AU: Ulysses. *The Astrophysical Journal*, **644**(1), 613.

Gosling, J. T., Eriksson, S., Phan, T. D., Larson, D. E., Skoug, R. M., & McComas, D. J. 2007a. Direct evidence for prolonged magnetic reconnection at a continuous X-line within the heliospheric current sheet. *Geophysical Research Letters*, **34**(6).

Gosling, J. T., Eriksson, S., Blush, L. M., Phan, T. D., Luhmann, J. G., McComas, D. J., Skoug, R. M., Acuña, M. H., Russell, C. T., & Simunac, K. D. 2007b. Five spacecraft observations of oppositely directed exhaust jets from a magnetic reconnection X-line extending $> 4.26 \times 10^6$km in the solar wind at 1 AU. *Geophysical Research Letters*, **34**(20), L20108.

Gosling, J. T., Eriksson, S., McComas, D. J., Phan, T. D., & Skoug, R. M. 2007c. Multiple magnetic reconnection sites associated with a coronal mass ejection in the solar wind. *Journal of Geophysical Research: Space Physics*, **112**(A8), A08106.

Gosling, J. T., Phan, T. D., Lin, R. P., & Szabo, A. 2007d. Prevalence of magnetic reconnection at small field shear angles in the solar wind. *Geophysical Research Letters*, **34**(15), L15110.

Gosling, J.T., & Pizzo, V.J. 1999. Formation and evolution of corotating interaction regions and their three dimensional structure. *Space Science Reviews*, **89**(1), 21–52.

Hesse, M., Schindler, K., Birn, J., & Kuznetsova, M. 1999. The diffusion region in collisionless magnetic reconnection. *Physics of Plasmas*, **6**(5).

Hesse, M., Birn, J., & Kuznetsova, M. 2001. Collisionless magnetic reconnection: Electron processes and transport modeling. *Journal of Geophysical Research: Space Physics*, **106**(A3), 3721–3735.

Hietala, H., Drake, J. F., Phan, T. D., Eastwood, J. P., & McFadden, J. P. 2015. Ion temperature anisotropy across a magnetotail reconnection jet. *Geophysical Research Letters*, **42**(18), 7239–7247.

Higashimori, K., & Hoshino, M. 2015. Ion beta dependence on the development of Alfvénic fluctuations in reconnection jets. *Journal of Geophysical Research: Space Physics*, **120**(3), 1803–1813.

Horbury, T. S., Burgess, D., Fränz, M., & Owen, C. J. 2001. Three spacecraft observations of solar wind discontinuities. *Geophysical Research Letters*, **28**(4), 677–680.

Horiuchi, R., & Sato, T. 1997. Particle simulation study of collisionless driven reconnection in a sheared magnetic field. *Physics of Plasmas*, **4**(2), 277–289.

Hoshino, M., Nishida, A., Mukai, T., Saito, Y., Yamamoto, T., & Kokubun, S. 1996. Structure of plasma sheet in magnetotail: Double-peaked electric current sheet. *Journal of Geophysical Research: Space Physics*, **101**(A11), 24775–24786.

Hoshino, M., Mukai, T., Yamamoto, T., & Kokubun, S. 1998. Ion dynamics in magnetic reconnection: Comparison between numerical simulation and Geotail observations. *Journal of Geophysical Research: Space Physics*, **103**(A3), 4509–4530.

Huba, J. D. 2005. Hall magnetic reconnection: Guide field dependence. *Physics of Plasmas*, **12**(1), 012322.

Hudson, P. D. 1970. Discontinuities in an anisotropic plasma and their identification in the solar wind. *Planetary and Space Science*, **18**(11), 1611 – 1622.

Hudson, P. D. 1971. Rotational discontinuities in an anisotropic plasma. *Planetary and Space Science*, **19**(12), 1693–1699.

Hughes, W. J. 1995. The magnetopause, magnetotail, and magnetic reconnection. *In:* Kivelson, M.G., & Russell, C. T. (eds), *Introduction to space physics*. Cambridge: Cambridge University Press.

Hundhausen, A. J. 1972. Interplanetary shock waves and the structure of solar wind disturbances. *NASA Special Publication*, **308**, 393.

Hundhausen, A. J. 1995. The solar wind. *In:* Kivelson, M.G., & Russell, C. T. (eds), *Introduction to space physics*. Cambridge: Cambridge University Press.

Innocenti, M. E., Goldman, M., Newman, D., Markidis, S., & Lapenta, G. 2015. Evidence of magnetic field switch-off in collisionless magnetic reconnection. *The Astrophysical Journal Letters*, **810**(2), L19.

Johnstone, A. D., Alsop, C., Burge, S., Carter, P. J., Coates, A. J., Coker, A. J., Fazakerley, A. N., Grande, M., Gowen, R. A., Gurgiolo, C., Hancock, B. K., Narheim, B., Preece, A., Sheather, P. H., Winningham, J. D., & Woodliffe, R. D. 1997. *Peace: A Plasma Electron and Current Experiment*. Dordrecht: Springer Netherlands. Pages 351–398.

Karimabadi, H., Krauss-Varban, D., & Omidi, N. 1995. Temperature anisotropy effects and the generation of anomalous slow shocks. *Geophysical Research Letters*, **22**(20), 2689–2692.

Karimabadi, H., Krauss-Varban, D., Omidi, N., & Vu, H. X. 1999. Magnetic structure of the reconnection layer and core field generation in plasmoids. *Journal of Geophysical Research: Space Physics*, **104**(A6), 12313–12326.

Karimabadi, H., Roytershteyn, V., Vu, H. X., Omelchenko, Y. A., Scudder, J., Daughton, W., Dimmock, A., Nykyri, K., Wan, M., Sibeck, D., Tatineni, M., Majumdar, A., Loring, B., & Geveci, B. 2014. The link between shocks, turbulence, and magnetic reconnection in collisionless plasmas. *Physics of Plasmas*, **21**(6).

Khotyaintsev, Y. V., Cully, C. M., Vaivads, A., André, M., & Owen, C. J. 2011. Plasma jet braking: Energy dissipation and nonadiabatic electrons. *Physical Review Letters*, **106**, 165001.

Kleva, R. G., Drake, J. F., & Waelbroeck, F. L. 1995. Fast reconnection in high temperature plasmas. *Physics of Plasmas*, **2**(1), 23–34.

Kowal, G., Lazarian, A., Vishniac, E. T., & Otmianowska-Mazur, K. 2009. Numerical tests of fast reconnection in weakly stochastic magnetic fields. *The Astrophysical Journal*, **700**(1), 63.

Krauss-Varban, D., & Omidi, N. 1995. Large-scale hybrid simulations of the magnetotail during reconnection. *Geophysical Research Letters*, **22**(23), 3271–3274.

Kuznetsova, M. M., Hesse, M., & Winske, D. 2001. Collisionless reconnection supported by nongyrotropic pressure effects in hybrid and particle simulations. *Journal of Geophysical Research: Space Physics*, **106**(A3), 3799–3810.

Lapenta, G. 2008. Self-feeding turbulent magnetic reconnection on macroscopic scales. *Physical Review Letters*, **100**, 235001.

Lapenta, G., & Brackbill, J. U. 2002. Nonlinear evolution of the lower hybrid drift instability: Current sheet thinning and kinking. *Physics of Plasmas*, **9**(5), 1544–1554.

Lazarian, A., & Vishniac, E. T. 1999. Reconnection in a weakly stochastic field. *The Astrophysical Journal*, **517**(2), 700.

Le, A., Egedal, J., Ohia, O., Daughton, W., Karimabadi, H., & Lukin, V. S. 2013. Regimes of the electron diffusion region in magnetic reconnection. *Physical Review Letters*, **110**(13), 135004.

Le, A., Egedal, J., Ng, J., Karimabadi, H., Scudder, J., Roytershteyn, V., Daughton, W., & Liu, Y.-H. 2014. Current sheets and pressure anisotropy in the reconnection exhaust. *Physics of Plasmas*, **21**(1).

Lepping, R. P., Acũna, M. H., Burlaga, L. F., Farrell, W. M., Slavin, J. A., Schatten, K. H., Mariani, F., Ness, N. F., Neubauer, F. M., Whang, Y. C., Byrnes, J. B., Kennon, R. S., Panetta, P. V., Scheifele, J., & Worley, E. M. 1995. The WIND magnetic field investigation. *Space Science Reviews*, **71**(1-4), 207–229.

Lin, R. P., Anderson, K. A., Ashford, S., Carlson, C., Curtis, D., Ergun, R., Larson, D., McFadden, J., McCarthy, M., Parks, G. K., Rème, H., Bosqued, J. M., Coutelier, J., Cotin, F., D'Uston, C., Wenzel, K. P., Sanderson, T. R., Henrion, J., Ronnet, J. C., & Paschmann, G. 1995. A three-dimensional plasma and energetic particle investigation for the wind spacecraft. *Space Science Reviews*, **71**(1-4), 125–153.

Lin, Y., & Lee, L. C. 1993. Structure of reconnection layers in the magnetosphere. *Space Science Reviews*, **65**(1-2), 59–179.

Lin, Y., & Lee, L. C. 1995. Simulation study of the Riemann problem associated with the magnetotail reconnection. *Journal of Geophysical Research: Space Physics*, **100**(A10), 19227–19237.

Lin, Y., & Swift, D. W. 1996. A two-dimensional hybrid simulation of the magnetotail reconnection layer. *Journal of Geophysical Research: Space Physics*, **101**(A9), 19859–19870.

Liu, Y.-H., Drake, J. F., & Swisdak, M. 2011. The effects of strong temperature anisotropy on the kinetic structure of collisionless slow shocks and reconnection exhausts. II. Theory. *Physics of Plasmas*, **18**(9), 092102.

Liu, Y.-H., Drake, J. F., & Swisdak, M. 2012. The structure of the magnetic reconnection exhaust boundary. *Physics of Plasmas*, **19**, 022110.

Lottermoser, R. F., Scholer, M., & Matthews, A. P. 1998. Ion kinetic effects in magnetic reconnection: Hybrid simulations. *Journal of Geophysical Research: Space Physics*, **103**(A3), 4547–4559.

Lyon, J. G., Fedder, J. A., & Mobarry, C. M. 2004. The Lyon-Fedder-Mobarry (LFM) global MHD magnetospheric simulation code. *Journal of Atmospheric and Solar-Terrestrial Physics*, **66**(1516), 1333 – 1350.

Manapat, M., Øieroset, M., Phan, T. D., Lin, R. P., & Fujimoto, M. 2006. Field-aligned electrons at the lobe/plasma sheet boundary in the mid-to-distant magnetotail and their association with reconnection. *Geophysical Research Letters*, **33**(5).

Mandt, M. E., Denton, R. E., & Drake, J. F. 1994. Transition to whistler mediated magnetic reconnection. *Geophysical Research Letters*, **21**(1), 73–76.

McComas, D. J., Gosling, J. T., Hammond, C. M., Moldwin, M. B., Phillips, J. L., & Forsyth, R. J. 1994. Magnetic reconnection ahead of a coronal mass ejection. *Geophysical Research Letters*, **21**(17), 1751–1754.

McComas, D. J., Bame, S. J., Barker, P., Feldman, W. C., Phillips, J. L., Riley, P., & Griffee, J. W. 1998. Solar Wind Electron Proton Alpha Monitor (SWEPAM) for the Advanced Composition Explorer. *Space Science Reviews*, **86**(1-4), 563–612.

Merka, J., Szabo, A., Slavin, J. A., & Peredo, M. 2005. Three-dimensional position and shape of the bow shock and their variation with upstream Mach numbers and interplanetary magnetic field orientation. *Journal of Geophysical Research: Space Physics*, **110**(A4), A04202.

Mistry, R., Eastwood, J. P., & Hietala, H. 2015a. Detection of small-scale folds at a solar wind reconnection exhaust. *Journal of Geophysical Research: Space Physics*, **120**(1), 30–42.

Mistry, R., Eastwood, J. P., Phan, T. D., & Hietala, H. 2015b. Development of bifurcated current sheets in solar wind reconnection exhausts. *Geophysical Research Letters*, **42**(24), 10513–10520.

Mistry, R., Eastwood, J. P., Haggerty, C. C., Shay, M. A., Phan, T. D., Hietala, H., & Cassak, P. A. 2016. Observations of Hall reconnection physics far downstream of the X Line. *Physical Review Letters*, **117**, 185102.

Mozer, F. S., Bale, S. D., & Phan, T. D. 2002. Evidence of Diffusion Regions at a Subsolar Magnetopause Crossing. *Physical Review Letters*, **89**(1), 015002.

Mozer, F. S., Angelopoulos, V., Bonnell, J., Glassmeier, K. H., & McFadden, J. P. 2008. THEMIS observations of modified Hall fields in asymmetric magnetic field reconnection. *Geophysical Research Letters*, **35**(17), L17S04.

Nagai, T., Shinohara, I., Fujimoto, M., Hoshino, M., Saito, Y., Machida, S., & Mukai, T. 2001. Geotail observations of the Hall current system: Evidence of magnetic reconnection in the magnetotail. *Journal of Geophysical Research: Space Physics*, **106**(A11), 25929–25949.

Nagai, T., Shinohara, I., Fujimoto, M., Machida, S., Nakamura, R., Saito, Y., & Mukai, T. 2003. Structure of the Hall current system in the vicinity of the magnetic reconnection site. *Journal of Geophysical Research: Space Physics*, **108**(A10).

Nakamura, M. S., Fujimoto, M., & Maezawa, K. 1998. Ion dynamics and resultant velocity space distributions in the course of magnetotail reconnection. *Journal of Geophysical Research: Space Physics*, **103**(A3), 4531–4546.

Ness, N. F., Behannon, K. W., Lepping, R. P., & Schatten, K. H. 1971. Use of two magnetometers for magnetic field measurements on a spacecraft. *Journal of Geophysical Research*, **76**(16), 3564–3573.

Neugebauer, M., & Goldstein, R. 1997. Particle and field signatures of coronal mass ejections in the solar wind. *Pages 245–251 of:* Crooker, N., Joselyn, A., & Feynman, J. (eds), *Coronal Mass Ejections*. Geophysical Monograph Series, vol. 99. Washington, DC: AGU.

Neugebauer, M., & Snyder, C.W. 1962 (Nov). *Preliminary Results from Mariner-II Solar Plasma Experiment*. Tech. rept. California Inst. of Tech., Pasadena. Jet Propulsion Lab.

Nishida, A., & Nagayama, N. 1973. Synoptic survey for the neutral line in the magnetotail during the substorm expansion phase. *Journal of Geophysical Research*, **78**(19), 3782–3798.

Nishida, A., Yamamoto, T., & Mukai, T. 1997. Results of the IASTP Program The GEOTAIL mission: Principal characteristics and scientific results. *Advances in Space Research*, **20**(4), 539 – 548.

Øieroset, M., Phan, T. D., Fujimoto, M., Lin, R. P., & Lepping, R. P. 2001. In situ detection of collisionless reconnection in the Earth's magnetotail. *Nature*, **412**(6845), 414–417.

Øieroset, M., Lin, R. P., Phan, T. D., Larson, D. E., & Bale, S. D. 2002. Evidence for electron acceleration up to ~ 300 keV in the magnetic reconnection diffusion region of Earth's magnetotail. *Physical Review Letters*, **89**, 195001.

Øieroset, M., Phan, T. D., & Fujimoto, M. 2004. Wind observations of asymmetric magnetic reconnection in the distant magnetotail. *Geophysical Research Letters*, **31**(12).

Øieroset, M., Phan, T. D., Haggerty, C., Shay, M. A., Eastwood, J. P., Gershman, D. J., Drake, J. F., Fujimoto, M., Ergun, R. E., Mozer, F. S., Oka, M., Torbert, R. B., Burch, J. L., Wang, S., Chen, L. J., Swisdak, M., Pollock, C., Dorelli, J. C., Fuselier, S. A., Lavraud, B., Giles, B. L., Moore, T. E., Saito, Y., Avanov, L. A., Paterson, W., Strangeway, R. J., Russell, C. T., Khotyaintsev, Y., Lindqvist, P. A., & Malakit, K. 2016. MMS observations of large guide field symmetric reconnection between colliding reconnection jets at the center of a magnetic flux rope at the magnetopause. *Geophysical Research Letters*, **43**(11), 5536–5544.

Otto, A. 2001. Geospace Environment Modeling (GEM) magnetic reconnection challenge: MHD and Hall MHD - constant and current dependent resistivity models. *Journal of Geophysical Research: Space Physics*, **106**(A3), 3751–3757.

Owens, M. J., & Forsyth, R. J. 2013. The heliospheric magnetic field. *Living Reviews in Solar Physics*, **10**(5).

Parker, E. N. 1957. Sweet's mechanism for merging magnetic fields in conducting fluids. *Journal of Geophysical Research*, **62**(4), 509–520.

Parker, E. N. 1958. Dynamics of the interplanetary gas and magnetic Fields. *The Astrophysical Journal*, **128**, 664.

Paschmann, G., Papamastorakis, I., Sckopke, N., Haerendel, G., Sonnerup, B. U. Ö., Bame, S. J., Asbridge, J. R., Gosling, J. T., Russell, C. T., & Elphic, R. C. 1979. Plasma acceleration at the Earth's magnetopause- Evidence for reconnection. *Nature*, **282**(5736), 243–246.

Paschmann, G., Papamastorakis, I., Baumjohann, W., Sckopke, N., Carlson, C. W., Sonnerup, B. U. Ö, & Lühr, H. 1986. The magnetopause for large magnetic shear: AMPTE/IRM observations. *Journal of Geophysical Research: Space Physics*, **91**(A10), 11099–11115.

Paschmann, G., Fazakerley, A. N., & Schwartz, S. J. 1998. Moments of plasma velocity distributions. *Pages 125–158 of:* Paschmann, G., & Daly, P. W. (eds), *Analysis methods for multi-spacecraft data.* Noordwijk, Netherlands: ESA Publication Division.

Paschmann, G., Haaland, S., Sonnerup, B. U. Ö., Hasegawa, H., Georgescu, E., Klecker, B., Phan, T. D., Rème, H., & Vaivads, A. 2005. Characteristics of the near-tail dawn magnetopause and boundary layer. *Annales Geophysicae*, **23**(4), 1481–1497.

Paschmann, G., Øieroset, M., & Phan, T. D. 2013. In-situ observations of reconnection in space. *Space Science Reviews*, **178**(2-4), 385–417.

Petschek, H. 1964. Magnetic field annihilation. *NASA Special Publication*, **50**, 425–439.

Phan, T. D., Gosling, J. T., Davis, M. S., Skoug, R. M., Øieroset, M., Lin, R. P., Lepping, R. P., McComas, D. J., Smith, C. W., Rème, H., & Balogh, A. 2006. A magnetic reconnection X-line extending more than 390 Earth radii in the solar wind. *Nature*, **439**(7073), 175–178.

Phan, T. D., Drake, J. F., Shay, M. A., Mozer, F. S., & Eastwood, J. P. 2007a. Evidence for an elongated ($>$ 60 ion skin depths) electron diffusion region during fast magnetic reconnection. *Physical Review Letters*, **99**(25), 255002.

Phan, T. D., Paschmann, G., Twitty, C., Mozer, F. S., Gosling, J. T., Eastwood, J. P., Øieroset, M., Rème, H., & Lucek, E. A. 2007b. Evidence for magnetic reconnection initiated in the magnetosheath. *Geophysical Research Letters*, **34**(14), L14104.

Phan, T. D., Gosling, J. T., & Davis, M. S. 2009. Prevalence of extended reconnection X-lines in the solar wind at 1 AU. *Geophysical Research Letters*, **36**(9), L09108.

Phan, T. D., Gosling, J. T., Paschmann, G., Pasma, C., Drake, J. F., Øieroset, M., Larson, D., Lin, R. P., & Davis, M. S. 2010. The dependence of magnetic reconnection on plasma and magnetic shear: Evidence from solar wind observations. *The Astrophysical Journal Letters*, **719**(2), L199.

Phan, T. D., Paschmann, G., Gosling, J. T., Øieroset, M, Fujimoto, M., Drake, J. F., & Angelopoulos, V. 2013a. The dependence of magnetic reconnection on plasma β and magnetic shear: Evidence from magnetopause observations. *Geophysical Research Letters*, **40**(1), 11–16.

Phan, T. D., Shay, M. A., Gosling, J. T., Fujimoto, M., Drake, J. F., Paschmann, G., Øieroset, M., Eastwood, J. P., & Angelopoulos, V. 2013b. Electron bulk heating in magnetic reconnection at Earth's magnetopause: Dependence on the inflow Alfvén speed and magnetic shear. *Geophysical Research Letters*, **40**(17), 4475–4480.

Phan, T. D., Drake, J. F., Shay, M. A., Gosling, J. T., Paschmann, G., Eastwood, J. P., Øieroset, M., Fujimoto, M., & Angelopoulos, V. 2014. Ion bulk heating in magnetic reconnection exhausts at Earth's magnetopause: Dependence on the inflow Alfvén speed and magnetic shear angle. *Geophysical Research Letters*, **41**(20), 7002–7010.

Pneuman, G. W., & Kopp, R. A. 1971. Gas-magnetic field interactions in the solar corona. *Solar Physics*, **18**(2), 258–270.

Pollock, C., Moore, T., Jacques, A., Burch, J., Gliese, U., Saito, Y., Omoto, T., Avanov, L., Barrie, A., Coffey, V., Dorelli, J., Gershman, D., Giles, B., Rosnack, T., Salo, C., & Yokota, S. et. al. 2016. Fast Plasma Investigation for Magnetospheric Multiscale. *Space Science Reviews*, **199**(1).

Priest, E., & Forbes, T. 2000. *Magnetic reconnection: MHD theory and applications*. New York: Cambridge University Press.

Priest, E. R. 1995. The sun and its magnetohydrodynamics. *In:* Kivelson, M.G., & Russell, C. T. (eds), *Introduction to space physics*. Cambridge: Cambridge University Press.

Pritchett, P. L. 2001. Geospace Environment Modeling magnetic reconnection challenge: Simulations with a full particle electromagnetic code. *Journal of Geophysical Research: Space Physics*, **106**(A3), 3783–3798.

Pritchett, P. L., & Coroniti, F. V. 2004. Three-dimensional collisionless magnetic reconnection in the presence of a guide field. *Journal of Geophysical Research: Space Physics*, **109**(A1), A01220.

Pu, Z. Y., Zhang, X. G., Wang, X. G., Wang, J., Zhou, X.-Z., Dunlop, M. W., Xie, L., Xiao, C. J., Zong, Q. G., Fu, S. Y., Liu, Z. X., Carr, C., Ma, Z. W., Shen, C., Lucek, E., Rème, H., & Escoubet, P. 2007. Global view of dayside magnetic reconnection with the dusk-dawn IMF orientation: A statistical study for Double Star and Cluster data. *Geophysical Research Letters*, **34**(20), L20101.

Pulupa, M. P., Salem, C., Phan, T. D., Gosling, J. T., & Bale, S. D. 2014. Core electron heating in solar wind reconnection exhausts. *The Astrophysical Journal Letters*, **791**(1), L17.

Raeder, J., Larson, D., Li, W., Kepko, L., & Fuller-Rowell, T. 2008. OpenGGCM Simulations for the THEMIS Mission. *Space Science Reviews*, **141**(1), 535–555.

Rème, H., Aoustin, C., Bosqued, J. M., Dandouras, I., Lavraud, B., Sauvaud, J. A., Barthe, A., Bouyssou, J., Camus, Th., & Coeur-Joly, O. 2001. First multispacecraft ion measurements in and near the Earth's magnetosphere with the identical Cluster ion spectrometry (CIS) experiment. *Annales Geophysicae*, **19**(10/12), 1303–1354.

Retinò, A., Sundkvist, D., Vaivads, A., Mozer, F., André, M., & Owen, C. J. 2007. In situ evidence of magnetic reconnection in turbulent plasma. *Nature Physics*, **3**(4), 236–238.

Ricci, P., Brackbill, J. U., Daughton, W., & Lapenta, G. 2004. Collisionless magnetic reconnection in the presence of a guide field. *Physics of Plasmas*, **11**(8), 4102–4114.

Rogers, B. N., Denton, R. E., & Drake, J. F. 2003. Signatures of collisionless magnetic reconnection. *Journal of Geophysical Research: Space Physics*, **108**(A3).

Rossi, B, & Olbert, S. 1970. *Introduction to space physics*. McGraw-Hill, New York.

Runov, A., Nakamura, R., Baumjohann, W., Zhang, T. L., Volwerk, M., Eichelberger, H. U., & Balogh, A. 2003a. Cluster observation of a bifurcated current sheet. *Geophysical Research Letters*, **30**(2), 1036.

Runov, A., Nakamura, R., Baumjohann, W., Treumann, R. A., Zhang, T. L., Volwerk, M., Vörös, Z., Balogh, A., Glassmeier, K. H., Klecker, B., Rème, H., & Kistler, L. 2003b. Current sheet structure near magnetic X-line observed by Cluster. *Geophysical Research Letters*, **30**(11), 1579.

Russell, C. T., Khurana, K. K., Huddleston, D. E., & Kivelson, M. G. 1998. Localized reconnection in the near Jovian magnetotail. *Science*, **280**(5366), 1061–1064.

Saito, Y., Mukai, T., Terasawa, T., Nishida, A., Machida, S., Hirahara, M., Maezawa, K., Kokubun, S., & Yamamoto, T. 1995. Slow-mode shocks in the magnetotail. *Journal of Geophysical Research: Space Physics*, **100**(A12), 23567–23581.

Sato, T. 1979. Strong plasma acceleration by slow shocks resulting from magnetic reconnection. *Journal of Geophysical Research: Space Physics*, **84**(A12), 7177–7190.

Schoeffler, K. M., Drake, J. F., & Swisdak, M. 2011. The effects of plasma beta and anisotropy instabilities on the dynamics of reconnecting magnetic fields in the heliosheath. *The Astrophysical Journal*, **743**(1), 70.

Scholer, M. 1989. Undriven magnetic reconnection in an isolated current sheet. *Journal of Geophysical Research: Space Physics*, **94**(A7), 8805–8812.

Sergeev, V., Runov, A., Baumjohann, W., Nakamura, R., Zhang, T. L., Volwerk, M., Balogh, A., Rème, H., Sauvaud, J. A., André, M., & Klecker, B. 2003. Current sheet flapping motion and structure observed by Cluster. *Geophysical Research Letters*, **30**(6), 1327.

Shay, M. A., & Drake, J. F. 1998. The role of electron dissipation on the rate of collisionless magnetic reconnection. *Geophysical Research Letters*, **25**(20), 3759–3762.

Shay, M. A., Drake, J. F., Rogers, B. N., & Denton, R. E. 2001. Alfvénic collisionless magnetic reconnection and the Hall term. *Journal of Geophysical Research: Space Physics*, **106**(A3), 3759–3772.

Shay, M. A., Drake, J. F., Swisdak, M., & Rogers, B. N. 2004. The scaling of embedded collisionless reconnection. *Physics of Plasmas*, **11**(5).

Slavin, J. A., Acuña, M. H., Anderson, B. J., Baker, D. N., Benna, M., Boardsen, S. A., Gloeckler, G., Gold, R. E., Ho, G. C., Korth, H., Krimigis, S. M., McNutt, R. L., Raines, J. M., Sarantos, M., Schriver, D., Solomon, S. C., Trvnek, P., & Zurbuchen, T. H. 2009. MESSENGER observations of magnetic reconnection in Mercury's magnetosphere. *Science*, **324**(5927), 606–610.

Smith, C. W., L'Heureux, J., Ness, N. F., Acuña, M. H., Burlaga, L. F., & Scheifele, J. 1998. The ACE Magnetic Fields Experiment. *Space Science Reviews*, **86**(1-4), 613–632.

Smith, E. J., Slavin, J. A., Tsurutani, B. T., Feldman, W. C., & Bame, S. J. 1984. Slow mode shocks in the Earth' magnetotail: ISEE-3. *Geophysical Research Letters*, **11**(10), 1054–1057.

Sonnerup, B. 1979. Magnetic field reconnection. *Pages 45–108 of:* Lanzerotti, L.J., Kennel, C.F., & Parker, E.N. (eds), *Solar system plasma physics*, vol. 1. North-Holland Publishing Company.

Sonnerup, B., & Cahill, L. J. 1967. Magnetopause structure and attitude from Explorer 12 observations. *Journal of Geophysical Research*, **72**(1), 171–183.

Sonnerup, B., & Scheible, M. 1998. Minimum and maximum variance analysis. *Pages 185–220 of:* Paschmann, G., & Daly, P. W. (eds), *Analysis Methods for Multi-Spacecraft Data*. Noordwijk, Netherlands: ESA Publication Division.

Sonnerup, B., Paschmann, G., Papamastorakis, I., Sckopke, N., Haerendel, G., Bame, S. J., Asbridge, J. R., Gosling, J. T., & Russell, C. T. 1981. Evidence for magnetic field reconnection at the Earth's magnetopause. *Journal of Geophysical Research: Space Physics*, **86**(A12), 10049–10067.

Stone, E. C., Frandsen, A. M., Mewaldt, R. A., Christian, E. R., Margolies, D., Ormes, J. F., & Snow, F. 1998. *The Advanced Composition Explorer*. Dordrecht: Springer Netherlands. Pages 1–22.

Sweet, P. A. 1958. The neutral point theory of solar flares. *Page 123 of: Electromagnetic phenomena in cosmical physics*, vol. 6.

Swisdak, M., Rogers, B. N., Drake, J. F., & Shay, M. A. 2003. Diamagnetic suppression of component magnetic reconnection at the magnetopause. *Journal of Geophysical Research: Space Physics (19782012)*, **108**(A5).

Swisdak, M., Opher, M., Drake, J. F., & Bibi, F. Alouani. 2010. The vector direction of the interstellar magnetic field outside the heliosphere. *The Astrophysical Journal*, **710**(2), 1769.

Taylor, M. G. G. T., Escoubet, C. P., Laakso, H., Masson, A., Hapgood, M., Dimbylow, T., Volpp, J., Sangiorgi, S., & Goldstein, M. L. 2015. The Science of the Cluster Mission. *Pages 159–179 of:* Cowley, S. W. H., Southwood, D., & Mitton, S. (eds), *Magnetospheric Plasma Physics: The Impact of Jim Dungey's Research*. Cham: Springer International Publishing.

Tenerani, A., Velli, M., Rappazzo, A. F., & Pucci, F. 2015. Magnetic reconnection: Recursive current sheet collapse triggered by 'ideal' tearing. *The Astrophysical Journal Letters*, **813**(2), L32.

Terasawa, T. 1983. Hall current effect on tearing mode instability. *Geophysical Research Letters*, **10**(6), 475–478.

Trattner, K. J., Petrinec, S. M., Fuselier, S. A., & Phan, T. D. 2012. The location of reconnection at the magnetopause: Testing the maximum magnetic shear model with THEMIS observations. *Journal of Geophysical Research: Space Physics*, **117**(A1), A01201.

Trenchi, L., Marcucci, M. F., Pallocchia, G., Consolini, G., Bavassano Cattaneo, M. B., Di Lellis, A. M., Rème, H., Kistler, L., Carr, C. M., & Cao, J. B. 2008. Occurrence of reconnection jets at the dayside magnetopause: Double Star observations. *Journal of Geophysical Research: Space Physics*, **113**(A7), A07S10.

Usami, S., Horiuchi, R., Ohtani, H., & Den, M. 2013. Development of multi-hierarchy simulation model with non-uniform space grids for collisionless driven reconnection. *Physics of Plasmas*, **20**(6).

Vasyliunas, V. M. 1975. Theoretical models of magnetic field line merging. *Reviews of Geophysics*, **13**(1), 303–336.

Volwerk, M., Glassmeier, K. H., Runov, A., Baumjohann, W., Nakamura, R., Zhang, T. L., Klecker, B., Balogh, A., & Rème, H. 2003. Kink mode oscillation of the current sheet. *Geophysical Research Letters*, **30**(6), 1320.

Walker, R. J., & Russell, C. T. 1995. Solar-wind interactions with magnetized planets. *In:* Kivelson, M.G., & Russell, C. T. (eds), *Introduction to space physics*. Cambridge: Cambridge University Press.

Webb, D. F., & Howard, T. A. 2012. Coronal Mass Ejections: Observations. *Living Reviews in Solar Physics*, **9**(1), 1–83.

Wolfe, J. H. 1972. The large-scale structure of the solar wind. *NASA Special Publication*, **308**, 170.

Yamada, M., Kulsrud, R., & Ji, H. 2010. Magnetic reconnection. *Reviews of Modern Physics*, **82**(1), 603–664.

Yin, L., Daughton, W., Karimabadi, H., Albright, B. J., Bowers, K. J., & Margulies, J. 2008. Three-dimensional dynamics of collisionless magnetic reconnection in large-scale pair plasmas. *Physical Review Letters*, **101**(12), 4.

Zeiler, A., Biskamp, D., Drake, J. F., Rogers, B. N., Shay, M. A., & Scholer, M. 2002. Three-dimensional particle simulations of collisionless magnetic reconnection. *Journal of Geophysical Research: Space Physics*, **107**(A9).

Zhdankin, V., Boldyrev, S., Mason, J., & Perez, J. C. 2012. Magnetic discontinuities in magnetohydrodynamic turbulence and in the solar wind. *Physical Review Letters*, **108**, 175004.

Zweibel, E. G., & Yamada, M. 2009. *Magnetic Reconnection in Astrophysical and Laboratory Plasmas.* Annual Review of Astronomy and Astrophysics, vol. 47. Pages 291–332.